SCALE EFFECTS IN CRYSTAL PLASTICITY

A Dissertation

by

GURUPRASAD PADUBIDRI JANARDHANACHAR

Submitted to the Office of Graduate Studies of
Texas A&M University
in partial fulfillment of the requirements for the degree of

DOCTOR OF PHILOSOPHY

May 2010

Major Subject: Aerospace Engineering

SCALE EFFECTS IN CRYSTAL PLASTICITY

A Dissertation

by

GURUPRASAD PADUBIDRI JANARDHANACHAR

Submitted to the Office of Graduate Studies of
Texas A&M University
in partial fulfillment of the requirements for the degree of

DOCTOR OF PHILOSOPHY

Approved by:

Chair of Committee,	Amine Benzerga
Committee Members,	Tahir Cagin
	Dimitris Lagoudas
	Arun Srinivasa
	Alan Needleman
Head of Department,	Dimitris Lagoudas

May 2010

Major Subject: Aerospace Engineering

ABSTRACT

Scale Effects in Crystal Plasticity. (May 2010)

Guruprasad Padubidri Janardhanachar, B.E., B. M. S. College of Engineering;

M.S., Indian Institute of Science

Chair of Advisory Committee: Amine Benzerga

The goal of this research work is to further the understanding of crystal plasticity, particularly at reduced structural and material length scales. Fundamental understanding of plasticity is central to various challenges facing design and manufacturing of materials for structural and electronic device applications. The development of microstructurally tailored advanced metallic materials with enhanced mechanical properties that can withstand extremes in stress, strain, and temperature, will aid in increasing the efficiency of power generating systems by allowing them to work at higher temperatures and pressures. High specific strength materials can lead to low fuel consumption in transport vehicles. Experiments have shown that enhanced mechanical properties can be obtained in materials by constraining their size, microstructure (e.g. grain size), or both for various applications. For the successful design of these materials, it is necessary to have a thorough understanding of the influence of different length scales and evolving microstructure on the overall behavior.

In this study, distinction is made between the effect of structural and material length scale on the mechanical behavior of materials. A length scale associated with an underlying physical mechanism influencing the mechanical behavior can overlap with either structural length scales or material length scales. If it overlaps with structural length scales, then the material is said to be dimensionally constrained. On the

other hand, if it overlaps with material length scales, for example grain size, then the material is said to be microstructurally constrained. The objectives of this research work are: (1) to investigate scale and size effects due to dimensional constraints; (2) to investigate size effects due to microstructural constraints; and (3) to develop a size dependent hardening model through coarse graining of dislocation dynamics.

A discrete dislocation dynamics (DDD) framework where the scale of analysis is intermediate between a fully discretized (e.g. atomistic) and fully continuum is used for this study. This mesoscale tool allows to address all the stated objectives of this study within a single framework. Within this framework, the effect of structural and the material length scales are naturally accounted for in the simulations and need not be specified in an *ad hoc* manner, as in some continuum models. It holds the promise of connecting the evolution of the defect microstructure to the effective response of the crystal. Further, it provides useful information to develop physically motivated continuum models to model size effects in materials.

The contributions of this study are: (a) provides a new interpretation of mechanical size effect due to only dimensional constraint using DDD; (b) a development of an experimentally validated DDD simulation methodology to model Cu micropillars; (c) a coarse graining technique using DDD to develop a phenomenological model to capture size effect on strain hardening; and (d) a development of a DDD framework for polycrystals to investigate grain size effect on yield strength and strain hardening.

To my family and all my teachers

ACKNOWLEDGMENTS

I would like to take this opportunity to show my gratitude to everyone who made my stay at Texas A&M University a memorable experience that I will cherish forever. The experiences I have had during my Ph.D., both academically and otherwise, have helped me grow as a researcher and person. To this, I sincerely thank my advisor, faculty members of Texas A&M university, and friends.

My ambition to obtain a doctoral degree was fulfilled mainly because of the support and guidance I received from my advisor, Dr. Amine Benzerga. He has helped me at various stages during my Ph.D. studies and this includes providing me with a well defined dissertation problem, equipping me with the necessary tools and techniques for achieving my dissertation objectives, and willingly sharing his knowledge and ideas with me. His active participation at every facet of my research work and mentoring has shaped my overall research outlook. He endured my disorganized way of working and taught me how to look beyond my natural way of looking at a problem to gain genuine insight. Perhaps the biggest impact he has had on me, is to bring some organization in my otherwise disordered way of living and working! I am extremely grateful to him for being my mentor.

I would like to express sincere thanks to my graduate committee: Dr. D. C. Lagoudas, Dr. Arun Srinivasa, and Dr. Tahir Cagin, for their service and providing useful criticism, which has served to improve the quality of my dissertation. My special thanks to the special committee member, Dr. Alan Needleman, for serving in my graduate committee and for driving all the way from Dallas to College Station to attend my dissertation defense. His feedback on my dissertation has been very useful and has led to new avenues for further extending my research.

Many thanks are due to Dr. Daniel Kiener from Lawrence Berkeley National

sanity and perspective in my daily routine student life. It will not be a stretch to mention that I have learned a lot about myself and life from my frequent, and often long, discussions and debates with Sujay. I will always look back at these quality and well spent moments fondly. I should also mention here that presence of Shreyas Balachandran, albeit infrequently and which can only be termed as a rare event, during coffee breaks, added some much needed humor to the occasion.

Finally, I would like to thank my family members for all their support and encouragement. The importance given to education by my parents has played a large role in my pursuing for doctoral degree. They made sure that I had a comfortable life without any responsibilities and worries so that I could focus solely on my research and dissertation work. I thank my sister for cheering me up with her jubilant personality every time I called home.

TABLE OF CONTENTS

LIST OF TABLES

LIST OF FIGURES

Figure   Page

Figure   Page

CHAPTER I

INTRODUCTION

A. Motivation

A knowledge of plasticity in metals is fundamental to the understanding of metal forming in manufacturing processes, material design and failure under extreme thermomechanical conditions. Recently, there has been a widespread interest in developing micro and nano engineering for a variety of applications ranging from integrated chips, medical devices to gadgets used for entertainment purposes (Spearing, 2000; Grayson et al., 2004; Ekinci and Roukes, 2005). Micro- and nano-scale single crystals, microcrystalline (MC), ultra-fine grain (UFG) and nanocrystalline (NC) materials are used extensively in the design of these products. For successful design of these materials a thorough knowledge of materials mechanical properties are necessary. In particular, inelastic material properties like yield strength, ductility, fatigue and ductile fracture play key role in designing reliable devices. For bulk crystalline materials these properties are well established and have been successfully used in the design of large structural components. However, a number of questions arise as device/sample geometry approach the size of microstructural features. Does the material inelastic behavior change with respect to bulk? Do size effects emerge under these conditions? If so, what are the governing mechanisms that affect deformation-induced microstructure? These questions and their implications on developing new technologies have generated renewed interest amongst the research community to study inelastic behavior of crystalline materials.

This dissertation follows the style of Journal of the Mechanics and Physics of Solids.

Microstructural features like grain boundaries, particle inclusions, precipitates, bilayer interfaces, etc., impose microstructural constraints on the material. *Microstructural constraints arise in a material when the characteristic length of deformation process is no longer negligible compared with the size of microstructural features.* At these length scales material mechanical properties are known to deviate from their bulk counterparts.

The effect of grain size on mechanical strength of crystals is well documented in the literature since the pioneering work by Hall (Hall, 1951) and Petch (Petch, 1953). Advances in MC, UFG and NC materials have demonstrated that there is an increased strength, hardness, reduced ductility, enhanced diffusivity, higher specific heat, enhanced thermal expansion coefficient in comparison with conventional crystalline materials (Gleiter, 1989; Meyers et al., 2006). While some of the changes in properties are desirable some are not. For example, the increase in strength comes at the cost of decrease in ductility of the crystal, which in general is not a desirable property in the design. These challenges can be overcome by designing heterogeneous microstructures with tailored properties (Koch, 2003). This requires an understanding of structure-property relationships in these materials.

Under the absence of microstructural constraints and at scales where device dimension is of the order of characteristic length of the deformation process the strength and failure behavior in materials are known to be different from their bulk counterparts (Greer et al., 2005; Gerberich et al., 2003). These size effects are primarily due to dimensional constraints. *A material free from externally imposed constraints is said to be dimensionally constrained when the characteristic length of the deformation process is no longer negligible compared with atleast one dimension of the deformed body.* The coupling between dimensional and microstructural constraints also poses challenges in the design of thin films (Arzt, 1998). The ratio of film thick-

ness to grain size, called the grain aspect ratio, is known to have an effect on the hardening and Bauschinger behavior of thin films (Nicola et al., 2006). Other microstructural features like grain orientation and grain boundaries are also known to affect the mechanical behavior of thin films. Depending on the microstructural feature, the material can undergo strengthening or weakening (Geers et al., 2006). These scale and size effects can have serious implications on the integrity and reliability of structural components and devices.

The challenge in the field of plasticity is to predict the mechanical response of crystalline materials along with the spatial and temporal evolution of the underlying organized defect microstructure. A continuum model which can address the above challenge is still lacking. Continuum based crystal plasticity models have been successful in modeling first order crystallographic phenomena like effect of crystal texture on elastic and plastic anisotropy, formability of sheets, etc., in bulk materials. However, as currently formulated, continuum crystal plasticity models are unable to predict the emergence of dislocation substructures. A model which can predict both the mechanical response as well as the underlying defect substructure is necessary because: (i) it provides insight into the structure-property relationship in materials; (ii) it can predict evolution of defect substructure which is relevant in severe plastic deformation processes used in grain refinement and hence can help in material design; and (iii) when characteristic length scale of dislocation substructures becomes of the order of dimension of deformed body deviations from conventional/bulk behavior would emerge. Further, at reduced structural and material length scales, microstructure is no longer statistically homogeneous and redundant, thus rendering homogenization of material by assuming sources of plasticity at every material point within a representative volume element not suitable.

Gradient and nonlocal plasticity theories have been developed to address some of

the phenomenon not captured by classical continuum crystal plasticity models. These theories set out to examine the influence of strain gradients and model scale effects on yield strength and strain hardening behavior. They generally involve the computation of geometrically necessary dislocations from gradients of plastic deformation, and predict size-dependent response when macroscopic strain gradients are imposed. However, these models fail to predict the emergence of a substructure and, hence, they cannot predict size effects in the absence of macroscopic strain gradients. A notable exception maybe the theory of field dislocation mechanics (Roy and Acharya, 2006), which is still under development. In addition, when a material is dimensionally and/or microstructurally constrained the stochastic nature of a finite number of dislocations account for the material response and these models cannot capture them. They also do not account for energy due to line curvature of dislocations, dislocation source strength and distribution, source truncation due to free surfaces, and long range effects due to signed dislocation segments, which can influence the material behavior at reduced scales. The idea of a fixed length scale governing the material behavior, as proposed by these models, also may not be considered general.

The continuum crystal plasticity models, gradient and nonlocal models, are primarily predictive in their scope and do not offer significant insight into the mechanisms influencing the mechanical response of materials. In a recent review on 'Viscoplasticity of heterogeneous metallic materials' by McDowell (2008) it is highlighted that one of the main current challenges in crystalline behavior *is to identify the key competing mechanisms for important phenomena such as size effects in plasticity.* Towards this end, a framework based on discrete dislocation dynamics (DDD) offers a promising alternative to address issues related to mechanical behavior of materials at reduced length scales. This is a mesoscale computational framework where plastic flow is due to the collective motion and interaction of an ensemble of dislocations. It accounts

for the long-range nature of dislocation stress fields and short-range dislocation interactions. The effect of different length scales is implicitly accounted for in the framework so that the mechanical response is a natural outcome of the simulations. Within a single framework it offers the capability to investigate mechanical behavior of materials due to dimensional constraints, microstructural constraints and also their coupling. They can also be used as part of multiscale modeling strategy to bridge the gap between atomistic models and continuum crystal plasticity models.

In summary, a continuum model which can predict material mechanical response and the underlying organized defect substructure is still lacking. A model which can address this challenge will provide insight into the structure-property relationship in materials, aid in material design by predicting defect microstructure evolution, and help to understand the behavior of materials which are dimensionally and microstructurally constrained. Also, an understanding of material mechanical response at reduced length scales is needed for designing reliable structural components, and efficient MEMS and NEMS devices. This has motivated the need to undertake the current study using DDD framework, which offers a promising alternative to address the issues raised by material behavior at reduced length scales.

B. Goal and objectives

The goal of this research is to further the understanding of crystal plasticity, particularly at reduced structural and material length scales. The focus is on plastic behavior of materials at low homologous temperatures. Limitations on structural length scale imposes dimensional constraints on the material. The material length scale, grain size, of a polycrystal leads to microstructural constraint on the material. A study on coupling effect due to both dimensional and microstructural constraints on the

material is not considered in this study.

The objectives of this research work are: (1) investigate scale and size effects due to dimensional constraints; (2) investigate size effects due to microstructural constraints; and (3) develop a size dependent hardening model through coarse graining of dislocation dynamics.

C. Background

1. Classical crystal plasticity

Historically metals have been subjected to plastic deformation by cold and hot working processes to develop specialized components like coins, wires, wheels etc. It was only after the work by Ewing and Rosenhain (Ewing and Rosenhain, 1900), during the late 19th century, understanding of mechanisms leading to the plastic behavior in metals began to mature. Their optical micrographs of polycrystalline Pb identified that plastic deformation took place by slip. They identified slip steps, formed by the development of slip bands along specific planes, at the specimen surfaces. They thus concluded that plastic deformation was caused by simple shear of certain families of planes along certain preferred directions. This observation was remarkable because it was only latter that the crystalline structure of metals was ascertained (Hull, 1919).

Following the discovery of the crystalline structure of metals, Taylor and Elam (1925), Orowan (1934) and Polanyi (1922) all independently confirmed that plastic yield would begin on a slip system when the resolved shear stress reached a critical value, independent of the orientation of the tensile axis. This is what is now commonly known as the Schmid law (Schmid, 1924). However, certain experimental observations like the observed shear strength in metals being almost orders of magnitude less than the theoretical shear strength could not be convincingly explained

during the 1920s. In the early 1930s Taylor (1934), Orowan (1934), and Polanyi (1934) explained the micromechanics of slip based on *dislocations*. Dislocations are linear lattice imperfections in crystalline materials. Taylor (1934) explained that the shear stress necessary for the motion of dislocations is very less and hence their glide results in shear strength which is more consistent with the observed experiments.
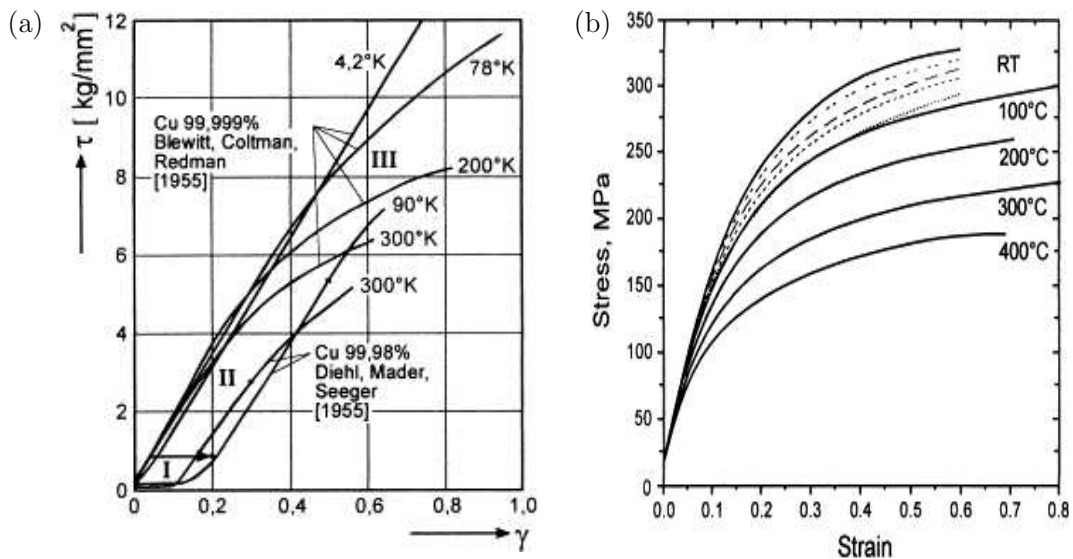
Fig. 1. (a) Shear stress versus shear strain curves for Cu single crystals of different orientations and for single slip orientation; (b) Compressive stress versus strain response of Cu polycrystals. This figure is taken from Kocks and Mecking (2003).

Typical shear stress versus shear strain response of bulk Cu single crystals in tension is shown in Fig. 1a (Kocks and Mecking, 2003). Fig. 1b shows typical stress versus strain response of Cu polycrystals (Kocks and Mecking, 2003). The deformation in both single and polycrystals is characterized by initial elastic response, yielding, and hardening. In particular three distinct regimes, differentiated by the slope of the curve, can be identified in single crystals oriented for single slip. These

three regimes are commonly called Stage I, Stage II and Stage III hardening. In single crystals oriented for multiple slip stage I is absent and the response is predominantly stage II and stage III hardening. This response is very similar to the hardening response observed in polycrystals. Later, advances in the field established that stage I hardening depends strongly on the orientation of the crystal; stage II hardening is athermal in nature and is rather insensitive to strain-rate and temperature with its value being a constant in the range of $\mu/200 - \mu/100$ (where μ is the shear modulus); and stage III is strongly affected by temperature and strain-rate (Kocks and Mecking, 2003).

One major challenge in developing a model is to qualitatively and quantitatively establish a relation between material microstructure and its macroscopic response. In the context of plastic deformation in metals and metallic alloys this amounts to identifying and describing lattice defects, for example dislocations, including their collective static and dynamic behavior that are responsible for macroscopic properties. Over the past few decades significant progress has been made in incorporating micromechanics, idealized by phenomenological representation, in continuum descriptions of plastic deformation. Early development of constitutive laws for elastic-plastic deformation of crystals is attributed to Taylor (1938). Since then, work by Hill (1966), Hill and Rice (1972) and Asaro and Rice (1977) have substantially contributed towards modeling of plastic deformation in materials. A fundamental premise upon which these models have been developed is that material flows through crystal lattice via dislocation motion; but the lattice with material embedded on it undergoes elastic deformation. Also, polycrystals are approximately modeled as a collection of single crystals. The readers are referred to Asaro (1983), Nagdhi (1990), and Dawson (2000) for an extensive overview on modeling aspects in crystal plasticity.

a.   Experiments on microstructurally constrained materials

Early experiments on mild steel by Hall (Hall, 1951) and Petch (Petch, 1953) have shown the sensitivity of polycrystal yield strength to grain size. They consistently observed an increase in polycrystal yield strength (σ_y) with decrease in grain size. This is commonly known as the Hall-Petch effect and is given by the equation,

$$\sigma_y = \sigma_0 + k_1 d^{-n} \tag{1.1}$$

where, σ_0, k_1 and n are constants. σ_0 is the friction stress that may include contributions from solutes and particles within the material. A generalization of Eq.(1.1) can be made for the flow stress if the constants σ_0 and k_1 are considered to be functions of strains. Hall-Petch relation has been found to be applicable for grain sizes all the way down to 10 nm as seen in Fig. 2. Recent experimental work (Ohno and Okumura, 2007) has demonstrated that the value of the exponent n is 0.5 for polycrystals with grain sizes up to 5 μm and below this it increases to almost 1.0. This increase in strength is usually attributed to dislocation pile-up at grain boundaries or due to the development of strain gradients within the material due to a mismatch in the grain orientations. Below 10 nm Hall-Petch relation breakdown and experimental findings have reported an inverse Hall-Petch effect (Chokshi et al., 1989; Kumar et al., 2003). This has been attributed to diffusional creep in NC samples (Chokshi et al., 1989) but there have been conflicting findings from other works that attribute the break down to the presence of flaws (Weertman, 2002; Meyers et al., 2006).

At strains beyond 5% experimental results show that the response of the polycrystal is weakly dependent on the grain size, and the work hardening rates converged to that of a coarse grained polycrystal Huang and Hansen (2003). However, within the grain size dependent strain regime, polycrystals with grain size $d < 5$ μm show a
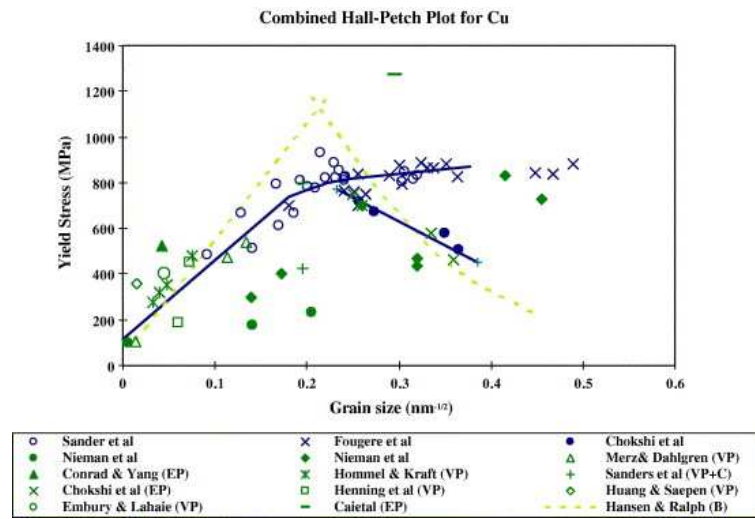
Fig. 2. Yield stress versus grain size plot for Cu polycrystals with grain size varying from coarse to nano range. The plot is taken from Meyers et al. (2006).

low transient hardening rate (Flinn et al., 2001; Sinclair et al., 2006; Dao et al., 2007). UFG Cu obtained from equal channel angular extrusion (ECAE) have demonstrated evidence of stable microstructure against fatigue-induced changes (Maier et al., 2006), flow stress anisotropy and Bauschinger effect (Haouaoui et al., 2006), in contrast to coarse grained specimens. The average grain size of a polycrystal is also known to affect the strain-rate sensitivity of the material (Zhang et al., 2004). These observations point towards the influence of microstructural constraint like grain size on the inelastic behavior of crystals.

There is a large body of experimental data that highlight the influence of microstructure and dimensional constraints on the inelastic response of crystals (Arzt, 1998). The high shear strength observed in the twisting of thin Cu wires (Fleck et al., 1994), increased bending hardening of ultra thin beams (Stölken and Evans, 1998) and indentation depth dependent hardness of crystals (Swadener et al., 2002) are some of

the examples that highlight the sensitivity of material properties to crystal dimensions. In all these experiments the material was subjected to an external loading, which led to the development of strain gradients. Ashby (Ashby, 1970) showed that the presence of strain gradients lead to the development of geometrically necessary dislocations in the materials for compatibility reasons, which lead to the observed size effect.

b. Experiments on dimensionally constrained materials

The size effects described till now are mainly due to the development of strain gradients within the material either due an imposed external loading or due to microstructural constraint. The question is does size effect exist in the absence of strain gradients. Recent micropillar experiments (Uchic et al., 2004; Dimiduk et al., 2005; Greer et al., 2005; Volkert and Lilleodden, 2006; Frick et al., 2008) have shown that size effects emerge even in unconstrained small samples subjected to homogeneous deformation.

One of the earliest work to explore the effect of only dimensional constraints on mechanical behavior (Suzuki et al., 1956; Fourie, 1967, 1968) reported almost no change in the yield strength and a slight increase in the hardening rate of submillimeter Cu single crystals. With advance in technology for processing micro and nano single crystals, there has been a surge of interest in exploring the size effects of unconstrained crystals using micro-bending, micro-compression and micro-tension experiments (see Figs 3a-c). In a typical micro-compression experiment, focus ion beam (FIB) microscope along with ion lathe technique is used to machine cylindrical compression samples into the surface bulk crystals, leaving the sample attached to the bulk at one end as shown in Fig. 3b. Nanoindentation using a flat tip nanoindenter is used to subject the micron and nano crystals under compression (Uchic

et al., 2004). Experiments on [269] Ni and Ni-based alloys of size in the range of 40 to 1.0 μm (Uchic et al., 2004; Dimiduk et al., 2005) have shown an increase in the strength of crystals upto 15 times (as compared to bulk Ni) with decrease in sample size. However, they did not observe a significant increase in the hardening rate of the crystals. They noted that as the crystal size approached 1 μm the stress-strain response was characterized by frequent strain bursts and increased finite discrete slip bands along the gauge length of the crystal as shown in Fig. 3b.

Experiments on $< 001 >$ oriented Au crystals below 1 μm also showed a trend towards increase in crystal strength with decrease in its size (Greer et al., 2005; Greer and Nix, 2006; Brinckmann et al., 2008). Flow stress as high as 800 MPa was reached in 200 nm specimen as compared to 25 MPa in a bulk sample at 10% strain. A comparative experimental study between Au (FCC crystal) and Mo (BCC crystal) showed that the slope of strengthening in Au is more than twice than that of Mo (Brinckmann et al., 2008). The Au specimens did not show significant increase in hardening rate but Mo specimens demonstrated substantial increase in hardening rate with decrease in specimen size.

The effect of specimen size and crystallographic orientation on Au crystals was studied by Volkert and Lilleodden (2006). They reported an increase in yield stress (defined at 5% strain) and hardening rate with decrease in specimen size. The hardening rate was determined to be as high as 50 times the bulk value of $\mu/100$. There were no significant differences quantitatively in the values of yield stress and hardening rate with changes in crystal orientation. However, the number of active slip system did depend on the crystal orientation. An increase in hardening rate by 10 times was reported in Frick et al. (2008) from experiments on [111] Ni crystals. The increase in flow stress with decrease in crystal size in their experiments are as shown in Fig. 3d. The critically resolved shear stress determined at 3% strain was in good

agreement with the data from [269] Ni reported in Dimiduk et al. (2005).
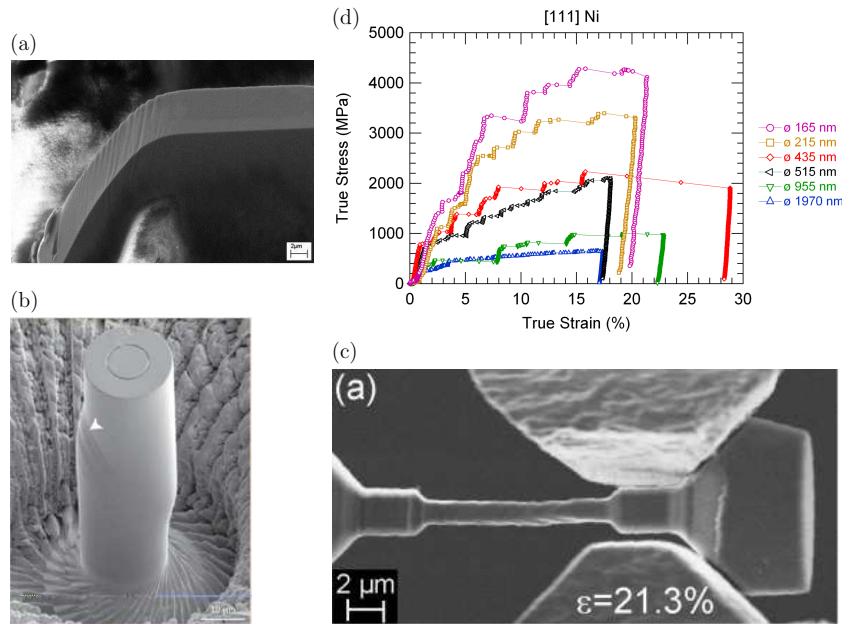
Fig. 3. Size effects due to dimensional constraints: (a) Scanning electron microscope (SEM) micrograph image of a deformed Cu microcrystal showing slip traces on the surface (Motz et al., 2005); (b) SEM image of a deformed Ni microcrystal subjected to micro-compression experiment showing traces of slip on the surface (Uchic et al., 2004); (c) SEM images of Cu microcrystals taken during in situ micro-tension experiment (Kiener et al., 2008a); and (d) Representative compressive true stress versus true strain response of Ni micropillars (Frick et al., 2008).

Several explanations have been proposed to explain the observed strengthening with decrease in specimen size. The role played by single ended dislocation sources on strengthening has been put forward in (Rao et al., 2007; Norfleet et al., 2008). In (Greer et al., 2005; Brinckmann et al., 2008) the competition between dislocation nucleation and dislocation exit at the free surface leading to a 'dislocation starved' condition has been proposed as the reason for strengthening. This hypothesis was

also supported by in-situ TEM compression experiments on Ni (Shan et al., 2008). A lack of favorable dislocation sources for nucleation thus requiring higher stresses for the nucleation of new dislocations for plastic deformation was the reason reported in Volkert and Lilleodden (2006). Combination of dislocation-dislocation interaction and higher stresses required for the nucleation of new dislocations was the reason proposed in Frick et al. (2008) for the observed increase in hardening rate and flow stress with decrease in sample size.

The influence of processing techniques used to produce micropillars on the observed size effects cannot be completely ruled out. Experiments on Mo-alloy specimens produced from directional solidification techniques behave like dislocation-free materials, with their yield stresses approaching theoretical strength. In these experiments (Bei et al., 2008a,b) there was no evidence of size effects. They argue that FIB techniques introduces extrinsic defects on the layer adjacent to the milled surface. These defects may include dislocations, implanted Ga ions or even intermetallic compounds and adjacent amorphous layers. Recent advances in conducting in situ tension experiments of micron and submicron Cu crystals have overcome the limitations on the aspect ratio of specimens used for conducting the compression tests (Kiener et al., 2008a). A higher hardening rate was demonstrated by specimens with aspect ratio 1:1 as compared to specimens with aspect ratio 5:1 and higher. Electron back scatter diffraction (EBSD) scans showed the development of significant misorientations of the crystal lattice of low aspect ratio specimens. These misorientations were believed to be caused by dislocation pile-ups and contribute to the hardening of the crystals.

The review of experimental facts highlight the lack of sufficient understanding regarding the underlying mechanism governing the size affected strengthening. The inconsistency in the hardening rate observed by different experimental groups is also not completely understood. The challenge in experiments is to isolate competing

mechanisms or factors contributing to the size affected plastic behavior in crystals. A theoretical undertaking, which provides control over the type of boundary condition, crystal form and its initial conditions, will be able to shed more light on the issue of scale effects in crystal plasticity.

2. State of the art modeling techniques

a. Gradient-based plasticity models

Classical crystal plasticity models cannot predict size effects observed in dimensionally and microstructurally constrained materials. These models do not possess length scale in their constitutive theory which can capture the size effects. Higher-order gradient theories, motivated by the observation of large strain-gradients in experiments (Fleck et al., 1994), incorporate a characteristic length scale as material property to capture the size effect. The framework of geometrically necessary dislocations (GNDs) introduced by Nye (Nye, 1953) and latter Ashby (Ashby, 1970) has provided a physical basis for higher-order gradient models. In these models plastic strain gradients in materials is related to the emergence of GNDs for maintaining lattice compatibility. This section provides a brief overview of mathematical description of GND density and its subsequent use in higher-order gradient models.

In a region of a crystal large enough for the effects of the dislocations within it to be averaged Nye defined a tensor α_{ij} (Nye, 1953). Nye defined this tensor as a number density of lines piercing a plane. The tensor α_{ij} is a representation of dislocations whose geometric properties are not canceled by other dislocations in the crystal lattice. This tensor is defined such that the net Burgers vector $\mathbf{B}$ of a unit area normal to the unit vector $\mathbf{r}$ is given by

$$B_i = \alpha_{ij} r_j \tag{1.2}$$

Consider dislocations with length parallel to the unit vector $\mathbf{t}$ and Burgers vector $\mathbf{b}$. If there are n dislocations crossing unit area normal to $\mathbf{t}$ then the number crossing unit area normal to unit vector $\mathbf{r}$ is given by $n\mathbf{t}.\mathbf{r}$. The corresponding Burgers vector is $\mathbf{b}(n\mathbf{t}.\mathbf{r})$, which when written in index notation takes the form,

$$B_i = b_i(nt_j r_j) \tag{1.3}$$

Comparing Eq.(1.3) and Eq.(1.2) the Nye's tensor α_{ij} is determined to be,

$$\alpha_{ij} = nb_i t_j \tag{1.4}$$

Arsenlis and Parks (1999) proposed a definition of Nye's tensor based on the description of dislocation density as line length in a reference volume. Here, for a dislocation with Burgers vector $\mathbf{b}$ and local unit tangent line direction $\mathbf{t}$, the Nye's tensor is defined as,

$$\alpha_{ij} \equiv \frac{1}{V} \int_L b_i t_j \mathrm{d}s \tag{1.5}$$

where V is the reference volume; $\mathrm{d}s$ is an element of arc length along the dislocation line; and L the total length of dislocation line within V. Considering each of the dislocation line segments separately with constant Burgers vector, Eq.(1.5) can be re-written as,

$$\alpha_{ij} \equiv \frac{1}{V} \sum_\xi^N b_i^\xi \int_l t_j^\xi \mathrm{d}s^\xi \tag{1.6}$$

where, l is the length of a dislocation segment of type ξ and N is the number of dislocation segments. The integral relation proposed has the the property of averaging the dislocation properties within a volume. Also, it can be observed from Eq.(1.6) that the only information needed from a dislocation line segment to calculate the Nye

tensor is its Burgers vector and two endpoints. Hence, Eq.(1.6) can be re-written as

$$\alpha_{ij} = \frac{1}{V} \sum_{\xi}^{N} \bar{l}^{\xi} b_i^{\xi} \bar{t}_j^{\xi} \qquad (1.7)$$

where, $\bar{l}^{\xi}$ is the secant length of the dislocation segment ξ; and $\bar{t}^{\xi}$ is the average tangent vector of dislocation segment ξ. Noting that dislocation density is line length in a volume; the summation of geometric dislocation lengths, $\bar{l}^{\xi}$, in a reference volume V, can be replaced by a summation of geometric dislocation density, ρ_{GND}^{xi}, in the volume

$$\alpha_{ij} = \sum_{\xi}^{N} \rho_{\text{GND}}^{\xi} b_i^{\xi} \bar{t}_j^{\xi} \qquad (1.8)$$

where, $\rho_{\text{GND}}^{\xi} \equiv \frac{\bar{l}^{\xi}}{V}$. It is this portion of the total dislocation density which has geometric consequences. The tensorial sum determined in Eq.(1.8) can be explicitly written for edge and screw dislocation line segments as,

$$\alpha_{ij} = \sum_{\kappa=1}^{N_s} \left(\rho_{\text{e}+}^{\kappa} - \rho_{\text{e}+}^{\kappa} \right) b_i^{\kappa} t_j^{\kappa} + \sum_{\kappa=1}^{N_s} \left(\rho_{\text{s}+}^{\kappa} - \rho_{\text{s}+}^{\kappa} \right) b_i^{\kappa} m_j^{\kappa} \qquad (1.9)$$

where subscripts ρ_{e} and ρ_{s} denote pure edge and screw dislocation density, respectively; the sign of the subscript + or - indicates the polarity of the dislocation density; κ denotes the slip-system; $\mathbf{m}^{\kappa}$ is unit vector in reference configuration corresponding to the slip direction; and $\mathbf{t}^{\kappa}$ corresponds to tangent line direction of edge dislocation density.

Fleck et al. (1994) developed a strain gradient theory of rate independent plasticity in a phenomenological manner based on dislocation theory to model size effects observed in their torsion experiments on micron Cu specimens. An internal constitutive length parameter was introduced in the constitutive relation to scale the rotational gradients. Physically, this material length parameter was related to the storage of GNDs. The model was successful in predicting the size dependent tor-

sional behavior of micron Cu wires and bending of thin beams (Stölken and Evans, 1998). It was also used to predict the indentation hardness but could not predict the 200 to 300% increase reported in experiments (De Guzman et al., 1993). Hence, this model was extended to account for both rotation and stretch gradient of deformation in the constitutive model by Fleck and Hutchinson (2001). This resulted in the introduction of two length scales in the constitutive relation. Nix and Gao (Nix and Gao, 1998) introduced the contribution of GND density directly in the Taylor relation between shear strength and dislocation density of the crystal. All the models described above are phenomenological in nature and depended on experiments to determine the material length scale. This drawback was overcome by the development of *mechanism based strain gradient plasticity* (Gao et al., 1999). They proposed a multiscale hierarchical framework in which at the microscale level the accumulation of GND density leads to an increase in the flow stress according to the Taylor relation. At the mesoscale they introduced higher order stresses as thermodynamic conjugates of the strain gradient such that the Clausius-Duhem inequality is satisfied.

There have been attempts to extend continuum crystal plasticity theory to account for strain gradients. This involves quantitatively interpreting and accounting for imperfect lattice structure in crystals. One way is to introduce strain gradient effect in the strain energy of the material. Maximum dissipation rate hypothesis can then be used to obtain the governing equations of motion for the material (Baek and Srinivasa, 2003). Acharya and Bassani (2000) showed that elastic distortion of the lattice is not compatible with a deformation that can be derived from a continuous displacement field. The lattice incompatibility is capable of representing lattice imperfections associated with GNDs. The lattice incompatibility is characterized by the gradient of the elastic distortion field. This term introduces an evolving length scale when introduced in the hardening response. This approach coupled with the

admittance of Taylor law at the individual grain level was used to predict grain size dependent hardening response (Acharya and Beaudoin, 2000) and the Hall-Petch relation (Evers et al., 2002; Abu Al-Rub and Voyiadjis, 2006) in polycrystals.

Strain gradient plasticity theories have been successful in predicting and explaining size effects observed in crystals due to an imposed gradient on the boundary and due to microstructural constraints. However, state of the art strain gradient plasticity theories are incapable of predicting size effects arising solely due to dimensional constraints in materials. Further, they are not capable of predicting the underlying defect substructure and its evolution with deformation.

b. Discrete dislocation dynamics

Discrete dislocation dynamics (DDD) framework provides a useful tool to address issues related to mechanical behavior of materials at a length scale intermediate between atomistic and continuum. The need for understanding the origins of heterogeneous plasticity and pattern formation in crystals (Mughrabi, 1983) lead to the development of DDD (Kubin et al., 1992; Kubin and Canova, 1992). In DDD, appropriate equations of motion (viscous drag) are integrated to obtain dynamical evolution of a system of dislocations. The characteristics of DDD framework include: (i) probe giving the accurate dynamical evolution of a dislocation system for a given set of atomistically-informed rules for short-range interactions; (ii) provides for determination and prediction of certain material properties at nearly atomic scale; (iii) offers a benchmark for verification of existing and yet to be developed continuum material models; and (iv) accurate integration requires time steps in the nanosecond range, limiting the total simulation time to less than a second on today's processors.

Typical boundary value problem (BVP) involves determining the displacement, strain and stress fields in a body Ω containing N dislocations subjected to boundary

tractions T_0 on surface S_f and displacements U_0 on surface S_u. The singular fields associated with dislocations preclude the direct application of finite element method (FEM) to solve the BVP. Lemarchand et al. (2001) developed a discrete-continuum framework to solve the BVP. In this framework, a 3D-DDD model solves for the dynamic and local interactions of dislocation lines and computes the plastic strain generated by dislocation line. FEM is then used to compute the displacement field that is the solution for the BVP. Currently, this procedure is limited to one dislocation per mesh element due to breakdown of the interpolation procedure at short distances. The mesh has to be refined down to a value that is typically the smallest distance between interacting segments, which sets limitations to the dimensions of the simulated configurations. More recently, extended finite element method (XFEM) has been used to solve the BVP (Gracie et al., 2007). In this model, FEM is used to determine the total stress field subject to prescribed internal discontinuities, i.e., dislocation slip. Displacement is decomposed into a continuous part and a discontinuous or an enriched part. Two enrichment functions are used in the model. The first adds a discontinuity on a closed-surface in the domain, for e.g., edge dislocation enrichment introduces a tangential jump of constant magnitude across slip plane. The second enrichment adds a field defined by analytical functions characteristics of core mechanics in the vicinity of core. However, the computational cost due to the need for refined mesh to account for local gradients in the fields is very large in this method.

3D and 2D DDD frameworks have been developed based on the method of superposition (Amodeo and Ghoniem, 1990; Kubin et al., 1992; Van der Giessen and Needleman, 1995; Zbib et al., 1998). In this method, the solution to the BVP is determined by superimposing the analytical infinite domain solution of each dislocation and an image field. FEM is used to determine the solution with boundary

tractions and displacements chosen to cancel the tractions and displacements due to infinite dislocation fields on the boundary. The computation of the long range dislocation interactions in this method goes as $O(N^2)$. This method has been extensively used in various studies like inelastic behavior of composite material (Van der Giessen and Needleman, 1995; Cleveringa et al., 1997), bending of crystals (Cleveringa et al., 1999), and fracture in crystals (Cleveringa et al., 2000; Balint et al., 2005a). Recently, both 3D and 2D DDD have been used to investigate size effects due to dimensional constraints (Deshpande et al., 2005; Benzerga and Shaver, 2006; Tang et al., 2007; Rao et al., 2008). 2D DDD frameworks have also been used to investigate the effect of microstructural constraints, imposed by grain boundaries, on the mechanical behavior of crystalline materials (Biner and Morris, 2002, 2003; Balint et al., 2005b). A detailed review of literature related to the application of DDD framework to investigate size effects due to dimensional constraints is provided in Chapter IV. Chapter VI provides a review of the application of DDD framework to investigate the effect of microstructural constraints, imposed by grain boundaries, on the mechanical behavior of crystalline materials.

c.   Molecular dynamics studies

Molecular dynamics simulation is being used to investigate the effect of dimensional as well as microstructural constraints on the strength of crystals. These simulations provide useful information regarding the underlying mechanisms leading towards strengthening in crystals under different constraints. Horstemeyer et al. (2001) performed molecular dynamics simulations using the embedded atom method (EAM) on Ni single crystals. Their simulations predicted size effects due to dimensional constraints with yielding dominated by nucleation of dislocations from the free surface of the crystal. The yield surface was found to scale inversely with the volume to surface

area ratio. Molecular dynamics simulations on Ni single crystals was also performed by Cao et al. (2008). They have explored the size range between 4 to 16 nm. The simulations predict size effects on the strength with the yield strength of the 4 nm crystal approaching close to the theoretical yield. The stress-strain response demonstrates zigzag like response. However, the size ranges explored in these calculations have not been able to be achieved in the experiments. Further, these molecular dynamics simulations show a trend towards softening upon yielding while experimental observations have been consistently showing a trend towards hardening (Volkert and Lilleodden, 2006; Frick et al., 2008).

Grain size effects on the strength and the validity of Hall-Petch effect in nanocrystalline materials have been explored using molecular dynamics simulations. Simulations with grain size in the range of 30 nm - 10 nm have predicted Hall-Petch like behavior (Van Swygenhoven and Spaczer, 1999). Below 10 nm experiments have predicted an inverse Hall-Petch like behavior (Dao et al., 2007). These observations were also made by recent molecular dynamics simulations (Yamakov et al., 2004; Wolf et al., 2005). Their simulations suggested a cross-over between a dislocation dominated deformation process to grain boundary mediated process with decrease in grain size. Based on these observations they have developed a stress-grain size deformation mechanisms maps. Simulations have also described the role of diffusion creep on inverse Hall-Petch effect (Desai et al., 2008). Large-scale molecular dynamics simulations have also been performed to investigate rate controlling mechanism of yielding in twinned Au nanowires (Deng and Sansoz, 2009b).

Molecular dynamics simulations are useful to predict and probe mechanisms for predicting grain size effects below 10 nm. Current computational power limit their analysis for a wide range of grain sizes varying from micrometers to a few nanometers. They are severely restricted by time scale limitations, which prevent

them from exploring large strain deformation mechanisms.

D.   Outline of the dissertation

This dissertation consists of six chapters. Chapter I presents motivation, goal, objectives and background literature related to the undertaken research work in this study. The review of literature particularly highlights recent advances made in understanding plastic behavior due to dimensional and microstructural constraints. The challenges faced by the modeling community to develop phenomenological, analytical and computational frameworks to simulate material behavior due to dimensional and microstructural constraints is succinctly presented. This overview establishes the capability of the mesoscale modeling technique, discrete dislocation dynamics (DDD), to address issues related to plastic deformation in crystalline materials due to dimensional and microstructural constraints.

DDD is used as the computational tool towards achieving the objectives of this research work. Chapters II, III and IV present results related to effect of dimensional constraint on plastic behavior. Simulation results shown in Chapter II establish that there is a significant increase in the strength of crystals with decrease in crystal dimension. More importantly, simulations predicted that not only flow stress but hardening rate also increases with decrease in crystal size for the first time. An analysis of microstructure evolution revealed the emergence of scale dependent GND density with the density being higher in smaller crystals.

Chapter III presents comparison between experimental measurements and simulation results for the evolution of plastic deformation and strain hardening in Cu micropillars. Both experiments and simulations showed a size affected hardening behavior in micropillars. The flow stress and hardening rate predicted from simulations

are in good agreement with the experimental results. Significant lattice misorientations were found in deformed pillars from experiments and simulations. Chapter IV provides a summary of the lessons learned and the contributions made from this study (Chapters II and III) as well as other work not yet published in light of the recent micropillar experiments and simulations available in the literature.

In Chapter V development of a phenomenological framework to model size dependent hardening in crystals is presented. This model is based on direct coarse graining of dislocation dynamics. The coarse graining technique, which captures the spatial and temporal evolution of defect microstructure, holds the promise of connecting the microstructure and the effective response in crystal plasticity.

Effect of microstructural constraint, due to grain size, on crystal plasticity is investigated in Chapter VI. In this chapter, description of the development of a DDD based polycrystal computational tool with enhanced short-range dislocation representation is presented. The results from the simulation show an increase in flow stress and hardening rate with decrease in grain size. The simulations are able to predict the Hall-Petch behavior observed in experiments.

CHAPTER II

SIZE EFFECTS UNDER HOMOGENEOUS DEFORMATION OF SINGLE
CRYSTALS: A DISCRETE DISLOCATION ANALYSIS *

A.   Overview

Mechanism-based discrete dislocation plasticity is used to investigate the effect of size on micron scale crystal plasticity under conditions of macroscopically homogeneous deformation. Long-range interactions among dislocations are naturally incorporated through elasticity. Constitutive rules are used which account for key short-range dislocation interactions. These include junction formation and dynamic source and obstacle creation. Two-dimensional calculations are carried out which can handle high dislocation densities and large strains up to 0.1. The focus is laid on the effect of dimensional constraints on plastic flow and hardening processes. Specimen dimensions ranging from hundreds of nanometers to tens of microns are considered. Our findings show a strong size dependence of flow strength and work-hardening rate at the micron scale. Taylor-like hardening is shown to be insufficient as a rationale for the flow stress scaling with specimen dimensions. The predicted size effect is associated with the emergence, at sufficient resolution, of a signed dislocation density. Heuristic correlations between macroscopic flow stress and macroscopic measures of dislocation density are sought. Most accurate among those is a correlation based on two state variables: the total dislocation density and an effective, scale-dependent measure of signed density.

—————

B.   Introduction

Plastic deformation in small volumes is characterized by well documented deviations from bulk behavior. Of particular significance among these deviations is the size-dependence of plastic flow properties at the micron and sub-micron scale; see e.g. (Fleck et al., 1994; Stölken and Evans, 1998; Nix and Gao, 1998; Swadener et al., 2002; Uchic et al., 2004; Greer et al., 2005; Dimiduk et al., 2005). This scale dependence of strength poses serious challenges to the effective design of small-scale structures, let alone the challenge of quantifying the uncertainty that results from the spread in the values of strength upon scale reduction.

Under circumstances where a strain gradient is imposed, such as under indentation (Nix and Gao, 1998; Swadener et al., 2002), the size effect is commonly attributed to a density of geometrically necessary dislocations (GNDs), which is needed to accommodate the so-imposed strain gradient. The connection between GNDs and what may be viewed as the plastic portion of the strain gradient is the underlying concept behind various augmented plasticity theories developed in recent years (Fleck et al., 1994; Gao et al., 1999; Fleck and Hutchinson, 2001; Acharya, 2001; Gurtin, 2002; Acharya, 2004); see (Forest and Sievert, 2003) for an exhaustive description of several classes of non-local theories.

By way of contrast, in the absence of strain gradients existing nonlocal plasticity theories would predict a size-independent response. Recent experiments have yet shown compelling evidence of size-dependency in micropillar compression (Uchic et al., 2004; Greer et al., 2005; Dimiduk et al., 2005; Volkert and Lilleodden, 2006; Greer and Nix, 2006). The fact that size effects also emerge under states of macroscopically homogeneous deformation has motivated alternative explanations of size-dependent plastic behavior. Dimiduk et al. (2005) investigated possible intrinsic

changes to dislocation mechanisms upon scale reduction and conclude that the observed size-dependent flow may be dominated by stochastic effects, including dislocation generation by a stress-dependent source distribution. This rationale of size-dependent flow being controlled by multiplication processes is corroborated by a number of discrete dislocation dynamics calculations of thin films (von Blanckenhagen et al., 2001), micropillar compression (Benzerga and Shaver, 2006) and grain-boundary sources (Espinosa et al., 2006). It remains that, while multiplication-controlled plasticity would significantly affect the elastic-plastic transition, it alone could not explain the effect of size on work-hardening; (e.g., Volkert and Lilleodden, 2006). It is difficult indeed to conclude from the micropillar experiments of Greer et al. (2005) and Dimiduk et al. (2005) whether the strengthening that occurs upon scale reduction is the result of increased yield strength or increased work-hardening rate at small strains.

Here we perform calculations where size effects emerge in the absence of macroscopic strain gradients and where the behavior is not multiplication controlled. Similar calculations were recently reported by Deshpande et al. (2005) but their calculations did not include forest hardening. Attention is focused on circumstances under which apparent macroscopic yield is essentially size independent but, due to microstructure evolution, the subsequent work hardening behavior is strongly size dependent. In that sense, the calculations here are complementary of those of Benzerga and Shaver (2006) and Deshpande et al. (2005) and aim at providing an alternative explanation of size-dependent plastic flow at the micron scale and below.

The analyses are carried out within the framework of mechanism-based discrete dislocation plasticity (M-DDP) developed by Benzerga et al. (2004). The dislocations are modeled as line defects in a linear elastic, isotropic solid so that the long-range interactions between them are directly accounted for. Superposition is used to rep-

resent the solution of the boundary value problem of interest in terms of the infinite medium singular fields for the discrete dislocations and image fields that enforce boundary conditions (Van der Giessen and Needleman, 1995). The short-range interactions are incorporated into the formulation through a set of constitutive rules that allow for approximate representations of key three-dimensional dislocation mechanisms in a two-dimensional framework, for the purpose of computational efficiency. These rules, which may be referred to as "2.5D" rules, account for junction formation and destruction, dynamic source creation and line tension. Within this framework, the stress–strain curve, including a two-stage response (Benzerga et al., 2004), the evolution of the dislocation structure and energy storage (Benzerga et al., 2005) are outcomes of the formulation and not constitutive assumptions.

In the present investigation, geometrically similar planar crystals are subject to nominally uniform compression at fixed applied strain rate. Global as well as local measures of flow stress and dislocation density are quantified and analyzed to develop a suitable structure–property relationship in terms of reduced state variables. The results indicate that, at the micron scale, geometrically necessary dislocations play an important role in setting the flow stress even under states of macroscopically homogeneous deformation.

C. Problem formulation

The formulation follows that of mechanism-based discrete dislocation plasticity (M-DDP) as described by Benzerga et al. (2004). It extends the original two-dimensional (2D) framework (Van der Giessen and Needleman, 1995) by incorporating key three-dimensional effects as a set of constitutive rules. In this mesoscopic model, plastic flow arises due to the nucleation and motion of edge dislocations modeled as line

singularities in a homogeneous and isotropic elastic medium. The challenge is to solve boundary value problems involving the collective motion and interaction of a large number of discrete dislocations. The formulation is an incremental one where at each time increment dislocation structure, stress, strain and displacements are determined. Assuming infinitesimal displacement gradients, superposition is used to describe the current state of the body in terms of the displacement, strain and stress fields as

$$\mathbf{u} = \tilde{\mathbf{u}} + \hat{\mathbf{u}}, \qquad \boldsymbol{\epsilon} = \tilde{\boldsymbol{\epsilon}} + \hat{\boldsymbol{\epsilon}}, \qquad \boldsymbol{\sigma} = \tilde{\boldsymbol{\sigma}} + \hat{\boldsymbol{\sigma}} \qquad (2.1)$$

The singular (˜) fields are obtained by the superposition of the fields $(\mathbf{u}^i, \boldsymbol{\epsilon}^i, \boldsymbol{\sigma}^i)$ associated with individual dislocations,

$$\tilde{\mathbf{u}} = \sum_{i=1}^{N} \mathbf{u}^i, \qquad \tilde{\boldsymbol{\epsilon}} = \sum_{i=1}^{N} \boldsymbol{\epsilon}^i, \qquad \tilde{\boldsymbol{\sigma}} = \sum_{i=1}^{N} \boldsymbol{\sigma}^i, \qquad (2.2)$$

with N the total number of dislocations in the sample. The (ˆ) fields are the image fields that correct for the actual boundary conditions. The latter are specified in terms of conventional tractions and displacements applied to portions of the boundary $\partial\Omega$ of a finite domain Ω. When dislocations are kept at a core distance from all boundaries, the (ˆ) fields are smooth and obey a well-posed boundary value problem, which is solved using the finite element method. The framework used in this investigation does not account for finite lattice rotations and shape changes due to slip. Deshpande et al. (2003) have developed a finite strain discrete dislocation plasticity model to account for finite lattice rotations and shape changes due to slip.

The glide motion of dislocation i is determined by the Peach-Koehler force, f^i, given by

$$f^i = \mathbf{m}^i \cdot \left(\hat{\boldsymbol{\sigma}} + \sum_{j \neq i} \boldsymbol{\sigma}^j \right) \cdot \mathbf{b}^i \qquad (2.3)$$

where $\mathbf{m}^i$ is the slip plane normal and $\mathbf{b}^i$ the Burgers vector with signed length b^i

and $b = |b^i|$.

Two types of dislocation Frank–Read sources are considered. Static sources are initially present with specified density and spatial distribution. Dynamic sources are formed in the course of the deformation due to dislocation interactions. Also, two types of dislocation obstacles are modeled: (i) initial stress-free point obstacles that represent precipitates; and (ii) dynamic obstacles that represent forest dislocations. The locations of initial, static sources and obstacles are randomly generated. A static source i nucleates a dipole when the magnitude of the Peach-Koehler force exceeds a critical value, $\tau_{0n}^i b$, for a prescribed time t_{0n}. The source strengths are randomly assigned from a Gaussian distribution with average $\bar{\tau}_{0n}$. The sign of the nucleated dipole depends on the sign of the Peach-Koehler force acting on the source. A dislocation may get pinned at a static obstacle and is released when the Peach-Koehler force at the location of the obstacle attains the value $\tau_{obs} b^i$, with τ_{obs} the obstacle strength.

When dislocations gliding on intersecting planes approach each other within a critical distance d^*, a junction is formed, irrespective of the sign of the interacting dislocations. Junction formation results in dynamic dislocation source and obstacle evolution during the deformation process. A junction which cannot be unzipped, for example due to cross-slip, is termed an *anchoring point*. A breakable junction is referred to as a *dynamic obstacle*. Such an obstacle is destroyed if the Peach-Koehler force acting on either dislocation comprising the junction attains or exceeds the breaking force, $\tau_{brk}^I b$. The breaking stress for junction I is configuration dependent and is given by:

$$\tau_{brk}^I = \beta_{brk} \frac{\mu b}{\mathcal{S}^I} \tag{2.4}$$

where $\mathcal{S}^I$ is the distance to the nearest junction in any of the two intersecting planes

and β_{brk} is a scaling factor for the junction strength. The dislocations forming a junction are released when the latter is destroyed and are free to glide along their respective slip planes.

At the level of refinement of a 2D model, the formation of an anchoring point can only be treated as a statistical event. The probability that a junction forms an anchoring point has the prescribed value p. Anchoring points lead to the formation of new, dynamic sources. A dislocation dipole is nucleated at source I when the value of the Peach-Koehler force at either junction forming the source exceeds the value $\tau_{\mathrm{nuc}}^{I} b$ during a time t_{nuc}^{I}. Both values depend on the local configuration and hence evolve dynamically. The nucleation stress is given by

$$\tau_{\mathrm{nuc}}^{I} = \beta_{\mathrm{nuc}} \frac{\mu b}{\mathcal{S}^{I}} \tag{2.5}$$

where β_{nuc} is a factor that reflects the strength of the source and $\mathcal{S}^{I}$ is the distance to the nearest junction on the slip plane where τ_{nuc}^{I} is being resolved. The nucleation time t_{nuc}^{I} is given by

$$t_{\mathrm{nuc}}^{I} = \gamma \frac{\mathcal{S}^{I}}{|\tau^{I}| b} \tag{2.6}$$

where γ is a material constant with units of a drag factor, and τ^{I} is the current resolved shear stress at the location of anchoring point I, exclusive of the junction self-stress. The nucleation conditions (2.5)–(2.6) result from a dislocation multiplication model first developed by Benzerga et al. (2004) and later improved by Benzerga (2008). Their model describes the dynamic bow-out of a dislocation segment using line tension approximations.

For determining the dislocation evolution it is necessary to account for the interaction of moving dislocations with junctions. Several options are physically possible which are discussed by Benzerga et al. (2004). Here the only mechanism for junction

destruction is unzipping, as described through Eq. (2.4). In particular, the mechanism of destruction by annihilation is not used. Thus, anchoring points cannot be broken in the simulations discussed below. Annihilation of two co-planar dislocations of opposite sign occurs by eliminating both dislocations when they are within a material-dependent critical annihilation distance, L_e, provided that none of them is involved in a junction. Dislocations are allowed to glide out of the crystal but geometry changes, such as step formation, are not accounted for.

There is an energy cost associated with the expansion of dislocation loops. But this is not explicitly taken into account in the two-dimensional formulation with loop expansion represented by dipole separation. Hence, to represent the additional energy cost associated with loop expansion in two-dimensions, a configurational force of magnitude $\mathcal{L}^i b^i$ and pointing from one dislocation constituting the dipole toward the other is introduced with

$$\mathcal{L}^i = -\alpha \frac{\mu b}{\mathcal{S}_d^i} \tag{2.7}$$

where α is the line tension parameter and $\mathcal{S}_d^i$ the algebraic distance between the dislocations, members of the same dipole, so that the sign of $\mathcal{L}^i$ depends on the sign of $\mathcal{S}_d^i$. Further details are given by Benzerga et al. (2005).

Dislocation glide is taken to be drag controlled following:

$$Bv^i = \text{sign}(\tau^i + \mathcal{L}^i)\langle|\tau^i + \mathcal{L}^i| - \tau_P\rangle b^i \tag{2.8}$$

with B the drag factor, v^i the glide velocity of dislocation i, $\tau^i = f^i/b^i$, $\mathcal{L}^i$ the line tension given by (2.7) and τ_P the Peierls stress. Note that τ^i differs from the resolved shear stress in that the stress field of dislocation i is excluded. The symbol $\langle \cdot \rangle$ denotes McCauley's brackets. To the neglect of line tension and frictional stress the right-hand side of (2.8) reduces to the glide Peach-Koehler force f^i defined by (2.3).

The difference between the M-DDP framework and other 2D discrete disloca-tion modeling resides in the set of additional constitutive rules (2.4)–(2.7) with (2.8) amended as appropriate. Accounting for these 2.5D rules is key to predicting the multi-stage hardening response of single crystals, as shown by Benzerga et al. (2004). The additional rules were derived using dislocation theory so that good estimates of all but one parameter (p which sets the probability of forming new sources) are generally known. Ranges for the parameters d^*, β_{brk}, β_{nuc}, γ and α were discussed by Benzerga et al. (2004).

Here, calculations are carried out for planar model face centered cubic crystals having dimensions $L \times H$, subject to plane strain uniaxial compression in the x_1–x_2 plane (Fig. 4). The surfaces at $x_2 = \pm H/2$ are traction free and the shear stress vanishes at $x_1 = \pm L/2$. A uniform displacement $u_1 = \pm U/2$ is prescribed along $x_1 = \pm L/2$. The rotation of the tensile axis is not restricted. There are two slip systems oriented at $\pm \varphi_0$ from the loading x_1–axis. The average compressive stress and the applied strain are given by, respectively,

$$\sigma = -\frac{1}{H} \int_{-H/2}^{H/2} \sigma_{11}(\pm L/2, x_2)\mathrm{d}x_2; \quad \varepsilon = -\frac{U}{L} \tag{2.9}$$

D.   Results

The calculations are carried out for geometrically similar specimens such that the aspect ratio $L/H = 3$ is kept fixed with L varied between 0.6 μm and 38.4 μm. The crystal orientation is defined by $\varphi_0 = 35.25°$. The material parameters, $\nu = 0.3$, $\mu = 26\,\text{GPa}$, $b = 0.25\,\text{nm}$, $B = 10^{-4}\text{Pa}\,\text{s}$ and $\tau_{\text{P}} = 0$, are taken to be representative of aluminum. The values of the parameters entering the "2.5D" constitutive rules are $d^* = 6b$, $p = 0.05$, $\beta_{\text{brk}} = \beta_{\text{nuc}} = 1$, $\gamma = 0.1B$ and $\alpha = 0$. The annihilation distance is taken to be equal to the critical distance for junction formation $L_e = d^* = 1.5\,\text{nm}$.
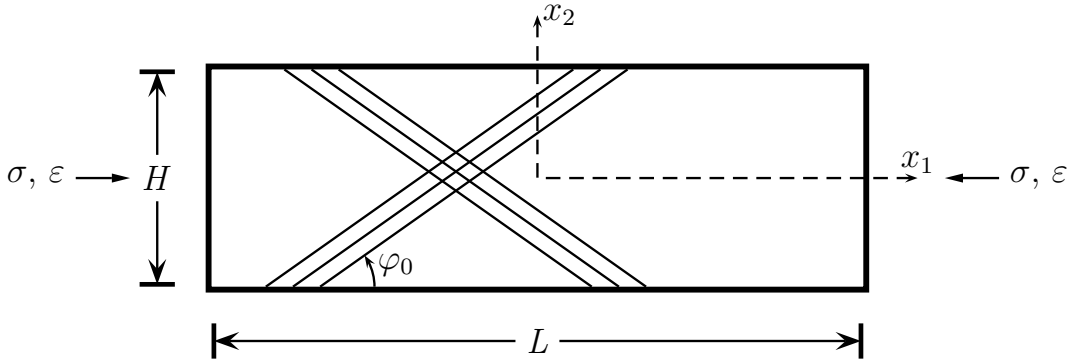
Fig. 4. Geometry of the compression problem for a planar model fcc crystal with two slip systems oriented at $\pm\varphi_0$ from the x_1–axis.

The analyses are carried out for initially dislocation free crystals but with potential static sources and obstacles randomly distributed on predefined slip planes, with densities $\rho_0 = 1.5 \times 10^{14} \mathrm{m}^{-2}$ and $\rho_{\mathrm{obs}} = 6 \times 10^{14} \mathrm{m}^{-2}$, respectively. Thus, the initial source density is two orders of magnitude larger than in the microcrystals tested by Dimiduk et al. (2005). This high value of ρ_0 is chosen to promote athermal hardening processes, which were found to be ineffective at low source density (e.g., a value of $10^{12} \mathrm{m}^{-2}$ was used by Benzerga and Shaver (2006)). On the other hand, the value of ρ_{obs} has little effect on the results. The mean and standard deviation of the initial source strength distribution are $\bar{\tau}_{0\mathrm{n}} = 50$ MPa and 10 MPa, respectively, $t_{0\mathrm{n}} = 10$ ns and $\tau_{\mathrm{obs}} = 150$ MPa. The slip plane spacing is set to $20b$. The imposed strain rate $\dot{\varepsilon} = -\dot{U}/L = 6.66 \times 10^4 \ s^{-1}$ is kept the same for all specimens. A time step of $\Delta t = 0.5$ ns is used to resolve the dynamics of dislocation nucleation and motion. Since the results are not sensitive to mesh density when the gradients of the (ˆ) fields are resolved, a uniform finite element mesh (60 and 20 elements along x_1 and x_2 respectively) is used for all specimens.

1. Flow stress and work-hardening

Typical stress versus strain responses are shown in Fig. 5 for selected specimens showing the overall transition from elastic to plastic regimes and from stage I to stage II hardening. Although the specimens are oriented for double slip from the outset, all responses exhibit some extent of stage I hardening because slip activity initiates on a few slip planes. At the scales considered here, this results in easy glide up to a few percent of strain. All specimens were taken well into stage II and some up to a strain of 0.1. The calculations corresponding to the $H = 6.4$ μm and $H = 12.8$ μm specimens were terminated prior to reaching the strain of 0.1 (Fig. 5b) when the number of dislocations was such that the computations were severely slowed down, e.g., over 465,000 dislocations were involved in the simulations in the $H = 12.8$ μm specimen at $\varepsilon \approx 0.06$.

Unlike in previous calculations (Benzerga and Shaver, 2006; Benzerga, 2008) there is no initial dislocation structure in the present calculations. Therefore, dislocation activity takes place at $\sigma \approx 105$ MPa, irrespective of specimen size. This value is consistent with a mean source strength value of 50 MPa and a Schmid factor $f_{\mathrm{S}} = (\sin 2\varphi_0)/2 = 0.47$ for both slip systems. Subsequently, there is a noticeable stress drop because the stress required for sustained plastic flow is smaller than the stress at initial yield. As shown by Benzerga and Shaver (2006) and Benzerga (2008), the post-yield stress drop is eliminated by incorporating an initial dislocation structure.

The specimen size affects the stress–strain curve in a number of respects. To quantify the size effect, the values of the 0.2% yield strength, σ_y, the rate of stage I hardening, Θ_{I}, the stress at the beginning of stage II, σ_{II}, and the rate of stage II hardening, Θ_{II}, are reported in Table I. For most specimen sizes three values are
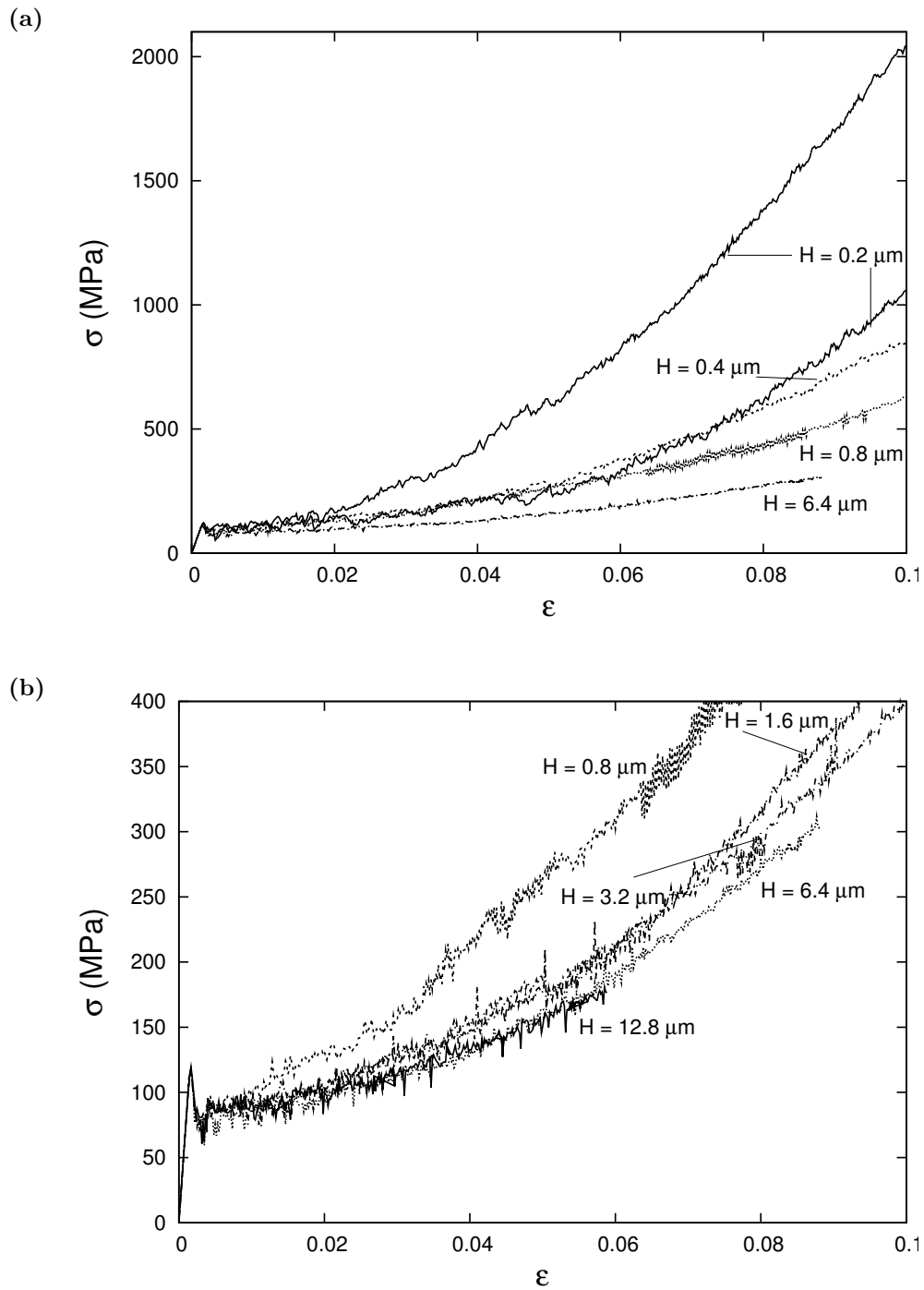
Fig. 5. Representative stress versus strain compression responses of the (a) $H = 0.2$ μm, 0.4 μm, 0.8 μm and 6.4 μm specimens; and (b) $H = 0.8$ μm, 1.6 μm, 3.2 μm, 6.4 μm and 12.8 μm specimens. A reduced stress range is shown in (b) and two realizations of the $H = 0.2$ μm specimen are shown in (a).

Table I. Characteristics of the multi-stage hardening response of geometrically similar crystals with a length to height ratio of 3. The symbols σ_y, σ_{II}, Θ_I and Θ_{II} refer to the 0.2% yield strength, the flow stress at the beginning of stage II, the rate of stage I hardening and the rate of stage II hardening, respectively. Up to three realizations are reported for each specimen size.

Size, H	σ_y	σ_{II}	Θ_I/μ	Θ_{II}/μ
(μm)	(MPa)	(MPa)		
	80	258.3	0.0366	0.192
0.2	115	175.0	0.0114	0.244
	77	208.3	0.0175	0.239
	95	186.6	0.0132	0.119
0.4	95	213.3	0.0179	0.128
	75	211.1	0.0172	0.080
	75	200.0	0.0193	0.071
0.8	90	190.0	0.0186	0.065
	85	151.1	0.0114	0.065
	80	156.0	0.0117	0.055
1.6	75	152.0	0.0125	0.044
	80	160.0	0.0131	0.050
	80	107.5	0.0053	0.037
3.2	65	100.0	0.0049	0.032
	72	133.3	0.0099	0.039
	70	101.7	0.0047	0.024
6.4				
	75	101.9	0.0041	0.029
	90	93.5	0.0030	0.022
12.8				
	75	90.9	0.0026	0.018

given which correspond to distinct realizations of the initial static source and obstacle distributions. The precise definition of the parameters listed in the table is given in Fig. 6. The instantaneous work hardening rate is defined as $\Theta = d\mathcal{T}/d\Gamma$, where $\mathcal{T} = f_S\sigma$ and $\Gamma = \varepsilon/f_S$ respectively refer to the macroscopic flow stress and shear strain, resolved on either slip system.

Most notable in the stress–strain curves of Fig. 5 is the effect of size on the stage II hardening rate, Θ_{II}. As shown in Table I other characteristics of the stress–strain response are also size-dependent. While the values of the yield strength σ_y exhibit a slight increase with decreasing specimen size (roughly 20% over the size range investigated) those of σ_{II} increase by nearly a factor of 3. Correspondingly, the stage I hardening rate, Θ_I, increases by one order of magnitude, Table I. The increase in the spread of the values of all characteristics with decreasing specimen size is also noteworthy.
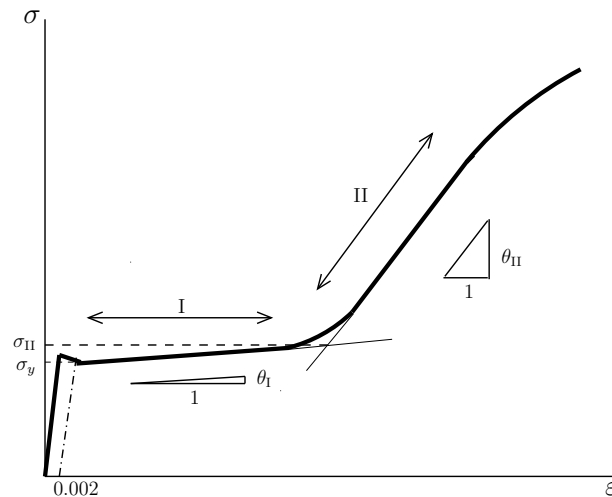
Fig. 6. Sketch of a typical stress–strain multistage response of a single crystal showing the definition of the strength and hardening quantities listed in Table I. Here $\theta_i = \Theta_i/f_S^2$ $(i = \text{I, II})$.

Fig. 7a depicts the values of the flow stress, σ_f, as a function of specimen height,

H, at various strain levels. Because of strain hardening the scaling of σ_f with size varies in the course of deformation. A power law of the form

$$\frac{\sigma_f}{\sigma_0} \equiv \frac{\mathcal{T}}{f_S \sigma_0} = \left(\frac{H}{H_0}\right)^{-x} \tag{2.10}$$

fits relatively well the data in Fig. 7a at all strain levels but the scaling exponent x increases from ≈ 0.1 at $\varepsilon = 0.02$ to over 0.4 at $\varepsilon = 0.1$. The effect of specimen size on stage II hardening is quantified in Fig. 7b. The work hardening rate Θ_{II} increases steadily with decreasing specimen size. The $\mu/200$ to $\mu/100$ range of bulk values of Θ_{II} is also depicted in Fig. 7b for comparison purposes. In the $H = 0.2$ μm specimen, the calculated value of Θ_{II}, averaged over three realizations, is about 20 times larger than the maximum bulk value. By way of contrast, in the largest specimen analyzed, the value of Θ_{II} is less than twice the bulk value. In addition, it is worth noting that the effect of size on Θ_{II} is enhanced for values of H in the sub-micron regime.

2.   Evolution of the dislocation structure

Fig. 8 shows the dislocation density, ρ, versus strain curves corresponding to the overall stress–strain responses in Fig. 5. Up to a strain of about 0.04 the evolution of the dislocation density is insensitive to specimen size. Beyond the 0.04 strain level the rate of increase of ρ is consistently increased with decreasing specimen size. In addition, for fixed specimen dimensions, the rate of dislocation accumulation decreases with increasing strain for $\varepsilon < 0.04$ so that the curves are concave downward. By way of contrast, the increase in ρ for $\varepsilon > 0.04$ is rather linear, except for the largest two specimens where the density versus strain curves retain the slightly concave shape. The corresponding evolution of total junction density is shown in Fig. 9a. The junction density increases with strain for specimens of all sizes, but there is a noticeable decrease in the junction production rate after some straining. Similar trends are ob-
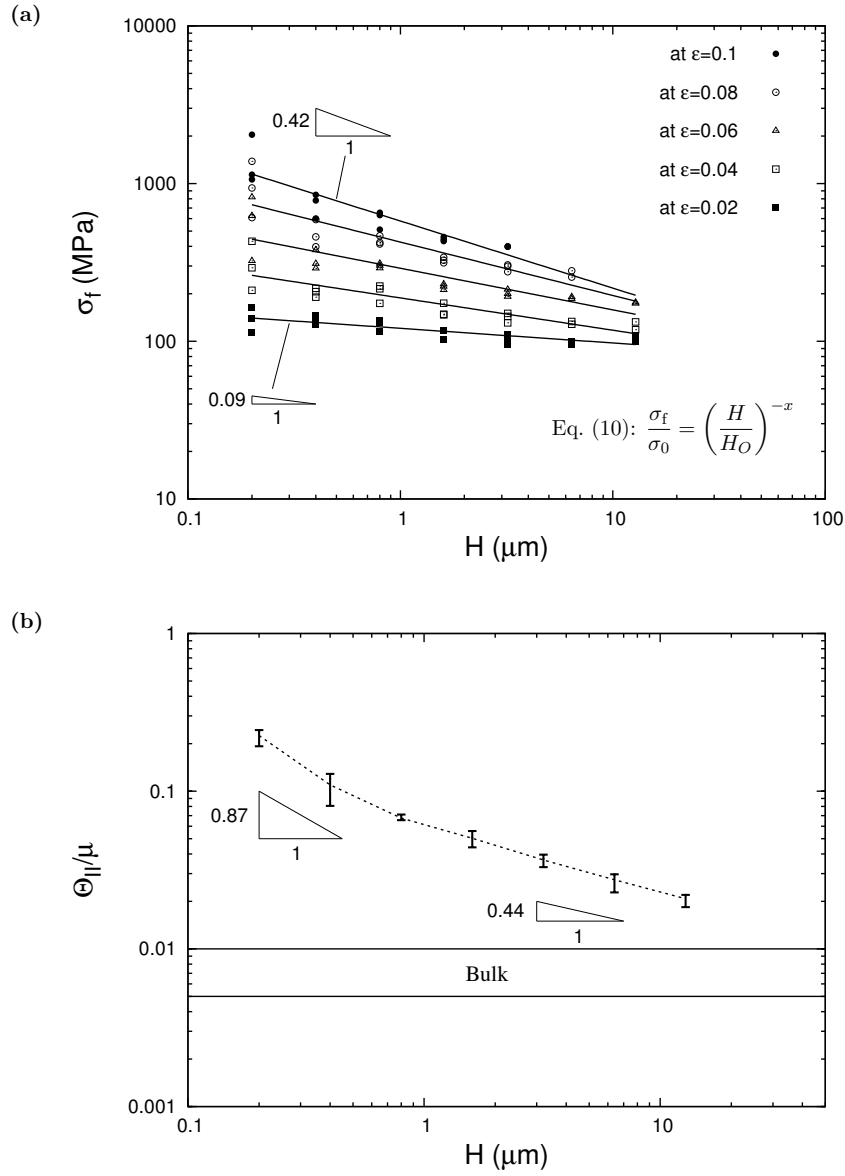
Fig. 7. (a) Flow stress, σ_{f}, versus crystal height, H, at various strain levels. Best fit lines following power law (2.10) are based on two or three realizations per specimen size. The value of the scaling exponent x in (2.10) is 0.09, 0.2, 0.26, 0.33 and 0.42 at $\varepsilon = 0.02$, 0.04, 0.06, 0.08 and 0.1, respectively. (b) Stage II work hardening rate, Θ_{II}, in units of the shear modulus μ, versus crystal height, H, showing two distinct scaling regimes with the best power law fits exhibited. Bounds of scatter bars correspond to actual maxima and minima from several realizations and averages are connected by the dotted line. Horizontal lines depict the typical, material-independent range of bulk values of Θ_{II}/μ.
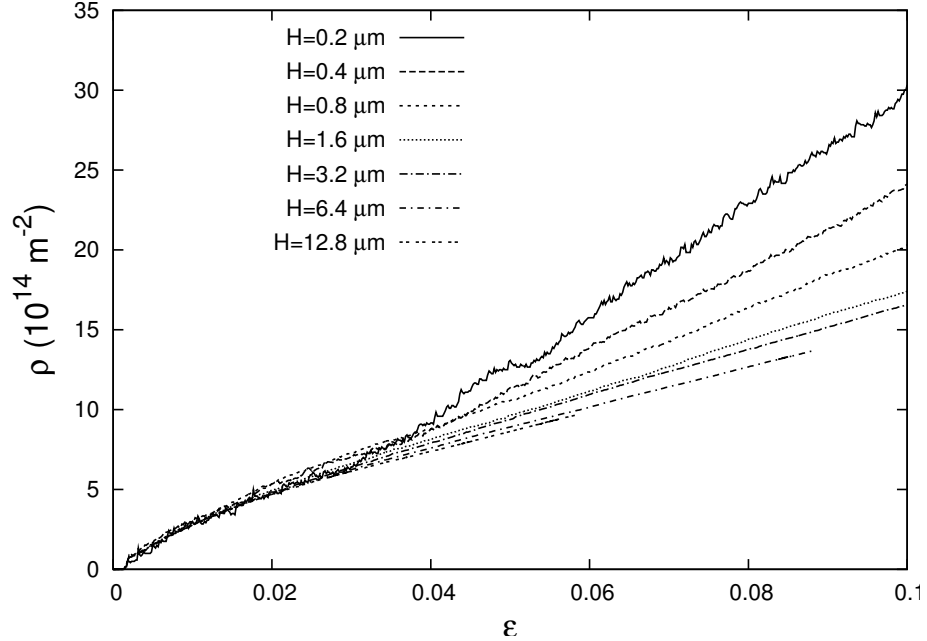
Fig. 8. Evolution of dislocation density with strain for selected realizations of all specimen sizes corresponding to the stress–strain responses of Fig. 5.

tained for the dynamic obstacle density (Fig. 9b) but the production rate of obstacles vanishes with continued deformation. This is due to the fact that after sufficient strain hardening, stress levels are so high that obstacles are more easily broken. Although not shown in the figure, the results indicate that the dynamic source production also decreases in rate with increasing strain but does not saturate. Anchoring points cannot be destroyed but large back-stresses on densely packed slip planes tend to shut down the sources located on these planes. This ultimately leads to a decrease in the production of dynamic sources.

Beyond the details of dislocation structure evolution described above, it is emphasized that there is little correlation between junction density and specimen size, at fixed overall strain. The dynamic obstacle density shows a more consistent decrease with increasing specimen size, but only for $H > 0.8$ μm. Whether all junctions or only the dynamic obstacles are chosen to represent the forest, the size dependence of
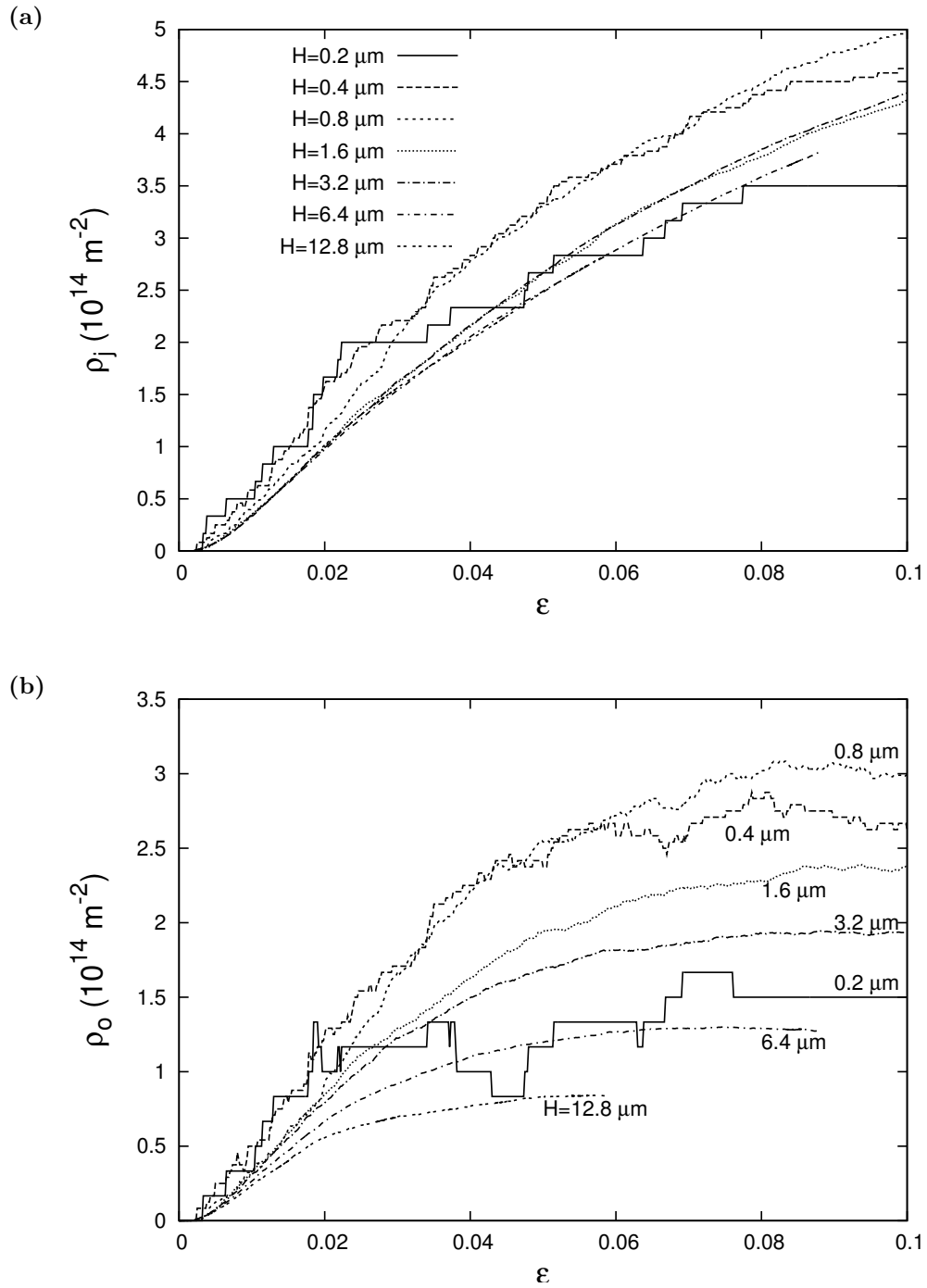
Fig. 9. (a) Total junction density versus strain for selected realizations of all specimen sizes; (b) corresponding evolution of dynamic obstacle density. At fixed strain $d\rho_o \leq d\rho_j$ since $\rho_j = \rho_o + \rho_a$ and the density ρ_a of anchoring points can only increase with strain or remain constant.

the flow stress cannot be correlated with the spacing between forest dislocations.

The dislocation distributions corresponding to a strain of 0.1 are shown in Fig. 10 for selected specimen sizes. Positive dislocations are shown in black whereas negative dislocations are shown in gray. Two specimens with $H = 0.2$ μm are shown to highlight the increased variability of the results in smaller specimens. In one realization of the $H = 0.2$ μm specimen, the dislocation structure (Fig. 10a, left) shows an excess of negative dislocations within the specimen, i.e. a residual Burgers vector. Interestingly, this realization is characterized with a higher flow stress and a larger value of the stage II hardening rate; see Fig. 5. In all other specimens the ratio of signed to total dislocation density at $\varepsilon = 0.1$ essentially vanishes over the volume of the specimen.

3.   Flow stress scaling

In physical theories of crystal plasticity, the dislocation density is commonly used as the structural parameter for macroscopic descriptions of plastic flow, with the flow stress governed by Taylor-like hardening following:

$$\mathcal{T} = A\mu b\sqrt{\rho} \tag{2.11}$$

where A is a constant in the range 0.3 to 0.5 when the athermal component of $\mathcal{T}$ is retained (Gil Sevillano, 1993). Fig. 11 shows the evolution of $\mathcal{T}$ with strain for selected specimen sizes. The flow stress is given in units of $\mu b\sqrt{\rho}$ to explore the validity of Eq. (2.11) at the micron scale. This plot clearly shows that the increase in dislocation density with decreasing specimen size (Fig. 8) does not suffice to explain the corresponding increase of the flow stress (Fig. 5). At fixed specimen size, there is a deformation regime where the bulk scaling law (2.11) holds with values of the pre-factor A within the range 0.3–0.5. The bigger the sample the larger the extent
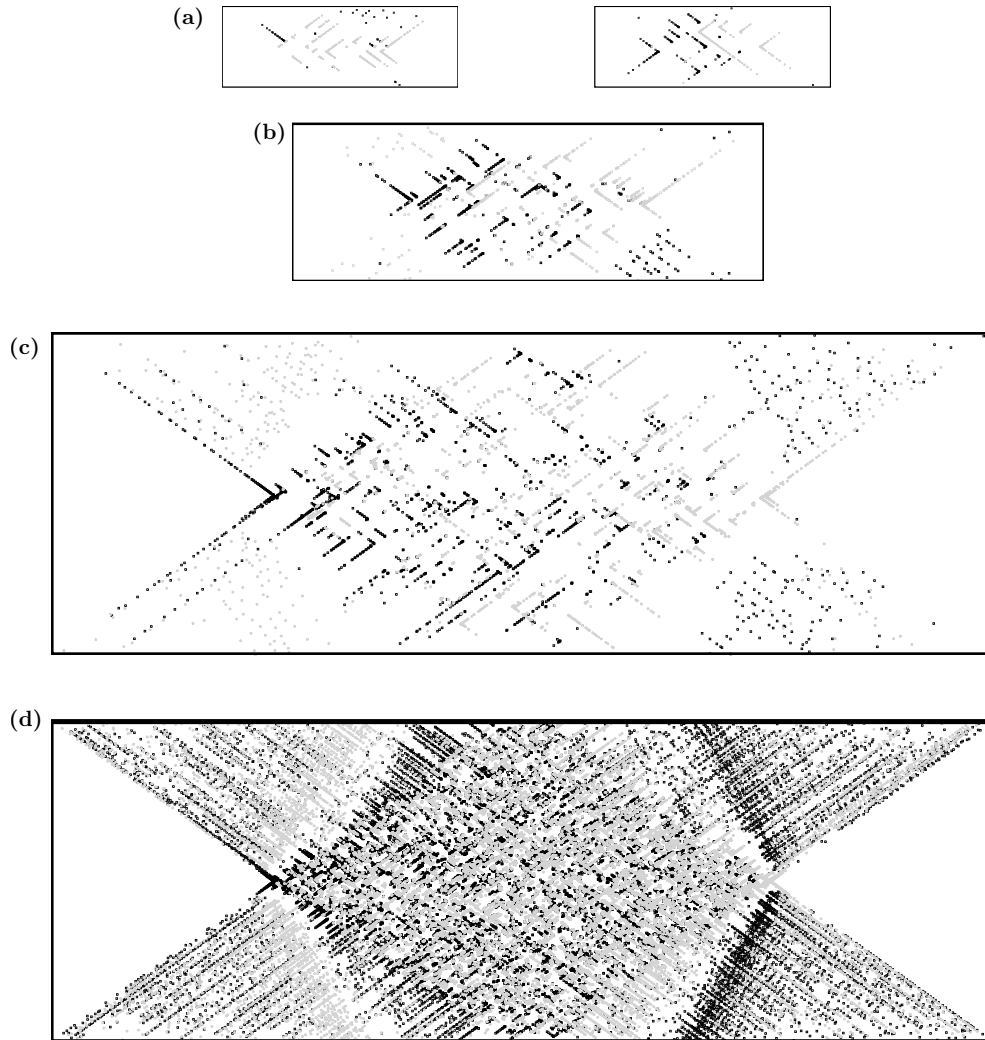
Fig. 10. Spatial distribution of dislocations at $\varepsilon = 0.1$ in the crystals of height (a) $H = 0.2$ μm; (b) $H = 0.4$ μm; (c) $H = 0.8$ μm (all scaled appropriately); and (d) $H = 3.2$ μm (not scaled). Positive dislocations are shown as black dots whereas negative dislocations are shown as gray dots. Two realizations are shown for the $H = 0.2$ μm specimen as in Fig. 5.

of this regime and the smaller the value of A. But a deviation from this behavior takes place for all specimen sizes. This deviation is more pronounced in stage II and is larger in magnitude for smaller specimens. The behavior in Fig. 11 indicates that, at the micron scale, (i) the dislocation density does not suffice to set the flow stress; and (ii) the spatial distribution of dislocations affects the flow stress, in a way not specified as yet, and this effect is inherently increased with decreasing sample size.

4. Local flow stress and dislocation density

In principle the applied loading can be accommodated by a uniform stress distribution. However, the presence of a dislocation structure and the heterogeneity of dislocation mediated slip lead to an inhomogeneous stress distribution. Fig. 12 shows contours of the axial stress σ_{11} corresponding to selected specimen sizes at a strain $\varepsilon = 0.1$ (see Fig. 20 on page 72 for an example of contours of the stress components σ_{22} and σ_{12}). The corresponding dislocation structures were shown in Fig. 10. In any given specimen, the spatial average of σ_{11} over the volume corresponds, in magnitude, to the overall stress given by Eq. (2.9). Clearly, at a strain of 0.1 the heterogeneous internal stress field has evolved in such a way that surface boundary layers have formed which are softer than the core of the specimen. The fact that the core is harder than regions located near the free surfaces is consistent with the experimental measurements of Fourie (1968). In the calculations, the formation of a hard core between softer boundary layers is associated with the increased propensity of dislocation intersections within the core, which enhance junction formation and subsequent forest hardening mechanisms.

In Fig. 12a two specimens with $H = 0.2$ μm are considered just like in Fig. 10a. The stress distributions are quite different in the two samples, especially at the strain of 0.1. In the sample shown on the right, stress concentrates along a band and this

(a)

(b)
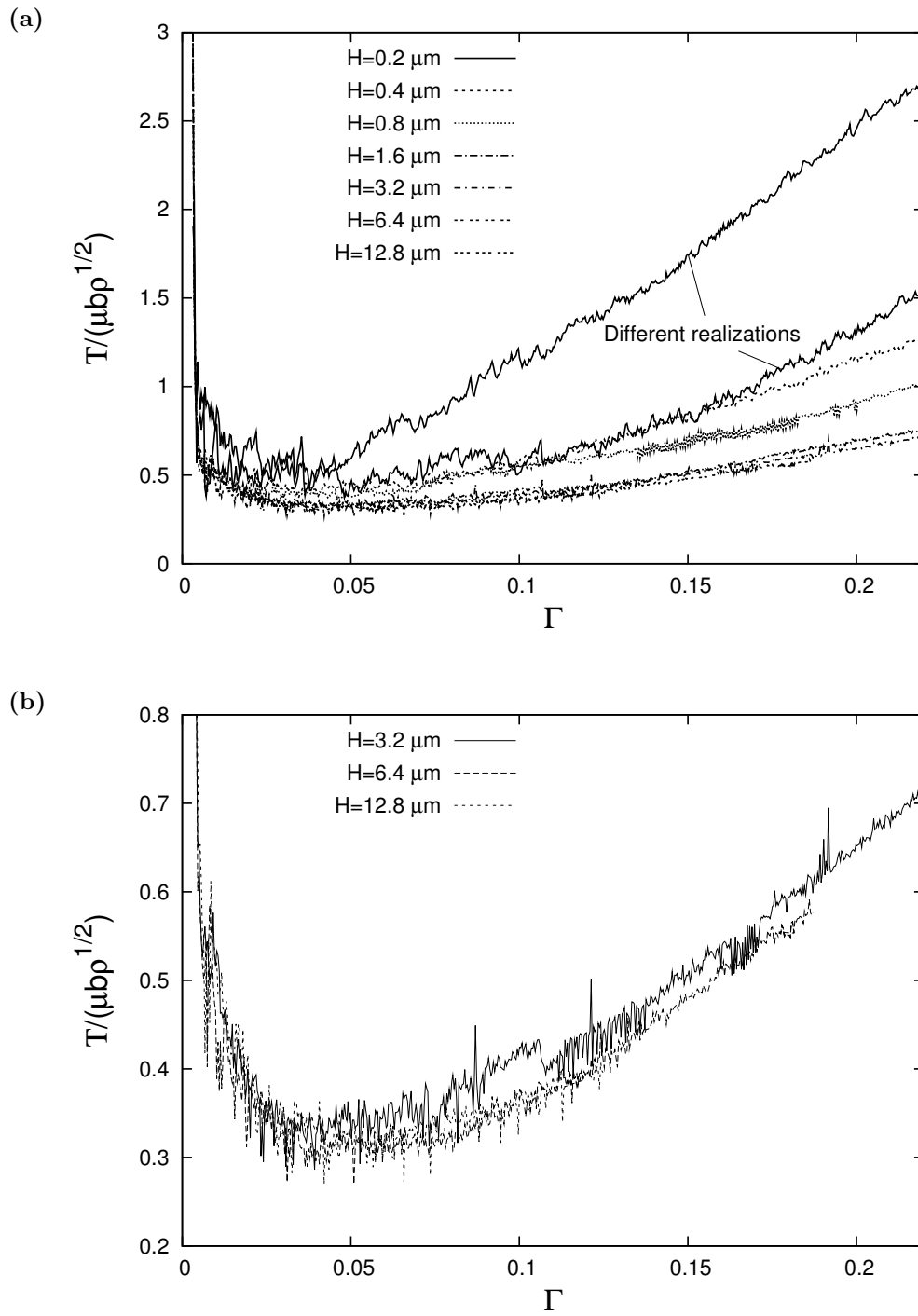
Fig. 11. Macroscopic flow stress, $\mathcal{T} = f_S\sigma$, in units of $\mu b\sqrt{\rho}$, versus macroscopic resolved shear strain, $\Gamma = \varepsilon/f_S$, with $f_S = 0.47$ the Schmid factor. The specimen realizations correspond to those in Figs. 5 and 8 for the stress–strain and density–strain curves, respectively.
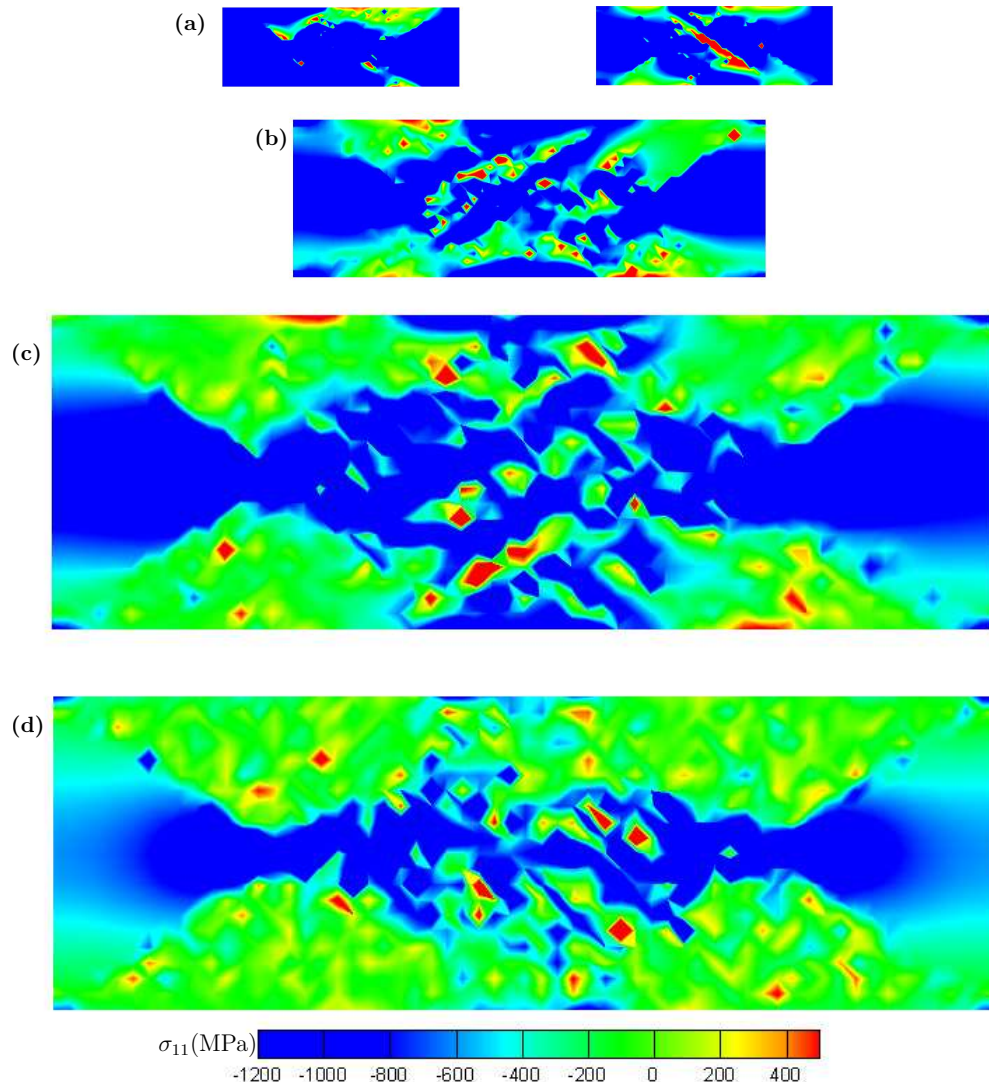
Fig. 12. Contours of axial stress σ_{11} at $\varepsilon = 0.1$ in crystals of height (a) $H = 0.2$ μm; (b) $H = 0.4$ μm; (c) $H = 0.8$ μm (all scaled appropriately); and (d) $H = 3.2$ μm (not scaled). Two realizations are shown for the $H = 0.2$ μm specimen as in Fig. 10.

may contribute to lower the overall flow stress and work hardening rate. This picture, together with the build-up of a residual Burgers vector in the sample shown on the left (recall Fig. 10a) is consistent with the scatter in the Θ_{II} values shown in Fig. 7b.

In order to quantify the flow stress variation across specimen height, averages of the axial stress were calculated over strips of equal thickness h, running parallel to the specimen axis. Define $\Sigma_{11}(x_2^n) = \langle \sigma_{11}(x_1, x_2) \rangle_{\Omega^n}$ with $\langle \cdot \rangle_X$ the spatial average over X and Ω^n a strip-like domain defined by $-L/2 \leq x_1 \leq L/2$ and $-h/2 \leq x_2 - x_2^n \leq h/2$ where $x_2^n = (n - \frac{1}{2})h - H/2$ refers to the center-coordinate of the strip. Fig. 13 shows the so-averaged axial stress, Σ_{11}, against the x_2 location of the strip.

The stress profiles in Fig. 13 reveal a number of interesting features. First, in any given specimen the flow stress is typically 3 times as large in the core than near the surface. Second, there essentially is a pointwise increase of the flow stress when the specimen size decreases. We may also notice that the flow stress is not uniform in the soft boundary layers. It attains a minimum at a distance, roughly 10 to 15% of the total specimen height, from the free surface. This effect is associated with the formation of nearly dislocation-free thin layers in the vicinity of the top and bottom free surfaces (Fig. 10). These thin layers are harder than regions located farther away from the surface (Fig. 12).

Also noticeable in Fig. 13 is the symmetry of the stress distribution about the x_1 axis for all but one realization of the $H = 0.2$ μm specimen. The asymmetry of the latter, already noticeable at $\varepsilon = 0.033$ (Fig. 13a), is such that the flow stress in the bottom half of the specimen is larger than the average flow stress of the whole specimen, which is approximately 2 GPa; see Fig. 5. This means that a tendency to bending has occurred inside the specimen, superposed onto the overall compressive stress state. This is consistent with the picture in Fig. 10a (left) and a residual Burgers vector. Although a significant portion of the strengthening in the $H =$
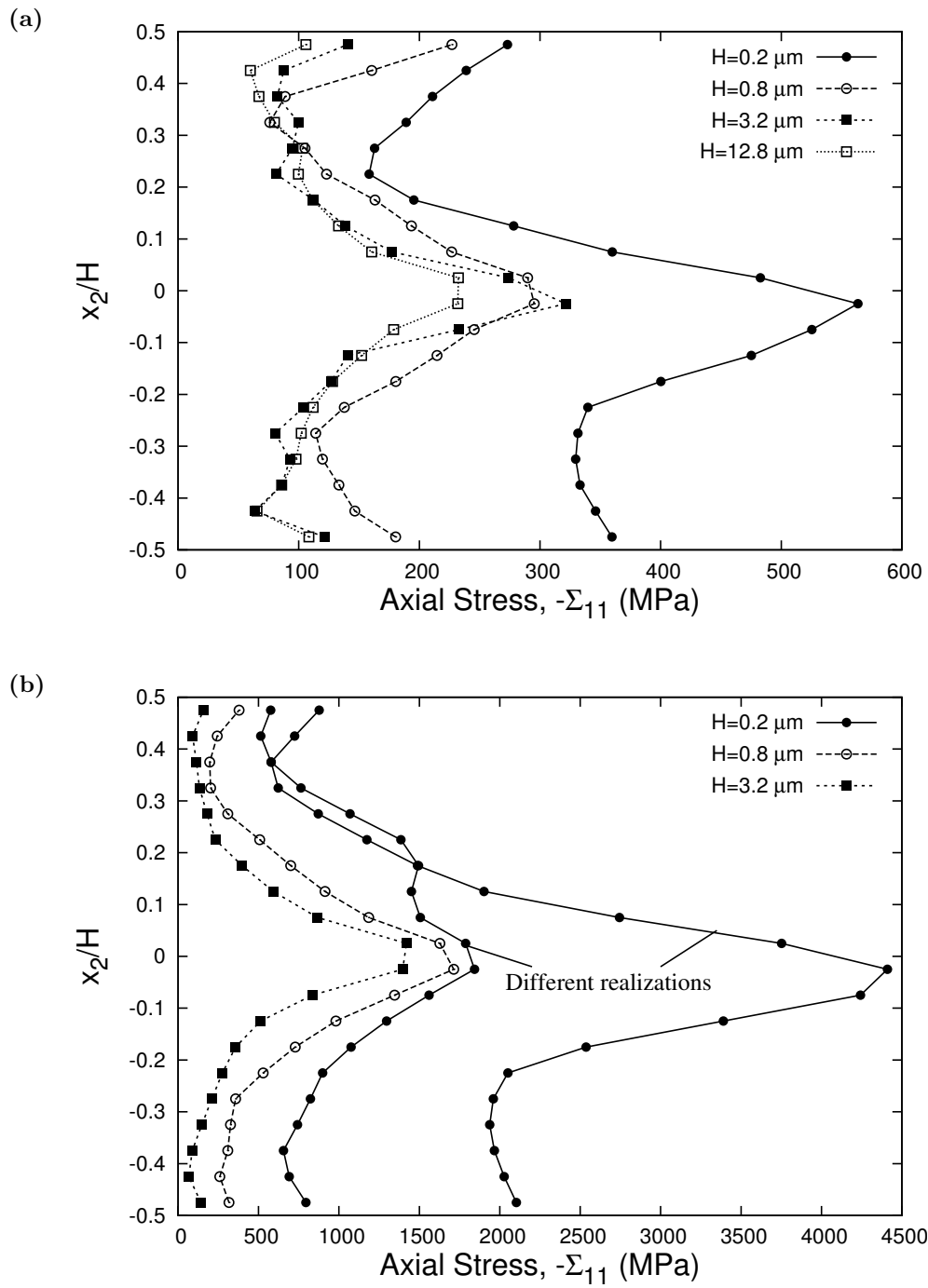
Fig. 13. Variation of the flow stress across the crystal height for selected specimen sizes (a) at $\varepsilon = 0.033$; and (b) at $\varepsilon = 0.1$. The local flow stress is identified with $|\Sigma_{11}|$, the axial stress averaged over horizontal domains.

0.2 μm specimen discussed above may be associated with a density of geometrically necessary dislocations (GNDs) induced by local lattice rotations within the specimen, this behavior does not explain the size dependence of flow stress and strain hardening depicted in Figs. 5 and 7 for $H \geq 0.4$ μm. Indeed, the net Burgers vector in all specimens with $H \geq 0.4$ μm is negligible in magnitude. As shown in Fig. 13b, the whole stress profiles are shifted toward larger stresses when the specimen size is decreased.

While the Taylor hardening equation (2.11) does not hold overall, the question arises as to whether it is valid locally. Local dislocation densities were calculated, consistent with the local flow stress definition above. The height h of the domains Ω^n sets the window of resolution. The dislocation density profiles obtained at a strain $\varepsilon = 0.1$ and using a resolution $h = 40$nm are shown in Fig. 14a for selected specimens. As expected, the distribution has a rather symmetric bell shape with the dislocation density being greater within the core region than outside of it. Fig. 14b depicts the deviation of local flow stress from what would have been its value had Taylor hardening applied locally. The deviation is minimum near the surfaces and maximum at the center. These plots clearly show that Taylor hardening breaks down at the microscopic scale as well.

<div align="center">5.   Distribution of local GND density</div>

Since the size-dependence of the overall flow stress is associated with an increase in stress throughout the specimen and not only within the core, the question addressed now is that of what relationship there is, if any, between local flow stress and local dislocation density. In particular, the way in which the signed dislocation density affects the local flow stress is of interest. The densities of positive and negative dislocations on slip system κ, $\rho_+^{(\kappa)}$ and $\rho_-^{(\kappa)}$, respectively, were evaluated separately.

(a)

(b)
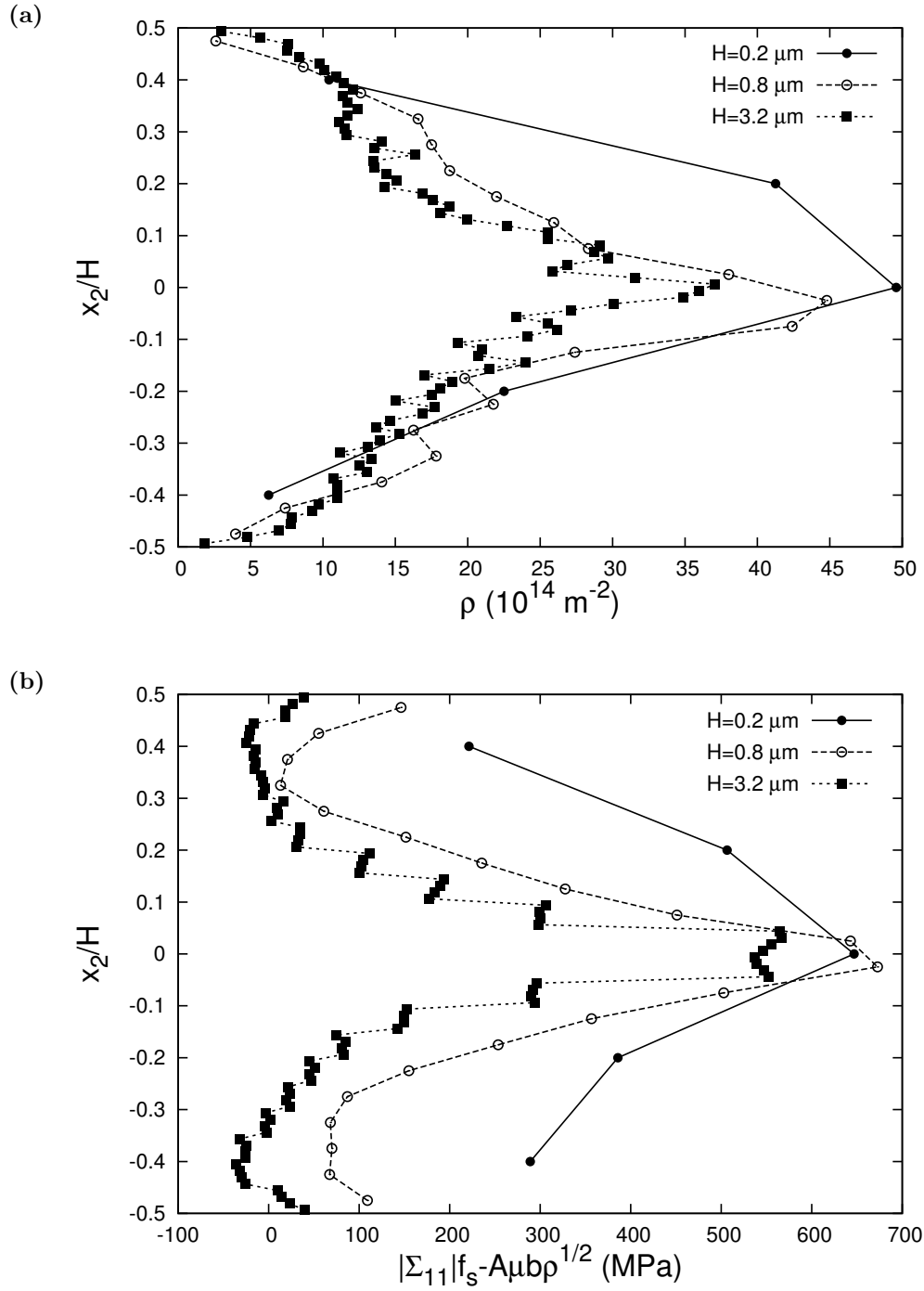
Fig. 14. (a) Variation of the dislocation density across the crystal height for selected specimen sizes at $\varepsilon = 0.1$. Local densities are calculated in horizontal domains of equal thickness $h = 40$ nm (see text). (b) Corresponding deviation of the local flow stress from ideal Taylor hardening, eq. (2.11) with $A = 0.3$. Both Σ_{11} and ρ are evaluated at the same resolution $h = 40$ nm.
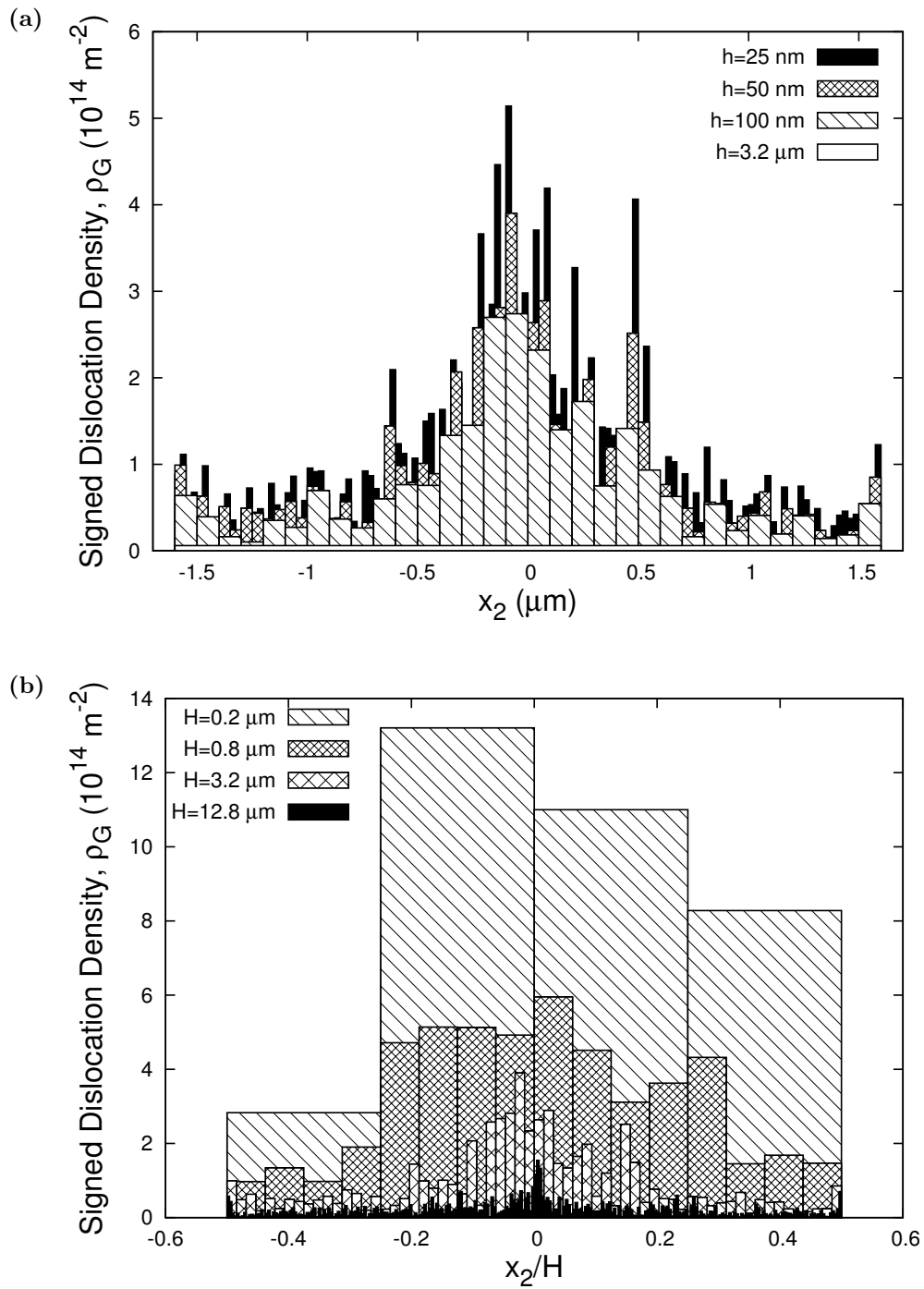
Fig. 15. Variation of the signed dislocation density, ρ_G, across crystal height at $\varepsilon = 0.1$. (a) Effect of the resolution h on ρ_G in the $H = 3.2$ μm specimen. (b) Effect of specimen size on ρ_G evaluated at the same resolution $h = 50$ nm for selected specimen sizes at $\varepsilon = 0.1$. For the specimen with height 12.8 μm the ρ_G was evaluated at a strain of $\varepsilon = 0.056$. The signed or GND density ρ_G is calculated using (2.18). See additional material in Appendix A on page 223.

The signed, or GND, density for slip system κ is defined as $|\rho_+^{(\kappa)} - \rho_-^{(\kappa)}|$. The total GND density, ρ_G, is defined using the net Burgers vector based on Nye's tensor (see Section. 1).

Clearly, both $|\rho_+^{(\kappa)} - \rho_-^{(\kappa)}|$ and ρ_G are resolution-dependent. Fig. 15a shows the through-thickness distribution of ρ_G corresponding to four different values of the resolution h in the $H = 3.2$ μm specimen strained to $\varepsilon = 0.1$. The method used to define local densities is the same as in the previous section. At the coarsest resolution $h = H$ the GND density only represents 0.3% of the total dislocation density, consistent with a macroscopically homogeneous deformation. However, a local GND density emerges at sufficient resolution. It peaks at the center of the specimen but all values are significant relative to the total dislocation density. As expected, the local GND density is highly resolution-dependent: the finer h the higher the fluctuations in ρ_G.

Fig. 15b depicts the through-thickness distribution of the GND density for the three specimens shown in Fig. 14 at $\varepsilon = 0.1$, in addition to one $H = 12.8$ μm specimen at $\varepsilon = 0.056$. The same resolution $h = 50$ nm was used for all specimens [1]. This value of h is sufficiently small in comparison with the smallest specimen ($H = 0.2$ μm) but large enough so that individual domains contain on average a large number of dislocations. Typically, at $\varepsilon = 0.1$ there were about 60 and 630 dislocations per domain analyzed in the $H = 0.2$ μm and $H = 3.2$ μm specimens, respectively. Fig. 15b reveals a trend for increasing local GND density upon a decrease in specimen size. The same trend is obtained when each slip system is analyzed separately.

It is worth emphasizing that, in all specimens with $H \geq 0.4\mu$m, the net GND

---

[1]Admittedly, fixing only 'h' does not lead to a constant domain area within which the GND density is determined when sample size is varied. Further analysis maybe be found in Chapter V and in Appendix A. The additional analysis also includes spatial maps of GND density.

density represents less than 10% of the total density up to $\varepsilon = 0.1$. Although the imposed deformation is macroscopically homogeneous a GND density emerges in microscopic domains. This finding highlights the role of a locally non-vanishing GND density in setting the local, and by way of consequence, the global flow stress. Quantifying the relationship between local flow stress and local GND density is, however, not a trivial task in view of the fact that the GND density is dependent upon resolution and vanishes overall. Only macroscopic, heuristic correlations can be envisaged using appropriately defined GND measures. One such correlation is developed in Section 7 below.

6. Bauschinger effect

In view of the build-up of a signed dislocation density at the micro-scale, significant back-stresses arise which contribute to the apparent work-hardening. In an attempt to quantify the effect of such back stresses, all specimens were unloaded to $\sigma = 0$. Fig. 16 shows the stress versus strain curves corresponding to unloading from two strain levels. Reverse plasticity takes place in all cases prior to complete unloading. This indicates a Bauschinger effect. When unloading from $\varepsilon = 0.033$, i.e. roughly the end of stage I, the Bauschinger effect is small in all specimens with $H \geq 0.4$ μm in comparison with the $H = 0.2$ μm specimen (Fig. 16a). By way of contrast, unloading from $\varepsilon = 0.067$ reveals a strong Bauschinger effect in all specimens that were deformed up to that strain (Fig. 16b). The $H = 12.8$ μm specimen was unloaded from the highest strain of 0.057 reached in the forward loading calculation. The corresponding curve is also shown in Fig. 16b.

In an accompanying paper we use a strain measure of the Bauschinger effect to show that the latter increases in magnitude with decreasing specimen size. Here, what we abstract from the results in Fig. 16 is that a significant portion of the simulated
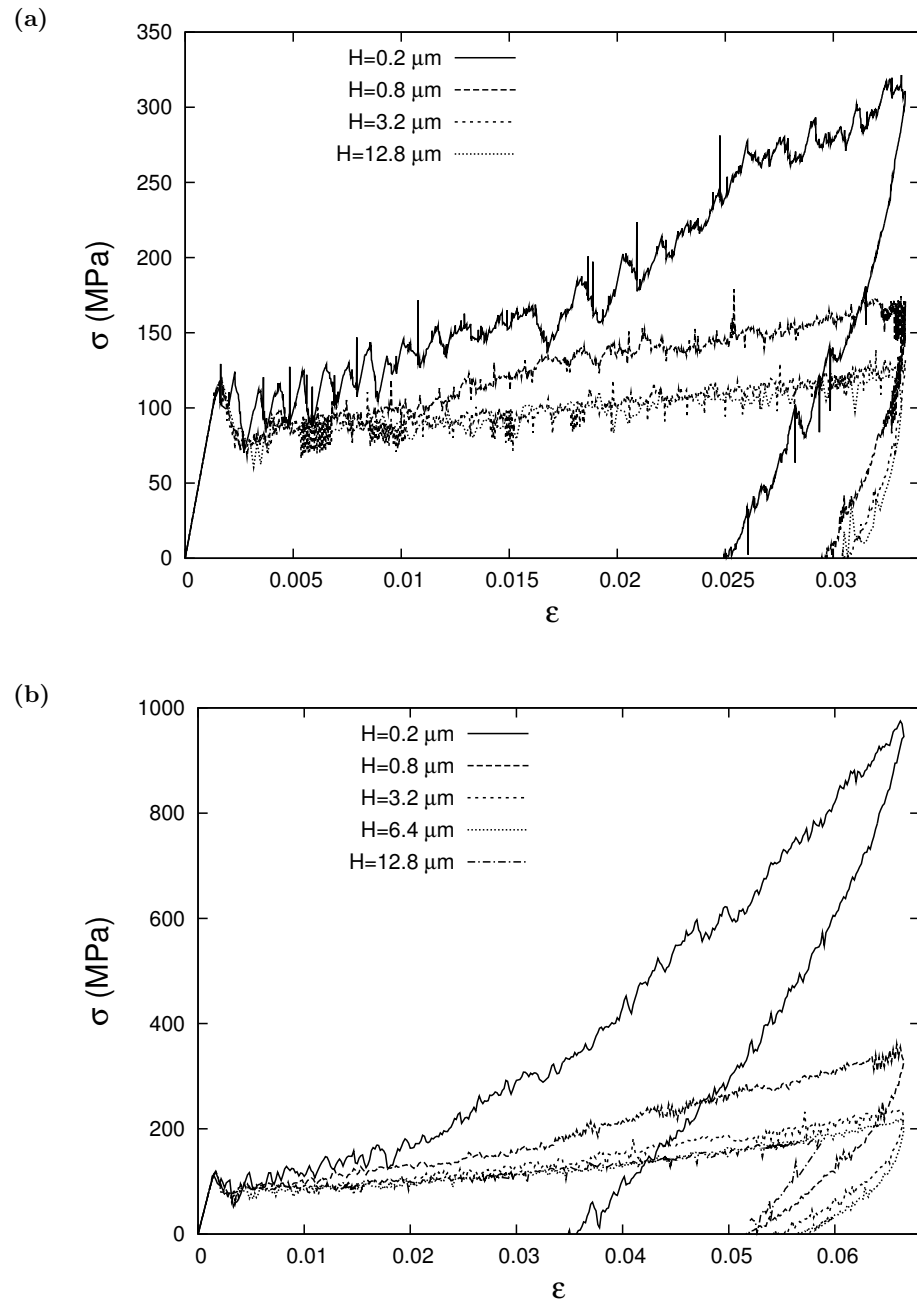
Fig. 16. Selected stress versus strain curves with unloading to $\sigma = 0$ from a strain of (a) $\varepsilon = 0.033$ showing a small Bauschinger effect. More data points are used to plot the loading and unloading behavior; and (b) $\varepsilon = 0.067$ showing a strong Bauschinger effect.

strain hardening is due to back-stresses associated with the rise of a micro-scale GND density. While the GND density vanishes at the macro-scale, the back-stress does not, because of its long-range character.

7. Development of a scaling law

The key features of the discrete dislocation analyses carried out here may be summarized as follows: (i) Taylor hardening breaks down globally and locally; (ii) the microscopic GND density does not vanish as opposed to the macroscopic GND density; and (iii) a significant portion of the observed strain hardening must be associated with evolving back stresses. With this in mind, it would be useful to develop a relationship between flow stress and appropriately chosen structural variables, it being understood that the total dislocation density alone does not describe the current state. Conclusions (ii) and (iii) above will guide the development of this new scaling law.

First, to describe the current state, the dislocation density is supplemented with an additional variable that may be viewed as an integral measure of the microscopic GND density. For each slip system κ, define

$$\bar{\rho}_{\mathrm{G}}^{(\kappa)} = \sum_{n=1}^{p} \frac{\Omega^n}{\Omega} |\rho_{+n}^{(\kappa)} - \rho_{-n}^{(\kappa)}| \tag{2.12}$$

where the local signed density is evaluated within domains Ω^n of resolution h that make up volume Ω. Here, $\Omega^n/\Omega = h/H = 1/p$ with p an integer. A similar density $\bar{\rho}_{\mathrm{G}}$ is defined as an average over all slip systems consistent with the net Burgers vector (see Section. 1). This new variable is termed *effective GND density*.

The distribution of local signed density (i.e., the $|\rho_{+n}^{(\kappa)} - \rho_{-n}^{(\kappa)}|$ terms in (2.12)) depends on the resolution h with the fluctuations increasing with decreasing h as illustrated in Fig. 15a. Fig. 17 shows the extent to which the effective GND density
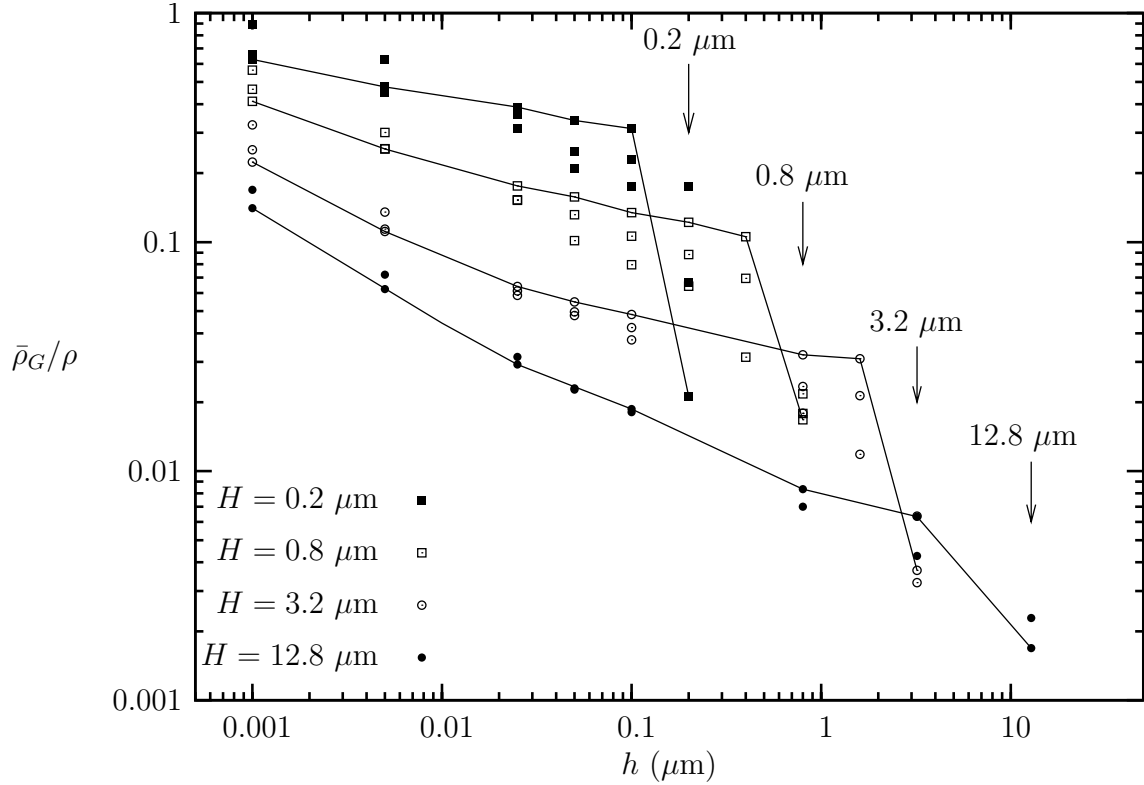
Fig. 17. Effective GND density, $\bar{\rho}_{\mathrm{G}}$, normalized by the total dislocation density versus resolution h for the $H = 0.2~\mu$m, $0.8~\mu$m and $3.2~\mu$m specimens at three strain levels, $\varepsilon = 0.033$, 0.067 and 0.1, and for the $H = 12.8~\mu$m specimen at $\varepsilon = 0.033$ and 0.056. Solid lines run through the points corresponding to either $\varepsilon = 0.1$ or $\varepsilon = 0.056$. The value of $\bar{\rho}_{\mathrm{G}}$ at resolution $h = H$ is identified with the actual GND density ρ_{G} in the specimen. The densities ρ_{G} and $\bar{\rho}_{\mathrm{G}}$ are calculated using (2.18) and (2.19), respectively. See additional material in Appendix A.

$\bar\rho_G$ is itself depending on resolution. For a given specimen size, the latter is varied from 1 nm to the full height H of the specimen. At any given resolution, and in most cases, three data points are shown which correspond to the three strain levels $\varepsilon = 0.033$, 0.067 and 0.1. At fixed specimen size and strain level, decreasing h leads to an increase in $\bar\rho_G$. This increase is the integral measure of microscopic GND density build-up. At the limit $h = H$, which sets the coarsest resolution, the effective GND density coincides with the actual GND density in the specimen at the current strain ($\bar\rho_G = \rho_G$). At the lower limit $h = 1$ nm, the dislocation spacing is nearly resolved so that $\bar\rho_G$ approaches the total density. In addition, at fixed resolution larger than 25 nm and different from the specimen size, the effective GND density is found to increase with increasing strain with the rate of increase being greater in smaller specimens.

Although definition (2.12) is resolution-dependent Fig. 17 shows that there is a resolution range over which the sensitivity of the effective GND density to resolution is small in comparison with its sensitivity to specimen size. Roughly speaking the upper and lower limits of that range are 100 nm and 25 nm.

Next, write the total density as $\rho = \bar\rho_G + (\rho - \bar\rho_G)$. Several correlations were investigated assuming a two-variable state law for the macroscopic flow stress $\mathcal{T}(\rho, \bar\rho_G)$. Because the overall flow stress is the same for either slip system, data corresponding to both slip systems was used to qualify the correlation with more data points. The following additive form has proven most effective based on fits to numerical results:

$$\mathcal{T} = \mathcal{T}^{(\kappa)} = A\mu b\sqrt{\rho^{(\kappa)} - \bar\rho_G^{(\kappa)}} + \mu l^2 \bar\rho_G^{(\kappa)} \tag{2.13}$$

where A and l are fitting constants. The proposed form is well-defined since $\bar\rho_G^{(\kappa)}$ cannot exceed the total density on slip-system κ as shown in Section. 1. The first term of (2.13) represents a variant of the classical size-independent forest hardening term whereas the second term represents the increase in flow stress associated with
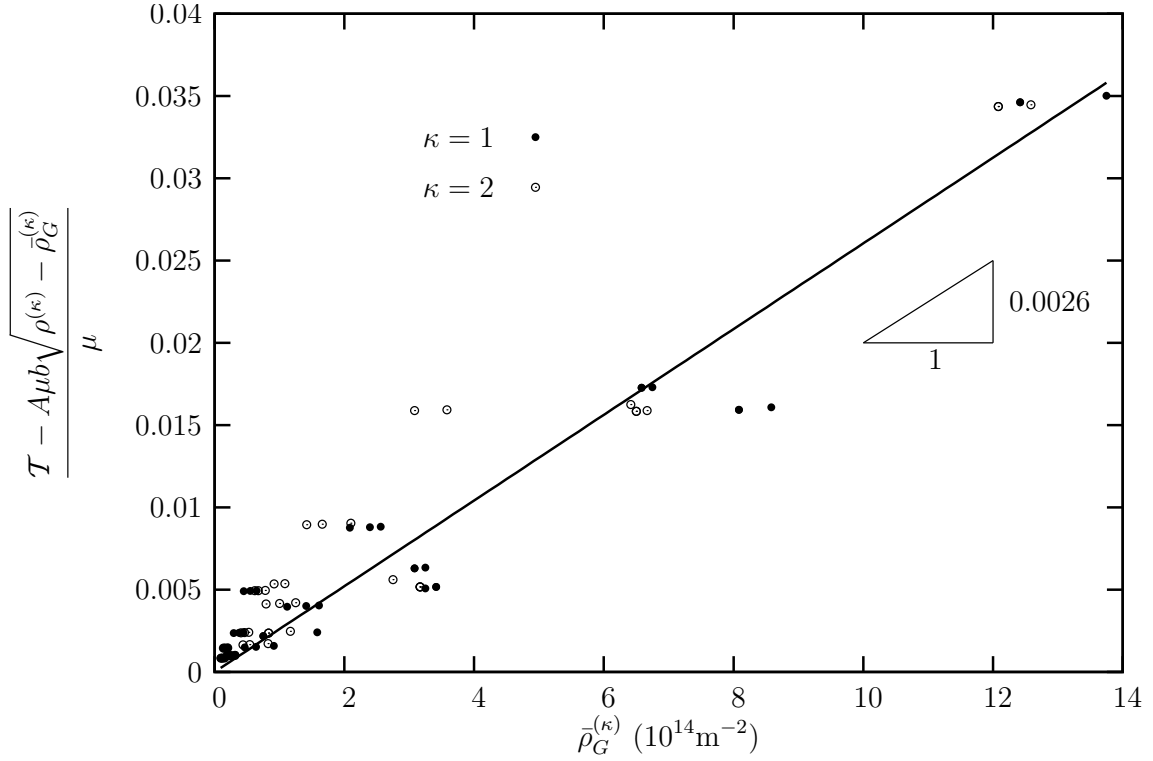
Fig. 18. Qualification of correlation (2.13) scaling the macroscopic flow stress $\mathcal{T}$ with two state variables: the dislocation density $\rho^{(\kappa)}$ and the effective GND density $\bar{\rho}_G^{(\kappa)}$, specified per slip-system κ to maximize the number of data points. $\bar{\rho}_G^{(\kappa)}$ is defined through (2.12). The data analyzed include the $H = 0.2$ μm (two realizations), 0.8 μm and 3.2 μm specimens at three strain levels, $\varepsilon = 0.033$, 0.067 and 0.1, and the $H = 12.8$ μm specimen at $\varepsilon = 0.033$ and 0.056. For each condition three values of the resolution h were used $h = 25$, 50 and 100 nm. There are a total of 84 points in the plot with some overlap. The length scale l in (2.13) is found to be 5.1 ± 2 nm with $A = 0.3$.

the effective GND density. The factor l has dimensions of a length but does not necessarily represent the length scale of the deformation process itself. The results in Fig. 17 clearly indicate that $\bar{\rho}_G$ (or $\bar{\rho}_G^{(\kappa)}$) would essentially vanish in a bulk sample so long as the dislocation spacing is not fully resolved. The scaling law (2.13) reduces then to the classical Taylor hardening equation (2.11).

In order to qualify the proposed correlation (2.13) the data corresponding to the $H = 0.2$, 0.8, 3.2 and 12.8 μm specimens within the 25 to 100 nm resolution range is gathered in Fig. 18. The data correspond to all strain levels shown in Fig. 17. Then viewing $\mathcal{T}$ as a function of $\rho^{(\kappa)}$ and $\bar{\rho}_G^{(\kappa)}$ the factors A and l were determined by linear regression, constraining A to lie between 0.3 and 0.5. The remarkable result is that, even though the effective GND density very much depends on resolution, the length parameter l in (2.13) was found to be independent of resolution. The fit in Fig. 18 was obtained using $A = 0.3$ and $l = 5.1 \pm 2$ nm. Eventually, if densities ρ and $\bar{\rho}_G$ are used in (2.13) the length l would be 4.0 ± 2.3 nm.

8. Slip patterns

Fig. 19 shows the distribution of slip at $\varepsilon = 0.1$ in the same specimens shown in Figs. 10 and 12. The computation of total slip γ_{tot} is explained in Section. 2. For all specimen sizes fine slip bands are generated along the whole gauge length of the specimen, in contrast with the slip patterns obtained by Benzerga (2008) in the low dislocation density case where the behavior was essentially multiplication-controlled. In sub-micron specimens, the calculations there exhibited single or a few intense slip bands extending across the specimen thickness. Here, the slip bands do not extend across the thickness because slip is restricted by dislocation interactions. The initial dislocation source density is high enough to promote forest hardening mechanisms even in the smallest specimens.
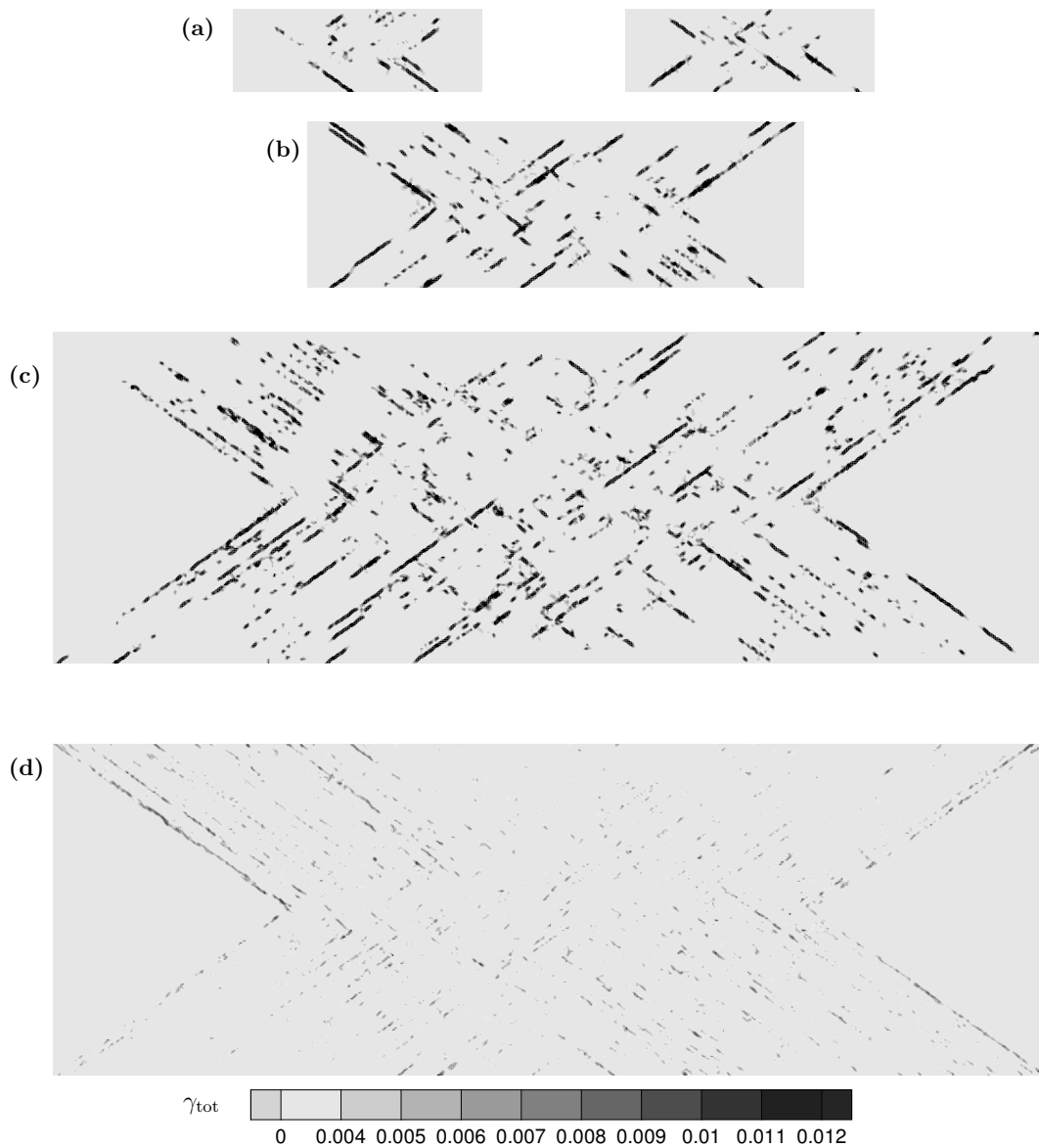
Fig. 19. Contours of total slip γ_{tot} at $\varepsilon = 0.1$ in crystals of height (a) $H = 0.2$ μm; (b) $H = 0.4$ μm; (c) $H = 0.8$ μm (all scaled appropriately); and (d) $H = 3.2$ μm (not scaled). Units are arbitrary. Two realizations are shown for the $H = 0.2$ μm specimen as in Figs. 10 and 12.

In addition, the slip patterns in Fig. 19 show that in larger specimens slip is more diffuse: the imposed strain rate is accommodated by many more slip bands per unit volume, but the slip bands are more intense in smaller specimens. Also, in regions with high dislocation densities the slip bands are consistently shorter: the dislocations remain the most effective obstacles to the motion of other dislocations in a single crystal.

E. Discussion

Mechanism-based discrete dislocation plasticity (M-DDP) has been used to analyze the effect of dimensional constraints on plastic flow in the absence of macroscopic strain gradients. A unique capability of the framework is that it permits analyses of the multi-stage hardening response of single crystals to be undertaken. In particular, the effect of size on work-hardening has been analyzed in detail. The results indicate that the work-hardening rate increases with decreasing specimen size. Our findings demonstrate that this strengthening is due to an increase in stress throughout the specimen when the specimen size is reduced. This increase in stress is associated with the emergence of a signed dislocation density at sufficient resolution. Evidently, the local GND, or signed, density is resolution dependent, but it is worth emphasizing that domains where the GND density does not vanish can be large enough to contain many dislocations and so can be viewed as statistically homogeneous with respect to plastic behavior.

Consistent with a macroscopically homogeneous deformation, no net GND density accumulates over the specimens in general. However, a non-vanishing local GND density emerges in the course of deformation as a result of an evolving dislocation structure. As described by Benzerga et al. (2004), specific dislocation patterns form

locally which involve dislocation wall formation, cell closure and cell subdivision. The process of cell closure for instance evolves through the formation of tilt walls that induce lattice misorientations across them. Arrays of geometrically necessary dislocations are formed subsequently to accommodate local lattice rotations. Such arrays were referred to as geometrically necessary boundaries (GNBs) by Benzerga et al. (2004). The fact that dislocation structures typical of single and polycrystal deformation involve the formation of GNBs is well appreciated in the literature (Hughes and Hansen, 1993). Although the patterns described above are planar, they do have in common with those described by Hughes and Hansen (1993) that they lead to significant lattice rotations and build-up of *local* GND density.

An important aspect of the behavior predicted by the M-DDP calculations here is that Taylor-like hardening breaks down at the macro-scale, i.e. that of the sample. The scaling law (2.11) characteristic of bulk behavior ceases to be valid even in the largest specimens analyzed after sufficient straining. In addition, the deviation from (2.11) is found to increase in magnitude and to occur at a lower strain with decreasing specimen size (Fig. 11). Previous discrete dislocation analyses carried out by Benzerga et al. (2004) within the same framework did not explore size effects. The values of $\Theta_{\mathrm{II}}/\mu = 0.022$ and 0.025 predicted in their analyses for specimens with $H = 2$ μm and 4 μm, respectively, are about three times the average bulk value and fall slightly below the curve in Fig. 7b. This difference is attributed to the lower strain rate of order 100 s^{-1} used by Benzerga et al. (2004). Also their analyses indicated that equation (2.11) was valid over the full strain range they investigated. One key difference between their analyses and those reported here is the strain level and dislocation density reached in the simulations. Here, the calculations were conducted up to a strain of 0.1 whereas those that exhibited comparable hardening rate in (Benzerga et al., 2004) were limited to strains of 0.05; also, the dislocation densities reached in

the present simulations are up to one order of magnitude higher.

Most importantly, the present M-DDP calculations demonstrate that Taylor-like hardening breaks down at the micro-scale, i.e. that of a non-vanishing GND density. This is best illustrated by the results selected in Fig. 14b. This finding raises fundamental questions regarding the formulation of augmented theories of plasticity. Many such theories are based on the understanding that plastic flow processes are inherently size-independent in the absence of strain gradients at the scale of the elementary volume. For instance, some theories presume as valid the scaling of the flow stress with the dislocation density at the micro-scale (Nix and Gao, 1998; Gao et al., 1999). Although the M-DDP analyses predict that the scaling law (2.11) breaks down under conditions of macroscopically homogeneous deformation, it is likely that (2.11) will break down under macroscopically inhomogeneous deformation as well.

The scale dependence of strength and hardening beyond yielding and in the absence of macroscopic strain gradients poses a challenge to modeling of plasticity at the micron scale. Nonlocal plasticity theories, in their current form, fail to capture size effects under nominally uniform deformation. In general, the length scales that enter such theories stem from dimensional considerations and thus are not tied to the physics of deformation. In addition, the length scales of nonlocal plasticity theories are fixed whereas plastic deformation involves evolving length scales. A coarse-grained version of so-called field-dislocation mechanics (Acharya, 2001, 2004; Roy and Acharya, 2006) begins to show the promise of predicting size-dependency in the absence of macroscopic gradients.

It remains that the size effect predicted by the calculations here is directly linked to GNDs. From that point of view, it is no different in essence from the plasticity size effect documented for nanoindentation of films or bending of foils. The scale at which

GNDs operate is smaller, however, under macroscopically homogeneous deformation. As a consequence, the scale dependence of plastic flow arises in a specimen size range below 10 μm or so. On the other hand, under inhomogeneous deformation this scale dependence is already noticeable for a specimen size about 100 μm (Stölken and Evans, 1998).

From the practical standpoint, because of the size dependence of strain hardening (Fig. 7b), the power law scaling (2.10) of the flow stress changes upon deformation. Our calculations predict a scaling exponent in the range 0 to 0.42 for strains ranging from yield to 0.1 (Figs. 5 and 7a). The discrete dislocation calculations of Benzerga and Shaver (2006) and similar recent unpublished work predict a value of x larger than unity whereas those carried out by Deshpande et al. (2005) predict $x = 0.5$, closer to the value predicted here at $\varepsilon = 0.1$. The main difference between the two sets of calculations is directly related to the density of initial dislocation sources. At low initial densities (typically 1 μm^{-2} and below) the behavior is multiplication controlled as in (Benzerga and Shaver, 2006). On the other hand, at high initial dislocation density (typically 100 μm^{-2} and above) the behavior is rather dislocation-interaction controlled. The two sets of studies are thus complementary of each other in that they explore two extreme scenarios, which help shed some light on the experimental results. Experimental reports of the flow stress scaling indicate values of the scaling exponent x ranging from 0.6 in Au microcrystals at $\varepsilon = 0.05$ (Volkert and Lilleodden, 2006) to 0.6–0.7 in Ni microcrystals at $\varepsilon = 0.01$ (for diameters larger than 1 μm) (Dimiduk et al., 2005) to a value as high as $x = 1.1$ at $\varepsilon = 0.1$ in gold microcrystals with diameters in the sub-micron range (Greer and Nix, 2006). Note that these experimental values are often determined after some plastic straining; hence they are not representative of the scaling of the flow stress over the full strain range. Yet the 0.6–1.1 range of experimental values is contained within the 0.4–1.5 range of predicted

values, and this suggests that the behavior observed in micropillars may be affected by multiplication as well as interaction processes but in proportions that may vary with density and strain level.

In light of the recent micropillar experiments along with discrete dislocation predictions like those presented here, it would be a subtle task to apportion the origin of size effects in previous experiments where strain gradients were superposed onto a homogeneous component of the applied strain. In particular, the enhanced size effect reported in recent studies (Swadener et al., 2002) for nanoindentation at the sub-micron scale may be the signature of the emergence of strain gradients and related GND densities at a scale much smaller than that associated with the gradient part of the imposed strain.

In our view, it is worthless to pursue a universal correlation between flow stress and dislocation density that would be valid at all scales. One should be content if a scaling law can be at all inferred and accept that the involved constants may be resolution-dependent. The results of the present M-DDP analyses have been used to derive and qualify a correlation between the *macroscopic* flow stress, the dislocation density and an appropriate *macroscopic* measure of the microscopic GND density. One remarkable aspect of the flow stress scaling relation (2.13) is that, while the effective GND density depends on resolution, factors A and l do not. Thus, the proposed correlation can be used as a fundamental law in physics-based phenomenological modeling of plastic behavior at the micron scale.

The additive form in the generalized Taylor equation (2.13) was motivated in part by the fact that there is a strong connection between the emergence of a local GND structure and the Bauschinger effect. At low strains the local GND density is very small relative to the total density. As a consequence the classical scaling law (2.11) holds (Fig. 11) and the Bauschinger effect is small (Fig. 16). By way of

contrast, at higher strains typical of stage II the local GND density is significant and so is the Bauschinger effect. Such a strong effect indicates that a significant portion of the flow stress results from back stresses. The effect of the latter is inherently different from that associated with forest hardening. It is therefore not surprising that a linear, rather than square root, dependence upon the effective GND density was found to fit better the M-DDP results.

Ultimately, there is no substitute to injecting appropriate physics in developing a better understanding of size-dependent plasticity. Despite the idealization inherent to the representation of dislocation reactions within M-DDP, the merit of the framework is to enhance the capability of mesoscale modeling at capturing the richness of collective dislocation behavior without too much compromise to computational power. Most calculations carried out here were run on a Linux desktop. Only those calculations corresponding to the largest three specimens were carried out on a supercomputer using a sequential code. Ongoing efforts at parallelizing the code and improving dislocation dynamics algorithms will impart further capabilities to the framework.

F. Conclusions

Discrete dislocation analyses of the uniaxial compression of single crystals potentially oriented for double slip have been carried out to investigate the effect of specimen size on plastic flow properties. The calculations are two-dimensional but key physics of the three-dimensional dislocation interactions were incorporated through additional constitutive rules. Such "2.5D" rules account for line tension, junction formation and destruction, and dynamic source and obstacle creation. Within this framework, plastic flow arises from the nucleation and subsequent motion of discrete dislocations. The

multi-stage hardening response as well as the evolving dislocation structure are natural outcomes of the simulations. In this work, a relatively high density of pre-existing internal Frank–Read sources was used to promote athermal hardening processes. Our conclusions are as follows.

- Strengthening upon scale reduction is predicted under nominally uniform compression. The size effect is significant for both the flow stress and the work-hardening rate. In particular, the stage II hardening rate increases by one order of magnitude within the range of specimen sizes explored here.

- The rate of dislocation accumulation increases with decreasing specimen size. However, the flow stress is not set by the dislocation density as in bulk plasticity; Taylor-like hardening breaks down at both macro- and micro-scales.

- Although in general no net GND density accumulates in the specimens, consistent with a macroscopically homogeneous deformation, a microscopic GND density emerges in the course of deformation, which strongly affects the microscopic, hence the macroscopic, flow stress.

- The emergence of a local GND density results from microstructure evolution and is associated with a strong Bauschinger effect. The evolution of the dislocation structure is promoted by increased dislocation interactions fostered by the usual athermal hardening processes, but with characteristic lengths comparable with the size of submicron-scale specimens. The size effect results.

- A new scaling law for the flow stress is proposed based on the discrete dislocation analyses. Two state variables are used: the dislocation density and an effective GND density. The latter depends on resolution but the scaling parameters do not.

- The size effect predicted here stems from interaction controlled behavior, which primarily affects the hardening and is promoted at high dislocation density. On the other hand, at low dislocation densities forest hardening mechanisms are less effective and the behavior may become multiplication-controlled. Both types of behavior may be invoked in interpreting the results of recent micropillar experiments.

G. Supplementary material

1. Calculation of the actual and effective GND densities

Consider a volume ω of crystalline material that is plastically deformed by slip on N_s slip systems. Assuming plane strain, the density of geometrically necessary dislocations over ω is defined as the Euclidean norm of the net Burgers vector, to be specified below, per unit material Burgers vector length, i.e.,

$$\rho_{\mathrm{G}} = \frac{||\mathbf{B}||}{b} = \frac{\sqrt{B_i B_i}}{b}. \tag{2.14}$$

Following the formulation in (Cermelli and Gurtin, 2001) a network of dislocations piercing a plane with unit normal $\mathbf{n}$ has a net Burgers vector $\mathbf{B}$ per unit area given by:

$$\mathbf{B} = \mathbf{G}\mathbf{n} \tag{2.15}$$

where $\mathbf{G}$ is the geometric dislocation tensor. Assuming infinitesimal rotations, and to the neglect of elastic strains, $\mathbf{G}$ reduces to Nye's tensor $\boldsymbol{\alpha}$ (Nye, 1953).

For pure edge dislocations under the assumed plane strain conditions $\mathbf{n}$ is chosen as the out of plane normal $\mathbf{e}_1 \times \mathbf{e}_2$ with $\mathbf{e}_1$ and $\mathbf{e}_2$ the base vectors in the x_1–x_2 plane of Fig. 4. The components of Nye's tensor on that base are written as (Arsenlis et al.,

2004)

$$\alpha_{ij} = \sum_{\kappa=1}^{N_s} (\rho_+^{(\kappa)} - \rho_-^{(\kappa)}) b_i^{(\kappa)} n_j \tag{2.16}$$

where $\mathbf{b}^{(\kappa)}$ is the Burgers vector of slip-system κ and is here written as $b\,\mathbf{s}^{(\kappa)}$ with $\mathbf{s}^{(\kappa)}$ a unit vector along the slip direction. Thus, under the conditions of the simulations here, equation (2.15) is specified in view of (2.16) as

$$B_i = b \sum_{\kappa=1}^{N_s} (\rho_+^{(\kappa)} - \rho_-^{(\kappa)}) s_i^{(\kappa)} \tag{2.17}$$

Denoting $\varphi^{(\kappa)}$ the oriented angle that defines slip direction on slip-system κ, measured from the x_1 axis, the formula used to calculate ρ_G is then obtained as

$$\rho_G = \sqrt{\left[\sum_\kappa (\rho_+^{(\kappa)} - \rho_-^{(\kappa)}) \cos \varphi^{(\kappa)}\right]^2 + \left[\sum_\kappa (\rho_+^{(\kappa)} - \rho_-^{(\kappa)}) \sin \varphi^{(\kappa)}\right]^2} \tag{2.18}$$

For the double slip configuration considered here, $\varphi^{(1)} = \varphi_0 = 35.25°$ and $\varphi^{(2)} = \pi - \varphi_0 = 144.75°$.

The effective GND density $\bar{\rho}_G$ is defined as

$$\bar{\rho}_G = \sum_{n=1}^{p} \frac{\Omega^n}{\Omega} \rho_{G\,n} \tag{2.19}$$

where $\rho_{G\,n}$ is the GND density calculated as in (2.18) but specified over the local domain Ω^n defined in the text.

Since a correlation of the form (2.13) is sought, the positiveness of $\rho^{(\kappa)} - \bar{\rho}_G^{(\kappa)}$, specified for each slip-system, is in question. The inequality $\rho^{(\kappa)} \geq \bar{\rho}_G^{(\kappa)}$, with $\bar{\rho}_G^{(\kappa)}$ given by (2.12), follows from the identity

$$\rho_n^{(\kappa)} = |\rho_{+n}^{(\kappa)} - \rho_{-n}^{(\kappa)}| + 2 \min(\rho_{+n}^{(\kappa)}, \rho_{-n}^{(\kappa)}) \tag{2.20}$$

which is valid for each domain Ω^n. If a correlation where $\rho - \bar{\rho}_G$ is used instead,

the inequality $\rho \geq \bar{\rho}_G$, with $\bar{\rho}_G$ given by (2.19), holds true because the actual GND density within a given domain cannot exceed the total density in that domain.

2. Determination of slip contours

Since in discrete dislocation plasticity, the plastic part of the deformation is associated with the evolution of displacement jumps across the slip planes, the displacement gradient field involves delta functions which need to be accounted for to compute the slip. To simplify the calculation, an approximation is used. A smooth strain rate field, $\dot{\varepsilon}^s$, is introduced in each finite element that is computed by differentiating the total displacement rate field $\dot{\mathbf{u}}$ in that element using the finite element shape functions. Then, within an element, the slip on the κth system is defined by

$$\gamma^{(\kappa)} = s_p^{(\kappa)} \dot{\varepsilon}_{pq}^s m_q^{(\kappa)} \tag{2.21}$$

where $\mathbf{s}^{(\kappa)}$ is the slip direction and $\mathbf{m}^{(\kappa)}$ the slip normal for slip system κ. Because $\gamma^{(\kappa)}$ includes contributions from all dislocations it does not represent the actual slip on system κ. It is rather viewed as a convenient measure for visualizing the slip patterns. The pointwise total slip is defined as $\gamma_{\text{tot}} = \sum_{\kappa=1,2} |\gamma^{(\kappa)}|$. Note that slip displacements associated with dislocations exiting at free surfaces are accounted for in (2.21) although no account is taken of actual geometry changes, e.g., creation of new free surface.

3. Stress contours

In the simulations, the crystal surfaces at $x_2 = \pm H/2$ are taken to be traction free. This boundary condition leads to $\sigma_{22} = \sigma_{12} = 0$ along the top and bottom surface of the crystal. Contour of σ_{22} and σ_{12} in a crystal of height $H = 3.2$ μm are shown at a strain of $\varepsilon = 0.1$ in Fig. 20a and b, respectively. The contour plots show that
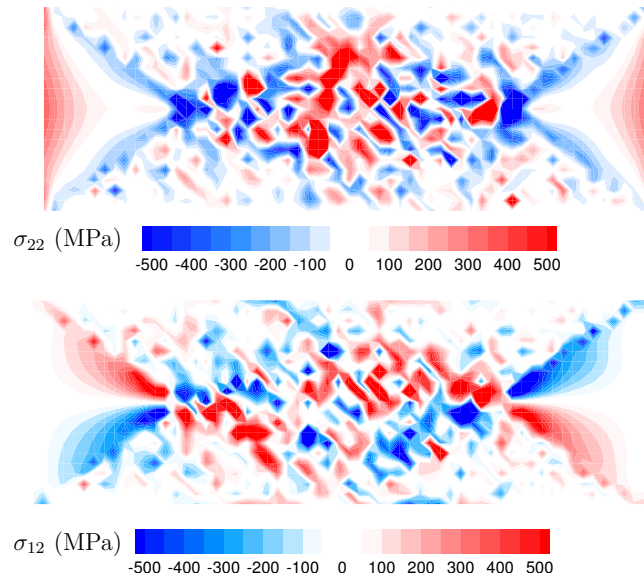
Fig. 20. Contours of stress: (a) σ_{22}; (b) σ_{12}. The contours are shown at $\varepsilon = 0.1$ in a crystal of height $H = 3.2 \ \mu$m.

along the top and bottom surfaces of the crystal σ_{22} and σ_{12} vanish; small regions of stresses seen along the top and bottom surface of the crystal in the contours are an artifact of the extrapolation in plotting nodal stress values.

CHAPTER III

STRAIN HARDENING IN MICROPILLAR COMPRESSION: EXPERIMENTS
AND MODELING

A.   Overview

Experimental measurements and simulation results for the evolution of plastic de-
formation and strain hardening in micropillars are compared. In the experiments,
the stress–strain response of high-symmetry Cu single crystals is determined using
micropillar compression. Pillars with either circular or square cross-sections, pillars
on a substrate and coated pillars are considered. Discrete dislocation simulations
are conducted within a two-dimensional plane strain framework with the dislocations
modeled as line singularities in an isotropic elastic medium. The pillar is modeled
using a planar crystal potentially oriented for multiple slip. Physics-based constitu-
tive rules are employed for an adequate representation of strain hardening. Both the
experiments and the computations show: (i) a steady strain-hardening behavior in
all pillars, (ii) a flow strength and hardening rate that increase with decreasing pillar
size and (iii) significant lattice misorientations after heavy deformation. Furthermore,
the experimental measurements and simulation results for the flow stress at various
strain levels and the hardening rates are in good quantitative agreement.

B.   Introduction

Materials harden when they are plastically deformed. In pure materials plastic resis-
tance comes from dislocation interactions and intersections. The mechanisms for this
resistance vary from one stage of deformation to another, with many details being
material specific. However, the main features of strain hardening remain the same,

as manifested for example by universal values of the work hardening rates when normalized by the material stiffness. This holds for both single and polycrystals (Argon, 2008).

Over the past few years, new experimental methods have been developed that enable probing of the mechanical response of materials at the scale of their microstructures. These techniques thus permit fundamental issues in crystal plasticity to be addressed and limits of current models to be examined. Among such methods, micropillar compression has been extensively used (Uchic et al., 2004; Dimiduk et al., 2005; Greer et al., 2005; Volkert and Lilleodden, 2006; Kiener et al., 2006; Frick et al., 2008; Kiener et al., 2008b); see Uchic et al. (2009) for a recent review. In general, a common trend emerges from pillar compression experiments with smaller being stronger. However, there are conflicting reports on whether strain-hardening is size-dependent and, if so, what the origin of the apparent hardening is. In addition, the strength of the scaling of flow stress with pillar diameter varies from one experimental data set to another. Therefore, there is a need for further experimental investigation coupled with analysis of plasticity in micron and sub-micron size objects, especially in the absence of imposed strain or stress gradients. In particular, design of experiments that allow an investigation of strain hardening at the micron and sub-micron scales has far reaching implications on physics-based plasticity modeling and simulation efforts.

Phenomenological models of plasticity do not include adequate representation of microstructural effects at the dislocation scales. In addition, current continuum models are incapable of providing a rationale for micropillar plasticity and size-effects. Under such circumstances, recourse to lower scale, higher resolution analyses is necessary. Fully discrete atomic-level methods, such as molecular dynamics (MD), have been used for understanding plasticity in nano-scale domains, e.g., (Horstemeyer et al.,

2001; Deng and Sansoz, 2009a). However, MD is incapable of resolving sample sizes ranging from 100 nm to over 10 microns, i.e., the range of pillar diameters considered in the experiments thus far. Alternatively, semi-discrete analyses may be used which are based on dislocation theory, i.e., linear elasticity for long-range dislocation interactions as well as suitably specified atomic-level input.

Progress on discrete dislocation dynamics (DD) simulations of micropillar plasticity has recently been reviewed by Uchic et al. (2009). Subtleties aside, three-dimensional (3D) simulations have essentially confirmed two strengthening mechanisms: the role of source strength distribution when sources are available, e.g., Rao et al. (2008) and El-Awady et al. (2009), and the imbalance between rates of dislocation generation and dislocation annihilation/immobilization when there is paucity of sources, e.g., Tang et al. (2007) and Rao et al. (2008). As noted by Uchic et al. Uchic et al. (2009), it is remarkable that some two-dimensional (2D) DD simulations (Benzerga and Shaver, 2006) had identified such strengthening mechanisms; see Benzerga (2008) for an elaboration on the second mechanism, termed exhaustion hardening.

None of the DD simulations above have discussed the transition to bulk-like behavior where forest hardening processes are generally expected to result in size independent response. However, the preliminary experimental results of Kiener et al. (Kiener et al., 2008b) as well as the DD simulations of Guruprasad and Benzerga (Guruprasad and Benzerga, 2008b) have independently revealed that size-dependent, steady strain-hardening can be obtained up to very large strains. Such behavior cannot be rationalized in terms of previously established strengthening mechanisms. The lack of investigations centered on size-affected strain hardening is not commensurate with the critical need for improved hardening models in continuum descriptions and is in part due to the absence of clear trends in most previously published experiments.

Driven by previous investigations (Kiener et al., 2008b; Guruprasad and Benz-

erga, 2008b), the objective of this work is to combine experiments and DD modeling and simulation in an investigation of (i) the propensity of micropillars to strain harden; and (ii) the size dependence of strain hardening. Micro-compression experiments were carried out on high symmetry Cu single crystalline micropillars made by focused ion beam (FIB) milling, with either circular or square cross-sections and diameters or side lengths from 8.2 down to 0.9μm (Kiener et al., 2008b). The choice of Cu is motivated by its technological use in micro- and nano-electronics applications, the availability of tensile data for micron-thick thin films (Hommel et al., 1999; Huang and Spaepen, 2000; Xiang and Vlassak, 2006; Gruber et al., 2008) as well as micro-tension specimens (Kiener et al., 2008a, 2009a), and by the vast literature concerning the hardening behavior of macroscopic samples (Diehl, 1956; Suzuki et al., 1956; Argon and Brydges, 1968; Prinz and Argon, 1980; Argon, 2008). In an additional set of experiments, pillars coated with a thin TiN film and pillars on a stiff MgO substrate were also used in an attempt to investigate the effect of boundary conditions (Kiener et al., 2009b). Strong effects of size on flow strength and strain hardening and a weak effect of cross-section shape were evidenced, with no significant effect of coating or substrate on the salient features.

The discrete DD formulation follows that of Guruprasad and Benzerga (Guruprasad and Benzerga, 2008b). Pillars with a square cross-section are modeled using a plane strain approximation. The simulations are conducted using the paradigm of 2.5D DD which, despite well known idealizations, represents well key physical aspects of crystal plasticity, including strain hardening (Benzerga et al., 2004). In this formulation, plastic flow arises from the collective motion and interaction of discrete edge dislocations, represented as line singularities in an elastic solid such that the long-range interactions among dislocations are directly accounted for. Atomic level input is incorporated through a set of constitutive rules for close-range interactions.

Chief among these are rules that lead to dynamic multiplication at junction-anchored Frank–Read sources and to effective dislocation storage at dynamically formed junctions. The boundary conditions are enforced by solving for an image field, following the superposition method in (Van der Giessen and Needleman, 1995). This 2.5D DD framework, which enhances the standard 2D model of van der Giessen and Needleman (Van der Giessen and Needleman, 1995), has predicted a range of features observed experimentally in bulk plasticity including Taylor hardening, stage I and stage II hardening with rates in keeping with experimental measurements, and refinement of the dislocation structure upon hardening.

In carrying out the comparison between experiments and modeling, few parameters related to the initial dislocation-source population and dynamic dislocation-junction population are chosen so as to obtain a good representation of the behavior of the largest specimens. Then, with all constitutive parameters fixed, the mechanical response beyond yielding is predicted for all other sizes. The computations provide insight into the mechanisms leading to the observed size dependence and the predictions are compared quantitatively with the experimental observations.

C.   Experiments

1.   Methods

The mechanical response of four sets of Cu micropillars (Table II) was investigated using flat punch indentation (Kiener et al., 2008b, 2009b). In this micro-compression technique, focused ion beam (FIB) machining is used to cut out specimens of desired shapes and dimensions out of a bulk single crystal. These pillar specimens are loaded in compression using a flat conical microindenter. A detailed description of the experimental setup can be found in (Kiener et al., 2009c). The nominal stress σ and

Table II. The four sets of micropillar samples tested.
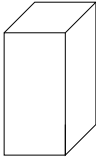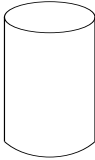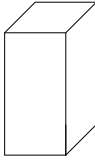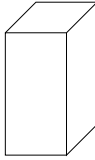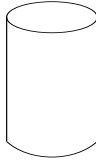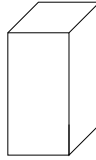
Sample	Cu ⟨100⟩	Cu ⟨111⟩	Cu ⟨100⟩/MgO	TiN/Cu ⟨111⟩
Shape				

Table III. Cross-section shape, crystal orientation, and the minimum and maxmimum equivalent diameter, D, of the pillars tested.

Cross section shape	Orientation/ constraint	Minimum equivalent diameter (μm)	Maximum equivalent diameter (μm)	Standard deviation (%)
Circular	Cu ⟨100⟩	0.8	6.7	11
Circular	Cu ⟨100⟩/MgO	0.98	1.08	6
Square	Cu ⟨111⟩	0.95	5.71	4
Square	Cu ⟨100⟩/MgO	0.41	1.07	4
Square	TiN/Cu ⟨111⟩	0.72	7.27	2

strain ε are determined from the measured load, P, and tip displacement, u, using the simple expressions:

$$\sigma = P/A; \quad \varepsilon = u/H, \tag{3.1}$$

where, H is the height of the pillar measured from the base and A is the cross-sectional area measured at half the pillar height after FIB machining. All samples (round and square) are represented by a dimensional parameter, D, corresponding to the diameter of a circle of area A. Table III lists ranges of D for all pillars tested. All specimens originated from high purity (99.999%) melt grown single crystal rods[1] with a diameter of 10 mm and either a $\langle 100 \rangle$ or a $\langle 111 \rangle$ orientation. Disks having 2 mm thickness were subsequently cut from these rods and bars with dimensions of $2 \times 2 \times 9$ mm^3 were cut using a diamond wire saw.

The first set of specimens were $\langle 100 \rangle$ micropillars having a round cross-section (Table II) with diameters varying from 6.7 to 0.8 μm (Table III). The second set of specimens were $\langle 111 \rangle$ pillars with a square cross-section and corresponding D between 0.9 μm and 5.7 μm. These pillars were fabricated using a dual beam FIB/SEM workstation[2] equipped with a Ga$^+$ ion source operated at 30 keV. All samples had an aspect ratio of about 2:1 following the suggestions of Zhang et al. (Zhang et al., 2006).

The third set of specimens (Table II) were square $\langle 111 \rangle$ pillars coated with TiN. These were made by physical vapor deposition of a 0.8 μm TiN film onto the top surface of one of the $\langle 111 \rangle$Cu disks, followed by FIB milling as above. The TiN coating is intended to serve as a stiff atomically bonded interface preventing possible dislocation escape through the top surface of the pillar. The fourth and final set of specimens

---

[1]purchased from MaTecK GmbH, Juelich, Germany.
[2]Leo XB1540, Carl Zeiss SMT AG, Oberkochen, Germany.

were $\langle 100 \rangle$ pillars on an MgO substrate. Pillars with both round and square cross-sections were produced from a 1 μm thick single crystalline film grown on MgO$\langle 100 \rangle$ (Purswani et al., 2006). In this case, the stiff substrate prevents dislocations from moving into the underlying bulk material. This stands in contrast with the situation in conventional micro-compression testing where the sample is connected to a base of the same material. However, the fabrication procedure narrowed the range of achievable D to values from 0.75 to 1 as limited by the film thickness.

Immediately after fabrication, the samples were transferred from the FIB into a scanning electron microscope (SEM)[3] to minimize exposure to air. Sample testing was performed in situ in this tungsten filament SEM using a microindenter[4] equipped with a flat conical diamond tip (Kiener et al., 2009c). The applied strain rate was about 3×10^{-3} s^{-1}.

Some details of specimen preparation are worth mentioning for completeness. After cutting, the $2 \times 2 \times 9$ mm^3 bars were electrochemically polished on the surface that later became the pillar top surface and on an adjacent side to remove the deformation layer from the cutting process. Removal was confirmed by large area electron backscatter diffraction (EBSD) imaging depicting no wavy deformation structure. To ensure free view of the whole sample during testing, without the need to tilt the whole testing apparatus, it is anticipated to locate the micro-compression samples possibly close to a sample edge. The electrochemical polishing inevitably led to a rounded sample edge. To restore a sharp edge and minimize the required time for FIB milling, the perpendicular sample side was carefully polished with a 1 μm grained alumina suspension. The deformation layer from this preparation step was found to be about

---

[3]Leo 440 Stereoscan, Carl Zeiss SMT AG, Oberkochen, Germany

[4]UNAT, ASMEC, Radeberg, Germany

5 μm thick from EBSD and cross-section FIB investigation. Therefore, as a general rule, another 10 μm of material were removed by coarse FIB cutting before starting the actual sample fabrication. The milling currents were reduced from 1000 pA for coarse milling to 100 pA for finishing of the desired sample dimensions. In the case of the Cu on MgO samples, no additional surface preparation was required, since the deposited film had a clean surface, and the MgO could be cleaved thus forming sharp edges.

The fabrication strategies applied to obtain square or round cross-sections are different, particularly in what regards tapering. Round pillars are relatively simple to realize. However, they tend to be tapered with potential issues associated with stress- and strain gradients (Frick et al., 2008; Kiener et al., 2009b). On the other hand, the samples with square cross sections were untapered. The fabrication procedure can be regarded as a simplified variant of the lathe milling procedure introduced by Uchic et al. (Uchic et al., 2004) with a base geometry that is less well defined. A significant advantage of this fabrication method is that it ensures a nominally uniform stress state over the sample height. Moreover, this square geometry is more directly comparable to the simulated sample geometry, as will be explained in Section D.

Finally, micro-tensile specimens oriented for single slip were tested following the procedure detailed in (Kiener et al., 2008a, 2009a). This data will be used solely for the purpose of model parameter calibration, as will be explained in Section 2.

2.   Experimental results

Fig. 21 shows SEM images recorded during in situ compression testing of two $\langle 100 \rangle$Cu micro-compression samples with diameters of 6 μm. They were fabricated with comparable dimensions just next to each other using the same FIB conditions. Loading was performed right after fabrication under displacement controlled (d.c.) mode (a-
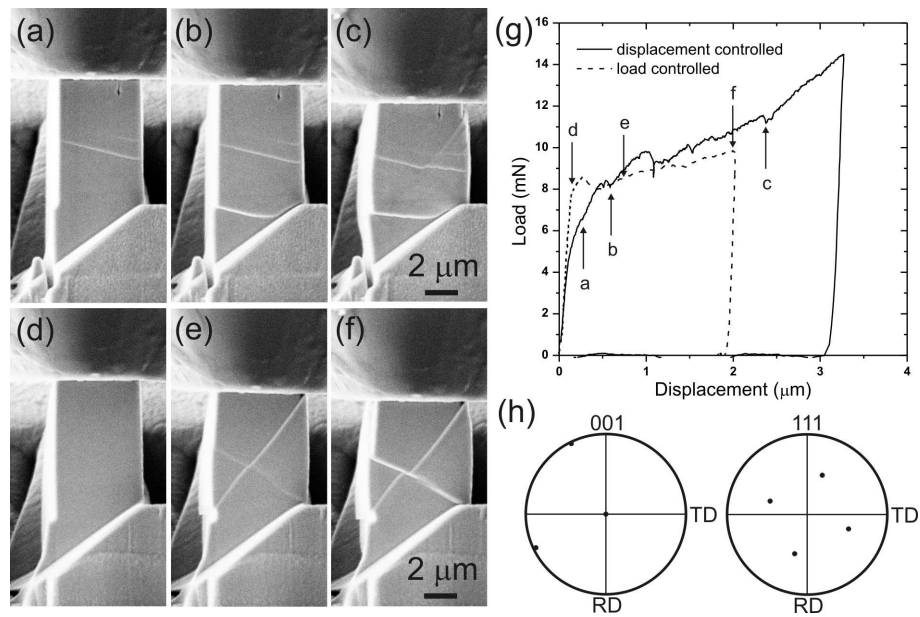
Fig. 21. (a-c) In situ SEM images of a $\langle 100 \rangle$Cu sample with size $D = 6.0$ μm compressed by a flat diamond punch under displacement controlled (d.c.) mode. Multiple slip on several slip planes is observed. (d-f) In situ SEM images of another $\langle 100 \rangle$Cu sample with similar dimensions loaded in load controlled (l.c.) mode. The specimen deformed in multiple slip on a limited number of slip planes. (g) Load - displacement data for the two samples. The d.c. sample shows a lower plastic limit and several load drops, while the l.c. sample sustains a higher plastic limit before undergoing plastic deformation including several displacement bursts. (h) Pole figure map of the two samples measured prior to deformation using electron backscatter diffraction.
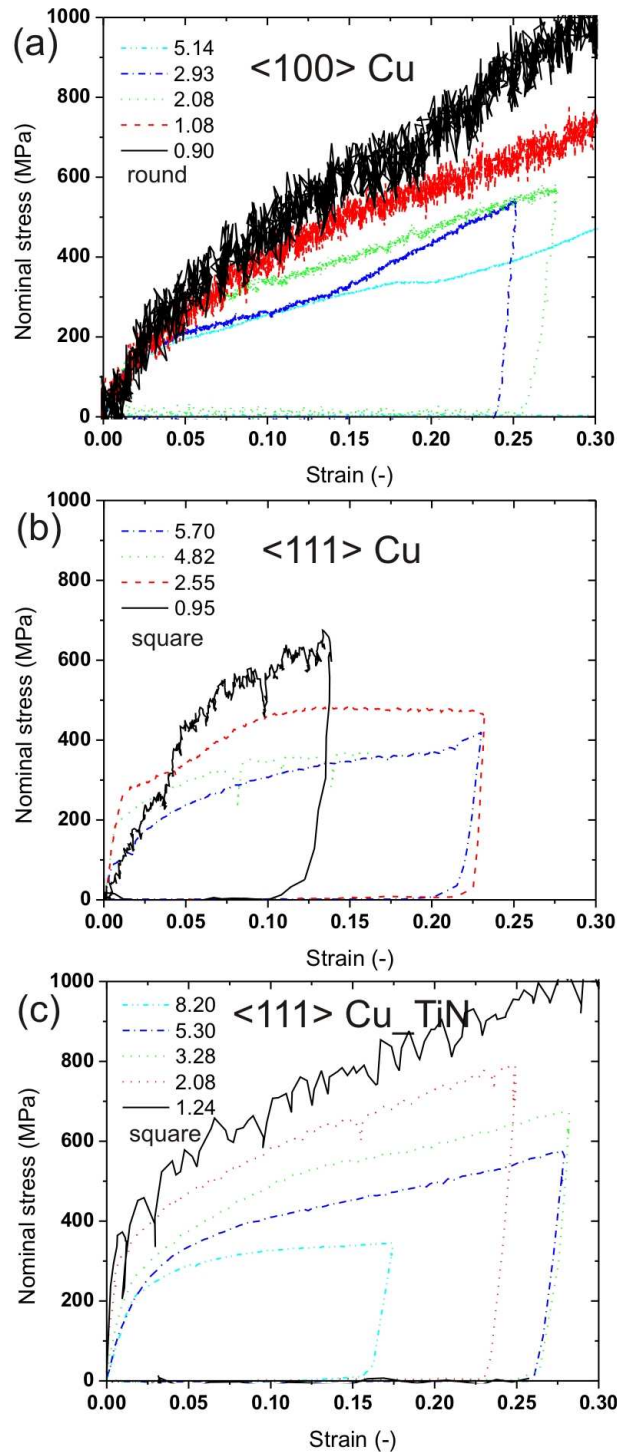
Fig. 22. Representative stress - strain curves showing a sample size effect for tested samples of: (a) tapered round shaped ⟨100⟩Cu; (b) straight square shaped ⟨111⟩Cu; and (c) straight square shaped ⟨111⟩Cu with a TiN top coating.

c), which was generally applied for this study, and under load controlled (l.c.) mode (d-f), which is very common in literature. Fig. 21g provides the recorded load versus displacement data, while a pole figure plot of the sample orientation before deformation is shown in Fig. 21h. It is apparent that both samples deform under multiple slip on equivalent slip systems. There is a more distributed slip characteristic observed for the d.c. mode, while slip is more confined to fewer glide planes in l.c. mode. Since the simulations presented in this study are run under d.c. mode, we will just use samples tested in d.c. mode for comparison to the simulation data.

Fig. 22 shows representative nominal stress versus strain curves only for the $\langle 100 \rangle$Cu, $\langle 111 \rangle$Cu, and $\langle 111 \rangle$Cu with TiN systems. The 18 tested $\langle 100 \rangle$Cu samples on MgO cover only a limited size range and are therefore not shown in Fig. 22 and Fig. 23. However, the data will be used later in Fig. 24. It should be mentioned that the curves shown in Fig. 22 differ in the used output data rate. Fig. 22a was recorded with 32 data points per second, Fig. 22b using 16 points per second, and Fig. 22c with 4 points per second. No general differences between the curves are observed, but noise tends to obscure fine details of the stress versus strain curve for 32 data points per second for the used experimental setup. This can of course be changed by binning the data using for example a moving average filter. In the case of only 4 data points per second, the resulting stress strain curves are devoid of noise, but lose some of the fine details.

For a discussion of size dependent hardening, the stress values at various amounts of strain were extracted and converted from normal stress to shear stress using the nominal Schmid factors of $f_s = 0.408$ for $\langle 100 \rangle$Cu and $f_s = 0.278$ for $\langle 111 \rangle$Cu. No changes of these values during straining were taken into account. The nominal shear stresses for strain values of 0.05, 0.10, 0.15, and 0.20 are plotted on a double logarithmic scale in Fig. 23a for $\langle 100 \rangle$Cu and in Fig. 23b for $\langle 111 \rangle$Cu and $\langle 111 \rangle$Cu with

TiN. Straight lines representing a best fit to the data were obtained if at least three data points were available for the crystal orientation and strain level.

The scaling exponent deduced from Fig. 23 is shown in Fig. 24 for all material systems and strain ranges with sufficient data points. A simple intersection method was used to determine the hardening rates in the non-linear low strain regimes. Comparable to the determination of a secant modulus versus a tangent modulus, this will underestimate the true hardening rate and consequently the scaling exponent. A more adequate fit can be applied once a more detailed understanding of the governing hardening process is achieved. No discrimination between $\langle 100 \rangle$Cu and $\langle 100 \rangle$Cu on MgO was made, since the limited size range of the $\langle 100 \rangle$Cu on MgO samples questions the feasibility of an extrapolation. Indication is given that the $\langle 111 \rangle$ direction is the most hardenable crystal direction, as observed in macroscopic testing of bulk crystals (Diehl, 1956; Suzuki et al., 1956). Moreover, a clear effect of the TiN top coating is evident. This was not observed at the previously reported flow stress values at a strain of 0.10 (Kiener et al., 2009b, 2006, 2009a), but is clearly depicted at lower strain values. Moreover, there is higher initial hardening for TiN coated samples. At a strain of 0.10 the data for the coated samples closely merges with the values observed for uncoated samples for strains equal or higher than 0.10.

D.   Modeling

1.   Formulation and simulation methods

This section describes the discrete dislocation dynamics model used in the simulation of micropillar compression. Cu micropillars are modeled as planar crystals subjected to uniaxial plane strain compression in the x_1 direction with deformation taking place in the x_1–x_2 plane. A schematic representing the geometry of planar crystals
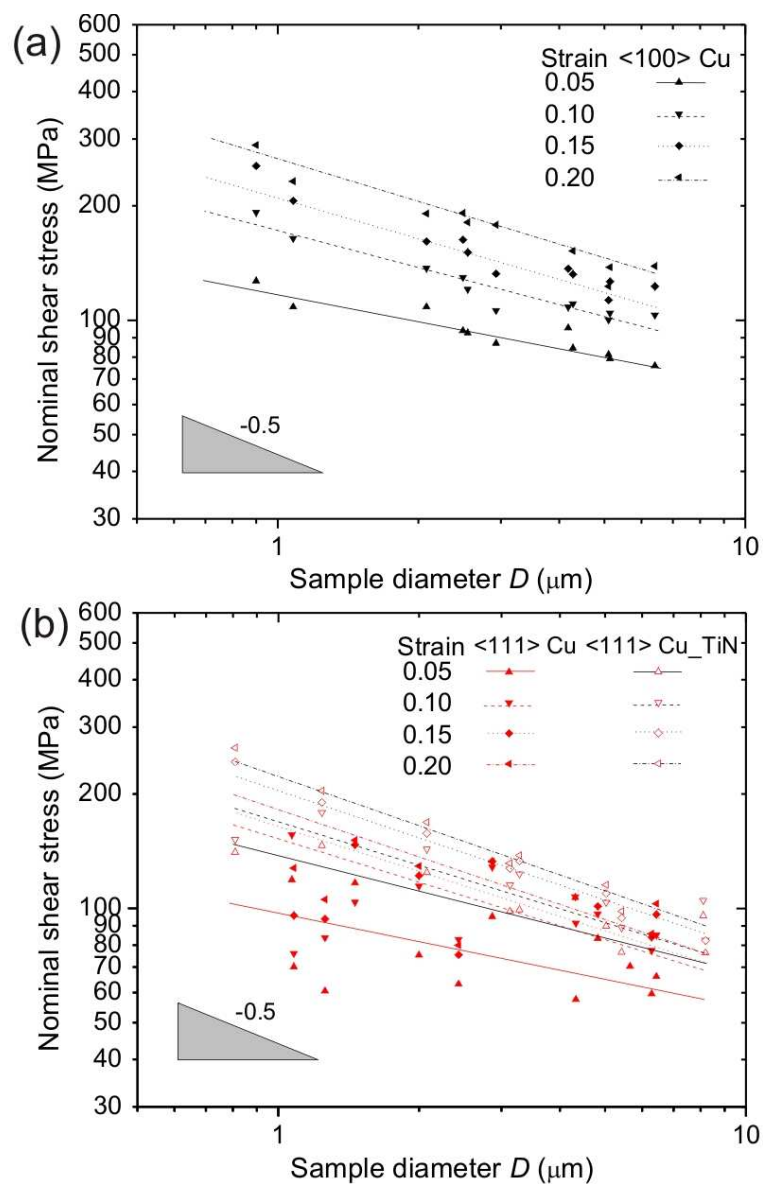
Fig. 23. Size dependent technical shear stress for strain values ranging from 0.05 to 0.20 for: (a) tapered round shaped ⟨100⟩Cu; (b) straight square shaped ⟨111⟩Cu and straight square shaped ⟨111⟩Cu with TiN top coating. The straight lines represent a best fit to the data sets.
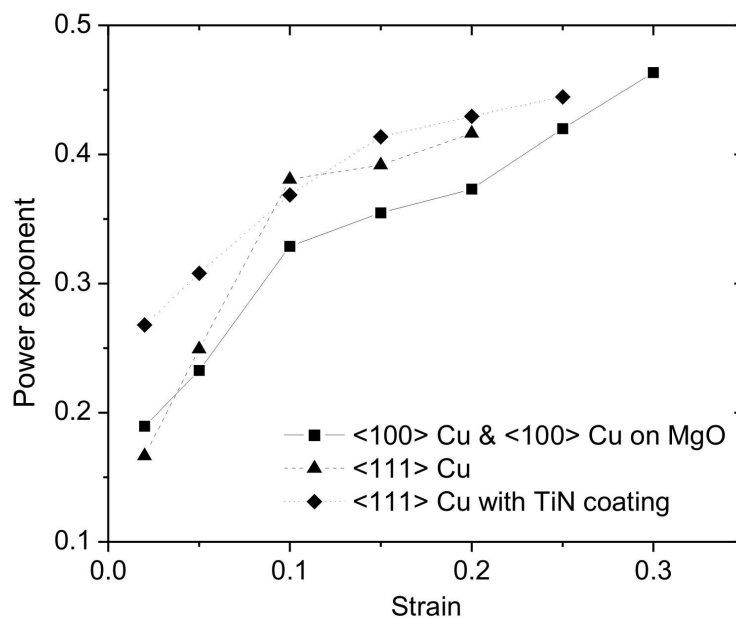
Fig. 24. The power exponent deduced from the best fit to the data in Fig. 23 is shown as a function of strain for the different samples investigated.
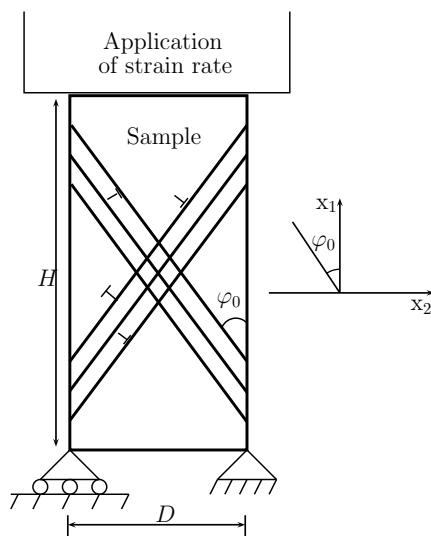
Fig. 25. Schematic showing the plane strain model of a micropillar oriented for symmetric double slip with two slip systems oriented at $\pm\varphi_0$ from the x_1 axis. The displacement boundary conditions applied allow the rotation of the crystal axis. The micropillar width is D and its height is H.

and boundary conditions used in the simulations are as shown in Fig. 25. Self-similar planar crystals with width D, height H and a fixed aspect ratio of $H/D = 2$ are considered. Each crystal has two potential slip systems on which dislocations can nucleate and glide. The two slip systems are oriented at $\pm 35.25°$ from the x_1-axis. The boundary conditions are such that surfaces at $x_2 = \pm D/2$ are traction free and the shear stress vanishes at $x_1 = \pm H/2$. A uniform displacement $u_1 = -U$ is prescribed along $x_1 = H/2$, the top surface. At the bottom surface one end is fixed to eliminate rigid-body rotation; but other nodes along this surface are constrained only along x_1 but are free to move laterally along the x_2 direction. This model allows for the rotation of the crystal axis.

In the simulations plastic flow arises due to the collective motion of dislocations, which are modeled as line singularities in a linear elastic, homogeneous isotropic medium with elastic constants μ (shear modulus) and ν (Poisson's ratio). A superposition method is used to solve the boundary-value problem described above in terms of the infinite medium singular fields for the discrete dislocations and image fields that enforce boundary conditions (Van der Giessen and Needleman, 1995). The finite element method is used to obtain the image field solutions. In this way, the long-range interactions between dislocations are directly accounted for. The short-range dislocation interactions are described below as given in (Benzerga et al., 2004). All simulations are carried out assuming infinitesimal displacement gradients.

The simulation follows an incremental procedure. At current time t the body is in equilibrium with the applied boundary conditions. The stress and displacement fields along with the positions of all the dislocations are known. During subsequent time step an increment of loading is applied and the solution requires the determination of forces on dislocations, updated dislocation structure, and corresponding updated stress and displacement fields. The glide motion of dislocation i is determined by the

Peach-Koehler force, f^i, given by,

$$f^i = \mathbf{m}^i \cdot \left(\hat{\boldsymbol{\sigma}} + \sum_{j \neq i} \tilde{\boldsymbol{\sigma}}^j \right) \cdot \mathbf{b}^i \tag{3.2}$$

where, $\mathbf{m}^i$ is the slip plane normal; $\mathbf{b}^i$ is the Burgers vector having magnitude b; $\hat{\boldsymbol{\sigma}}$ is the image stress field; and $\tilde{\boldsymbol{\sigma}}^j$ is the singular stress field of dislocation j.

Initially there are no dislocations inside the crystal, but a random distribution of Frank-Read sources and point obstacles are considered. A dislocation dipole is nucleated from a source when the Peach-Koehler force acting on it exceeds a critical value $\tau_{\mathrm{nuc}} b$ for a prescribed time $t_{0\mathrm{n}}$. The source strengths are randomly assigned from a Gaussian distribution with average $\bar{\tau}_{\mathrm{nuc}}$. The sign of the nucleated dipole depends on the sign of the Peach-Koehler force acting on the source. A dislocation may get pinned at a static obstacle and is released when the Peach-Koehler force at the location of the obstacle attains the value $\tau_{\mathrm{obs}} b^i$, with τ_{obs} being the obstacle strength. The glide velocity v^i of dislocation i is given by:

$$Bv^i = f^i - \alpha \frac{\mu b}{\mathcal{S}_{\mathrm{d}}^i} b^i \tag{3.3}$$

where B is the drag factor and the second term represents the line tension, α being a parameter and $\mathcal{S}_{\mathrm{d}}^i$ the algebraic distance between the dislocations, members of the same dipole. Annihilation of two co-planar dislocations of opposite sign occurs by eliminating both dislocations when they are within a material-dependent critical annihilation distance, L_e. Apart from the line tension, this basic set of constitutive rules was first proposed by Kubin et al. (Kubin et al., 1992) and extensively used in subsequent 2D calculations, e.g., (Van der Giessen and Needleman, 1995; Cleveringa et al., 1997; Deshpande et al., 2003; Nicola et al., 2006; Miller et al., 2004).

Key short-range 3D dislocation interactions included as constitutive rules in the

2D model are: (a) formation of junctions; (b) junction stabilization; (c) unzipping/break-away of junctions; and (d) formation and activation of dynamic sources. When dislocations gliding on intersecting planes approach each other within a critical distance d^*, a junction is formed, irrespective of the sign of the interacting dislocations. A junction which is stabilized and cannot be unzipped becomes an anchoring point for a new dynamic source. A breakable junction is referred to as a dynamic obstacle. Such an obstacle is destroyed if the Peach-Koehler force acting on either dislocation comprising the junction attains or exceeds the breaking force, $\tau_{\mathrm{brk}}^I b$. The breaking stress for junction I is configuration dependent and is given by:

$$\tau_{\mathrm{brk}}^I = \beta_{\mathrm{brk}} \frac{\mu b}{\mathcal{S}^I} \tag{3.4}$$

where $\mathcal{S}^I$ is the distance to the nearest junction in any of the two intersecting planes; β_{brk} is a scaling factor for the junction strength.

The stabilization of junction, for example due to cross-slip, can only be treated as a statistical event in the current 2D representation. The probability of a junction becoming an anchoring point is prescribed to be p, typically a low value. These anchoring points lead to the formation of dynamic sources from which new dislocations can be nucleated. A dislocation dipole is nucleated at source I when the value of the Peach-Koehler force at either junction forming the source exceeds the value $\tau_{\mathrm{nuc}}^I b$ during a time t_{nuc}^I. Both values depend on the local configuration and hence evolve dynamically. The nucleation stress is given by

$$\tau_{\mathrm{nuc}}^I = \beta_{\mathrm{nuc}} \frac{\mu b}{\mathcal{S}^I} \tag{3.5}$$

where β_{nuc} is a factor that reflects the strength of the source and $\mathcal{S}^I$ is the distance to the nearest junction on the slip plane where τ_{nuc}^I is being resolved. The nucleation

time t_{nuc}^I is given by

$$t_{\text{nuc}}^I = \gamma \frac{\mathcal{S}^I}{|\tau^I|b} \tag{3.6}$$

where γ is a material constant with units of a drag factor, and τ^I is the current resolved shear stress at the location of anchoring point I, exclusive of the junction self-stress. In summary, junction formation results in dynamic dislocation source and obstacle evolution during the deformation process and this is key to adequate simulation of strain hardening.

The average compressive stress is computed by averaging the tractions on the top surface and the applied strain is calculated as:

$$\sigma = -\frac{1}{D} \int_{-D/2}^{D/2} \sigma_{11}(H/2, x_2)\mathrm{d}x_2; \quad \varepsilon = -\frac{U}{H} \tag{3.7}$$

where, σ_{11} is the normal stress along x_1 direction. These quantities are directly comparable with experimental measurements (3.1). Hence the same notation is used.

During the simulations the evolution of total dislocation density is continuously monitored. However, dislocation density alone as a structural parameter may not be sufficient to explain the observed macroscopic behavior in micron and sub-micron specimens. At these small scales the specimen size begins to interact with the characteristic length of dislocation substructures developed in the specimens. Hence we also monitor the evolution of geometrically necessary dislocation (GND) density. GNDs do not vanish at sufficient resolution of the size of dislocation substructure developed in the specimen. To facilitate this, the net GND density (ρ_{GND}) and the effective GND density ($\bar{\rho}_{\text{GND}}$) are evaluated at each time increment in the discrete dislocation calculations following the methodology presented in (Guruprasad and Benzerga, 2008a). In a sub-domain ω within a body Ω subject to boundary tractions and displacements

the GND density is given by:

$$\rho_{\mathrm{GND}}(\omega) = \sqrt{\left[\sum_{\kappa}(\rho_+^{(\kappa)} - \rho_-^{(\kappa)})\cos\varphi^{(\kappa)}\right]^2 + \left[\sum_{\kappa}(\rho_+^{(\kappa)} - \rho_-^{(\kappa)})\sin\varphi^{(\kappa)}\right]^2} \qquad (3.8)$$

where, $\varphi^{(\kappa)}$ is the angle that defines the slip direction on slip-system κ; $\rho_+^{(\kappa)}$ and $\rho_-^{(\kappa)}$ represent the positive and negative dislocation density on the slip-system κ, respectively. In particular, the net GND density over the whole volume Ω is $\rho_{\mathrm{GND}} \equiv \rho_{\mathrm{GND}}(\Omega)$. By defining a uniform and structured grid on the body Ω, and using Eq. 3.8 we can obtain spatial distribution of GND density at a desired resolution.

To quantify the effect of the build-up of GND densities over sub-domains ω on the actual volume Ω a new quantity termed effective GND density is defined as:

$$\bar{\rho}_{\mathrm{GND}} = \sum_{n=1}^{N} \frac{\Omega^n}{\Omega} \rho_{\mathrm{GND}}(\Omega^n) \qquad (3.9)$$

where, Ω^n is the n-th grid element defining a sub-domain ω; N is the total number of elementary domains/grids in the body Ω; $\rho_{\mathrm{GND}}(\Omega^n)$ is the GND density calculated from (3.8) but specified over Ω^n. It is emphasized here that net GND density ρ_{GND} is uniquely defined but effective GND density $\bar{\rho}_{\mathrm{GND}}$ is not because of the resolution dependence.

2. Choice of parameters

The simulations are carried out with elastic constants, $\mu = 47$ GPa and $\nu = 0.34$, Burgers vector $b = 0.255$ nm, and drag factor $B = 10^{-4}$ s^{-1} representative of Cu. A slip plane spacing of $40b$ is used in all specimens. An initial dislocation source density of $\rho_{nuc} = 20 \times 10^{12}$m^{-2} is considered in the simulations. All specimens were subjected to a constant strain rate of $\dot{\varepsilon} = -10^4$ s^{-1} with a time step of $\Delta t = 0.5$ ns used to resolve dynamics of dislocation nucleation and motion.
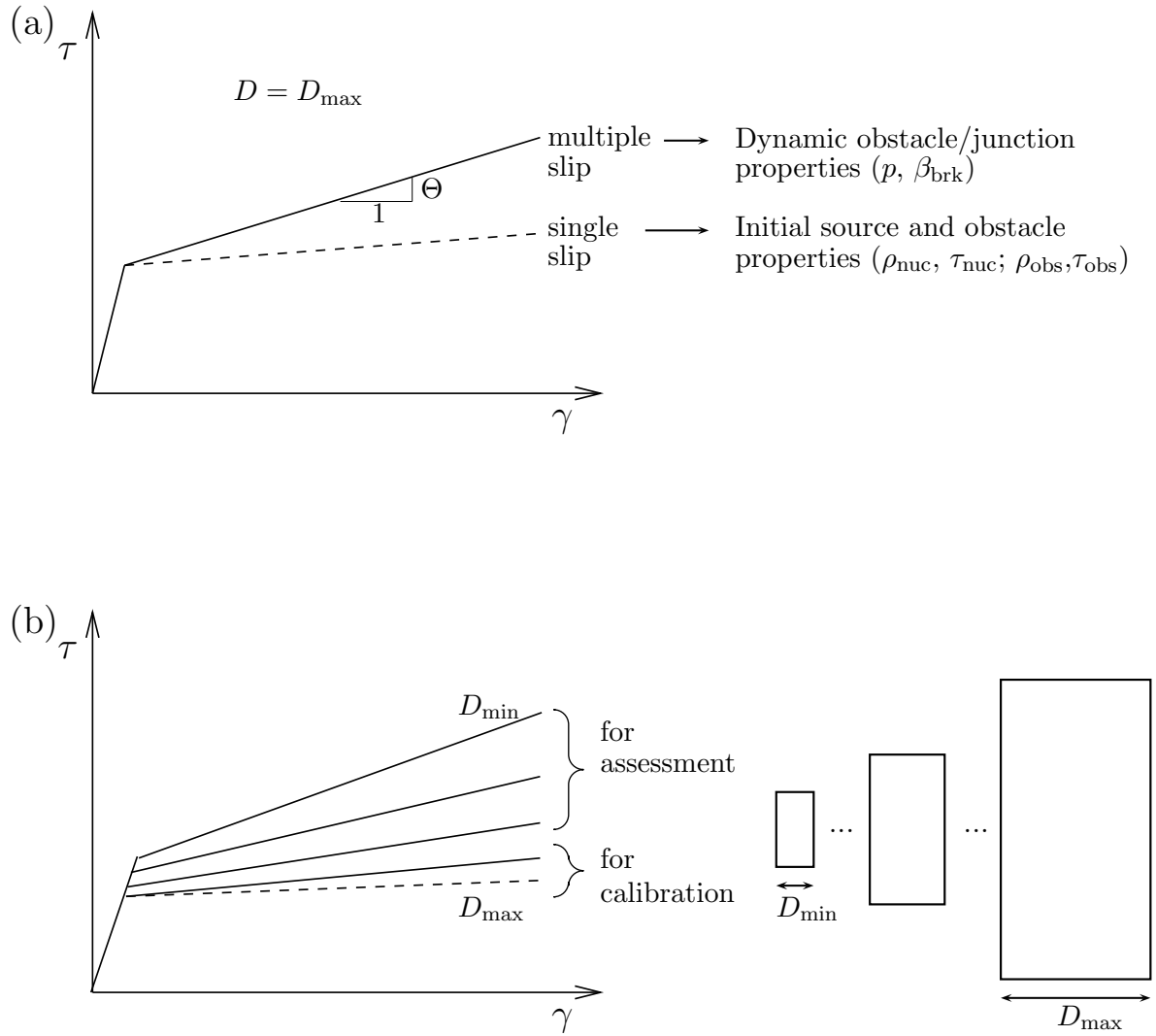
Fig. 26. Schematic highlighting the steps followed in the calibration of the parameters which enter into the simulations: (a) The initial source and obstacle properties (ρ_{nuc}, $\bar{\tau}_{\text{nuc}}$, ρ_{obs}, τ_{obs}) were calibrated to match the apparent yield and hardening observed in the micro-tension experiment on a crystal oriented for single slip. The parameters governing the junction/dynamic obstacle strength (β_{brk}) and the probability of junctions stabilizing (p) were calibrated to achieve hardening observed in the micro-compression experiment on a crystal oriented for multiple slip; (b) The parameters obtained from the calibration step was used to investigate size-effect in crystals by reducing the width down to D_{min}.

Key parameters related to the initial source/obstacle population and to the dynamic junction population are chosen from a two-step calibration process, as schematically shown in Fig. 26. A systematic size-effect investigation is then carried out by fixing these parameters and varying only the width of the crystal D as described in Fig. 26b. Specifically, the calibrated parameters are: the average initial source strength $\bar{\tau}_{nuc}$, initial obstacle density ρ_{obs}, the junction strength parameter β_{brk} and the anchoring point formation probability p. In the first step, $\bar{\tau}_{\mathrm{nuc}}$ and ρ_{obs} are calibrated based on a fit, in the average sense, to a micro-tension experiment conducted on crystal with size $D = 3.0$ μm and oriented for single slip. This set of parameters is then used in the second step to calibrate β_{brk} and p on the compression response of one of the largest pillars tested. The rationale behind this procedure is that β_{brk} and p affect the hardening response whereas $\bar{\tau}_{\mathrm{nuc}}$ and ρ_{obs} primarily affect the apparent yield strength.

The principle of calibration step 1 is described in Section 1. It was found that an average source strength of $\bar{\tau}_{\mathrm{nuc}} = 20$ MPa and an obstacle density of $\rho_{\mathrm{obs}} = 20 \times 10^{12}$ m^{-2} provided a good fit between the experiment and the simulation response as shown in Fig. 27a. This set of parameters leads to a value of $\tau_{\mathrm{Y}} = 23.6$ MPa. We notice a deviation from the elastic slope in simulations shown in Fig. 27a at this shear stress. This is followed by transient hardening regime up to a shear stress of 30 MPa, beyond which we notice a very agreement between the experiment and the simulation response.

The parameters chosen above were then used in the compression of a crystal with width $D = 5.7$ μm and oriented for symmetric double slip with $\varphi_0 = \pm 35.25°$. The values determining junction strength, β_{brk}, and probability of junction stabilizing, p, in simulation are chosen such the the hardening behavior observed in the micro-compression test of $\langle 111 \rangle$ Cu with width $D = 5.7$ μm is achieved. A junction strength
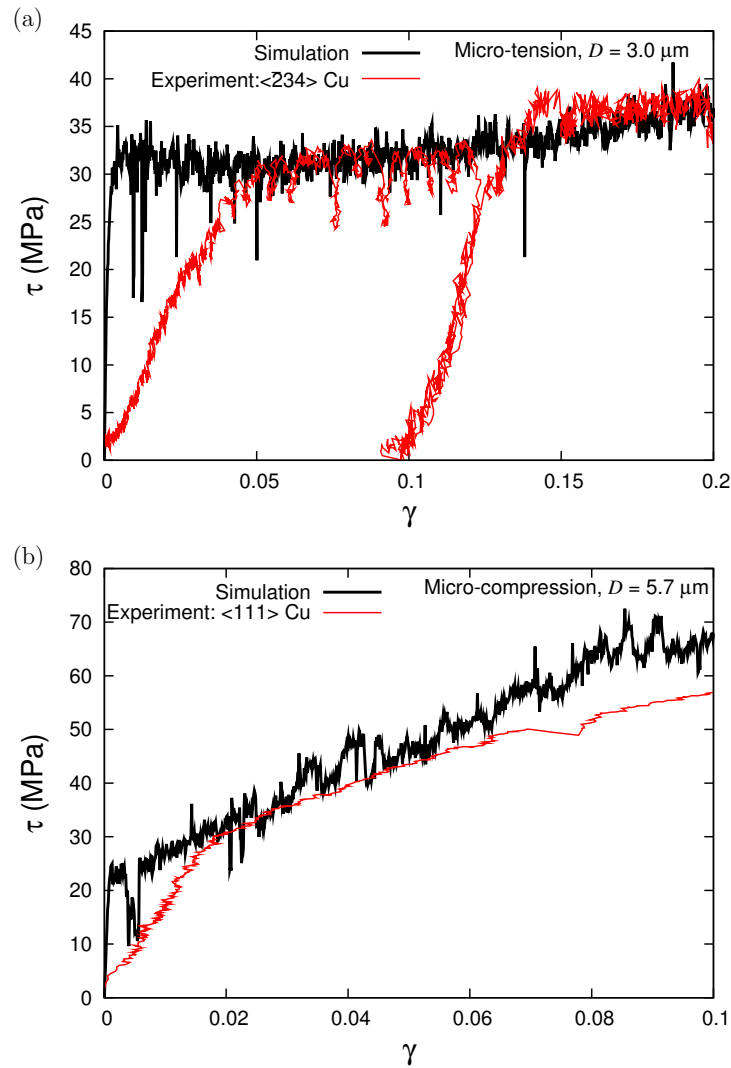
Fig. 27. Plots showing the comparison between shear stress (τ) versus shear strain (γ) response between simulations and experiments in the calibration step: (a) Micro-tension simulation response is shown in comparison to micro-tension experiment on $\langle\bar{2}34\rangle$ Cu for a crystal with size $D = 3.0$ μm. In the simulation and the experiment the crystal is oriented for single slip; (b) Micro-compression simulation response is shown in comparison to to micro-tension experiment on $\langle 111 \rangle$ Cu for a crystal with size $D = 5.7$ μm. The crystal is oriented for symmetric double slip in simulation and multiple slip in experiment.

value of $\beta_{\mathrm{brk}} = 5$ and probability of junction stabilizing $p = 0.01$ was found to achieve the hardening observed in the micro-compression test. Fig. 27b shows the comparison between the simulation and the experimental result. Within the shear strain range of $\gamma = 0.02 - 0.1$, the hardening rate in the simulations averaged over three different realizations of initial source and obstacle distribution is 439 ± 11 MPa. This value is within the range of typical bulk stage II hardening rate, $\mu/200 - \mu/100$.

Additional parameters of atomistic character are assigned values based on estimates from 3D DD analyses, atomistic calculations or theory (Benzerga, 2009). In view of the universality of scaling laws in bulk plasticity, the key trends are not sensitive to particular choices of many such parameters. The values of the parameters used in the simulations which enter in the equations governing the short range interactions and dislocation glide relation are: $d^* = L_{\mathrm{e}} = 1.5$ nm, $\beta_{\mathrm{nuc}} = 1$, $\gamma = 1000B$, $\alpha = 0.3$. The critical time for nucleation of dislocations from a source is fixed at $t_{0\mathrm{n}} = 10$ ns.

3. Simulation results

In the simulations the crystal width D is varied within the range 0.4–9.6 μm with a fixed aspect ratio of $H/D = 2$. In this section, results are presented to highlight the qualitative and quantitative features emerging from the size-effect investigation. The simulation results presented here use the fixed set of material parameters given in Section 2 and determined from calibration procedure. Crystals oriented for symmetric double slip are subjected to uniform compression for a range of sizes which include those corresponding to the experiments. For each size of the crystal atleast three realizations corresponding to a fixed source and obstacle density but different initial distribution of source and obstacles was simulated.

In Fig. 28a and b the shear stress versus shear strain response is shown for crystals with width $D = 2.08$ μm and $D = 1.08$ μm, respectively. For the purposes of
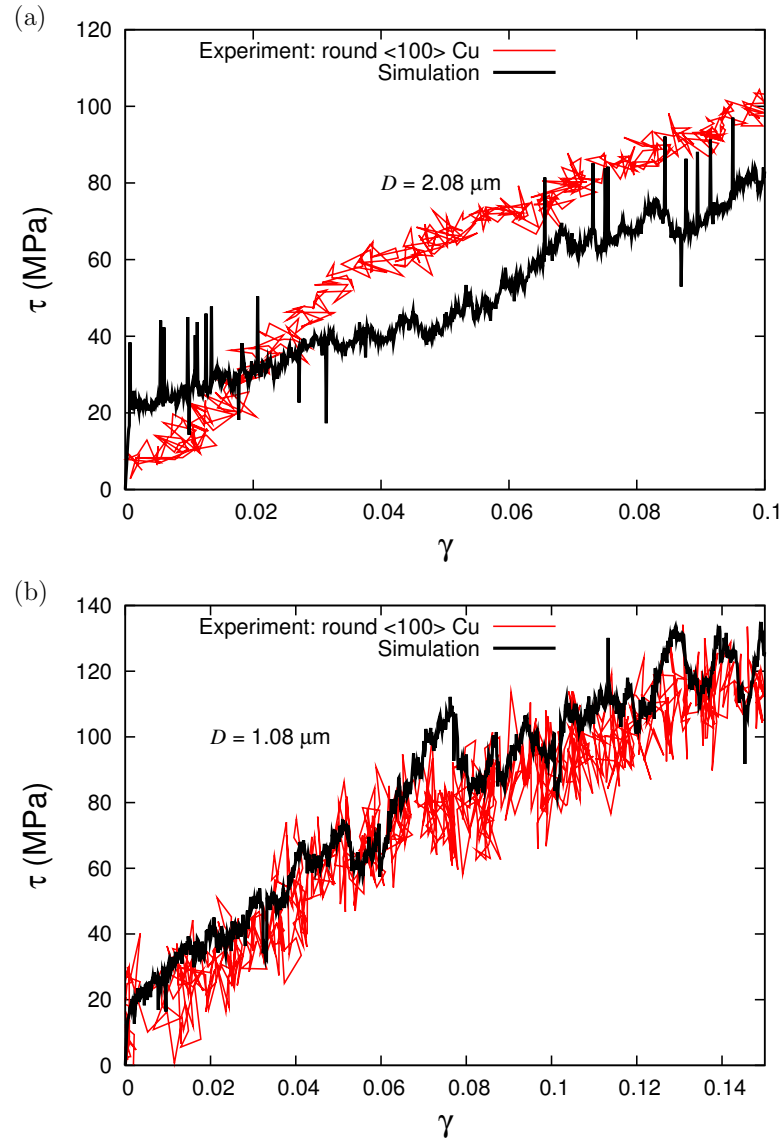
Fig. 28. Plots showing the prediction of shear stress (τ) versus shear strain (γ) response from the simulations as compared to experiments for selected samples: (a) Comparison between the round $\langle 100 \rangle$ Cu and simulation for crystal with size $D = 2.08$ μm; (b) Comparison between the round $\langle 100 \rangle$ Cu and simulation for crystal with size $D = 1.08$ μm.
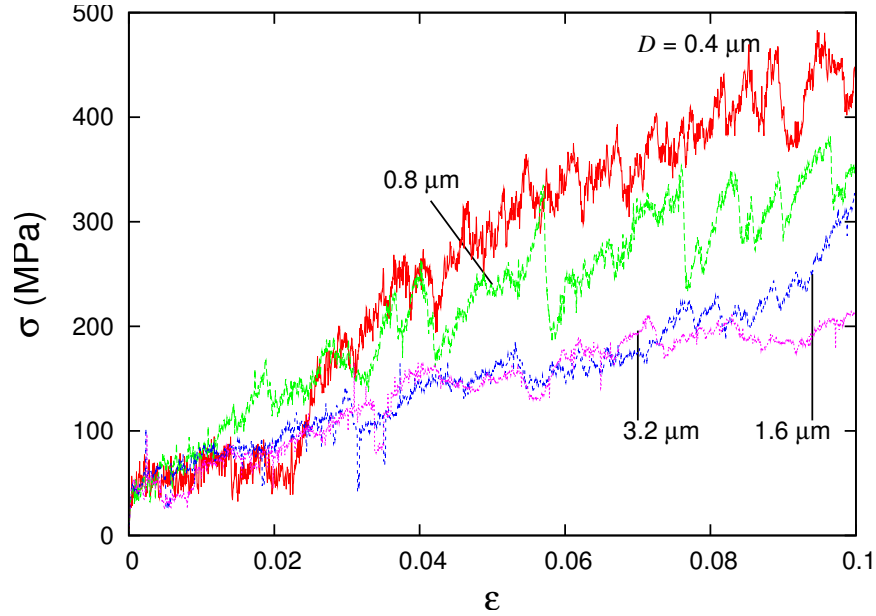
Fig. 29. Representative stress (σ) versus imposed strain (ε) response from simulations are shown for crystals with size varying from $D = 0.4$ - 3.2 μm.

comparison the experimental response from crystals of the same size is shown. Since the orientation along which the crystals are loaded in simulations and experiments are different, appropriate Schmid factor ($f_s = 0.471$ in simulation; $f_s = 0.408$ for $\langle 100 \rangle$ Cu) was used for the two set of stress versus strain curves to obtain the shear stress versus shear strain response. From Fig. 28a and b we notice a good agreement between the simulation and experimental shear stress versus shear strain response. Right after the onset of yield the simulations are able to capture the strain hardening noticeable in the experiments. The shear stress averaged from three realizations in the simulations for the crystal with width $D = 2.08$ μm is 71.7 ± 10.6 MPa at a shear strain of $\gamma = 0.1$. The corresponding value in the experiment is 100 MPa. In the crystal with width $D = 1.08$ μm the shear stress averaged from three realizations is 98.6 ± 23.6 at a shear strain of $\gamma = 0.15$. This compares well with the experimental value of 110 MPa, measured at a shear strain of $\gamma = 0.15$.

Representative stress versus strain response for crystal width in the range $D = 0.4 - 3.2$ μm is shown in Fig. 29. A general trend of increase in flow stress and strain hardening with decrease in the specimen size is observed. Subsequent to yield, all the specimens with the exception of the crystal with width $D = 0.4$ μm begin to show strain hardening. This feature is similar to the trend observed in the experimental curves. The crystal with width $D = 0.4$ μm does not show much hardening until a strain of $\varepsilon = 0.02$. However, beyond this strain the crystal begins to harden at a much faster rate than the other specimens.

The evolution of dislocation density during deformation for the crystal with $D = 0.4$ μm and $D = 5.7$ μm is shown in Fig. 30. In the specimen with width $D = 5.7$ μm the dislocation density builds-up at a rapid rate in both slip systems from the onset of plastic deformation. Within the strain range shown the density continues to increase and the rate of increase is similar in both slip systems. The activation of both slip systems from the onset of plastic deformation precludes the observation of a two stage stress-strain response in the simulation. On the other hand, we do not observe a build-up of dislocation density in any of the two slip systems of the specimen with $D = 0.4$ μm until strain a of $\varepsilon = 0.02$. Beyond a strain of $\varepsilon = 0.02$ we notice that the rate of increase in the dislocation density is different in the two slip systems. This suggests that in smaller crystals due to the discreteness of source distribution there can be localization of slip. Also, it explains the lack of hardening in the smaller specimen until a strain of $\varepsilon = 0.02$ and the hardening observed beyond this strain. We also gather from Fig. 30 that the build-up in the dislocation density is more in the crystal with width $D = 5.7$ μm than in the crystal with width $D = 0.4$ μm. However, the flow stress values reached in the crystal with width $D = 0.4$ μm is larger than those reached in the crystal with width $D = 5.7$ μm. This suggests the breakdown of Taylor-law, where the flow stress scales as the square root of the total dislocation
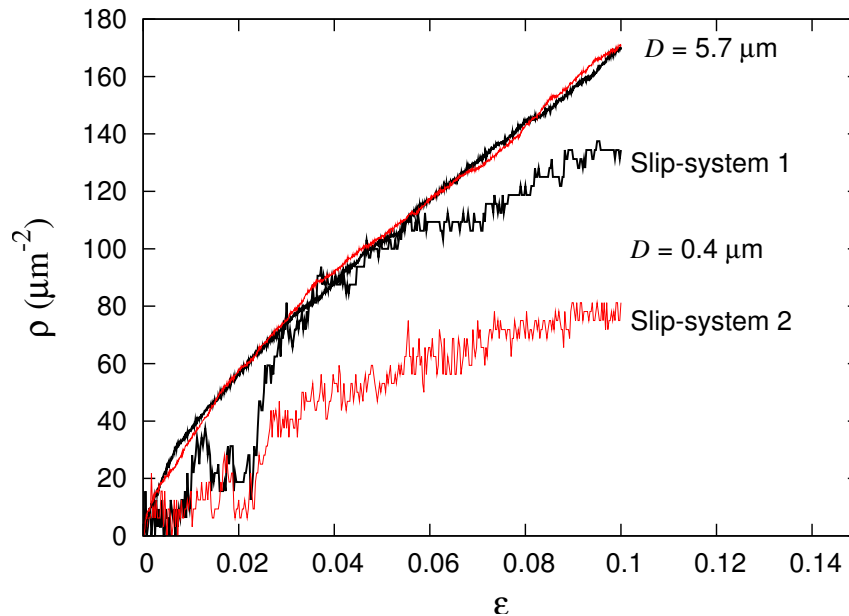
Fig. 30. Evolution of the dislocation density (ρ) in the simulations with strain (ε) at two slip systems is shown for crystals with size $D = 0.4$ μm and $D = 5.7$ μm.

density.

Deformed configurations at a strain of $\varepsilon = 0.1$ is shown for crystals with width 0.4 μm, 1.6 μm and 5.7 μm in Fig. 31. All the specimens show evidence of double slip. However, in the crystal with width $D = 0.4$ μm we observe localization of slip along one of the two slip systems. This is also reflected from the dislocation density evolution curves for the two slip systems shown in Fig. 30. In crystals with width $D = 1.6$ μm and $D = 5.7$ μm slip is more evenly distributed along the height of the specimens and evidence of barreling during deformation is observed.

The effect of crystal size on the dislocation structure that develops and on the stress distribution in the x_1 direction (σ_{11}) is shown in Fig. 32a. In the crystal with width $D = 0.4$ μm the concentration of dislocations is only along a few slip planes. However, in crystals with width $D = 1.6$ μm and $D = 5.7$ μm, one can see the development of dislocation structure near the center the crystal. Near the

$D = 0.4~\mu$m $\qquad\qquad\qquad$ $D = 1.6~\mu$m $\qquad\qquad\qquad$ $D = 5.7~\mu$m
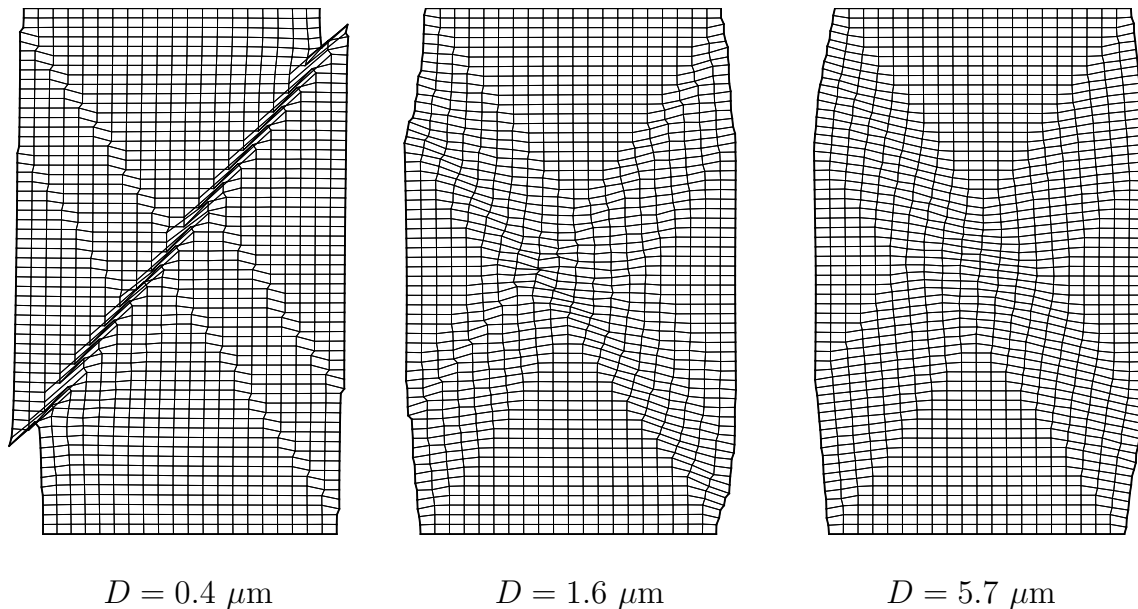
Fig. 31. Deformed configurations in the simulations of crystals with size $D = 0.4~\mu$m, 1.6 μm and 5.7 μm are shown at a strain level of $\varepsilon = 0.1$.

crystal center there are more slip plane intersection points leading to the formation of junctions, which pin the dislocations and prevent them from escaping at the free surfaces. Overall, we observe a general trend where the crystal central region is harder than its surface. The stress near the core region is almost 5 times the values reached near the surface. The distribution of stress near the soft regions is not uniform in general and small pockets of hard dislocation free regions are observed very close to the free surface.

In Fig. 32b contours of GND density (ρ_{GND}), determined based on the methodology presented in Section. D, is shown. A resolution of 50×50 nm^2 is used while determining the spatial distribution of GND density. In all the specimens we notice that the GND density is higher at the crystal central region than near the surfaces. Consistent with the macroscopically homogeneous deformation in the crystal, the net GND density in the crystal with width $D = 5.7~\mu$m constitutes only 0.3% of the

total dislocation density at a strain of $\varepsilon = 0.1$. However, with decrease in crystal size the net GND constitutes a larger percentage of the total dislocation density with the value being as high as 63% in the crystal with width $D = 0.4$ μm. The GND density accumulation is accompanied by disturbances in lattice rotation fields as shown in Fig. 32c. In large crystals ($D = 5.7$ μm) we notice formation of domains of large lattice rotation fields (κ). It is observed that these domains are not oriented along the slip planes. The lattice rotation fields are typically found to be high at the central region of the crystal with its magnitude being as high as 3°. With decrease in size of the crystal the formation of large domains of lattice rotation fields vanish. A common feature observed from the lattice rotation contours is the fragmentation of rotation fields associated with mismatches in the sign of adjacent rotation fields in the crystals.

E.   Comparison of experimental and computational results

In this section quantitative and qualitative comparison between the experimental and simulation results are presented. Quantitative comparison is made on the effect of crystal size on flow stress and strain hardening rate. Similarities in the features of deformed configurations, nearest neighbor misorientations and global misorientations in crystals from EBSD studies in the experiments are qualitatively compared with simulation results. Finally, the capability of the simulations to quantify microstructural features in the crystal which can provide a means to explain the observed size dependent behavior in the crystals is shown.

The simulation results and experimental data for flow stress versus crystal width at a strain of $\varepsilon = 0.05$ and $\varepsilon = 0.1$ is shown in Fig. 33. Overall, the simulation results are able to capture the increase in crystal flow stress with decrease in specimen size
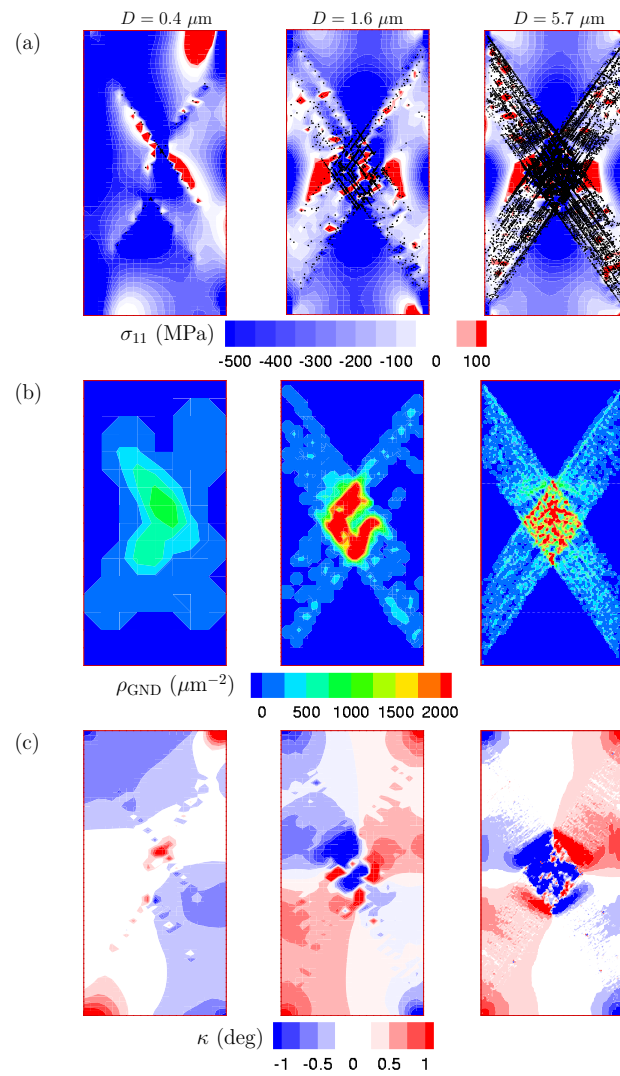
Fig. 32. Contour plots are shown at a strain level of $\varepsilon = 0.1$ in crystals with size $D = 0.4$ μm, 1.6 μm and 5.7 μm: (a) Contour plots of axial stress, σ_{11}, with dislocation structure superposed on it; (b) Contour plots of GND density, ρ_{GND}; and (c) Contour plots of lattice rotations, κ.
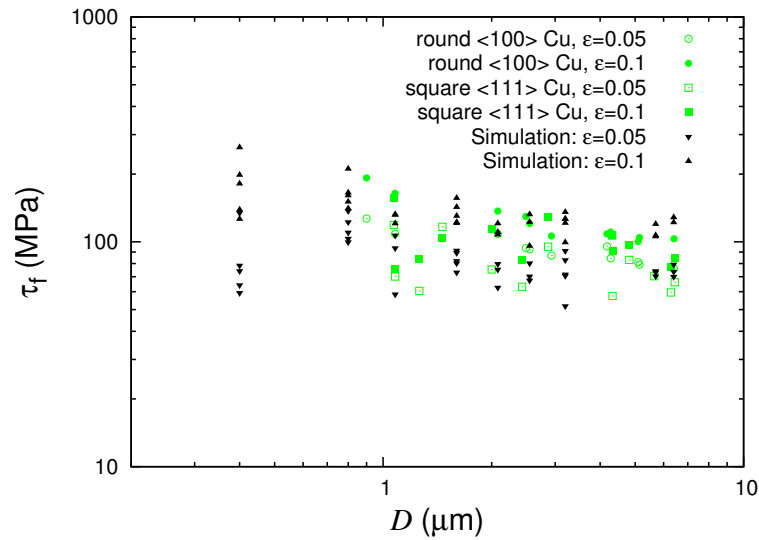
Fig. 33. The shear stresses (τ_f) from the simulations for various crystal widths (D) are shown in comparison to experimental data from round $\langle 100 \rangle$ Cu and square $\langle 111 \rangle$ Cu at strains of $\varepsilon = 0.05$ and 0.1.

observed in the experiments. The simulation results also reveal a trend where the flow stress scatter increases with decrease in crystal size. The power scaling exponent determined from the simulations at $\varepsilon = 0.05$ is 0.092 ± 0.041. At a strain of $\varepsilon = 0.05$ the resolved flow stress values in the crystal with width $D = 0.4$ μm are less than in crystals larger than it. This is because a steady build-up of dislocation density in these crystals does not take place immediately after the onset of yield as shown in Fig. 30. This results in a low value of the exponent calculated. The power exponent from the simulations at a strain of $\varepsilon = 0.1$ is 0.17 ± 0.03. The increase in the power scaling exponent with increase in strain is due to the size-effect in the strain hardening observed in the crystals. The large standard deviation observed in the values of the power exponents determined from the simulations reflects the increase in the scatter of the resolved flow stress values with decrease in the crystal size. For example, at a strain of $\varepsilon = 0.1$ the resolved flow stress in the crystals with width $D = 0.4$ μm is

found to vary between 238 MPa - 118 MPa.

A discussion on strain hardening in the classical macroscopic sense is done based on true stress versus true strain data. On a micrometer scale an experimental determination of true stress versus strain curves as possible in computational studies is desirable and seemingly within reach when using in situ SEM testing approaches. However, as depicted in Fig. 34, there are situations where even during continuous observation of sample deformation it remains questionable to ask for the actual contact area or the smallest cross section. These strain localizations at the sample/punch interface should be minimized in micro-tensile testing (Kiener et al., 2008a), allowing a more accurate determination of true stress values. The inclination of the flat punch in Fig. 34 is an artifact of the slow scanning direction of the electron beam from the left to the right while the punch moves down. Hence, to calculate the hardening rates between two reference strains (ε), values of stress (σ) were calculated under the assumption of homogenous deformation and volume conservation at respective strains, which is a common approach (Frick et al., 2008; Greer et al., 2006, 2005). The strain hardening rate is then given by, $\Theta = f_s^2 \dfrac{\Delta \sigma}{\Delta \varepsilon}$; where, f_s is the Schmid factor. In the present case, this procedure is justified by the investigated multiple slip orientation and the confirmative in situ observation. A similar approach was followed in the simulations to determine the hardening rate between two reference strains.

Fig. 35 shows the comparison between the strain hardening rates obtained from experiments and simulations. The normalized strain hardening rate from the simulations, determined between the strain range of $\varepsilon = 0.02 - 0.1$, are shown with the normalized strain hardening rate from the experiments, determined between the strains of $0.02 - 0.05$, for different crystal widths. Both simulations and experiments show size-effect on the hardening rate. Overall, there is a good agreement between the normalized hardening data from simulations and experiments in crystals with width
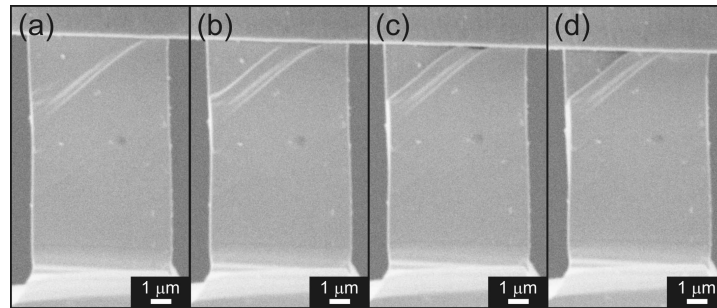
Fig. 34. In situ SEM images of a ⟨100⟩Cu sample during compression. The inclination of the top surface of the diamond punch is a result of the electron beam scanning from the left to the right during image acquisition while the sample was compressed. It is noted that there was a loss of contact in the center of the contact area in (c).
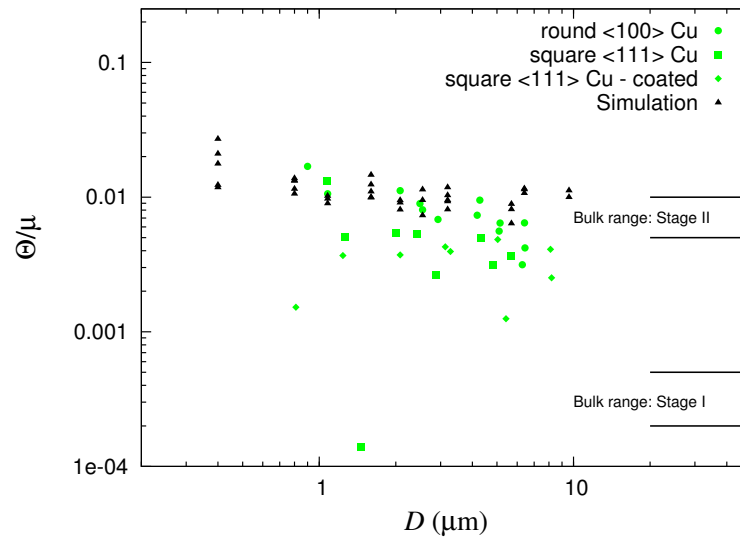
Fig. 35. Strain hardening rate (Θ) data normalized by the Cu shear modulus (μ) for crystals of various sizes are shown from simulations and experiments on round ⟨100⟩ Cu, square ⟨111⟩ Cu, and square ⟨111⟩ Cu coated with TiN. The hardening rate in the simulations is determined between the strains of $\varepsilon = 0.02 - 0.1$ and in the experiments between the strains of $\varepsilon = 0.02 - 0.05$. These data are shown in comparison to the normalized bulk stage I and stage II hardening rate (Argon, 2008).

lesser than $D = 6.0$ μm. The simulations predict the hardening rate in the crystal with width around $D = 0.4$ μm to be almost 2 times the bulk stage II hardening rate limit. A notable observation from Fig. 35 is the discrepancy in hardening rates predicted by simulations and experiments for crystal widths larger than $D = 6.0$ μm. The hardening rates predicted by the simulations in crystals with width $D = 6.4$ μm and $D = 9.6$ μm are within the bulk stage II hardening rate of $\mu/100 - \mu/200$. This is expected in the simulations because these sufficiently large crystals, oriented for symmetric double slip, show build up of dislocation density in both the slip systems right after the onset of yield. This behavior was already noticeable in the crystal with width $D = 5.7$ μm as shown in Fig. 30. This response is typical of bulk crystals.

The strain hardening rates observed in the simulations and experiments in this investigation are lower in values than those reported for stage II hardening rate presented in (Guruprasad and Benzerga, 2008b). The difference in the hardening behavior observed in the two sets of simulations can be attributed to the way in which junctions are modeled. In (Guruprasad and Benzerga, 2008b) the junctions formed were considered to be unbreakable. However, during the simulations the character of this junction can change from a dynamic obstacle to a stable junction if the criterion for junction stabilization is met. However, in the present investigation the junctions are not considered unbreakable. This allows for relaxation of stresses within the crystals during the breaking of junctions.

To understand the mechanisms leading to the hardening, the local microstructure of deformed samples was further analyzed. Thus, the two samples shown in Fig. 21 were subject to electron backscatter diffraction (EBSD) investigation after deformation. Due to the high compressive strain of 18.4% and 28.3%, respectively, large slip steps on the sample surface complicated EBSD investigation. Therefore, both sample surfaces were FIB polished using an ion current of 100 pA. An inclined
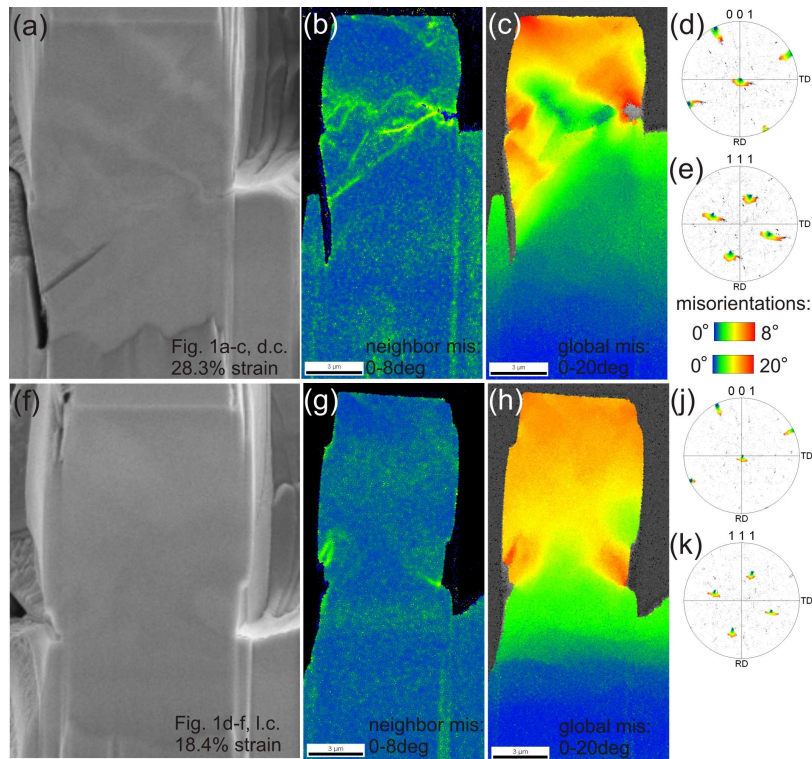
Fig. 36. Electron backscatter diffraction (EBSD) investigation of the deformed samples shown in Fig. 1. (a, f) Inclined SEM view of the FIB polished surface of the sample shown in Fig. 1a-c and d-f, deformed up to 28.3% and 18.4% strain, respectively. The crack like feature in Fig. 1a is the rest of a slip step that was not polished away. (b, g) Nearest neighbor misorientation and (c, h) global misorientation with respect to the undeformed sample base. (d, j) ⟨001⟩ pole figure and (e, k) ⟨111⟩ pole figure with the same color code applied as for the global misorientation maps. Fragmentation in the misorientation maps and much stronger peak broadening in the pole figure maps is observed for the upper sample deformed to higher strains.

SEM view is shown in Fig. 36a for the sample shown in Fig. 21a-c loaded to a strain of 28.3%, and in Fig. 36f for the sample shown in Fig. 21d-f loaded to a strain of 18.4%. The crack like feature in Fig. 36a is the rest of a slip step that was not completely removed by FIB polishing. Subsequently, EBSD investigations were performed with a step size of 25 nm. Fig. 36b and g show nearest neighbor misorientations maps with the color code ranging from $0°$ to $8°$. A larger number of highly misoriented boarders are observed for the stronger deformed sample. Furthermore, the global misorientations with respect to the undeformed sample base increases with increasing maximum strain, as depicted in Fig. 36c and h. Note that in these images the color code ranges from $0°$ to $20°$. The increasing crystal fragmentation observed in the previous images is also reflected in the $\langle 100 \rangle$ and $\langle 111 \rangle$ pole figures shown in Fig. 36d, j and Fig. 36e, k, respectively, where increased peak broadening in multiple directions is seen. The same color code as for the misorientation maps was applied. These observations can be correlated to the load-displacement data in Fig. 21g, where the stronger deformed sample shows significantly increased hardening after point c. This could have been the start of the fragmentation process, which did not occur in the other sample, since it was not loaded to such high strains.

Deformed configurations, GND density contour and lattice rotation contour figures from simulations are shown in Fig. 37. The width of the crystal, $D = 6.4 \ \mu$m, is comparable to the width of the crystal shown from experiments in Fig. 36. Figs. 37a-c correspond to the simulations from the current investigation, where the junctions are modeled as breakable. These figures are shown at a strain level of $\varepsilon = 0.1$. Fig. 37d correspond to simulations presented in (Guruprasad and Benzerga, 2008b), where the junctions were modeled as unbreakable junctions. Only central part of this crystal, which has an aspect ratio of $H/D = 3$, is shown at a strain level of 0.083.

The deformed configuration in Fig. 37a shows that the slip is not local or confined

to a few active slip planes; but it is distributed over the height of the crystal. There is a clear evidence of the crystal deforming by double slip. Contours of GND density, which can be thought of as representing the nearest neighbor misorientations within the crystal, are shown in Fig. 37b. A resolution of 50×50 nm^2 was used to determine the spatial distribution of the GND density in the crystal. The GND density is found to be higher in magnitude at the central region in the crystal than near the surfaces. This feature is similar to large number of local misorientation boundaries observed in Fig. 36b at the center of the crystal. An observation of the lattice rotation field, κ, in Fig. 36c reveal that at the central region of the crystal the the magnitude of the rotation field is as high as 3°, and there is a mismatch in the sign of the rotation fields. A similar feature was observed in the simulations presented in (Guruprasad and Benzerga, 2008b) as shown in Fig. 37d. This mismatch in the sign of the large magnitude rotation fields at the central region indicates fragmentation process which was also observed in experiments, as highlighted in Fig. 36c.

The DD framework used in the simulations readily allows the quantification of the dislocation substructure evolution in the crystals during the deformation. Transmission electron microscopy studies can be done in the experiments to quantify the dislocation substructure (Norfleet et al., 2008). Fig. 38 shows the total dislocation density (ρ) in the simulated crystals at a strain of $\varepsilon = 0.1$ for various sample widths (D). A general trend of decrease in the total dislocation density with decrease in the crystal width was observed. The total dislocation density in the crystal with width $D = 6.4$ μm was found to be as high as 386 μm^{-2}, while in the crystal with width $D = 0.4$ μm it was as low as 44 μm^{-2}. This result is in stark contrast to the findings reported in (Norfleet et al., 2008) from TEM investigation of Ni microcrystals in the range of 1 μm - 20 μm. Also, in the present investigations we see a continuous increase in the density of dislocations with deformation. However, in (Norfleet et al., 2008)
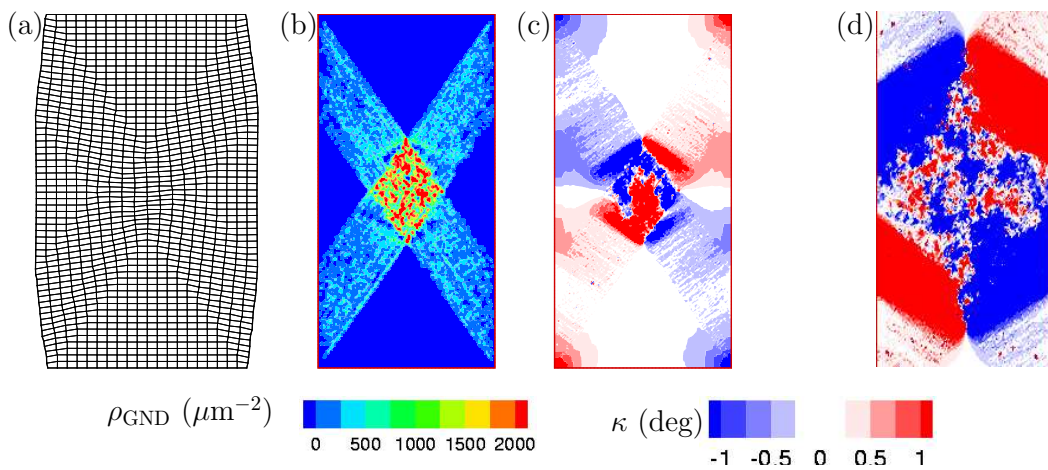
Fig. 37. Deformed configuration and contour plots are shown for crystal with size $D = 6.4$ μm, aspect ratio (H/D) of 2:1, and initial source density of $\rho_{\mathrm{nuc}} = 20 \times 10^{12}$ m^{-2} at a strain level of $\varepsilon = 0.1$: (a) Deformed configuration showing symmetric double slip in the crystal; (b) GND density (ρ_{GND}) contour plot; and (c) Lattice rotation (κ) plot. (d) Lattice rotation (κ) in a crystal with size $D = 6.4$ μm, aspect ratio (H/D) of 3:1 and an initial source density of $\rho_{\mathrm{nuc}} = 1.5 \times 10^{14}$ m^{-2} is shown at a strain level of $\varepsilon = 0.083$. Only the central part of the crystal is shown for clarity. In (c) and (d) we notice fragmentation of rotation fields at the central region of the crystal.
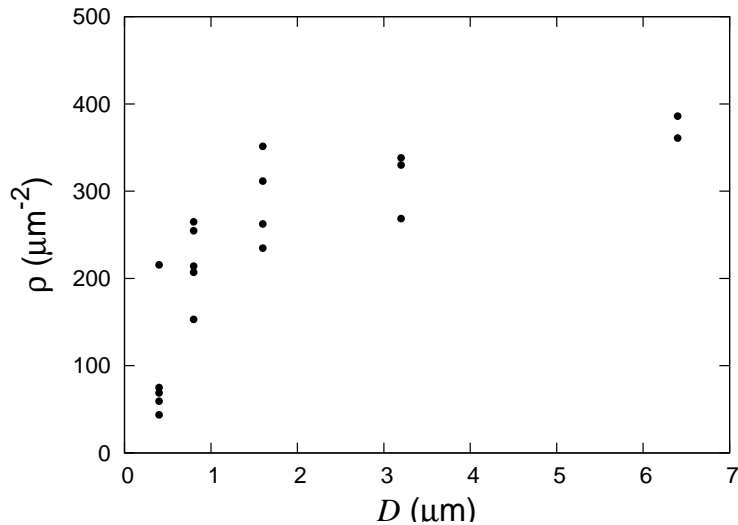
Fig. 38. Total dislocation density (ρ) in crystals at a strain of $\varepsilon = 0.1$ is shown as a function of crystal size D.

the dislocation density was not found be a function of the imposed strain. This is because in (Norfleet et al., 2008) after the initial exhaustion hardening regime significant hardening, as reported in this investigation, was not present. Finally, the presence of significant density of dislocations in crystals with widths as small as 0.4 μm in the simulations suggest that the crystals are not 'starved' of dislocations.

The methodology presented in Section. D is used to quantify local dislocation substructures in terms of GND density in the crystal. This methodology allows for the determination of spatial as well as temporal evolution of the GND density. Spatial distribution of GND density in crystals for various crystal widths are shown in Fig. 32b and Fig. 37b. In Fig. 39a and c we show the effective GND density ($\bar{\rho}_{\text{GND}}$) as defined by Eq. 3.9, as a function of crystal width (D); the two trends shown correspond to two different choice of resolution used in the calculation of $\bar{\rho}_{\text{GND}}$. Fig. 39a is determined keeping the thickness of the resolution, $h = 200$ nm, constant for specimens of all the size but the length of the resolution is always equal to the length of the sample. This

procedure does not lead to maintaining the a constant domain area while determining $\bar{\rho}_{\text{GND}}$ for samples of different sizes. The Fig. 39 correspond to calculations where the resolution size was kept constant at 200×800 nm^2 in all the samples. Two trends are observed from Fig. 39a and c: (a) $\bar{\rho}_{\text{GND}}$ increases with decrease in the crystal width; and (b) the scatter in the value of $\bar{\rho}_{\text{GND}}$ increases with decrease in crystal width. This trend is similar to the trend observed in flow stress scaling with crystal width (Fig. 33). These observations suggest that the emergence of GND density and its significant contribution to the total dislocation density will play a role in the size-effect on flow stress and hardening in small crystals. In crystals with size $D = 6.4$ μm and larger the hardening is governed by forest hardening mechanisms, as indicated by a high value of total dislocation density and low value of $\bar{\rho}_{\text{GND}}$. Fig. 39b and d show the average number of dislocations per domain ($\langle N \rangle$) for the two choice of resolutions chosen for the calculation of $\bar{\rho}_{\text{GND}}$. Except in a few realizations of samples with size $D = 0.4$ μ, all the other samples atleast had more than 10 dislocations per domain, which was used in the calculation of $\bar{\rho}_{\text{GND}}$.

F. Conclusions

The focus of this study was to gain insight into the evolution of plastic deformation and strain hardening in micropillars through experiments and simulations. Micro-compression experiments have been carried out on high-symmetry Cu micropillars with square as well as circular cross-sections. The samples included micropillars on substrate, and coated pillars. Cu micropillars, oriented for multiple slip, are modeled as planar crystals subjected to plane strain compression using discrete dislocation dynamics. It does not account for the effect of substrate and coating on pillars. In this framework, long range interactions due to dislocations are naturally accounted for
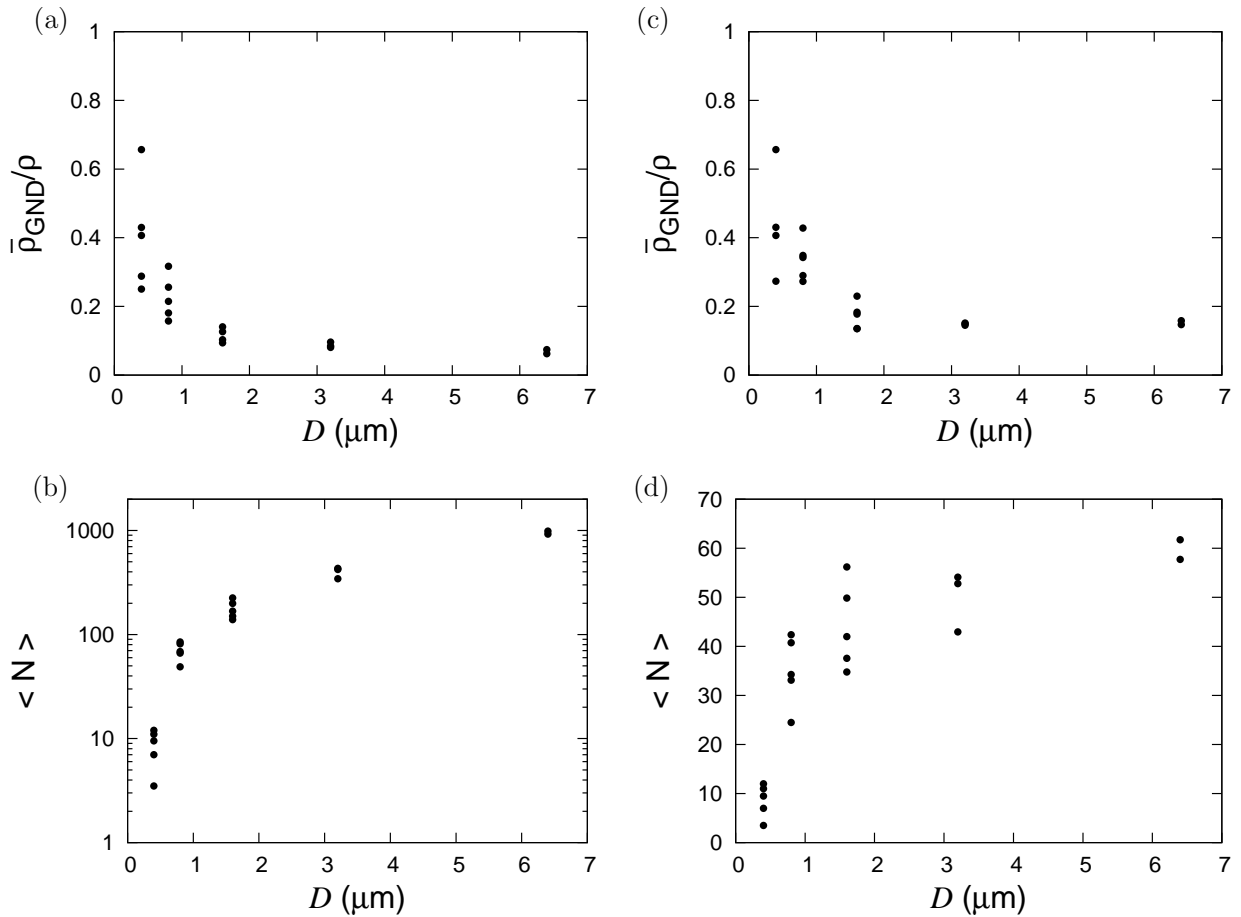
Fig. 39. (a) Effective GND density ($\bar{\rho}_{GND}$) normalized by the total dislocation density (ρ) in crystals at a strain of $\varepsilon = 0.1$ is shown as a function of crystal size D. (b) Average number of dislocations per domain ($\langle N \rangle$) used in the calculation of (a) is shown as a function of crystal size D. A resolution size of $h = 200$ nm and length equal to the size of the sample is used in the determination of (a) and (b); (c) Effective GND density ($\bar{\rho}_{GND}$) normalized by the total dislocation density (ρ) in crystals at a strain of $\varepsilon = 0.1$ is shown as a function of crystal size D. (d) Average number of dislocations per domain ($\langle N \rangle$) used in the calculation of (c) is shown as a function of crystal size D. A constant resolution size of 200×800 nm^2 is used in the determination of (c) and (d).

through elasticity; key short-range dislocation interactions are incorporated through constitutive rules. These rules include: junction formation, stabilization and nucleation from stable junctions which act as anchoring points, and their evolution with deformation. For adequate representation of the behavior of bulk crystal, parameters related to initial dislocation-source, obstacle and dynamic-junction population are chosen based on a calibration process with experimental data. Subsequently, fixing these parameters a systematic study of size effects on Cu micropillars has been carried out using simulations. The main findings from this study are:

- Both the experiments and simulations predict size affected plastic deformation in micropillars. In particular, flow stress as well as strain hardening rate increases with decrease in pillar size.

- There is a good qualitative and quantitative agreement between experiments and simulations on plastic deformation, flow stress at different strains and strain hardening rate of Cu micropillars upto the strains reached in calculations.

- Electron backscatter diffraction of deformed micropillars showed significant lattice misorientations after heavy deformations. Similar features were also observed in deformed samples from simulations.

- Simulations showed that there is an emergence of GND density due to nearest neighbor misorientations within the micropillars. Further, quantification of dislocation structure within the micropillars showed that: (i) there is a significant density of dislocations even in the smallest pillars used in calculations; (ii) the magnitude of effective GND density normalized by the total dislocation density and its scatter increases with decrease in pillar size. The size effect observed in micropillars is rationalized on the basis of an emerging GND density within the

pillars due to an evolving dislocation structure.

G. Supplementary material

1. Calibration step 1

The yield stress in the DD simulations is primarily governed by the average initial dislocation source strength ($\bar{\tau}_{\mathrm{nuc}}$), the standard deviation of the source strength distribution (Σ_{nuc}), point obstacle density (ρ_{obs}), and obstacle strength (τ_{obs}). These four parameters are chosen such that the apparent yield observed in the micro-tension experiment of $\langle\bar{2}34\rangle$ Cu with width $D = 3.0$ μm is achieved. Since the specimen was oriented for single slip its deformation is predominantly dominated by source and obstacle properties and hence allows for a good calibration of these parameters used in simulations. The number of parameters to be calibrated is reduced from four to two by fixing the obstacle strength to $\tau_{\mathrm{obs}} = 150$ MPa and considering the standard deviation of the source strength to be $\Sigma_{\mathrm{nuc}} = 0.25\bar{\tau}_{\mathrm{nuc}}$. This reduces the problem to determining two parameters, $\bar{\tau}_{\mathrm{nuc}}$ and ρ_{obs}, which leads to an apparent yield observed in the micro-tension experiment. Using the analytical relation given in (Chakravarthy and Curtin, 2010) between the yield stress (τ_{Y}), obstacle density (ρ_{obs}), and the average source strength ($\bar{\tau}_{\mathrm{nuc}}$) a first estimate for the parameters is made. The parameters are then used in the simulation of a crystal with width $D = 3.0$ μm, oriented for single slip with $\varphi_0 = 28.8°$. This slip configuration has a Schmid factor of $f_{\mathrm{s}} = 0.422$, which is the same as the Schmid factor for $\langle\bar{2}34\rangle$ Cu specimen tested in the experiment. From the first estimate the values of the parameters are changed until a good fit is obtained between the simulation and the experimental result.

The yield stress τ_{Y} is related to the obstacle density and the average source strength by the following expression in (Chakravarthy and Curtin, 2010):

$$\tau_{\mathrm{Y}} = \sqrt{m \frac{L_{\mathrm{obs}}}{L_{\mathrm{obs}}^{*}} \frac{\mu b}{\pi(1-\nu)} \frac{\tau_{\mathrm{obs}}}{L_{\mathrm{obs}}} + \tau_{\mathrm{nuc}}^{2}} \qquad (3.10)$$

In Eq. 3.10 τ_{Y} is defined as the stress at which dislocations nucleated from sources achieve flow past obstacles in their path. The average obstacle spacing L_{obs} is related to the obstacle density as $L_{\mathrm{obs}} = 1/(\rho_{\mathrm{obs}}d)$. It is the weakest of the sources which nucleate first and hence the active sources are typically from the lower set of the source strength distribution; thus, $\tau_{\mathrm{nuc}} = \bar{\tau}_{\mathrm{nuc}} - 2\Sigma_{\mathrm{nuc}}$. The ratio $L_{\mathrm{obs}}^{*}/L_{\mathrm{obs}}$ is a material independent parameter based on the statistical considerations of the obstacle spacing with a value of 6.7. The value of numerical factor m for obstacles randomly distributed around the sources is, $m = 4.5$.

CHAPTER IV

MICROPILLAR PLASTICITY: A DISCRETE DISLOCATION DYNAMICS
PERSPECTIVE

A. Introduction

The growing interest in miniaturization of technology has demanded the need to understand mechanical behavior of materials at small length scales. In these materials, there is overlap between a length scale associated with physical phenomenon influencing mechanical property and structural or material length scale. Under these circumstances material mechanical properties deviate from known bulk properties. Recent advances in experimental technique has made it possible to study the influence of dimensional constraints on the plastic behavior of materials without the influence of microstructural constraints. This chapter focuses on the progress made in experimental, and simulation work towards understanding the size affected plastic behavior in materials due to dimensional constraints. In particular, it provides a summary of key results and findings from the current research work.

B. Micropillar experiments

This section summarizes the salient features of micropillar fabrication techniques, testing, and its mechanical response. Potential factors related to fabrication techniques and testing methodology which affect the mechanical response of micropillars is also discussed. Finally, dislocation mediated mechanisms identified from experiments that govern the mechanical response of micropillars is presented.

1. Micropillar fabrication and testing

Micro-compression of FCC single crystals has been the focus of a number of recent experimental investigations. In particular, the materials of interest have been Ni (Uchic et al., 2004; Dimiduk et al., 2005; Frick et al., 2008), Au (Greer et al., 2005; Volkert and Lilleodden, 2006), Cu (Kiener et al., 2009c), and Al (Ng and Ngan, 2008b). Technological relevance coupled with a large body of knowledge related to the bulk plasticity behavior of these materials have made them the popular choice in micro-compression experiments. Samples for micro-compression experiments are prepared from these materials predominantly from focus ion beam (FIB) micromilling technique.

FIB micromilling allows to prepare a series of isolated single crystal micropillars with size below 40 μm in diameter within the surface of bulk samples. The micropillar size which can be FIB micromilled is limited by the time taken by the fabrication process. For a micropillar of diameter 40 μm, the time taken for FIB micromilling is almost 3 days (Dimiduk et al., 2005). Depending on the procedure used during the FIB micromilling, one can achieve either a perfect cylindrical sample with the desired aspect ratio or a tapered sample with larger than desired gauge length. Cylindrical micropillar samples can be achieved by adopting the lathe milling technique in which ion beam is at an oblique angle to the bulk sample surface (Uchic et al., 2004; Dimiduk et al., 2005). On the contrary, if ion beam is perpendicular to the bulk sample surface it leads to a tapered sample (Greer et al., 2005; Volkert and Lilleodden, 2006; Frick et al., 2008). The control provided in the fabrication of the sample by lathe milling procedure over the later method however comes at the cost of increased processing time. A major concern of samples prepared from FIB micromilling is the presence of an irradiation damage layer created by the impact of highly accelerated Ga^+ ions.

More recently, sample preparation based on selective etching of directionally solidified alloys has been developed to prepare micropillars free of irradiation damage layers (Bei et al., 2008a). Microelectronics-based fabrication technique which extends on the FIB based micromilling (Uchic et al., 2004) is used to make samples smaller than 300 nm (Brinckmann et al., 2008).

A schematic of the experimental setup commonly used in the micro-compression test is as shown in Fig. 1. The method is based on an extension of typical nanoindentation test. Samples prepared from any of the fabrication methods described above are tested at room temperature using nanoindentation system. A diamond or canonical indenter with flat tip is used to load the sample either under displacement controlled (Dimiduk et al., 2005; Greer et al., 2005) or load controlled (Volkert and Lilleodden, 2006; Frick et al., 2008) mode. Typical applied displacement rates are in the range of $0.2 - 5$ nm/s and applied loading rates are in the range of $0.8 - 100$ μN/s.

2.   Micropillar mechanical behavior

The primary focus of the micropillar experiments has been to investigate the effect of sample size on material strength. In particular, most of the research has concentrated on the scaling of flow stress with sample size (Uchic et al., 2004; Dimiduk et al., 2005; Greer et al., 2005; Brinckmann et al., 2008; Ng and Ngan, 2008a) and to a lesser extent on the effect of sample size on material strain hardening (Volkert and Lilleodden, 2006; Frick et al., 2008). A common trend observed in all the experiments is an increase in the flow stress with decrease in size of the sample. This phenomenon has been observed for crystals below 40 μm down to 160 nm for various FCC crystals and more recently in some BCC crystals (Brinckmann et al., 2008) as well. It should be noted here that the strengthening observed in these experiments is unlike those observed in whiskers which contain a very small density of dislocations in them. The
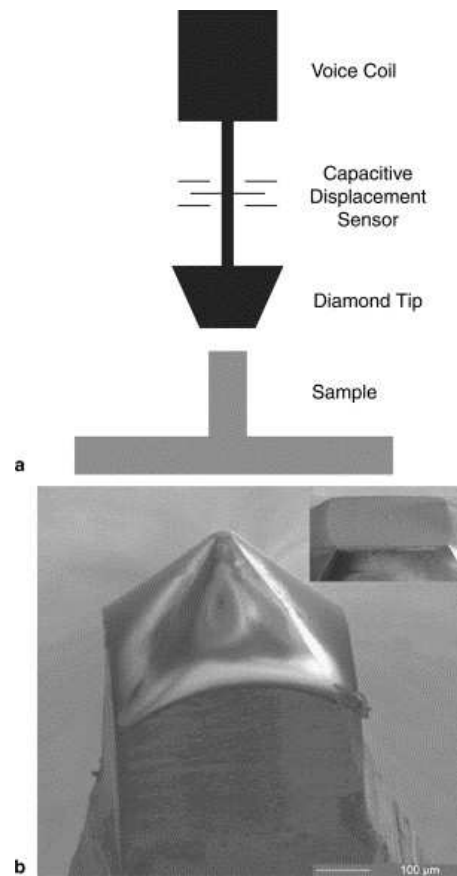
Fig. 40. Schematic of micropillar experimental setup. The black are in (a) represents the nanoindentation system and the lower gray are represents the micropillar sample machined into the surface of bulk single crystal. An SEM image of flat diamond tip is shown in (b). This figure is taken from Dimiduk et al. (2005).

Table IV. Compilation of data from micropillar experiments. The following notations
are used in the table: E is the material Young's modulus; ρ_{int} is the initial
dislocation density; $\sigma_{\text{f}-\text{min}}$ is the flow stress corresponding to the smallest
sample tested; $\sigma_{\text{f}-\text{max}}$ is the flow stress corresponding to the largest sample
tested; n_{min} is the lowest scaling exponent of flow stress determined; n_{max}
is the highest scaling exponent of flow stress determined. The lowest and
largest scaling exponents correspond to exponents determined at a lower and
higher value of strain corresponding to an equation of the form $\sigma_{\text{f}} = \sigma_0 D^n$;
where D is the size of sample. The flow stress values correspond to: [a] flow
stress at 1% strain; [b] flow stress at 10% strain; [c] flow stress at 0.2% strain;
[d] flow stress at 5% strain.

Material	Pillar diameter (μm)	E (GPa)	ρ_{int} (m^{-2})	$\sigma_{\text{f}-\text{min}}$ (MPa)	$\sigma_{\text{f}-\text{max}}$ (MPa)	n_{min}	n_{max}	References
Ni$\langle 269 \rangle$	1 - 40	205	3×10^{12}	53[a]	411[a]	-0.64	-	Dimiduk et al. (2005)
Ni[111]	0.16 - 2	308	$\approx 10^{12}$	636[b]	3888[b]	-0.69	-0.86	Frick et al. (2008)
Au$\langle 001 \rangle$	0.2 - 0.95	48.5	-	157[b]	590[b]	-	-0.97	Brinckmann et al. (2008)
Au	0.18 - 8.5	78	-	40[c]	563[c]	-0.61	-	Volkert and Lilleodden (2006)
Al	0.86 - 6.3	70	$\approx 10^{12}$	48[d]	240[d]	-0.92	-	Ng and Ngan (2008b)
Cu$\langle 100 \rangle$	0.9 - 6.7	126	$\approx 10^{13}$	253[b]	472[b]	-0.19	-0.3	Kiener et al. (2009c)
Mo$\langle 100 \rangle$	0.98 - 0.2	329	-	2850[b]	1325[b]	-	-0.45	Brinckmann et al. (2008)
Nb(100)	0.9 - 0.1	145	-	2188.8[b]	456[b]		-1.06	Kim et al. (2009)

observation of increase in crystal strength with decrease in sample size even in the presence of a relatively large density of dislocation of the order of 10^{12}m^{-2} is the remarkable discovery and observation from the micropillar experiments.

Table IV provides a summary of results compiled from micropillar experiments for various FCC crystals. It gives the range of pillar diameter, Young's modulus of the material, initial dislocation density, minimum flow stress recorded which corresponds to the largest sample tested, maximum flow stress recorded which corresponds to the smallest sample tested, and flow stress scaling exponent. Where data available, minimum scaling exponent corresponding to scaling determined at a low strain value and maximum scaling exponent corresponding to scaling determined at a high strain value are provided. The initial dislocation density in most of the experiments are in the range of $10^{12} - 10^{13}\text{m}^{-2}$. In all the experiments the flow stress values reached by the smallest sample tested is significantly higher than its bulk counterpart. For example, the flow stress reached in 160 nm Ni sample is more than 70 times the flow stress recorded in the Ni sample of size 40 μm. An interesting observation from Table. IV is the values reported for flow stress scaling exponent by different experimental groups. In general, from Table IV we notice that the scaling exponent as low as -0.19 and as high as -1.0 have been reported in the experiments. Also, an increase in the value of scaling exponent with increase in strain has been observed in experiments. Frick et al. (2008) observed in Ni micropillar experiments that the scaling exponent increased from -0.69 to -0.86 with increase in strain from 3% to 10%. Similarly, Kiener et al. (2009c) observed in their Cu micropillar experiments that flow stress increased from -0.19 to -0.3 with increase in strain from 5% to 10%.

The increase in flow stress scaling exponent with increase in strain has been attributed to the ability of the micropillars to strain harden and size effect observed in strain hardening (Frick et al., 2008; Kiener et al., 2009c). Frick et al. (2008) and

Volkert and Lilleodden (2006) report strain hardening rate almost 20 times the bulk range for samples as small as 200 nm; while Kiener et al. (2009c) report a value which is 2 times the bulk range for the sample with size 800 nm. The reason for differences in scaling of flow stress observed from different experimental groups has not been clearly identified and rationalized. Also, not all the micropillar experiments report on the effect of sample size on strain hardening rate of micropillars. Dimiduk et al. (2005), Greer et al. (2005) and Ng and Ngan (2008b) only mention about the size effect on the initial transient hardening observed at very low strains. They do not quantify hardening rate beyond the initial transient regime.

The stress versus strain response observed from the micropillar experiments is unlike the response typically observed in their bulk counterparts. In micropillar experiments, the stress versus strain curves are characterized by intermittent elastic or near elastic loading followed by strain bursts. Attempt was made by Dimiduk et al. (2006) to characterize these discrete slip events. Their analysis revealed a power-law scaling between number of discrete slip events and its magnitude suggesting that a linear regime exists in which the probability of observing a displacement event of a given magnitude decreases as the event size increases. In the experiments by Kiener et al. (2009c) the stress versus strain response demonstrated a steady hardening response and a lack of intermittent elastic loading followed by strain bursts.

3. Influence of fabrication and testing method on micropillar mechanical behavior

When analyzing the micropillar experimental results careful attention needs to be provided at the fabrication and testing method employed during the experiment for an accurate assessment of the intrinsic material properties. Primary issues related to fabrication and testing which might have an influence on micropillar mechanical response and currently under investigation are: (i) difficulty to fabricate micropillars

with uniform cross-section along its gauge length for samples below 1 μm; (ii) presence of an irradiation-damage layer on micropillar surface created by high impact Ga^+ ions; (iii) lateral sample compliance; and (iv) misalignment between flat-punch tip and sample top surface.

Inability to fabricate micropillars with uniform cross-section along its gauge length results in taper of the sample. Taper angle of magnitude 3.5° has been observed in Ni samples by Frick et al. (2008). There has been finite element based numerical study (Zhang et al., 2006) which has suggested that a taper of 2.86° in samples with an aspect ratio of 2:1 to 5:1 can lead to an artificial hardening. However, Frick et al. (2008) has observed that the stress gradient between the top and bottom surface of the sample is well below 50% but the increase in stress beyond yield is well above 350% and hence strain hardening cannot be a result of primarily sample taper. Also, taper is self-similar across the range of micropillar diameter tested and yet there is a consistent trend of sample size on flow stress and strain hardening. While the influence of taper on measured values of flow stress and strain hardening rate cannot be ignored it does not affect the overall trend of increased strengthening due to a reduction in sample size.

Micropillar sample fabrication using FIB technique induces an irradiation-damage layer on the surface due to high impact Ga^+ ions. However, experiments have not be done to ascertain if the presence of irradiation-damage layers translates into strengthening in micropillar experiment. Recent in-situ nanocompression experiments have shown that the high density of small dislocation loops, due to ion beam irradiation, at the surface escaped upon application of loading. This phenomenon was termed 'mechanical annealing'. Also, Greer et al. (2005) and Greer and Nix (2006) processed samples using different fabrication techniques to prepare samples with varying degrees of ion beam irradiation effect. Despite the varying degree of irradiation ef-

fect in the samples the flow stress data measured in these experiments were similar. This suggested that irradiation-damage layer might not play a significant role in the strengthening observed in micropillar experiments.

Kiener et al. (2008a) conducted micro-tension tests on Cu micropillars. They observed that the flow stresses obtained from these tests were almost 4 times lesser than the flow stresses observed in micro-compression tests. This result highlighted the strong influence of stiff lateral constraint offered by the bulk material the sample is attached to on flow stress data in micro-compression tests. Kiener et al. (2009a) showed that if the lateral compliance in micro-compression test was reduced by placing the sample on a needle tip then the flow stress values obtained are similar to those obtained from micro-tension test. Another issue of importance is the misalignment between the flat-punch tip and the sample top. A large misalignment can underestimate the material modulus, yield and the strain hardening in the test due to plastic instability. In fact, this is one of the reason why yield is not usually defined at the 0.2% strain; instead different groups have probed the flow stress values at larger strains to determine the saturation stress where the effect of sample misalignment or sample taper effect maybe minimized. The readers are referred to the article by Kiener et al. (2009b) for a discussion on the influence of experimental constraints on micro-compression tests.

Attempts are being made to characterize the initial internal defect microstructure, their evolution and their effect on the overall macroscopic response using transmission electron microscopy (TEM) (Norfleet et al., 2008; Frick et al., 2008; Ng and Ngan, 2008b) and X-ray diffraction (XRD) (Maass et al., 2007, 2008). The slip traces and bands in Ni samples observed by Norfleet et al. (2008) revealed dislocation structures similar to those observed in bulk crystals during stage I hardening. They also reported an increase in dislocation density during the initial stage of deformation and

significant dislocation activity on non-primary slip planes. Frick et al. (2008), apart from identifying increase in dislocation density, also reported lattice rotation upto 3° of the micropillar relative to the substrate. XRD studies by (Maass et al., 2007, 2008) also showed evidence of local lattice distortions due to pre-existing dislocations or low angle boundaries, inside the micropillars.

Summary of experimental work has unequivocally shown that there is an overall increase in sample strength with decrease in sample size. There are also evidence that show significant increase in strain hardening rate in crystals with decrease in their sample size; however, this finding has not been reported by all the experimental groups and uncertainties exist in the assessment of these results. Further, the summary highlighted the role played by fabrication and testing methods on the experiments. A systematic research to characterize the importance of each fabrication and testing method, though currently underway, is still lacking. Evidence from TEM and XRD studies of the micropillars have revealed that dislocation structure and local lattice gradients play a role in the strengthening observed in micropillars. However, a direct correlation between the defect microstructural details and macroscopic response has not been completely established.

C. Micropillar simulation predictions

This section provides an overview of the simulation efforts which have been performed and are currently underway to understand the phenomenon of size affected strengthening observed in micropillar experiments. In particular, the focus is on 3D as well as 2D discrete dislocation dynamics (DDD) based simulation studies. First, simulation results based on 3D-DDD are presented. This is followed by 2D-DDD investigations from the current investigation. Comparison of experimental and 2D-DDD simulation

studies are also presented. Explanation for the observed size-effect on strengthening based on simulations are finally discussed.

Simulations offer the advantage of investigation of size-effect in micropillars under idealized conditions without the influence of factors like, pillar taper angle, irradiation-damage layer, lateral sample compliance, misalignment, among other issues. Hence, simulations allows one to study the intrinsic material behavior without the influence of fabrication and testing methodology. Simulations also have the capability to model micropillars to reproduce actual experimental conditions that includes some of the factors listed above; thus providing more insight into the experimental observations. However, idealizations inherent to the simulation models, limitations on simulation cell size and simulation time due to computational challenges, approximations related to initial defect source structure strength and distribution limit the scope with which one can explore the micropillar mechanical behavior in accurate detail.

1.   3D discrete dislocation dynamics simulations

A majority of the simulation studies performed to understand micropillar mechanical behavior are based on 3D-DDD (Rao et al., 2008; El-Awady et al., 2008; Senger et al., 2008; Weygand et al., 2008; El-Awady et al., 2009; Akarapu et al., 2010; Zhou et al., 2010). This approach naturally accounts for dislocation glide, short-range dislocation interactions, and dislocation interactions with free surfaces. However, this comes at the cost of severe computational resources and hence limits the ability of the studies to relatively smaller simulation cells and very low strains. A consequence of this is the inability of these models to explore a wide range of pillar sizes to investigate the transition of mechanical behavior of crystals from size affected to typical bulk response. Restrictions on the range of strain levels which can be reached by these

Table V. Compilation of data from micropillar experiments. The following notations are used in the table: E is the material Young's modulus; ρ_{int} is the initial dislocation density; $\sigma_{\mathrm{f-min}}$ is the flow stress corresponding to the smallest sample tested; $\sigma_{\mathrm{f-max}}$ is the flow stress corresponding to the largest sample tested; $n_{\min}$ is the lowest scaling exponent of flow stress determined; $n_{\max}$ is the highest scaling exponent of flow stress determined. The lowest and largest scaling exponents correspond to exponents determined at a lower and higher value of strain corresponding to an equation of the form $\sigma_{\mathrm{f}} = \sigma_0 D^n$; where D is the size of sample. The flow stress values correspond to: [a] flow stress at 1% strain; [b] flow stress at 0.5% strain; [c] flow stress at 0.2% strain.

Material	Pillar diameter (μm)	E (GPa)	ρ_{int} (m^{-2})	$\sigma_{\mathrm{f-min}}$ (MPa)	$\sigma_{\mathrm{f-max}}$ (MPa)	$n_{\min}$	$n_{\max}$	References
Ni	0.5 - 20.0	157	$10^{12} - 10^{13}$	50^a	840^a	-0.43	-0.84	Rao et al. (2008)
Ni	0.25 - 5.0	200	$1 - 5 \times 10^{12}$	88^b	797^b	-0.69	-	El-Awady et al. (2009)
Ni	0.5 - 1.0	200	2.5×10^{13}	373^a	683^a	-0.67	-	Zhou et al. (2010)
Al	0.5 - 2.0	72	2×10^{13}	51^c	120^c	-0.57	-	Senger et al. (2008)
Cu	0.2 - 2.5	129	10^{13}	435^c	1562^c	-	-	Akarapu et al. (2010)
Al	0.4 - 3.2	70	10^{12}	70^a	900^a	-0.83	-1.01	Benzerga (2009)

simulations preclude the study of strain hardening behavior in microcrystals. Despite the limitations, these simulations have been able to qualitatively and quantitatively capture some salient features of micropillar experiments. They have also shed light on the possible dislocation mediated mechanisms which can lead to size effects in micropillars.

Table V provides a summary of results compiled from DDD simulations. Except for the data from work by Benzerga (2009), all the other data are from 3D-DDD simulations. In the 3D-DDD simulations the largest crystal size considered was 20 μm (Rao et al., 2008) and the smallest crystal size considered was 0.2 μm (Akarapu et al., 2010). In all the 3D-DDD simulations an initial density of Frank-Read sources are considered from which dislocations are nucleated. The Frank-Read source density considered in the simulations are in the range of $10^{12} - 10^{13}$ m^{-2}. However,

due to lack of sufficient information about the initial microstructure configuration from experiments differences exist between different simulations in the distribution of these Frank-Read sources. Senger et al. (2008) and Weygand et al. (2008) considered Frank-Read sources of constant length. A more common approach is to consider a random distribution of Frank-Read sources whose length is restricted by the size of the crystal (Rao et al., 2008; El-Awady et al., 2009; Akarapu et al., 2010; Zhou et al., 2010). Differences also exist based on distribution of Frank-Read sources on one slip system (El-Awady et al., 2008), randomly distributed (Rao et al., 2008), or on all possible slip systems (Senger et al., 2008; El-Awady et al., 2009; Akarapu et al., 2010; Zhou et al., 2010). Tang et al. (2008) considered a network of dislocations as initial microstructure which was generated by a relaxation procedure mimicking a thermal annealing process.

All the 3D-DDD simulations presented in Table V are able to capture the size-effect observed in micropillar experiments. Difference, however, exist in the stress-strain response reported from various 3D-DDD simulations. Senger et al. (2008) and Weygand et al. (2008) obtain a near perfect plastic or small hardening depending on initial source distribution following the yield. Rao et al. (2008), El-Awady et al. (2009) and Zhou et al. (2010) are able to reproduce stress-strain response which is qualitatively similar to micropillar response; the response is characterized by intermittent elastic or near elastic loading and strain bursts. The flow stress scaling exponent predicted from 3D-DDD simulations are given in Table V. The scaling exponent predicted from 3D-DDD simulations are in the range of -0.4 to -0.85. The variability of the scaling exponent predicted in the work by Rao et al. (2008) is dependent on the initial dislocation source density used in the simulations. Rao et al. (2008) observed that the scaling exponent decreased with increase in the initial dislocation source density. The high scaling exponent of -0.87 observed by Frick et al. (2008) was

that a strain of 10% due to size-effect observed in strain hardening rate. However, the strain levels reached by the 3D-DDD simulations are very small and they do not show any size-effect on strain hardening observed in micropillar experiments (Volkert and Lilleodden, 2006; Frick et al., 2008).

Simulations from 3D-DDD (Rao et al., 2008; El-Awady et al., 2009) have attributed the observed size-effect and the transient-hardening response at small strain regime in micropillars to two mechanisms: (a) source-truncation; and (b) exhaustion hardening. The initial source strength distribution is refined when a Frank-Read (FR) source interacts with the free surface and creates two single-ended sources with length smaller than the initial FR source. Among all the available single-ended sources it is the source with the largest length which sets the flow stress observed in micropillars. Similar observation was first reported by Benzerga and Shaver (2006) using 2D-DDD simulations. The exhaustion hardening is an outcome of lack of sufficient number of mobile dislocations within the micropillars to accommodate the applied loading. In a bulk crystal there are many potential mobile dislocation segments which can accommodate the applied loading. However, in micropillars there are only a finite number mobile dislocation segments and a source can be shut-off during deformation due to forest-hardening processes. Subsequently, the stress has to be increased to activate the next weakest source in micropillars leading to the transient-hardening response observed in the small strain regime in simulations.

2.   2D discrete dislocation dynamics simulations

In this section results and insight gained on the mechanical behavior of micropillars from 2D-DDD simulations are presented. In particular, attention is focused on 2D-DDD simulations from the current research work and its contribution to the ongoing discussion on micropillar plasticity. Flow stress and strain hardening rate predicted
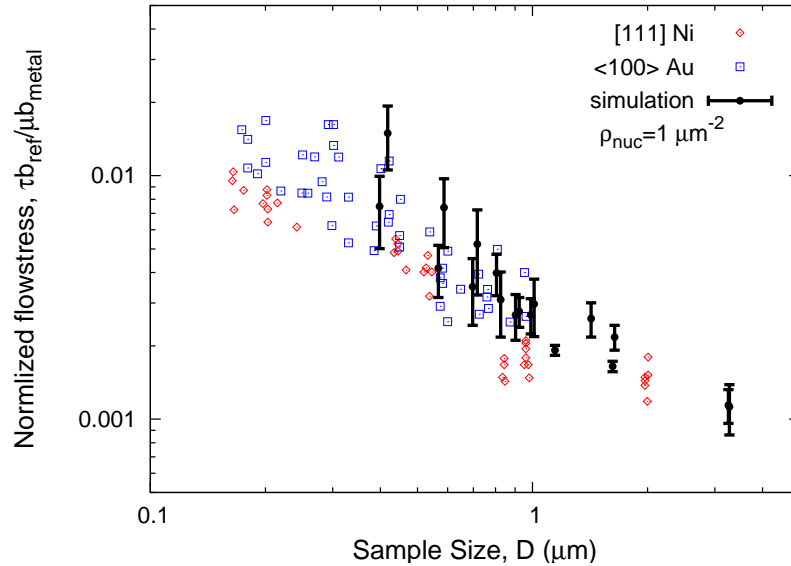
Fig. 41. Comparison is shown between flow stress data from Ni (Frick et al., 2008) and Au (Brinckmann et al., 2008) micropillar experiments and simulation results from (Benzerga, 2009). The flow stress scaling exponent is close to -1.0 in both experiments and simulations. All the data shown are suitably normalized.

from simulations are compared with experimental data. Analysis of deformed micropillars in simulations reveal possible mechanisms which aid to explain the observed size-effects on flow stress and strain hardening. Details regarding the formulation of 2D-DDD framework and constitutive rules included to account for short-range dislocation interactions can be found in Chapter II and III. 2D-DDD simulations (Benzerga and Shaver, 2006; Benzerga, 2009; Guruprasad and Benzerga, 2008b) have been able to capture the salient features of mechanical response of micropillars. Benzerga and Shaver (2006) and Benzerga (2009) have shown that at very low initial dislocation source density, of the order of 10^{12} m^{-2}, stress-strain response is characterized by flow intermittency at coarse time scales. The applied strain rate is predominantly accommodated by elastic loading followed by relaxation. On the other hand, at high initial dislocation source densities, of the order of 10^{13} m^{-2} and 10^{14} m^{-2}, the stress-strain

response was similar to bulk crystal characterized by a steady hardening following the yield. However, the observed strain hardening rates were higher than the known bulk range and was dependent on micropillar size (Guruprasad and Benzerga, 2008b). These two sets of simulations with low and high initial dislocation source densities have been able to capture the range of experimental results reported in experiments on flow stress scaling, and size effect on strain hardening.

Fig. 41 shows flow stress predicted from simulations for various micropillars in comparison to experimental results. The flow stress data is normalized with material shear modulus (μ) and Burger's vector. The reference Burger's vector $b_{\text{ref}} = 0.25$ nm used in simulations. These simulation results correspond to calculations with an initial dislocation source density of 10^{12} m^{-2}. It can be observed that flow stress predicted from simulations for micropillars of various sizes compare well with experimental results reported by Greer et al. (2005); Brinckmann et al. (2008) and Frick et al. (2008). Flow stress scaling of -1.09 and -0.97 was determined by Greer et al. (2005) and Brinckmann et al. (2008) at low strains, while Frick et al. (2008) inferred a flow stress scaling of -0.86 at a strain of 10%. Simulations predict a value of -0.83 and -1.01 depending on the source length cut-off used in the calculations. Flow stress versus sample size data from simulations performed with an initial dislocation source density of 10^{13} m^{-2} and 10^{14} m^{-2} is shown in Fig. 42. Experimental data from Cu micropillars (Kiener et al., 2009c) are shown for the purpose of comparison. It should be noted here that simulations with initial dislocation source density of 10^{13} m^{-2} were specifically performed for Cu micropillars as described in Chapter III. Flow stress predicted from simulations agree well with the experimental values. However, we notice that the flow stress predicted from simulations with an initial dislocation source density of 10^{14} m^{-2} are on the higher side. This is because of the significant hardening rate observed in these simulations, where junctions were
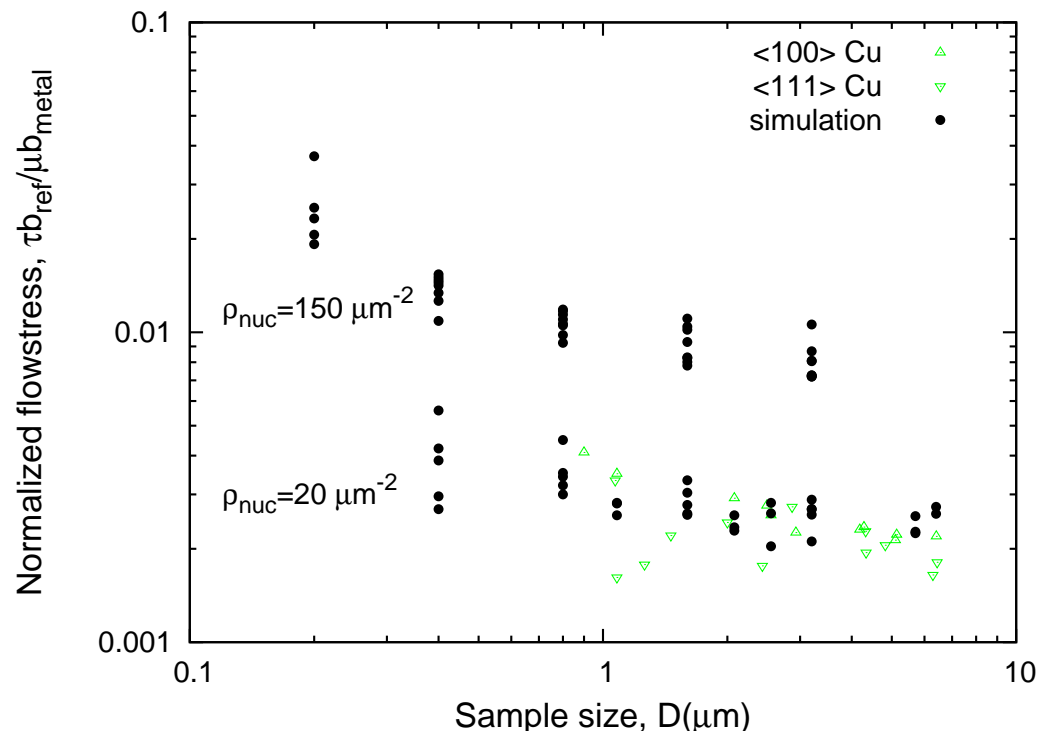
Fig. 42. Comparison is shown between flow stress data from Cu (Kiener et al., 2009c) and simulation results from the current study. These data correspond to lower scaling exponent of flow stress data from experiments and simulations. All the data shown are suitably normalized.
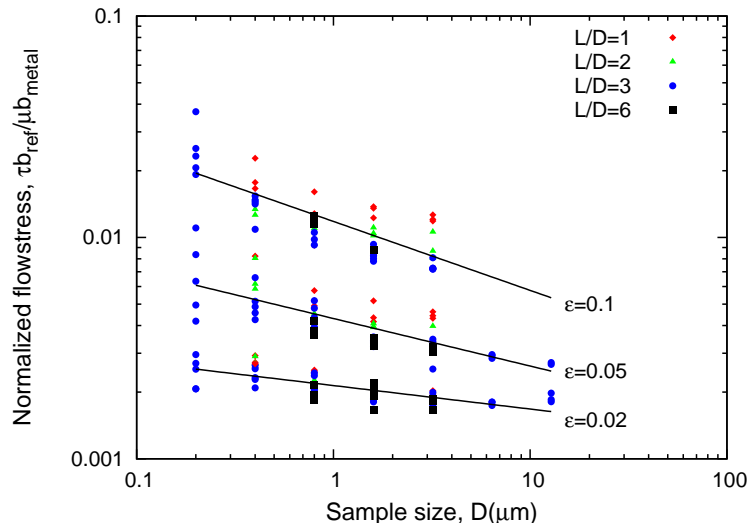
Fig. 43. Flow stress from simulations for crystals with aspect ratio (L/D) of 1, 2, 3 and 6. The slip planes are oriented at an angle of $\pm 35.25°$ to the loading direction in all the simulations. The initial dislocation source density is $\rho_{\text{nuc}} = 1.5 \times 10^{14}$ m^{-2}. The flow stress scaling exponent corresponding to data at a strain of $\varepsilon = 0.02$ is -0.10 and the scaling exponent corresponding to $\varepsilon = 0.1$ is -0.31.

treated as unbreakable. However, the flow stress scaling of -0.42 predicted from these simulations is close to scaling of -0.3 reported by Kiener et al. (2009c) at a strain of 10%.

Additional simulations were carried out to explore the effect of sample aspect ratio (L/D) on the trends observed above. Fig. 43 shows normalized flow stress versus sample size for various micropillar sizes at different strains. The sample aspect ratio was varied between 1-6. Irrespective of the sample aspect ratio, the simulations predicted an increase in flow stress with decrease in size. Further, with increase in strain the flow stress scaling was found to increase. Flow stress scaling, determined by accounting all the simulations irrespective of its aspect ratio, was found to increase from -0.1 at a strain of 2% to -0.31 at a strain of 10%. The effect of active slip systems
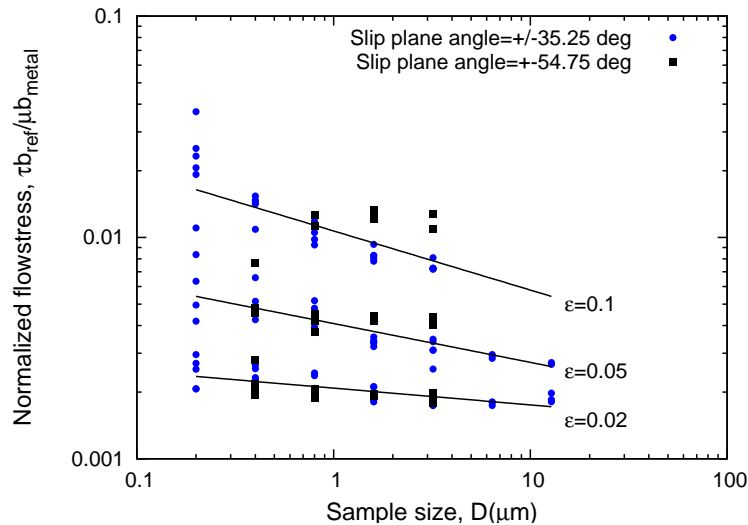
Fig. 44. Comparison of normalized flow stress data between simulations for crystals with slip system oriented at $\pm 35.25°$ and $\pm 54.75°$. The aspect ratio (L/D) of the crystals was 3. The initial dislocation source density is $\rho_{\text{nuc}} = 1.5 \times 10^{14}$ m^{-2}.

on flow stress prediction in micropillars is shown in Fig. 44. These simulations were carried out on micropillars with $L/D = 3$ and an initial dislocation source density of 10^{14} m^{-2}. The two slip systems considered were: (a) $\pm 35.25°$; and (b) $\pm 54.75°$. At low strains the flow stress predictions from the two sets of simulations are similar. However, with an increase in strain there is a noticeable difference in the flow stress values predicted; with micropillars oriented at $\pm 54.75°$ being relatively harder than micropillars oriented at $\pm 35.25°$. Within the 2D idealization of micropillars in simulations, the number of potential sites for junction formation is more in crystal with slip planes oriented at $54.75°$ than in crystals with slip planes oriented at $35.25°$; with all other geometric dimensions being similar. This increases the chance of junctions formation, which can potentially act as dynamic obstacles and block dislocations, in the crystal with slip planes oriented at $54.75°$. This increase in resistance to slip leads
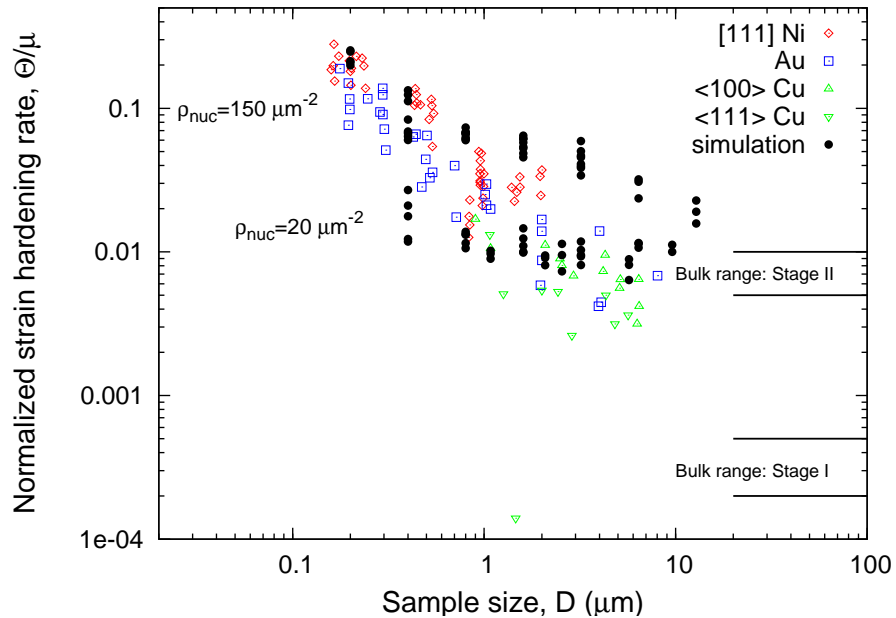
Fig. 45. Comparison is shown between strain hardening rate from Ni (Frick et al., 2008), Au (Volkert and Lilleodden, 2006), and Cu (Kiener et al., 2009c) micropillar experiments and simulation results from the current study. Simulation results correspond to an initial source density of $\rho_{\mathrm{nuc}} = 20 \times 10^{12}$ m^{-2} and 1.5×10^{14} m^{-2}. The strain hardening rate data is normalized with respect to material shear modulus (μ).

to an increase in hardening observed in these crystals relative to the crystals with slip planes oriented at 35.25°.

Comparison between strain hardening rate predicted from simulations and experiments is shown in Fig. 45. The strain hardening rate data is normalized by the material shear modulus (μ). The simulation results correspond to cases with an initial dislocation source density of 10^{13} m^{-2} and 10^{14} m^{-2}. All simulations correspond to micropillars with $L/D = 3$ and slip planes oriented at $\pm 35.25°$. Both experiments and simulations predict an increase in strain hardening rate of micropillars with decrease in size. Strain hardening rate as high as 20 times the bulk stage II hardening

rate has been predicted in micropillars as small as 200 nm. Frick et al. (2008) reports that strain hardening rate scales as -1 with micropillar size. The corresponding scaling factor from simulations with an initial dislocation source density of 10^{14} m^{-2} is -0.85. The strain hardening rate predicted from experiments on Cu micropillars is lower than those predicted on Ni (Frick et al., 2008) and Au (Volkert and Lilleodden, 2006). Strain hardening rate predicted from simulations with an initial dislocation source density of 10^{13} m^{-2} compares well with this data.

Fig. 47 shows normalized strain hardening rate versus initial dislocation source density in samples with size $D = 0.8$ μm. The initial dislocation source density was varied in the range 10^{13} m^{-2} to 10^{14} m^{-2}. All the calculations predicted a strain hardening rate which is larger than the bulk stage II hardening range. Also, the strain hardening rate did not significantly vary with variation in the initial dislocation source density; within the range explored in the calculations. However, with decrease in initial dislocation source density there was scatter in the predicted strain hardening rate.

Deformed configurations of three planar crystals with size $D = 3.2$ μm and aspect ratio of 1, 2 and 3 are shown at a strain of $\varepsilon = 0.1$. All the crystals are oriented for symmetric double slip. These results correspond to simulations with an initial dislocation source density of 10^{14} m^{-2}. Despite the random distribution of dislocation nucleation sites within the crystals and differences in geometry of samples, the samples deformed in double slip. The slip observed is not local or confined to a few active slip planes but it is distributed over the length of the specimen. There are no indications of bending of samples during the deformation. Evidence of localized slip are however rare events which can occur in smaller samples as shown in Fig. 31 (Chapter III).

Contours of lattice rotation fields in samples are shown in Fig. 49. These results
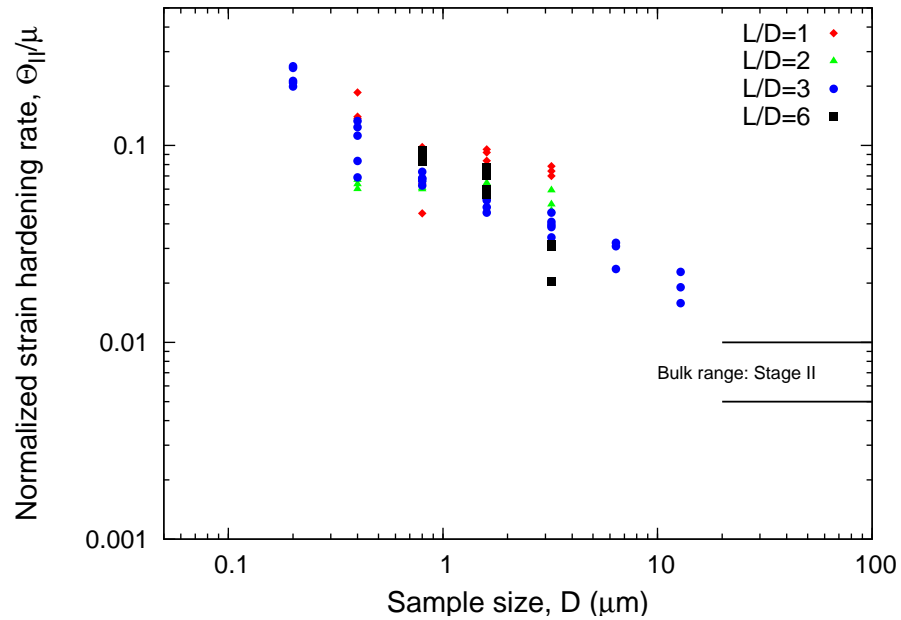
Fig. 46. Normalized stage II hardening rate (Θ_{II}/μ) versus sample size (D) from simulations for crystals with aspect ratio (L/D) of 1,2,3,6. These data correspond to flow stress data shown in Fig. 43.

correspond to the samples shown in Fig. 48b and c, respectively. Domains of large lattice rotations, not necessarily aligned along the slip planes, are formed in both the crystals. Within the crystals gradients of local lattice rotations can be observed, despite the imposed homogeneous deformation.

Locally within the crystal there is an emergence of geometrically necessary dislocation (GND) density to accommodate the gradients in lattice rotation fields. Contours of GND density distribution within the crystals are shown in Fig. 50. Fig. 50a and b correspond to the results shown in Fig. 49. The GND density contours are at a resolution of 50×50 nm^2 following the methodology presented in Chapter III. It is observed that at the central region of the crystals there is relatively higher GND density than near the free surface. At the central region dislocation patterns, like cell
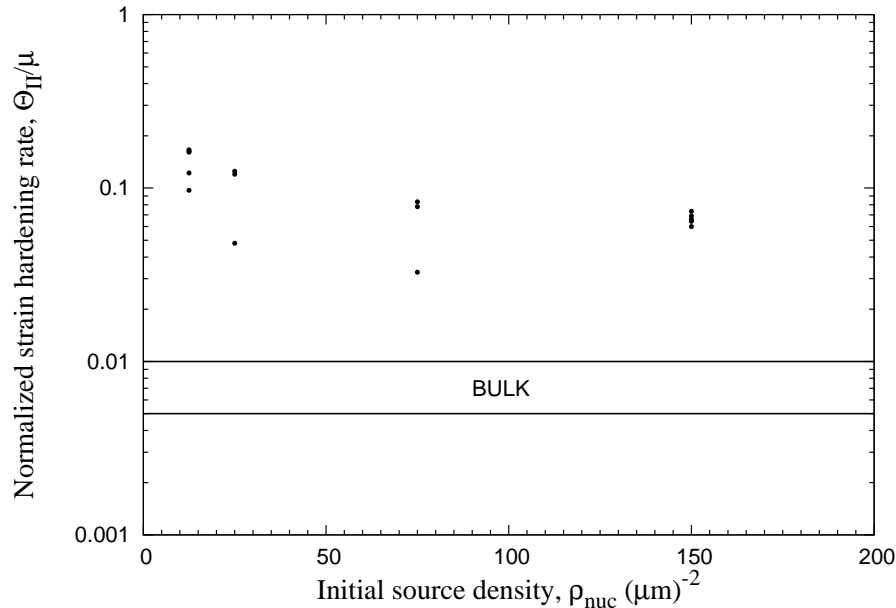
Fig. 47. Normalized stage II hardening rate from simulations for a crystal with size $D = 0.8$ μm is shown as a function of initial dislocation source density. The aspect ratio of the crystal is $L/D = 3$ and the crystal is oriented at $\pm 35.25°$ to the loading direction.

walls, are formed leading to the observed high density. Also, bands of high GND density emerge out of the extreme slip plane intersection points from both the crystals. These high GND density regions correspond to tilt wall-like dislocation structures formed at these locations. The local emergence of GND density is considered to be the key mechanism leading to the observed size effect in flow stress and hardening in samples with high initial dislocation source density.

At low initial dislocation source densities ($\approx 10^{12}$ m^{-2}) formation of dislocation structures, like cell walls, are not common phenomenon. Size effects observed in these simulations were explained by Benzerga and Shaver (2006) based on the source strength distribution in micropillars. Later, similar ideas were also put forward based on 3D-DDD simulations (Rao et al., 2008; El-Awady et al., 2009). Benzerga (2009)

argued that at low initial dislocation source density the size effect is due to statistics of source strength distribution and exhaustion hardening. The exhaustion hardening here refers to imbalance between dislocation nucleation from source and dislocation escape.

D.   Conclusions and outlook

Recent contributions from experiments and simulations in the field of micropillar plasticity is reviewed in this study. In particular, focus was on the findings from the current research work and its relevance to the field of micropillar plasticity. In this study, 2D-DDD framework is used to investigate micropillar plasticity. Within this framework, key short-range dislocation interactions are modeled as constitutive rules and they include: junction formation; junction stabilization; and nucleation of dislocations from stable junctions which act as anchoring points. The simulations were able to capture the salient features of micropillar plasticity observed in experiments. A summary of key findings from literature review and simulation results from this study are as follows:

- A review of experimental work on micropillars revealed that there is strengthening upon scale reduction. The scaling of flow stress obtained from various investigations ranged from as high as -1.0 to as low as -0.3. An increase in strain hardening rate with decrease in sample size was also observed in some experiments. However, there are inconsistencies in the reporting of strain hardening rate in the literature and not all the experiments reported on the size affected hardening behavior of micropillars.

- 3D-DDD as well as 2D-DDD have been used to investigate the size affected strengthening behavior in micropillars. 3D-DDD has been able to capture
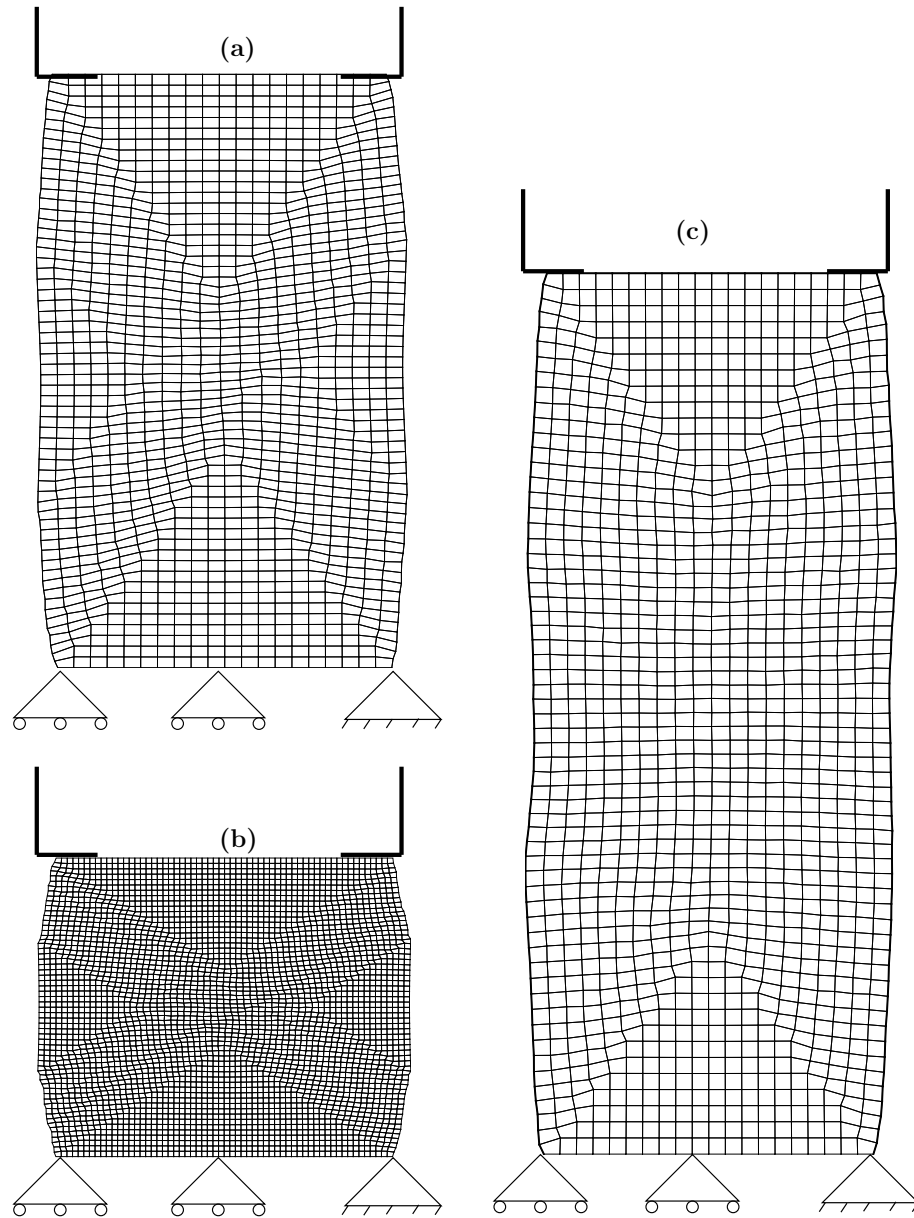
Fig. 48. Deformed configurations of crystals with size $D = 3.2$ μm and at a strain level of $\varepsilon = 0.1$ for crystals with an aspect ratio of: (a) $L/D = 2$; (b) $L/D = 1$; and (c) $L/D = 3$. The applied strain rate boundary condition is shown schematically.
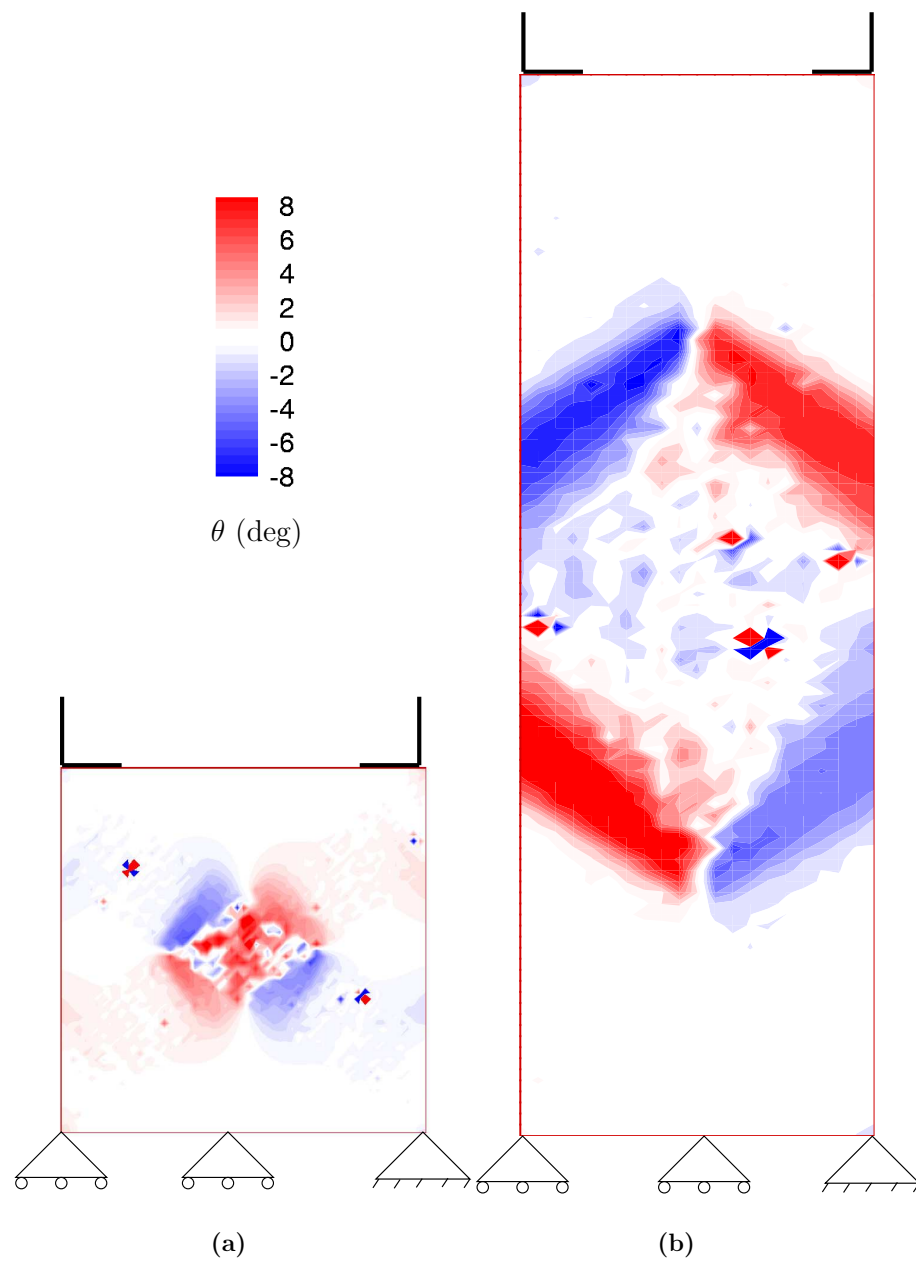
Fig. 49. Contours of lattice rotations are shown at a strain level of $\varepsilon = 0.1$ for crystals with size $D = 3.2$ μm and aspect ratio of: (a) $L/D = 1$; and (b) $L/D = 3$.

Fig. 50. Contours of GND density contours are shown at a strain level of $\varepsilon = 0.1$ for crystals with size $D = 3.2~\mu$m and aspect ratio of: (a) L/D=1; and (b) $L/D = 3$.

salient features of micropillar plastic behavior like: stress-strain response; and size effect on flow stress. These 3D-DDD investigations, however, were not able to capture the range of flow stress scaling observed in the experiments. Also, they did not report on the effect of sample size on strain hardening rate.

- 2D-DDD investigation from this study has been able to shed some light on the plastic behavior of micropillars. Simulation results were able to capture the size effect on flow stress as well as strain hardening rate. The study revealed that when the initial dislocation source density is high ($\approx 10^{13}$ m^{-2} - 10^{14} m^{-2}) the stress-strain response is characterized by steady hardening response. The flow stress scaling predicted in this case, -0.4, agreed well with the lower range of values determined from experiments. A good agreement was also obtained between the size affected hardening behavior in micropillars between simulations and experiments.

- 2D-DDD simulations, independent of the current research work, has shown that when the initial dislocation source density is low (≈ 1012 m^{-2}) the scaling obtained from simulations is -1.0, which agrees well with the higher range of scaling predicted from experiments. This work along with the current study has been able to span the range of scaling on flow stress determined from experiments.

- Analysis of 2D-DDD simulations highlight the transition from forest hardening dominated regime to exhaustion hardening dominated regime depending on the sample size and initial dislocation source density. In the high initial dislocation source density case the size effect on strengthening is due to the evolution of the dislocation structure and its interaction with free surfaces; while in the low initial dislocation source density case, the size effect is due to initial source

strength distribution affected by source truncation, followed by dynamic operation of source and rare events.

- A review of experimental work on micropillars has highlighted potential factors involving sample fabrication technique, geometry, and testing methodology, which might affect micropillar plasticity. The current research work attempted to address some of these issues by performing simulations with samples of different aspect ratio, slip system angle and initial dislocation source density. Simulations involving sample taper, effect of substrate and FIB induced irradiation-damage layer on sample are other studies that need to carried out to gain more insight into micropillar plasticity.

CHAPTER V

A PHENOMENOLOGICAL MODEL OF SIZE-DEPENDENT HARDENING IN CRYSTAL PLASTICITY*

A. Overview

A phenomenological model of plastic deformation is proposed which captures the size-dependence of plastic flow strength and work-hardening in pure FCC crystalline materials. Guided by discrete dislocation dynamics analyses, the treatment is based on two structural variables determining the mechanical state of the material. A complete description of plastic behavior is achieved given two inherently different statements for the evolution of structure, supplemented by a new kinetic equation, which specifies the hardening law in differential form at fixed structure. Evolution of the first state variable is set by phenomenology; it accounts for the cardinal bulk phenomena of athermal hardening and dynamic recovery, in addition to geometric storage. The second state variable is kinematically determined so that an evolution equation need not be formulated explicitly in rate form. The model formulation leaves unaltered the classical treatment of dynamic recovery. However, since there virtually is no experimental data on the temperature and strain-rate dependence of plastic flow at the micron scale, emphasis is laid on athermal behavior. In this limit, the model equations are integrated following specified strain paths to give the flow strength at current structure. Model predictions are assessed through comparison with results from discrete dislocation analyses of geometrically similar crystals subject to compression.

B. Introduction

Phenomenological theories of plastic flow and work hardening in single and poly-crystals are quite mature, especially for face-centered cubic and like materials at low homologous temperature (Kocks et al., 1975; Gil Sevillano, 1993; Kuhlmann-Wilsdorf, 1999; Kocks and Mecking, 2003). A widely accepted model of work hardening is one developed by Kocks, Mecking and co-workers (Mecking and Kocks, 1981; Estrin and Mecking, 1984; Kocks and Mecking, 2003). It is based on considerations of slip kinetics at fixed dislocation structure and dislocation density evolution, with guidance from extensive experimental measurements and observations. As it stands, the model strictly applies to *bulk* crystalline solids. Since no length scale enters the constitutive relations, the model does not capture the size-dependence of strength and work hardening at the micron scale, e.g. (Swadener et al., 2002; Uchic et al., 2004; Greer and Nix, 2006; Dimiduk et al., 2005; Volkert and Lilleodden, 2006; Frick et al., 2008). To date several attempts have been made to incorporate a length-scale dependence in the model (Acharya and Beaudoin, 2000; Verdier et al., 2006; Abu Al-Rub and Voyiadjis, 2006; Evers et al., 2002). Notable among these is the inclusion in Ref. (Acharya and Beaudoin, 2000) of a physically-motivated measure of lattice incompatibility in the dislocation density evolution equation, thus resulting in a net effect of geometrically necessary dislocations (GNDs) on incremental hardening moduli. A common assumption in (Acharya and Beaudoin, 2000; Verdier et al., 2006; Abu Al-Rub and Voyiadjis, 2006) is that the fundamental Taylor equation giving the flow strength in terms of dislocation density as

$$\mathcal{T} = \mathcal{T}_0 + A\mu b\sqrt{\rho}, \tag{5.1}$$

remains unaltered at the micron scale. Here, $\mathcal{T}_0$ and A are constants; μ is the shear modulus and b the Burgers vector strength.

The present paper starts from the premise that the validity of Taylor hardening, or the Bailey-Hirsch relationship (5.1), is questionable at micron-scale resolutions. Since plastic deformation is inherently heterogeneous, the dislocation density is a spatially fluctuating quantity and a simple back-of-the-envelope derivation shows that the very format of equation (5.1) cannot be scale-independent. Physically, any type of dislocation–dislocation interactions results in a flow strength scaling with the square root of the dislocation density, whether the interactions are long-ranged (Taylor, 1934) or short-ranged (Gil Sevillano, 1993). However, at a resolution of non vanishing GND density in the sense discussed in (Arsenlis et al., 2004; Guruprasad and Benzerga, 2008b), whether the additional strengthening due to GNDs would be consistent with the format of equation (5.1) remains unfounded physically. Furthermore, recent discrete dislocation dynamics calculations (Guruprasad and Benzerga, 2008b) strongly suggest that Taylor hardening breaks down in microcrystals subject to nominally uniform compression; also see (Ng and Ngan, 2008a).

The objective of this paper is to extend the validity of the classical Kocks-Mecking-Estrin model down to the micron scale. In reaching that objective, we build on previous work by Acharya and Beaudoin (Acharya and Beaudoin, 2000) and extensively use results from the discrete dislocation simulations of Guruprasad and Benzerga (Guruprasad and Benzerga, 2008b). One promising route to quantitative understanding of size-dependent strength is to connect rates of work hardening with structural measures that are expressible solely in terms of kinematics. This seems now possible based on advances made in recent years (Arsenlis and Parks, 1999; Acharya and Bassani, 2000; Acharya, 2004; Cermelli and Gurtin, 2001; Gurtin, 2006) for the characterization of geometrically necessary dislocations. Meanwhile, the Taylor alias

Bailey-Hirsch equation (5.1) is relaxed. Of course, it is still required that any extension of the model would recover the kinetic equation (5.1) in the limit of bulk material. The challenge is to specify the dependence of $\mathcal{T}$ vis-a-vis the enhanced representation of structure. In the proposed model, the constitutive statement is contained in a differential form of the hardening law so that the flow strength becomes a derived, instead of a primitive, quantity. The paper is organized as follows. In Section C the new work-hardening model is developed. In Section D the framework of mechanism-based discrete dislocation plasticity (M-DDP) is introduced and a methodology for model assessment is presented. Results from dislocation dynamics simulations and model predictions are presented and discussed in Section E, followed by concluding remarks.

C. Work hardening model

The classical hardening model of Kocks and Mecking (Kocks and Mecking, 2003) strictly applies to the bulk behavior of pure materials across a wide range of temperatures and strain rates. It relies on a flow stress equation of the type (5.1) supplemented by a dislocation density evolution equation. Thermal activation enters in (5.1) through A. In the classical theory, the evolution of the dislocation density accounts for dislocation accumulation due to forest interactions and dynamic recovery due to dislocation annihilation and cross-slip. Mechanical behavior of single and polycrystals, which is reflected in well-characterized stages of deformation, can thus be analyzed with the work hardening rate θ derived from the two ingredients above. θ is dominated by its athermal component during stage II, then gradually decreases with increasing stress following remarkable scaling of the Voce type (Estrin and Mecking, 1984). Although phenomenological in nature, this theory has strong

experimental grounding and may be considered as the most complete physical theory of work-hardening.

In extending the theory to the micron scale, attention is mostly focused on the athermal component of the flow stress. A single-parameter relation of the type (5.1) is presumed no longer valid at micron scale resolution where the local dislocation distribution affects the flow stress beyond the zeroth order moment of that distribution, i.e., the density. During stage II, for instance, forest hardening processes, which are dominated by dislocation-dislocation interactions, lead to an evolving dislocation structure and result in the formation of dislocation patterns (Mughrabi, 1983). Approaches based on single-parameter relations such as (5.1) do not account for the effect of the dislocation *substructure* on flow stress and hardening, or perhaps weakly through A. However, in micro-scale specimens the interaction between the characteristic lengths of these patterns and specimen dimensions results in peculiar behavior, not necessarily observed in bulk samples. One way to incorporate such effects is to acknowledge that at some sufficient resolution, the density of geometrically necessary dislocations does not vanish, and to seek its contribution to the flow stress.

At the relevant scale of description, the density of geometrically necessary dislocations can be quantified based on the net Burgers vector $\mathbf{B}$ as

$$\rho_{\mathrm{G}} = \frac{||\mathbf{B}||}{b} \tag{5.2}$$

where $||.||$ refers to the Euclidean norm and b is the material Burgers vector length. Following the formulation in (Cermelli and Gurtin, 2001; Gurtin, 2006), a network of dislocations piercing a plane with unit normal $\mathbf{n}$ has a net Burgers vector $\mathbf{B}$ per unit area given by:

$$\mathbf{B} = \mathbf{Gn} \tag{5.3}$$

where $\mathbf{G}$ is termed the geometric dislocation tensor. In the context of small transformations, $\mathbf{G}$ is simply (minus) the curl of the displacement gradient. In fact, it may be viewed as a measure of lattice incompatibility associated with dislocations (Acharya and Bassani, 2000; Bassani, 2001). In general, for an arbitrary dislocation network, Eqs. (5.2) and (5.3) do not provide a unique description of the GND state and, as elaborated upon in (Arsenlis and Parks, 1999), some minimization procedure would be necessary to define uniquely the GND state at the current point. In anticipation of the validation approach, to be described below based on direct discrete dislocation analyses, we note that under plane strain deformation with only pure edge dislocations as the carriers of plasticity, Eqs. (5.2) and (5.3) suffice to define the GND density ρ_{G}.

Next, the GND density measure defined above is taken to affect the evolving state in two ways (i) it contributes to dislocation density accumulation; (ii) it enhances the rate of hardening. Introducing Γ as a measure of cumulated slip work-conjugate with $\mathcal{T}$, the evolution of the dislocation density is given by:

$$\frac{\mathrm{d}\rho}{\mathrm{d}\Gamma} = k_0 \rho_{\mathrm{G}} + k_1 \sqrt{\rho} - k_2 \rho \tag{5.4}$$

The last two terms in (5.4) correspond to dislocation storage and dynamic recovery, respectively, as in the original model (Mecking and Kocks, 1981; Kocks and Mecking, 2003) with k_1 a constant and k_2 a material-dependent function of strain-rate and temperature. It is the first term in (5.4) that represents the effect of GNDs following a proposal by Acharya and Beaudoin (Acharya and Beaudoin, 2000). Here, k_0 is a non-dimensional constant. It is appropriate to mention that all three phenomena (storage due to a forest, recovery and "geometric" storage) are present from the outset of plastic deformation albeit some might dominate in any given stage of deformation.

The new model differs from recent ones available in the literature through the

hardening law. Models based on the Taylor relation (5.1) invariably lead to a hardening rate that is directly proportional to the dislocation density rate in (5.4) just as in the classical models (Kocks and Mecking, 2003). In other words, according to the models in (Kocks and Mecking, 2003) and (Acharya and Beaudoin, 2000) the only way the flow stress can increase is through an increase in the dislocation density, irrespective of whether the latter is affected by the current GND content. A corollary of what precedes is that if one imagines two neighboring states of the material characterized by the same dislocation density but with different dislocation arrangements then there is not net change in the flow stress between these two states. We postulate that this cannot hold in micron scale specimens. Thus, a scale effect of internal stress on hardening is inherent to our concept. In the proposed model, the net change of the flow stress $\mathrm{d}\mathcal{T}$ at the current state is given by superposition of a bulk hardening component, which in stage II is solely set by forest interactions, and a GND state dependent component. Generically, this statement is contained in writing:

$$\mathrm{d}\mathcal{T} = \Theta^{\infty}(\rho; \dot{\Gamma}, T)\mathrm{d}\Gamma + \Theta_{\mathrm{G}}(\rho_{\mathrm{G}}, \rho)\mathrm{d}\Gamma \tag{5.5}$$

where Θ^{∞} is the hardening rate of the bulk material, and in that regard it may depend on strain rate and temperature T depending on the stage of deformation, and the function Θ_{G} remains to be specified. To that end we begin by observing that, if attention is focused on stage II hardening, then Θ_{G} cannot depend on the GND density alone for it is evident that ρ_{G} is an evolving quantity while the hardening rate is constant. Furthermore, since any length scale that would enter the description should evolve with the state, it would be reasonable to take Θ_{G} dependent upon the dislocation density as well. Yet, determining a suitable function Θ_{G} is not a trivial matter. One plausible choice, which is corroborated by the physical arguments above and inspired by careful analysis of the discrete dislocation calculations of Guruprasad

and Benzerga (Guruprasad and Benzerga, 2008b), consists of writing

$$\Theta \equiv \frac{\mathrm{d}\mathcal{T}}{\mathrm{d}\Gamma} = \Theta^\infty + \delta\mu\frac{\rho_\mathrm{G}}{\rho} \tag{5.6}$$

where μ is the elastic shear modulus as above and δ a non-dimensional constant. It is emphasized that integration of (5.6) following a given strain path ultimately results in a size-dependent flow strength at fixed strain rate and temperature. This can be seen by noticing that the ratio ρ_G/ρ is scale dependent. Alternatively, the $1/\rho$ term may be likened to the square of a length scale, as for example in (Bassani, 2001), except that this length scale is fixed there whereas it evolves here.

It is a fundamental nature of the constitutive structure considered here that the flow stress depends on the path followed in (ρ,ρ_G) space and hence cannot, in general, be expressed as a point function of the variable (ρ,ρ_G). Nevertheless, it is worth illustrating the size-dependence of flow strength that would result in the model. In doing so, we neglect the contribution of the dynamic recovery term. The hardening equation (5.6) is integrated analytically from an initial state with flow stress $\mathcal{T}_i$ and dislocation density ρ_i to a neighboring state with flow stress $\mathcal{T}$ and dislocation density ρ using the dislocation density evolution equation (5.4). The integration is carried out keeping ρ_G fixed during the strain increment. The flow stress is then derived in closed form as

$$\mathcal{T}-\mathcal{T}_i = \frac{2\Theta^\infty}{k_1}(\sqrt{\rho}-\sqrt{\rho_i})+\left(\frac{2\Theta^\infty k_0\rho_\mathrm{G}}{k_1^2} + \frac{2\delta\mu}{k_0}\right)\log\left(\frac{k_1\sqrt{\rho_i} + k_0\rho_\mathrm{G}}{k_1\sqrt{\rho} + k_0\rho_\mathrm{G}}\right)+\frac{2\delta\mu}{k_0}\log\left(\sqrt{\frac{\rho}{\rho_i}}\right) \tag{5.7}$$

The first term in (5.7) is the usual Taylor hardening term. The last two terms reflect the contribution of the GND density to strengthening. This effect is explicit in the second term but implicit (through the parameter δ) in the third term.

D.   Model assessment

In order to assess the proposed extension of the Kocks-Mecking-Estrin model down to the micron scale, recourse to direct discrete dislocation dynamics simulations is appropriate, since many of the assumptions underlying the model are grounded in dislocation theory. The framework of mechanism-based discrete dislocation plasticity (M-DDP) is particularly well-suited for such a task, although the assessment is currently possible only in the athermal limit.

1.   Mechanism-based discrete dislocation plasticity

The framework was developed by Benzerga et al. (Benzerga et al., 2004) and recently used by Guruprasad and Benzerga (Guruprasad and Benzerga, 2008b) in analyses of size-dependent hardening in single crystals subject to compression loading. In M-DDP key dislocation mechanisms are taken into account so that the multi-stage single-crystal hardening response is a natural output of the simulation and not an input as in continuum-based frameworks. The model involves solving boundary value problems arising due to the collective motion of a large number of discrete dislocations in an incremental way. At each time step the dislocation structure, stress and displacements are determined. Assuming small transformations, superposition of the singular infinite-medium dislocation fields and image fields is used to determine the mechanical fields. The image fields correct for the actual boundary conditions. In a two-dimensional idealization, edge dislocations are considered under assumed plane strain conditions. The glide motion of dislocation i is determined by the Peach-Koehler force, f^i, given by

$$f^i = \mathbf{m}^i \cdot \left(\hat{\boldsymbol{\sigma}} + \sum_{j \neq i} \boldsymbol{\sigma}^j \right) \cdot \mathbf{b}^i \tag{5.8}$$

where $\mathbf{m}^i$ is the slip plane normal and $\mathbf{b}^i$ the Burgers vector having magnitude $|\mathbf{b^i}| = b$.

Initially, a random distribution of Frank-Read type point sources and point obstacles is generated on prescribed slip planes. Under load, a dislocation dipole is nucleated from a source when the local resolved shear stress exceeds a source-dependent critical value, τ_{0n}, during a critical time t_{0n}. Glide dislocations may get pinned at obstacles and released if the local stress exceeds the obstacle strength τ_{obs}. Dislocations may escape at free surfaces and co-planar dislocations of opposite sign may annihilate if they fall within a critical distance L_e from each other. The above-mentioned rules were developed in (Van der Giessen and Needleman, 1995) based on an early work of Kubin et al. (Kubin et al., 1992). These rules are supplemented by so-called "2.5D" constitutive rules that incorporate some 3D dislocation interactions (Benzerga et al., 2004). These include dynamic junction formation and destruction, production of dynamic sources of the Frank–Read kind and line tension. Line tension is explicitly considered in the formulation to account for the energy associated with the expansion of dislocation loops. Dislocation motion is prescribed through the viscous drag relationship:

$$Bv^i = (\tau^i + \mathcal{L}^i)b^i \tag{5.9}$$

with B the drag factor, v^i the glide velocity of dislocation i, $\tau^i = f^i/b^i$ and $\mathcal{L}^i$ the line tension. A junction is taken to form when two dislocations gliding in intersecting slip planes fall within a critical distance, d^*, from each other. A junction thus formed can either act as an obstacle or an anchoring point and this is considered to be a statistical event. The probability that a junction forms an anchoring point has a prescribed value, p. A breaking strength is specified as $\tau_{brk}^I = \beta\mu b/\mathcal{S}^I$ for junction I, with β a constant and $\mathcal{S}^I$ a nearest-junction spacing. Multiplication from dynamic sources is taken to occur for a critical stress having the same form, $\mathcal{S}^I$ being now

the spacing between anchoring points, and which has to be exceeded during a critical time $t_{\mathrm{nuc}}^I = \gamma \mathcal{S}^I / |\tau^I| b$ with γ a constant. Details may be found in Ref. (Benzerga et al., 2004).

The methodology developed in (Guruprasad and Benzerga, 2008b) to quantify the emergence of geometrically necessary dislocations (GNDs) has been implemented to monitor the evolution of the GND density during the simulations. Based on characterizations of the GND state presented in (Acharya and Bassani, 2000; Cermelli and Gurtin, 2001; Arsenlis et al., 2004), Guruprasad and Benzerga (Guruprasad and Benzerga, 2008b) arrived at the following formula giving the GND density over any sub-domain ω of the body Ω of interest:

$$\rho_{\mathrm{G}}(\omega) = \sqrt{\left[\sum_\kappa (\rho_+^{(\kappa)} - \rho_-^{(\kappa)}) \cos \varphi^{(\kappa)}\right]^2 + \left[\sum_\kappa (\rho_+^{(\kappa)} - \rho_-^{(\kappa)}) \sin \varphi^{(\kappa)}\right]^2} \qquad (5.10)$$

where $\varphi^{(\kappa)}$ is the angle that defines the slip direction on slip-system κ with respect to the loading axis, $\rho_+^{(\kappa)}$ and $\rho_-^{(\kappa)}$ are, respectively, the positive and negative dislocation density on slip-system κ within ω. When body Ω is subjected to macroscopically homogeneous deformation such as compression, the GND density ρ_{G} vanishes if determined within the whole volume of the body, i.e., $\rho_{\mathrm{G}}(\Omega) \approx 0$, where the approximate character of the statement is due to statistical effects associated with dislocation escape at free surfaces. Locally, however, there exist sub-domains ω (containing many dislocations) over which the GND density ρ_{G} does not vanish. Evidence for this is taken from the analyses of Guruprasad and Benzerga (Guruprasad and Benzerga, 2008b) who discussed the evolving GND state in relation with plasticity size effects.

2.   Setup of M-DDP simulations

All the calculations were carried out assuming small strains and rotations for a planar crystal having dimensions $L \times H$, subject to plane strain uniaxial compression. The planar crystal was loaded such that there were two slip systems oriented at $\pm 35.25°$ from the loading axis. The specimen height, H, was varied within the range 0.2–12.8 μm and the aspect ratio was $L/H = 3$ for all specimens. Material properties representative of aluminum were used with $\nu = 0.3$, $\mu = 26$ GPa, $b = 0.25$ nm and $B = 10^{-4}$ Pa s. The values of the parameters entering the "2.5D" constitutive rules were $d^* = 6b$, $p = 0.05$, $\beta_{\mathrm{brk}} = \beta_{\mathrm{nuc}} = 1$, $\gamma = 0.1B$ and $\alpha = 0$. The annihilation distance was taken to be equal to the critical distance for junction formation $L_e = d^* = 1.5$ nm. Initial dislocation sources were randomly generated on prescribed slip planes with density 1.5×10^{14} m^{-2}. Their strengths were generated from a Gaussian distribution with mean value $\bar{\tau}_{0\mathrm{n}} = 50$ MPa and standard deviation 10 MPa. The critical nucleation time was $t_{0n} = 10$ ns for all sources. Also, initial obstacles were randomly generated with density 6×10^{14} m^{-2} and strength $\tau_{\mathrm{obs}} = 150$ MPa. A displacement rate was imposed at one end of the specimen and scaled with specimen length so that the applied strain rate $\dot{\varepsilon} = -\dot{U}/L = 6.66 \times 10^4$ s^{-1} was kept the same for all specimens, irrespective of their size. A fixed time step of 0.5 ns was used.

3.   Method of assessment

Ideally, it is at the scale of a non-vanishing GND density that one would seek validation of the hardening model of Section C. This, however, presents some difficulties in terms of defining local measures of flow stress and cumulated slip in the M-DDP calculations. In what follows, a global assessment of the model is proposed instead. To account for the effect of locally non-vanishing GND densities an *effective GND*

density is defined over the entire domain Ω as:

$$\bar{\rho}_{\mathrm{G}} = \sum_{n=1}^{p} \frac{\Omega^n}{\Omega} \rho_{\mathrm{G}}(\Omega^n). \tag{5.11}$$

Here, Ω^n is the n-th element of a uniform grid defined over Ω, p is the total number of grid elements and $\rho_{\mathrm{G}}(\Omega^n)$ is the GND density within Ω^n, calculated from (5.10). The effective GND measure (5.11) is evaluated at each time increment in the discrete dislocation calculations.

Similarly, an effective flow stress and effective cumulated slip are defined based on the computed uniaxial response in compression. Under displacement controlled loading, the net axial stress and strain are computed as:

$$\sigma = -\frac{1}{H} \int_{-H/2}^{H/2} \sigma_{11}(\pm L/2, x_2)\mathrm{d}x_2; \quad \varepsilon = -\frac{U}{L} \tag{5.12}$$

σ and ε are the only non-zero macroscopic stress and strain components, respectively. The effective flow stress and cumulated slip are thus defined as:

$$\bar{\mathcal{T}} = f_{\mathrm{S}}\sigma; \quad \bar{\Gamma} = \left(\varepsilon - \frac{\sigma}{\bar{E}}\right)/f_{\mathrm{S}} \tag{5.13}$$

where $f_{\mathrm{S}} = 0.47$ is the Schmid factor and $\bar{E}$ is the plane strain elastic modulus.

In what follows, when predictions of the work-hardening model of Section C are plotted against the M-DDP results, one should bear in mind that it is the effective quantities that are displayed for the latter. For clarity, the bars will be dropped from the flow stress and cumulated slip notations, but not from the effective GND density to avoid confusion. In a sense, the method of assessment is similar to what is usually done to identify isotropic hardening models in conventional plasticity models based on data from uniaxial testing.

E.   Results

Representative flow stress versus cumulated plastic strain responses are shown in Fig. 51a for specimens with height $H = 0.2$ μm, 0.8 μm, 3.2 μm and 12.8 μm. The results clearly show that the overall hardening behavior is affected by specimen dimensions within the size range investigated. The corresponding evolution of the dislocation density with Γ is depicted in Fig. 51b. Although there is some variation of the total dislocation density with specimen size, this variation does not provide a consistent explanation of the size-dependence of work-hardening, Fig. 51a. The results reported here are consistent with those in (Guruprasad and Benzerga, 2008b). The reader is referred to (Guruprasad and Benzerga, 2008b) for details in analyzing the M-DDP results in terms of size effects on the 0.2% yield strength, stage I and stage II characteristics, flow stress scaling and its evolution with strain, emergence of local GND densities along with an in-depth analysis of resolution effects on the latter.

The evolution of the effective GND density is shown in Fig. 51c. The selected curves correspond to the stress–strain responses of Fig. 51a. $\bar{\rho}_G$ is computed using (5.11) and a grid of horizontal strips of length L and height $h = 50$nm, irrespective of specimen size. In order to check the dependence of the results upon grid resolution and definition, other grids were used, including a grid of square elements of side length $h = 50$nm. As discussed in (Guruprasad and Benzerga, 2008b), the results are expectedly resolution-dependent but the general trends remain the same. In particular, for given grid resolution and topology $\bar{\rho}_G$ is found to increase at a faster rate in smaller specimens, just as depicted in Fig. 51c. The value of $\bar{\rho}_G$ is found to be as large as 40% of the total dislocation density in the $H = 0.2$ μm specimen while in the $H = 12.8$ μm specimen it is found to be less than 2%. This build-up of effective

(a)

(b)

(c)
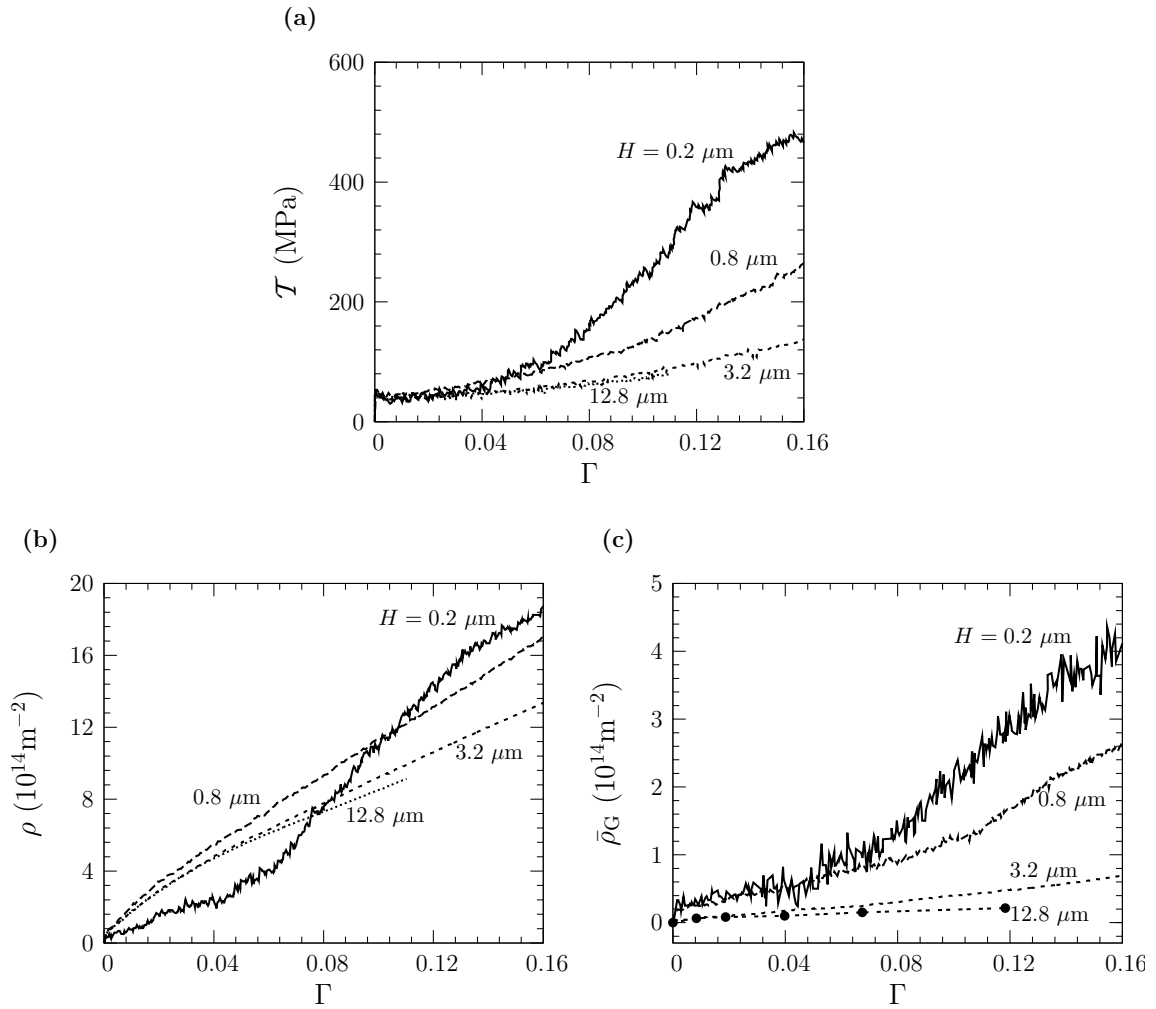
Fig. 51. Discrete dislocation dynamics results: (a) Representative curves of flow stress, $\mathcal{T}$, versus cumulated plastic strain, Γ, in compression of specimens with height $H = 0.2$ μm, 0.8 μm, 3.2 μm and 12.8 μm. (b) Evolution of the dislocation density, ρ, with Γ for the same specimens. (c) Corresponding evolution of the effective GND density, $\bar{\rho}_{\mathrm{G}}$, with Γ. See additional material in Appendix A.

GND density ($\bar{\rho}_{\mathrm{G}}$) takes place while there is essentially no net accumulation of GND density (ρ_{G}) in the specimens. The fact that $\rho_{\mathrm{G}} \approx 0$ is in keeping with the state of macroscopically homogeneous deformation in uniaxial compression[1].

It is interesting that mere reduction in specimen dimensions leads to faster accumulation of effective GND density. It is even more so without imposition of any gradients in the macroscopic fields. Analysis of the results indicates that two factors contribute to this rather curious phenomenon. First, the smaller the specimen the shorter the distance from active sources to free surfaces, so that dislocation escape is more likely to occur. This reflects a *statistical* contribution to the geometric density. However, this is not the dominant factor. The main contribution comes from microstructure evolution and how the latter is affected by specimen dimensions. One key aspect of mechanism-based DDP, in comparison with strictly 2D models, is the complex evolution of the dislocation structure as plastic deformation proceeds. As described in (Benzerga et al., 2004) and (Guruprasad and Benzerga, 2008b), specific dislocation patterns develop naturally in the simulations, as dictated by the fundamental constitutive rules. Although these are meant to represent dislocation interactions at short range, the net result is the development of a highly heterogeneous slip pattern with associated internal stresses that have a much longer range than would be predicted without enhanced rules for short-range interactions. The dislocation patterns that form subsequently may be characterized by an evolving spectrum of internal length scales. For the sake of discussing the results, it suffices to think of one dominant internal length scale, which characterizes the deformation process and which, of course, evolves with it. It is the interaction of this internal length scale with specimen dimensions that leads to the size-dependence of the structural measure that

---

[1]Exceptionally, two realizations of the $H = 0.2~\mu$m specimen had ρ_{G} greater than 20% of the total density.

is $\bar{\rho}_\mathrm{G}$, as shown in Fig. 51c.

Since the evolution of the dislocation structure is not independent of kinematic constraints, it is natural to expect that more effective accumulation of GND density in smaller samples be also accompanied by more visible disturbances in lattice rotation fields. In Fig. 52 contours of the in-plane lattice rotation θ are shown which correspond to the same realizations discussed so far. The lattice rotation maps are acquired at the same overall strain of $\varepsilon = 0.06$. Let us bear in mind that edge effects are negligible and that the overall hardening response is mostly affected by what happens in the central regions of the specimens where dislocation intersections occur more effectively. In the $H = 12.8\ \mu$m specimen the wavelength associated with fluctuations in θ within the central region is much smaller than the specimen height H. In addition, the magnitude of the lattice rotation is rather weak. On the other hand, in the central region of the $H = 0.2\ \mu$m specimen, the wavelength of the lattice rotation field is comparable with H and its magnitude is much stronger (larger than 3°). These observations corroborate our statement above that the size-dependence of the GND density is rooted in the evolving dislocation structure and highlight the correlation between the length scales characterizing the current structure and the gradients of local fields such as lattice rotations.

Most notable in the mechanical response of the crystals shown in Fig. 51a is the effect of specimen size on the hardening rate in stage II, Θ_II. This effect is quantified in Fig. 53, where new results are superposed onto those of Ref. (Guruprasad and Benzerga, 2008b). Each datum point correspond to one M-DDP calculation. Each value reported for Θ is obtained by numerical differentiation of the effective flow stress with respect to the effective cumulated slip, as explained in (Benzerga et al., 2004). For reference, the $\mu/200$ to $\mu/100$ range of work-hardening rates for bulk materials, i.e., the Θ^∞ of Eq. (5.6), is depicted by two horizontal lines. Hence, the calculated

(a)

0.2μm

(b)

0.8μm

(c)

3.2μm

(d)

12.8μm

θ (deg)

-3 -2.5 -2 -1.5 -1 -0.5 0 0.5 1 1.5 2 2.5 3
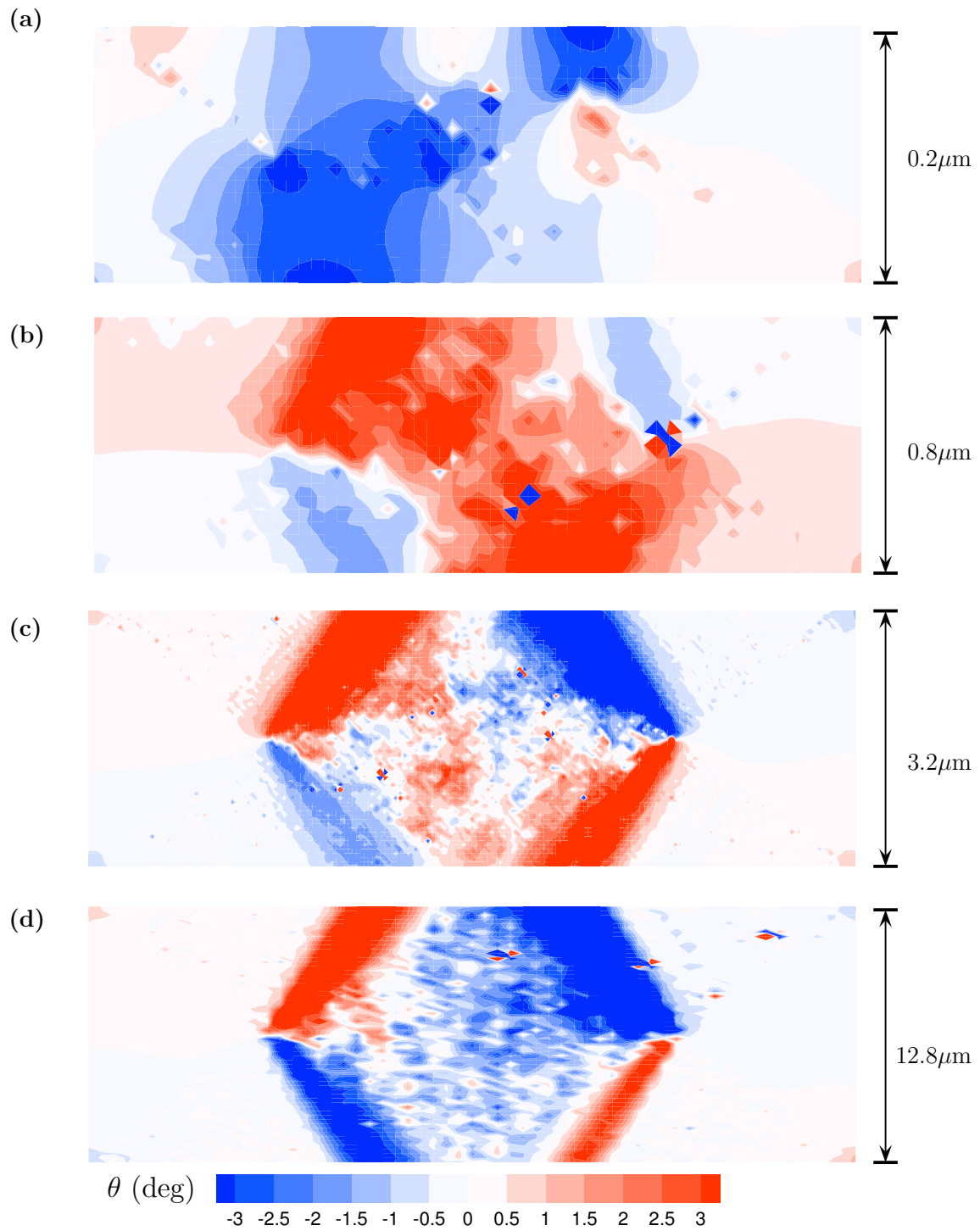
Fig. 52. Contours of lattice rotation, θ, at a strain of $\varepsilon = 0.06$ for single crystal specimens with height (a) $H = 0.2$ μm; (b) $H = 0.8$ μm; (c) $H = 3.2$ μm; and (d) $H = 12.8$ μm.

value of Θ_{II} for the smallest specimen ($H = 0.2~\mu$m), averaged over all realizations, is about 20 times larger than the bulk value. By way of contrast, in the largest specimen analyzed ($H = 12.8~\mu$m), the value of Θ_{II} is less than twice the bulk value. Also reported in Fig. 53 is a large set of experimental data on copper taken from (Suzuki et al., 1956). To the best of our knowledge, Suzuki et al. have carried out the most thorough investigation of size effects on work hardening in single crystals down to specimen diameters of 100μm. The overwhelming majority of their data points fall within the range of bulk values with a clear trend for increasing scatter with decreasing specimen size. It is particularly encouraging that some of the measured values of Θ_{II} in specimens with diameters smaller than, say 500μm are approximately equal to those predicted by the M-DDP calculations for the $H = 12.8~\mu$m specimens.
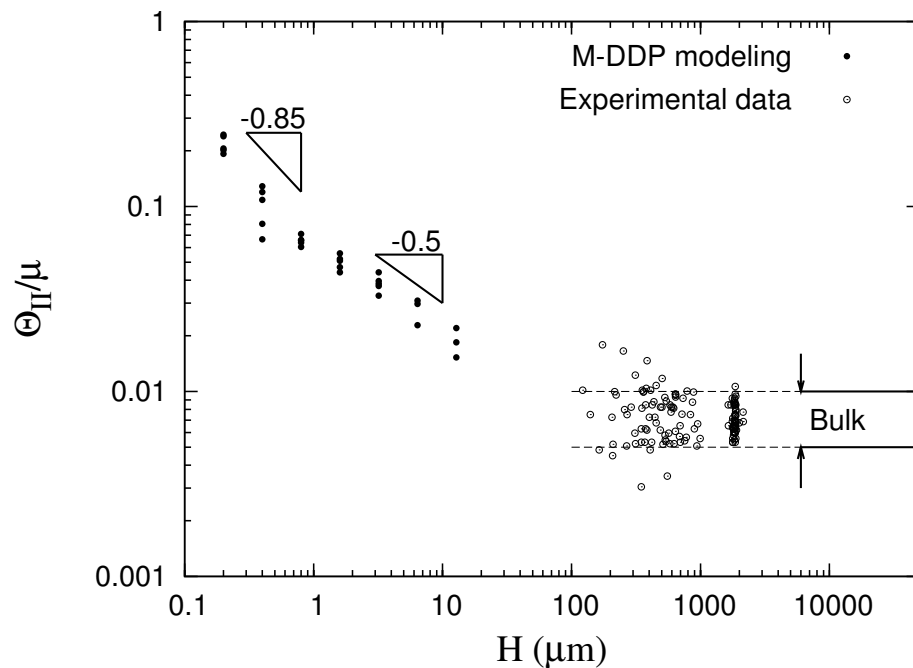
Fig. 53. Stage II hardening rate, Θ_{II}, in units of shear modulus, μ, versus specimen height, H. Experimental data is taken from Suzuki et al. (1956).

It is worth noting that the effect of size on Θ_{II} is enhanced for values of H in the sub-micron regime. Thus, if a power law scaling of the type $\Theta_{\mathrm{II}}/\mu = (H/H_0)^x$ is sought with H_0 a reference length, then the best fit is obtained with a scaling exponent $x = -0.85$ for $H \le 1\mu$m and $x = -0.5$ for $H > 1\mu$m. This is depicted by the two scaling regimes in Fig. 53. Also, it can be observed that with decrease in specimen size there is an increase in the scatter of the Θ_{II} values (recall that a log scale is used in Fig. 53). However, trends based on average values are all consistent with the above.
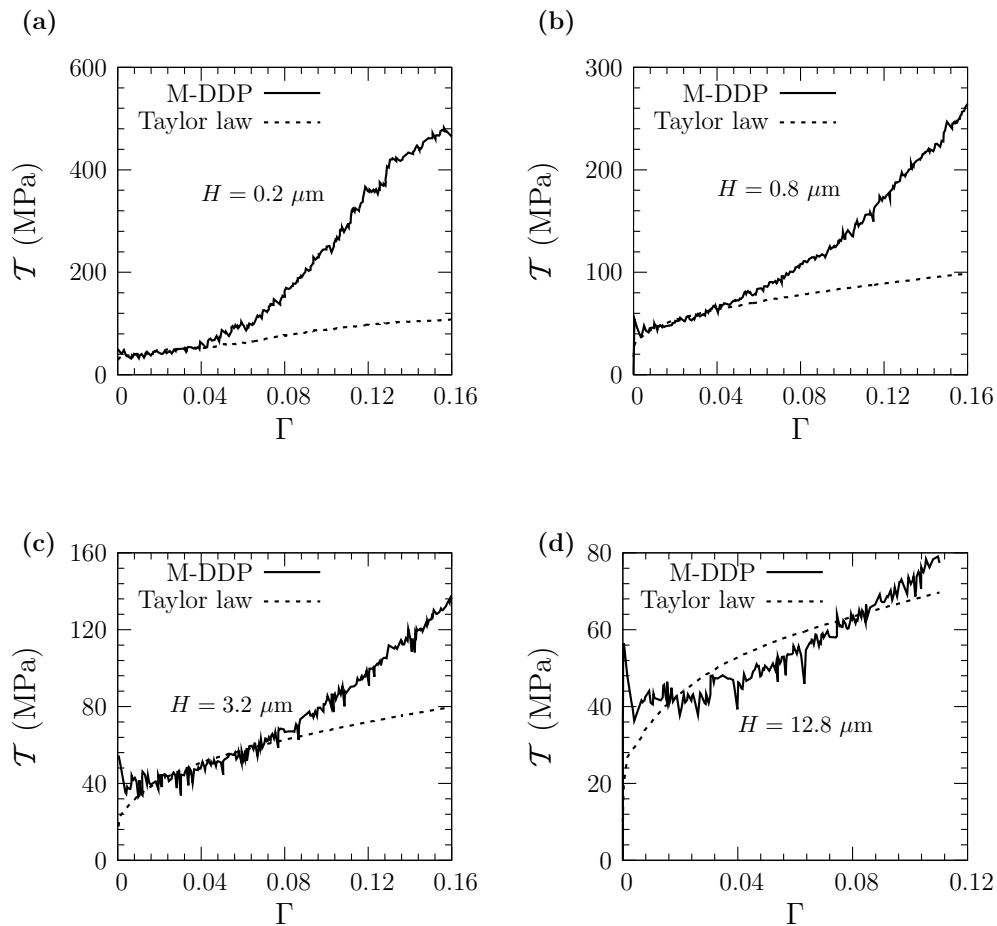
Fig. 54. M-DDP results versus Taylor hardening predictions for the flow stress in specimens with: (a) $H = 0.2 \ \mu$m; (b) $H = 0.8 \ \mu$m; (c) $H = 3.2 \ \mu$m; and (d) $H = 12.8 \ \mu$m. The value of the constant in (5.1) is $A = 0.3$.
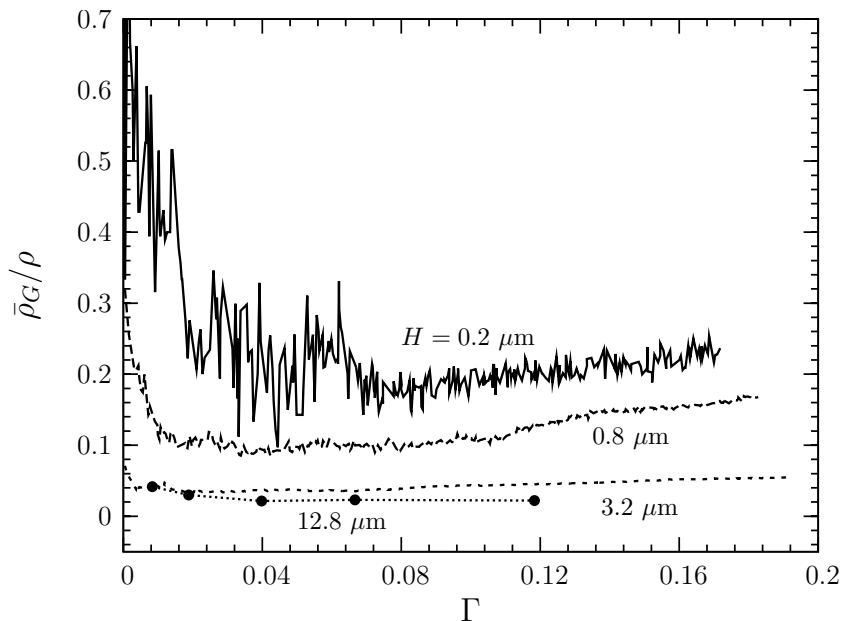
Fig. 55. Evolution of the effective GND density, $\bar{\rho}_G$, normalized by the total dislocation density, ρ, with deformation for specimens with height $H = 0.2$ μm, 0.8 μm, 3.2 μm and 12.8 μm. See additional material in Appendix A.

Before we proceed to assessment of the work-hardening model, it is worthy to establish, for the record, the inability of the Bailey-Hirsch or Taylor relationship (5.1) to capture the size-dependence of the flow stress, that is even when evolution of dislocation density is taken from the dislocation dynamics results[2]. M-DDP results and Taylor hardening predictions are compared in Fig. 54 for selected calculations corresponding to $H = 0.2$ μm, 0.8 μm, 3.2 μm and 12.8 μm. The reference values, $\mathcal{T}_0$ and ρ_0, were taken to correspond to $\mathcal{T}$ and ρ from the M-DDP calculation at $\Gamma = 0.03$, a strain level beyond which stage II hardening is found to be dominant. Also, the value of the constant A in (5.1) was taken to be 0.3 in all cases. Comparison between M-DDP results and Taylor hardening predictions clearly demonstrates that there ini-

---

[2]It is evident that if the dislocation density is obtained by integration of (5.4) with $k_0 = 0$, as in the original KME model, then the Taylor equation would simply lead to a size-independent response.

tially is a deformation regime where the Taylor hardening law gives a reasonable prediction of the flow stress. However, a deviation from this behavior takes place for all specimens after sufficient straining. The smaller the specimen the larger the deviation of the Taylor prediction; see e.g. Fig. 54a. Note that the trends are consistent with the expectation that equation (5.1) would work well for bulk specimens. Indeed, a good prediction is obtained for the 12.8 μm specimen throughout the deformation (Fig. 54d). It is worth emphasizing that it is the value of ρ computed from DD that is used to assess equation (5.1). This was done to minimize the effect of differences between model and DD simulations in terms of predicted dislocation density evolution. The discrepancy between the KME model predictions and DD results would be greater than shown in Fig. 54 if one strictly integrates (5.4), holding $k_0 = 0$, since the response predicted by the KME model is size-independent. Therefore, the results of Fig. 54 are taken as evidence that, at the micron scale, a model of the flow stress based on the total dislocation density as the only state variable is not enough, even under macroscopically homogeneous deformation such as the uniaxial compression loading considered here. Furthermore, an amendment of the KME model that is simply based on the proposal (5.4) as an evolution law for the dislocation density would not suffice. This is so because the additional hardening that would result from (5.4) in view of (5.1) scales as $\rho_{\mathrm{G}}/\sqrt{\rho}$, a quantity that is found to increase significantly with continuing deformation, according to the DD simulations.

A key observation inferred from the discrete dislocation simulations relates to the evolution of the dislocation structure. Although the total dislocation density and the effective GND density both increase with strain (Fig. 51), their ratio $\bar{\rho}_{\mathrm{G}}/\rho$ remains nearly constant with strain. This is illustrated in Fig. 55 for the same specimen sizes and realizations discussed thus far. In addition, it is clear from the figure that the ratio $\bar{\rho}_{\mathrm{G}}/\rho$ increases with decreasing specimen size. Both observations from the M-DDP

results, i.e., the constance of $\bar{\rho}_G/\rho$ with plastic strain and its size-dependence, provide strong support to the format of equation (5.6) giving the instantaneous hardening rate, a key ingredient of the model.

In what follows, we identify the material constants δ, k_0, k_1 and k_2 appearing in (5.6) and (5.4) based on DD results corresponding to the $H = 3.2$ μm specimen. Subsequently, we compare model predictions with DD results for all realizations of the other specimens. To that end, the coupled non-linear differential equations (5.6) and (5.4) are integrated using a forward scheme from an initial state (ρ_0, ρ_{G0}, τ_0) and using, at each incremental step, the value of ρ_G calculated from DD. Such a procedure would qualify the physical hardening model leaving the prediction of ρ_G to appropriate kinematical treatments (Acharya and Beaudoin, 2000; Evers et al., 2002). The choice of the sample set with $H = 3.2$ μm for parameter identification is rationalized as follows: (i) the values of $\bar{\rho}_G$ computed from DD are large enough to identify k_0 in (5.4) and δ in (5.6) with a good confidence interval; (ii) the scatter in both $\bar{\rho}_G$ and $\mathcal{T}$ is small. Using this approach, the constant $\delta = 0.48$ in (5.6) was obtained using a least-square fit to M-DDP data plotted in terms of $\mathrm{d}\mathcal{T}/\mathrm{d}\Gamma$ versus strain for all five realizations of the $H = 3.2$ μm specimen. In doing so, an estimate of Θ^∞ was taken to be 260 MPa, which is the value of the athermal hardening rate of a bulk specimen. Next, the constants k_0, k_1 and k_2 in (5.4) were determined using the same realizations for $H = 3.2$ μm based on numerical evaluation of the rates $\mathrm{d}\rho/\mathrm{d}\Gamma$. The best fit in an ensemble average sense was obtained using $k_0 = 22.8$, $k_1 = 516.9$ μm^{-1} and $k_2 = 10.0$.

With the model coefficients thus determined, Fig. 56 shows the comparison, in terms of dislocation density versus strain, between model predictions and M-DDP results. In Fig. 56a the good correspondence obtained for $H = 3.2$ μm simply validates the calibration of material constants k_0, k_1 and k_2; the predictions for the $H = 0.8$ μm

and 12.8 μm specimens are very good. In addition, the model is capable of capturing the scatter associated with different realizations for a given specimen size as shown in Fig. 56b for $H = 0.2$ μm. We emphasize that the origin of scatter in model predictions is not inherent. It is the consequence of using DD results to infer the values of $\bar{\rho}_G$ for use in (5.4) and (5.6) at the current integration step. However, the results of Fig. 56 show that the scatter in ρ is mostly effected by GND density build-up. This provides further support to the format of Eq. (5.4).

(a)   (b)
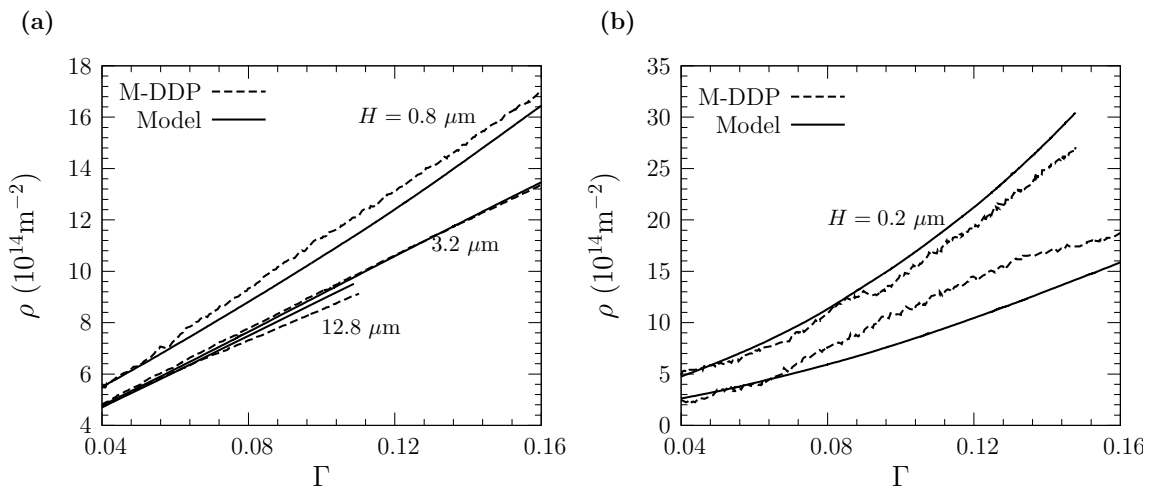
Fig. 56. M-DDP results versus model predictions for the dislocation density in speci-
mens with: (a) $H = 0.8$ μm and $H = 12.8$ μm (M-DDP data for 3.2 μm was
used for calibration; see text); (b) $H = 0.2$ μm (two realizations).

The model prediction for the flow stress is illustrated in Fig. 57 for two different realizations of the specimens with $H = 0.2$ μm, 0.8 μm and 3.2 μm, and for one realization each for the $H = 6.4$ μm and 12.8 μm specimens. The comparison is restricted to the range $\Gamma = 0.04$–0.16 to avoid the transient behavior at smaller plastic strains. For a given specimen the values of the reference parameters $\mathcal{T}_0$ and ρ_0 are the values corresponding to $\mathcal{T}$ and ρ at $\Gamma = 0.04$ from the M-DDP simulations.

The results in Fig. 57 show that the model picks up very well the size-dependence of the flow stress and reasonably well the scatter observed for smaller specimens.

F. Concluding remarks

In this paper, a model of size-dependent work-hardening in crystal plasticity has been developed. The model is phenomenological in nature but has good physical grounding. It is an extension of the well received Kocks–Mecking–Estrin model to the micron scale. The treatment is based on two state variables: the total dislocation density and the GND density, Eq. (5.2). The main novelty resides in a relatively simple kinetic equation at fixed structure parameters, Eq. (5.6). The new equation specifies the hardening law in differential form and was developed based on careful analysis of discrete dislocation dynamics results, where the GND density was monitored continuously using Eq. (5.10). The evolution of structure is specified explicitly for the dislocation density, the rate of which is affected by the GND density through Eq. (5.4). On the other hand, since the GND density is kinematically determined no explicit evolution equation is specified for it. Thus, the physical hardening model must be supplemented by a mechanical model containing a statement about the GND state. Frameworks capable of such characterization are available in the literature (Acharya and Bassani, 2000; Evers et al., 2002; Acharya, 2004; Gurtin, 2006).

Critical insight was gained from discrete dislocation dynamics simulations in the course of model development. In addition, a subset of the simulations was used to calibrate the model parameters. Thus, taking the DD results as reference naturally raises the question of how reliable the simulation predictions are. While the observed trends warrant verification from fully 3D simulations, there is no reason why the fundamental trends would be mere artifact of idealizations inherent to the "2.5D"
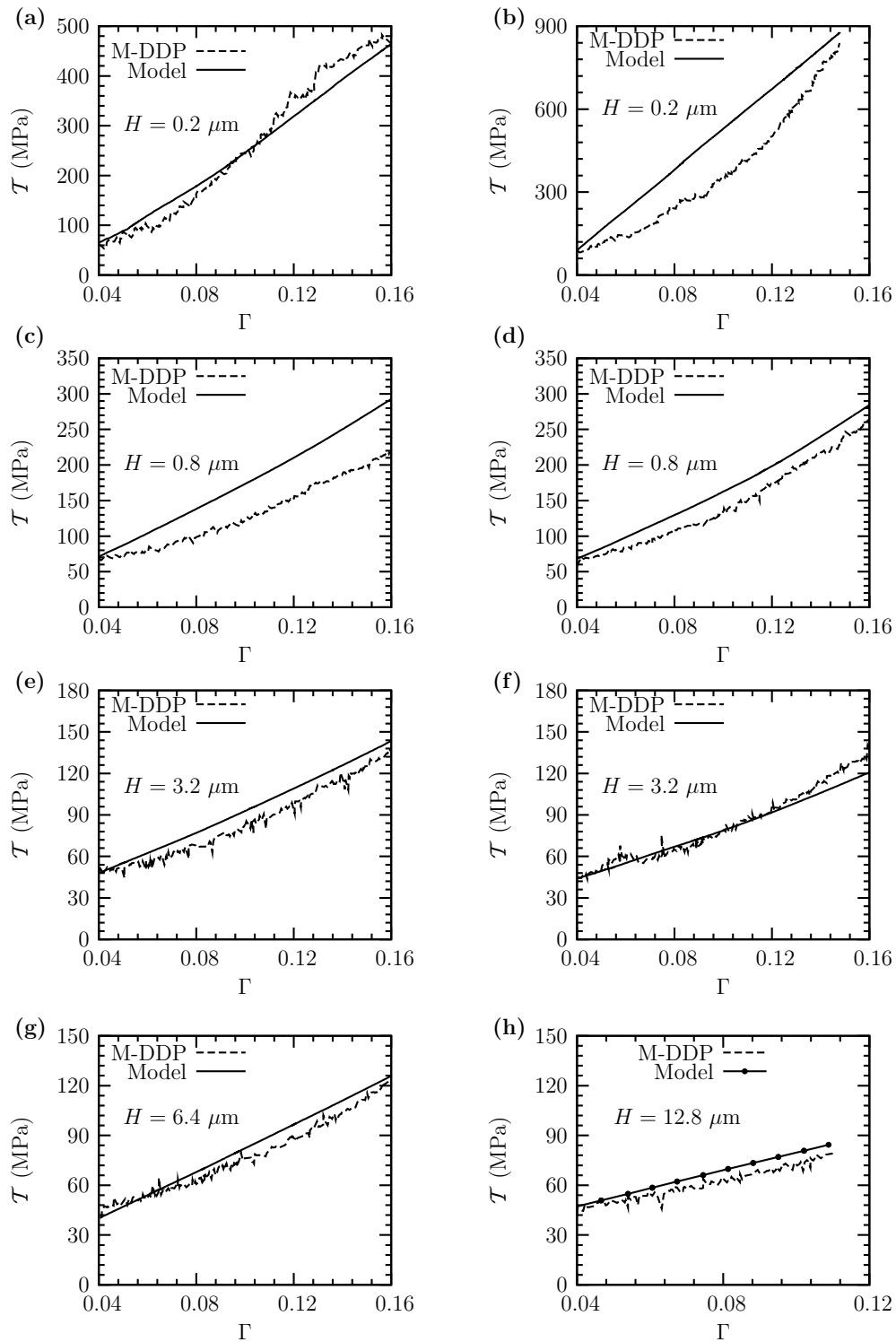
Fig. 57. M-DDP results versus model predictions for the size-dependent flow stress in specimens with: ((a),(b)) $H = 0.2$ μm; ((c),(d)) $H = 0.8$ μm; ((e),(f)) $H = 3.2$ μm; (g) $H = 6.4$ μm; and (h) and $H = 12.8$ μm. For $H \geq 3.2$ μm scatter in simulated stress–strain responses is insignificant.

model. The constitutive rules used to describe short-range dislocation interactions contain a level of idealization, just like in any other model. In particular, their specific formulation is debatable. However, one must observe that the rules were formulated at the fundamental level of individual dislocations, and the same rules were applied to all crystals, irrespective of their dimensions. Within the "2.5D" paradigm of M-DDP, the size-dependent response comes out as the manifestation of collective dislocation behavior.

The proposed model addresses the physical aspects of work-hardening at the micron scale. Its implementation to solve boundary-value problems would require, however, an additional statement for a flow rule, which is expected to affect the GND density, albeit indirectly. Granted that the discrete dislocation calculations do reveal a fundamental fact about work-hardening, the new model possesses the capability of predicting size-dependency of work-hardening when the GND density is fully specified. Further fundamental understanding of work-hardening at the micron scale would require experimental work targeted at GND density measurements. Very recent experiments indicate qualitative support to both M-DDP and model predictions (Frick et al., 2008). Finally, we observe that for work hardening to take place in crystalline specimens with sub-micron dimensions, initial dislocation densities of the order of 10^{13} m^{-2} or higher must be present. For densities lower than say 10^{12} m^{-2}, other types of disturbance to plastic flow would occur (Benzerga and Shaver, 2006; Benzerga, 2008; El-Awady et al., 2008; Benzerga, 2009). This sets implicit limits of validity for the proposed model.

CHAPTER VI

GRAIN SIZE EFFECT IN POLYCRYSTALS: A DISCRETE DISLOCATION
DYNAMICS ANALYSIS

A. Introduction

Microcrystalline (MC), ultra-fine grain (UFG) and nanocrystalline (NC) materials
have been the focus of widespread research over the past couple of decades owing to
their superior mechanical properties as compared to coarse-grained materials (Gleiter,
1989; Dao et al., 2007). Refinement of grain size from coarse-grained materials has
resulted in an increase in material yield strength, superior wear resistance, enhanced
plastic formability at low temperatures etc., among other improvements (Kumar et al.,
2003). However, these improved mechanical properties come at the cost of a reduction
in ductility and toughness. Efforts are on to understand the governing mechanisms
underlying mechanical properties of these materials with the aim to arrive at an op-
timal set of mechanical properties with a balance between strength, ductility and
toughness (Koch, 2003). However, this task to connect the underlying material mi-
crostructure to its macroscopic property continues to be a challenge in the field of
mechanics as well as materials science.

Hall (1951) and Petch (1953) noted that the yield strength in polycrystals is
inversely proportional to the square-root of grain size. The phenomenon of increase in
polycrystal strength with decrease in size is known as the Hall-Petch effect. Following
this discovery, there has been a number of experimental studies probing the strength of
polycrystals for a range of grain sizes all the way down to 10 nm and below (Meyers
et al., 2006). It is now established that strengthening in polycrystals is sustained
with refinement of grain size down to 10 nm; below this grain size some studies have

reported an inverse Hall-Petch effect (Chokshi et al., 1989; Meyers et al., 2006; Dao et al., 2007).

Classically, following the work by Eshelby et al. (1951) and Hirth and Lothe (1968), Hall-Petch effect is attributed to the scaling of dislocation pile-ups at the grain boundaries with grain size. Pile-ups at grain boundaries leads to build up of backstress at dislocation sources and hence require an increase in stress resolved along its slip plane to nucleate dislocations. Explanations based on the correlation between flow stress and dislocation density coupled with the mean free path of dislocation motion was also used to explain the Hall-Petch effect Embury (1971). Hirth (1972) proposed a model where the grain was assumed to have a composite microstructure with a hard grain boundary region and an interior core. It was shown that depending on the area occupied by the hard grain boundary region the yield stress in polycrystal can vary as $d^{-1/2}$ or d^{-1}. Though these analytical models provide information about the possible governing mechanisms leading to grain size effects in polycrystals they are, however, based on analysis of a single grain and do not predict the ensemble behavior of dislocations on multiple grains.

Recently there have been a number of investigations based on discrete dislocation dynamics framework and molecular dynamics which have attempted to provide insight into the effect of grain size on polycrystal mechanical behavior. Grain size effects on strength in NC materials have been explored using molecular dynamics simulations. Molecular dynamics simulations predicted a Hall-Petch like behavior in NC materials with grain size in the range of 30 nm - 10nm (Van Swygenhoven and Spaczer, 1999). Below 10 nm experiments have predicted an inverse Hall-Petch like behavior (Dao et al., 2007). These observations were also made by recent molecular dynamics simulations (Yamakov et al., 2004; Wolf et al., 2005). Their simulations suggested a cross-over between a dislocation dominated deformation process to grain

boundary mediated process with decrease in grain size. Based on these observations they have developed stress-grain size deformation mechanisms maps (Yamakov et al., 2004). Simulations have also described the role of diffusion creep on inverse Hall-Petch effect (Desai et al., 2008). Molecular dynamics simulations are useful to predict and probe mechanisms for predicting grain size effects below 10 nm. Current computational power limit their analysis for a wide range of grain sizes varying from micrometers to a few nanometers. They are severely restricted by time scale limitations, which prevent them from exploring large strain deformation mechanisms.

Discrete dislocation dynamics (DDD) offers a promising alternative to investigate mechanical behavior of polycrystals over a range of grain sizes varying from a few micrometers to few nanometers. In DDD framework dislocation nucleation, dislocation glide, dislocation-dislocation interactions and their interaction with grain boundaries are naturally accounted for. Biner and Morris (Biner and Morris, 2002, 2003) have studied the evolution of flow stress for grain sizes ranging from 16 to 2 μm under shear deformation. They noticed that at small strain values the flow stress scaled as $d^{-1/2}$, where d is the grain size. However, with increasing deformation and an expanding region of dislocation pile-ups inside the grain the flow stress scaling was close to d^{-1}. Lefebvre et al. (2007) explored the region below 2 μm upto 500 nm using 2D DDD enhanced with additional rules to account for junction formation. Their simulations predicted Hall-Petch effect in their with the flow stress scaling as $d^{-1/2}$. In their simulations the rate of increase of dislocation density was found to scale with the inverse of the grain size leading to the strengthening of the crystals. Grain sizes below 500 nm were explored in the 2D DDD simulations of Balint et al. (2008). They observed that the strengthening in crystals was due to blocking of slip transmission between grains. Attempt has been made to allow for dislocations to glide across the grain boundaries by Li et al. (2009). 2D DDD polycrystal frameworks have also been

used to address problems on thin films where coupled grain size and film thickness effects prevail (Nicola et al., 2006; Kumar et al., 2009).

Except for the 2D DDD framework by Lefebvre et al. (2007) none of the other 2D DDD models accounted for short-range dislocation interactions like junction formation. A 2D DDD framework which accounts for key short-range dislocation interactions should be able to capture features of coarse grain size polycrystal. Subsequently, a gradual reduction in grain size should naturally be able to capture microstructural changes within grains due to constrains offered by grain boundaries.

In this work, we enhance the 2D DDD framework developed by Balint et al. (2008) by incorporating additional rules to account for dislocation expansion, junction formation, junction stabilization and nucleation of sources from stable junctions which act as anchoring points. The effect of these additional rules on the polycrystal mechanical response and on its microstructure is discussed. This framework is then used to do a systematic investigation of grain size effects in MC and UFG polycrystals. Attempt is made to explain the observed grain size effect on mechanical behavior based on characterizing the dislocation microstructure within grain using the methodology developed in Chapter II.

B.   Polycrystal discrete dislocation dynamics formulation

This section provides an overview of the polycrystal discrete dislocation dynamics formulation developed in this work. The formulation builds on the framework described by Balint et al. (2008). The original formulation by Balint et al. (2008) is enhanced by including key 3D short-range dislocation interactions as constitutive rules in the 2D model. In particular, the formulation allows for the formation of dislocation junctions, stabilization of junctions, breaking of junctions and nucleation of dislocations

from stabilized junctions which act as anchoring points. Polycrystals are idealized as planar unit cells of size $L \times L$ consisting of square grains with size $d \times d$. Each grain g consists of active slip systems oriented at an angle of $\varphi^{g(\kappa)}$ with respect to the x_1 axis; where κ refers to the slip system. A schematic describing the geometry of the unit cell with square grains is as shown in Fig. 58.
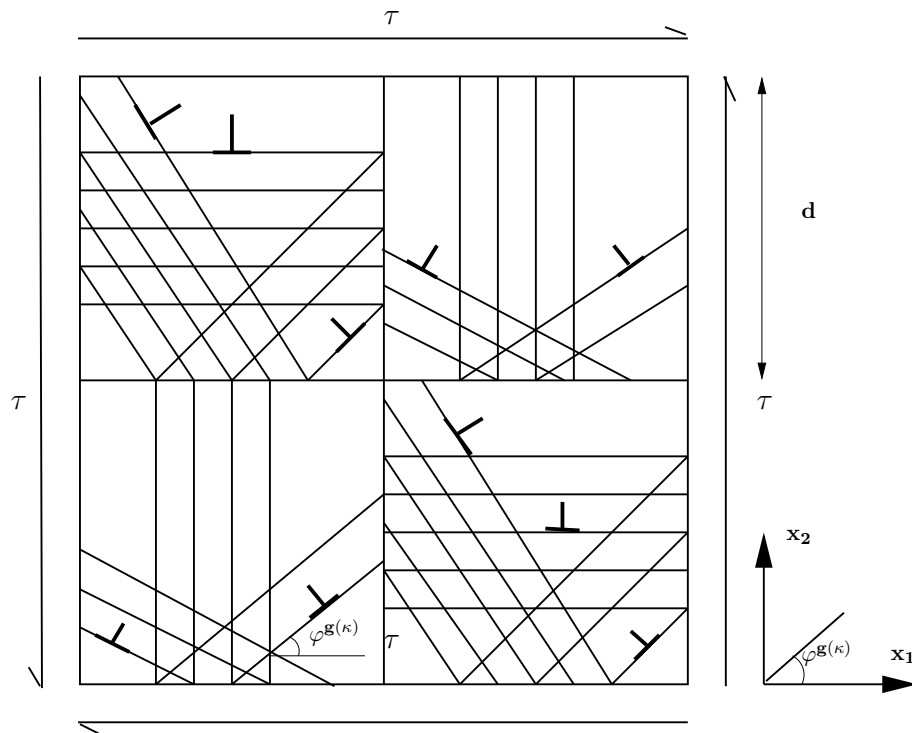
Fig. 58. Sketch of the pure shear problem with doubly periodic boundary conditions. Individual square grains g consist of active slip systems (κ) oriented at an angle of $\varphi^{g(\kappa)}$ with respect to the x_1 axis.

The unit cell is subjected to doubly periodic pure shear by imposing the displacement boundary condition given by,

$$\Delta u_i = \varepsilon_{ij} \Delta x_j \tag{6.1}$$

where, Δu_i is the difference between displacements on opposite sides of the unit cell specified by the difference position vector Δx_j. The strain components are specified as $\varepsilon_{12} = \varepsilon_{21} = \gamma/2$ and $\varepsilon_{11} = \varepsilon_{22} = 0$, where γ is the applied shear strain. The work conjugate shear stress is given by,

$$\tau = \frac{1}{2L^2} \int_C (T_1 x_2 + T_2 x_1) \, \mathrm{d}C \tag{6.2}$$

where, $T_i = \sigma_{ij} n_j$ is the traction on the boundary C of the unit cell with n_j the outward unit normal.

In the simulations, unit cells are assumed to be homogeneous linear elastic isotropic materials with Young's modulus E and Poisson's ratio ν. Dislocations, whose collective motion and interaction leads to the plastic deformation in the unit cell, are described as line defects with only edge character. The boundary value problem described above is solved following the superposition technique presented in Van der Giessen and Needleman (1995) incrementally. At each time increment, dislocation structure, stress, strain and displacements are determined. Assuming infinitesimal displacement gradients, the current state of the body, in terms of displacements, strains and stresses, is given by,

$$\mathbf{u} = \tilde{\mathbf{u}} + \hat{\mathbf{u}}, \qquad \boldsymbol{\epsilon} = \tilde{\boldsymbol{\epsilon}} + \hat{\boldsymbol{\epsilon}}, \qquad \boldsymbol{\sigma} = \tilde{\boldsymbol{\sigma}} + \hat{\boldsymbol{\sigma}} \tag{6.3}$$

The singular (˜) fields are obtained by the superposition of the fields $(\mathbf{u}^i, \boldsymbol{\epsilon}^i, \boldsymbol{\sigma}^i)$ associated with individual dislocations,

$$\tilde{\mathbf{u}} = \sum_{i=1}^{N} \mathbf{u}^i, \qquad \tilde{\boldsymbol{\epsilon}} = \sum_{i=1}^{N} \boldsymbol{\epsilon}^i, \qquad \tilde{\boldsymbol{\sigma}} = \sum_{i=1}^{N} \boldsymbol{\sigma}^i, \tag{6.4}$$

where, N is the total number of dislocations in the sample. The singular dislocation fields for each dislocation is determined analytically by considering them to be

present in a linear elastic isotropic homogeneous infinite medium. These fields are not periodic. The periodicity is enforced by the image fields, denoted by ˆ, which corrects for and enforces the actual boundary condition given in Eq. (6.1). The grain boundaries of the unit cell and the unit cell boundary are considered as impenetrable boundaries for the dislocations.

The discrete dislocation rules presented here are general in scope and can be used for either a single crystal or for a grain in a polycrystal. Here, it is specialized for a grain in a polycrystal. Within each grain, the glide of the dislocation is determined by the glide component of Peach-Koehler force, f^i, given by,

$$f^i = \mathbf{m}^i \cdot \left(\hat{\boldsymbol{\sigma}} + \sum_{j \neq i} \boldsymbol{\sigma}^j \right) \cdot \mathbf{b}^i \tag{6.5}$$

where $\mathbf{m}^i$ is the slip plane normal and $\mathbf{b}^i$ the Burgers vector having magnitude b. Dislocation glide is taken to be drag controlled following:

$$Bv^i = f^i - \alpha \frac{\mu b}{\mathcal{S}_{\mathrm{d}}^i} b^i \tag{6.6}$$

where B is the drag factor and the second term represents the line tension, α being a parameter and $\mathcal{S}_{\mathrm{d}}^i$ the algebraic distance between the dislocations, members of the same dipole; v^i the glide velocity of dislocation i. Initially there are only static Frank-Read sources present with a specified density and spatial distribution. The other type of FranK-Read sources considered in the framework are dynamic sources, which are formed during plastic deformation due to dislocation interactions. The two types of dislocation obstacles modeled are: (i) stress-free point obstacles that can be thought to represent sessile defects and precipitates, for example; and (ii) dynamic obstacles that represent junctions formed during plastic deformation. The spatial distribution of initial static sources and stress-free point obstacles is randomly

generated. Dislocation dipole is nucleated from a static source i when the magnitude of the Peach-Koehler force acting on it exceeds a critical value, $\tau_{0n}^i b$, for a prescribed time t_{0n}. The strength of the static sources are randomly assigned from a Gaussian distribution with average $\bar{\tau}_{0n}$. The sign of the nucleated dipole depends on the sign of the Peach-Koehler force acting on the source. A dislocation may get pinned during glide at a point obstacle. The dislocation is released when the Peach-Koehler force at the location of the point obstacle attains a value $\tau_{obs} b^i$, with τ_{obs} the obstacle strength.

Key 3D short-range dislocation interactions included at the level of individual grains in the framework are: (i) formation of dislocation junctions; (ii) stabilization of junctions; (iii) nucleation of dislocations from stable junctions which are anchoring points; and (iv) annihilation of dislocations. When dislocations gliding on intersecting planes approach each other within a critical distance d^*, a junction is formed, irrespective of the sign of the interacting dislocations. Junctions thus formed can act as either a dynamic dislocation source or dynamic obstacle during the deformation process. Also, their density evolves during the course of deformation. A stable junction which cannot be unzipped, for example due to cross-slip, is termed an *anchoring point* and a breakable junction is referred to as a *dynamic obstacle*. A dynamic obstacle is destroyed when the Peach-Koehler force acting on either dislocation comprising the junction attains or exceeds the breaking force, $\tau_{brk}^I b$. The breaking stress for junction I is configuration dependent and is given by:

$$\tau_{brk}^I = \beta_{brk} \frac{\mu b}{\mathcal{S}^I} \tag{6.7}$$

where $\mathcal{S}^I$ is the distance to the nearest junction in any of the two intersecting planes and β_{brk} is a scaling factor for the junction strength. The dislocations forming junctions and pinned at these junctions are released when the latter is destroyed. The released dislocations are free to glide.

The formation of an anchoring point by junction stabilization, for example due to cross-slip, is treated as a statistical event in our 2D model. The probability of a junction forming an anchoring point has a prescribed value p. These anchoring points lead to the formation of new dynamic sources. A dislocation dipole is nucleated at dynamic source I when the value of the Peach-Koehler force at either junction forming the source exceeds the value $\tau_{\mathrm{nuc}}^I b$ during a time t_{nuc}^I. Both values depend on the local configuration and hence evolve dynamically. The nucleation stress is given by

$$\tau_{\mathrm{nuc}}^I = \beta_{\mathrm{nuc}} \frac{\mu b}{\mathcal{S}^I} \tag{6.8}$$

where β_{nuc} is a factor that reflects the strength of the source and $\mathcal{S}^I$ is the distance to the nearest junction on the slip plane where τ_{nuc}^I is being resolved. The nucleation time t_{nuc}^I is given by

$$t_{\mathrm{nuc}}^I = \gamma \frac{\mathcal{S}^I}{|\tau^I| b} \tag{6.9}$$

where γ is a material constant with units of a drag factor, and τ^I is the current resolved shear stress at the location of anchoring point I, exclusive of the junction self-stress. When two co-planar dislocations of opposite sign glide within a material-dependent critical, L_e, they are annihilated.

In a typical simulation, a unit cell is subjected to boundary tractions and displacements. At the current time step, the dislocation structure in each grain is known from the procedure outlined above. The geometrically necessary dislocation (GND) density over any sub-domain, $\omega \subseteq \Omega$, defined within a grain g is obtained following the formulation described in Appendix A of Chapter II as,

$$\rho_{\mathrm{GND}}^g(\omega) = \sqrt{\left[\sum_{\kappa=1}^{N_s} (\rho_+^{g(\kappa)} - \rho_-^{g(\kappa)}) \cos \varphi^{g(\kappa)}\right]^2 + \left[\sum_{\kappa=1}^{N_s} (\rho_+^{g(\kappa)} - \rho_-^{g(\kappa)}) \sin \varphi^{g(\kappa)}\right]^2} \tag{6.10}$$

where, N_s denotes the number of active slip systems under the imposed loading;

$\rho_+^{g(\kappa)}$ and $\rho_-^{g(\kappa)}$ represent the positive and negative dislocation density on slip-system κ in grain g, respectively; and $\varphi^{g(\kappa)}$ denote the oriented angle that defines the slip direction on slip-system κ in grain g, measured from the x_1-axis. At each time step the GND density can be obtained from a straightforward computation using (5.10). The argument ω is kept here to emphasize that the computation is resolution dependent. This comes from the fact that the per-system signed density, $\rho_+^{g(\kappa)} - \rho_-^{g(\kappa)}$, is evaluated within ω in grain g. Likewise, the GND density on slip system κ in a grain g is simply:

$$\rho_{\text{GND}}^{g(\kappa)}(\omega) = \left| \rho_+^{g(\kappa)} - \rho_-^{g(\kappa)} \right| \tag{6.11}$$

Using either (6.10) or (6.11), maps of spatial distribution of GND density can be generated at desired resolution. Define a uniform and structured grid on body Ω of each grain g; The grid element size sets the resolution. The element-level values of GND density are then extrapolated to the nodes of the grid, which allows to generate contours of GND density. Because of the structured topology of the grid, we will exclusively use Eq. (6.10) in generating GND maps. GND density contours provide snapshots of the frozen dislocation structure. In the current model, the GND density arising from lattice misorientations across grain boundaries are not captured; since, grain boundaries are modeled as impenetrable obstacles to dislocations.

C.   Simulation setup and parameters

Calculations are carried out on a unit cell with dimension of 10×10 μm^{-2} with grain size ranging from 5.0 μm to 0.72 μm. The polycrystal unit cell consists of two types of square grains in a checker-board type arrangement. The slip systems are oriented at $\pm 54.75°$ and $35.25°$ with respect to the x_1 axis in the two types of grains considered in the checker-board arrangement. Individual grains are considered to be elastically

isotropic with Young's modulus $E = 70$ GPa and Poisson's ratio $\nu = 0.33$. The magnitude of Burger's vector $b = 0.25$ nm. These values are representative of Al. An initial dislocation source density of $\rho_{\text{nuc}} = 20 \times 10^{12}$ m^{-2} is considered in all the simulations with an average source strength of $\bar{\tau}_{\text{nuc}} = 50$ MPa, standard deviation of $\Sigma_{\text{nuc}} = 10$ MPa; critical time for nucleation of dislocation dipoles from sources is $t_{\text{nuc}} = 10$ ns. The initial point obstacle density considered in the simulations is $\rho_{\text{obs}} = 20 \times 10^{12}$ m^{-2}; the obstacle strength is $\tau_{\text{obs}} = 150$ MPa. Initially there are no dislocations in the simulations and the aforementioned density of static point sources and obstacles are randomly distributed on the slip planes, which are separated by $100b$. The drag coefficient $B = 10^{-4}$ Pas. The critical distance for dislocation annihilation is $L_{\text{e}} = 6b$.

The values of the parameters entering the constitutive rules governing the additional short-range dislocation interactions considered in this work are given by: $d^* = 6b$, $p = 0.01$, $\beta_{\text{nuc}} = 1$, $\beta_{\text{brk}} = 10$, and $\gamma = 1000B$. A time step of $\Delta t = 0.5$ ns and a loading rate of $\dot{\gamma} = 2000$ s^{-1} is used in all the simulations.

D. Results and discussion

In this section results from simulations of doubly periodic cells with square grains are presented. First, simulation results are presented to highlight the effect of new additional rules incorporated in the formulation on the unit cell macroscopic response. Subsequently, the new formulation is used to investigate grain size effect on the macroscopic response of polycrystals. Insight is gained from probing the dislocation structure, substructure and stress distribution within simulation unit cells to understand the effect of grain size in MC and UFG polycrystals.

The effect of line tension parameter α on the macroscopic response of the unit
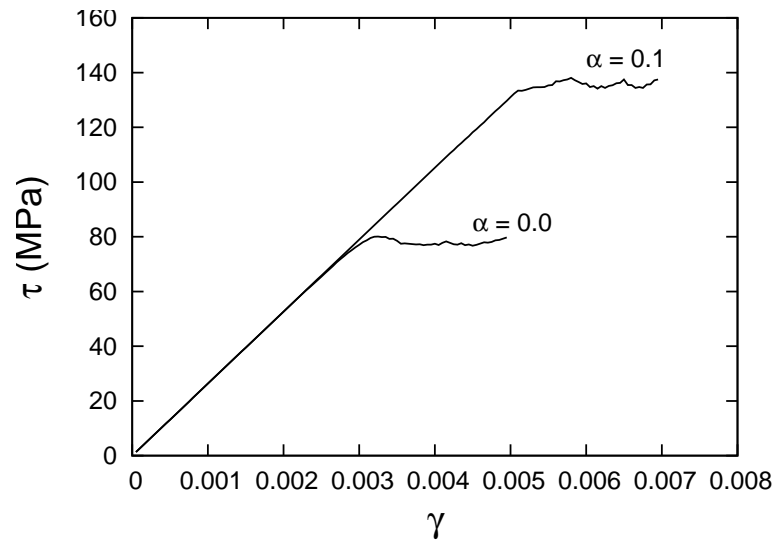
Fig. 59. Average shear stress (τ) versus shear strain (γ) response in a unit cell with line tension parameter $\alpha = 0.0$ and $\alpha = 0.1$. The calculations are performed considering only static initial sources and obstacles in the unit cell. The grain size of the unit cell is $d = 5.0$ μm for both the cases.

cell is shown in Fig. 59. The average shear stress versus shear strain response is shown for the case with $\alpha = 0.0$ and $\alpha = 0.1$ for a unit cell with grain size of $d = 5.0$ μm. In these simulations only static initial sources and obstacles are considered. Formation of junctions, dynamic obstacles, dynamic sources and their evolution is not considered in these simulations. Fig. 59 shows that increasing the value of α increases the 0.2% offset strain yield stress and the subsequent flow stress of the unit cell. The 0.2% offset strain yield stress in the simulation with $\alpha = 0.0$ is 80 MPa while the yield stress of the unit cell in the simulation with $\alpha = 0.1$ is 140 MPa. The increase in the yield and the flow stress in the simulation with $\alpha = 0.1$ is due to the additional energy cost associated with the expansion of the dislocation loop accounted for in the simulations as given by Eq. 6.6.

Fig. 60 shows the comparison between average shear stress versus shear strain response in simulations for the case with only static initial (SI) sources and obstacles
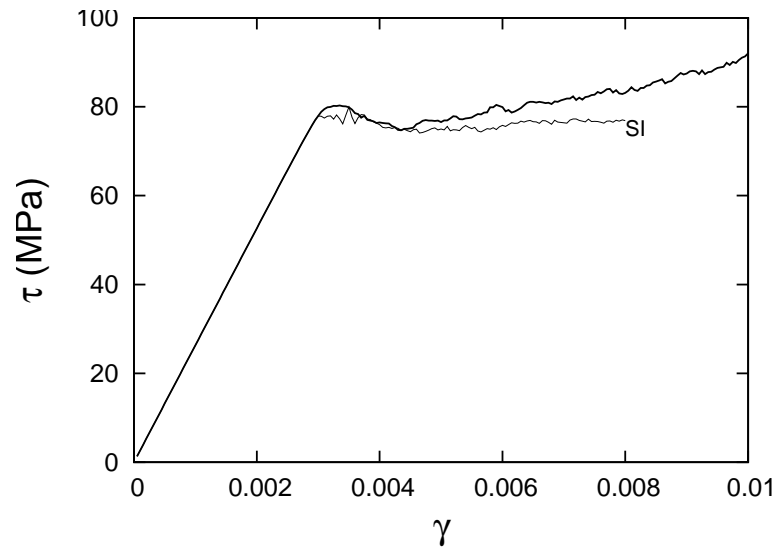
Fig. 60. Average shear stress (τ) versus shear strain (γ) response is shown for the calculation where dynamic sources and obstacles formation allowed in the calculation. For comparison the response of a unit cell with only static initial (SI) sources and obstacles is shown. A grain size of $d = 5.0$ μm is considered in both the calculations.

and the case where junction formation, dynamic obstacle and dynamic source evolution is considered. In these simulations the effect of line tension parameter α is not included. A grain size of 5.0 μm is considered in the unit cells. It is observed from the average shear stress versus shear strain response that the simulation with only static initial sources and obstacles show almost perfect plastic response beyond yield. When junctions are allowed to form, and dynamic obstacle and source evolution is accounted for in the simulation, an appreciable hardening is observed in the unit cell response beyond yield. The 0.2% offset shear strain yield stress is around 77 MPa in both the simulations. An average shear stress value of 91 MPa is reached at a shear strain of $\gamma = 0.01$ in the simulation where junction formation, dynamic obstacle and source evolution is accounted for.

The evolution of defect microstructure in terms of total dislocation density (ρ),

pinned dislocation density (ρ_{pin}), and junction density (ρ_{jun}) characterized as dynamic obstacles and sources is shown in Fig. 61. For the purpose of comparison, evolution of total dislocation density and pinned dislocation density from simulations with only static initial sources and obstacles are also shown. The total dislocation density increases with deformation in the case where junction formation, dynamic obstacle and source evolution is accounted for and in the case with only static initial sources and obstacles (Fig. 61b). At the low strains reached, the difference in the magnitude of the total dislocation density between the two formulations is not significant but is expected to develop gradually as plastic strain accumulates. A noticeable difference is observed in the density of the pinned dislocations between the two cases as shown in Fig. 61b. The pinned dislocation density shown here accounts for only those dislocations which are pinned at either point obstacle or dynamic obstacles. It is seen that the pinned dislocation density is higher when junction formation and pinning at junctions which are dynamic obstacles is accounted for in the simulation as compared when only point obstacles are present. The dynamic obstacles act as additional pinning points for dislocations. This can contribute to hardening in two ways: (i) it can lead to an increase in the backstress at a source; and (ii) it limits the effective mean free path of dislocations to a value smaller than the grain size.

The evolution of the junction density characterized by dynamic obstacles, and source evolution is shown in Fig. 61c. Overall, the dynamic obstacle density increases with increase in deformation. Initially, there is some fluctuation with the dynamic obstacle density but with increase in the total dislocation density the dynamic obstacle density also increases. One can corelate this increase in dynamic obstacle density with the increase in pinned dislocation density seen in Fig. 61b. The dynamic source density also increases with deformation. However, due to the low probability of junctions becoming anchoring points ($p = 0.01$) their density is significantly lower
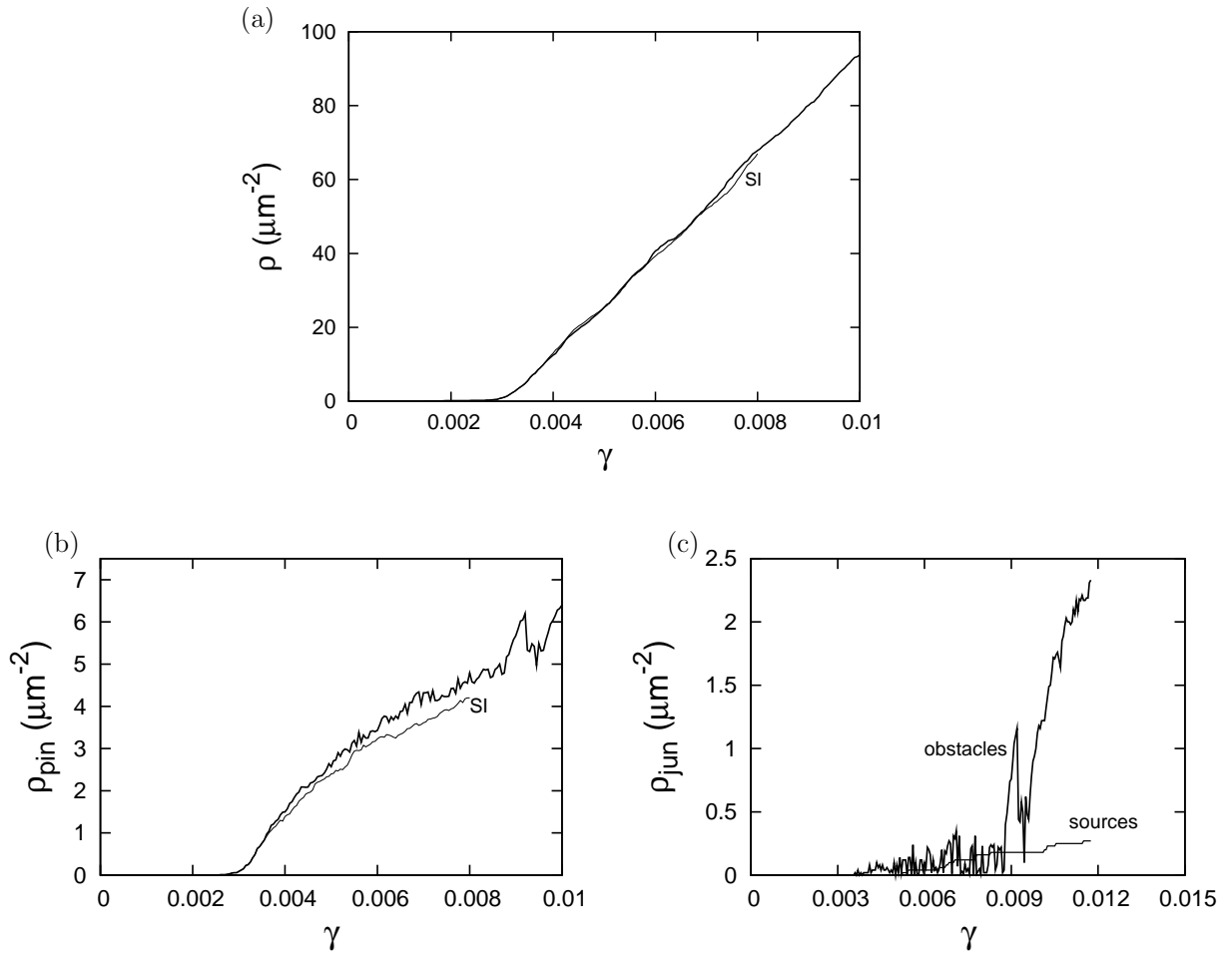
Fig. 61. Evolution of total dislocation density (ρ) and pinned dislocation density (ρ_{pin}) with average shear strain (γ) is shown for calculation where dynamic sources and obstacles formation is considered in the simulation in (a) and (b), respectively. The calculation with only static initial sources and obstacles (SI) is shown for comparison. (c) Evolution of the junction density (ρ_{jun}) with average shear strain (γ) is shown. The total junction density is the sum of density of dynamic obstacles and dynamic sources.
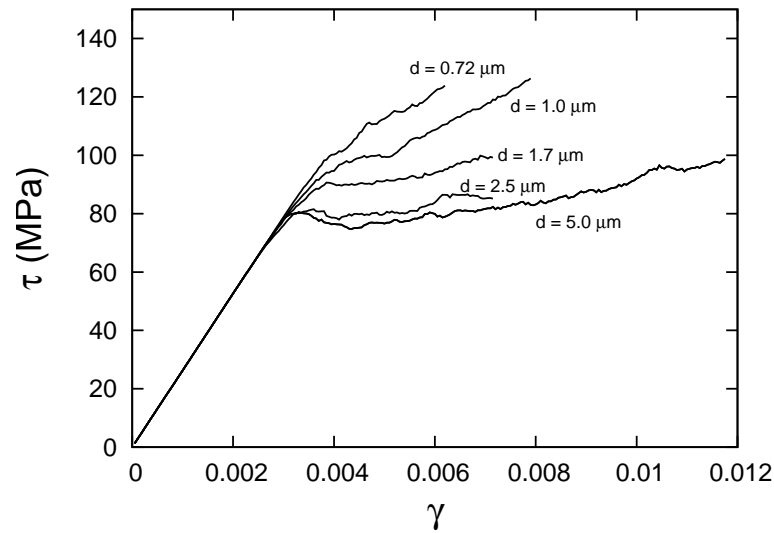
Fig. 62. Average shear stress (τ) versus shear strain (γ) response of unit cells with grain size (d) varying from 5.0 μm - 0.72 μm.

than the dynamic obstacle density. The dynamic sources once formed are considered unbreakable and cannot be annihilated. Also, these dynamic sources do not act as pinning points. They only act as new sources from which dislocation dipoles can be nucleated when the critical condition as given by Eq. 6.8 and Eq. 6.9 is reached.

Simulations on unit cells with grain sizes (d) varying from 5.0 μm - 0.72 μm is performed to investigate the grain size effect on the macroscopic response of the polycrystal unit cell. At grain sizes smaller than 0.72 μm, the time increment used in the simulations was not able to resolve dislocation glide before the dislocation encounters a grain boundary. This implicitly set the range of grain sizes which can be explored in the simulations. The average shear stress (τ) versus shear strain (γ) response from the simulations for various grain sizes are shown in Fig. 62. It can be seen from Fig. 62 that with decrease in grain size there is an increase in the yield stress of the unit cell. Also, a trend of increasing strain hardening rate of the unit cell with decrease in grain size can also be observed from Fig. 62. Fig. 63 shows the yield stress (τ_y) at 0.2% offset shear strain for unit cells with different grain sizes as a
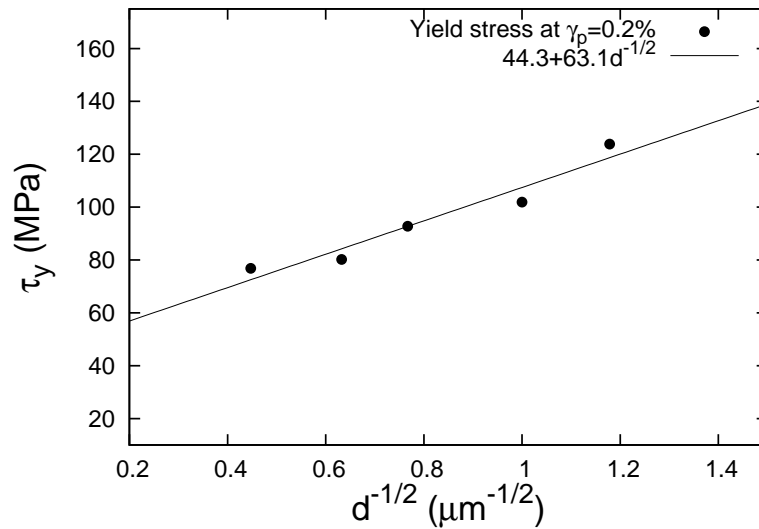
Fig. 63. Yield stress determined at 0.2% offset shear strain is shown as a function of grain size (d).

function of grain size. The solid line in Fig. 63 is the fit based on Hall-Petch relation given by,

$$\tau = \tau_0 + kd^{-1/2} \tag{6.12}$$

It is observed from Fig. 63 that the simulation results compare very well to the Hall-Petch relation with the values of the constants determined to be $\tau_0 = 44.3$ MPa and $k = 63.1$ MPa μm$^{1/2}$. Huang and Hansen (2003) have noted that the value of k is 40 MPa μm$^{1/2}$ for recrystallized aluminum and 140 MPa μm$^{1/2}$ for cold worked aluminum.

Spatial distributions of dislocation structure superposed on internal stress distribution in the unit cell for the two extreme grain sizes considered in this study are shown in Fig. 64 at 0.2% offset shear strain. The spatial distribution of dislocation structure reveals isolated glide dislocations, short dislocation pile-ups near junctions, as well as dislocations piled-up at the grain boundaries. In the unit cell with a grain size of $d = 5.0$ μm (see Fig. 64a) we notice pile-ups of dislocations both

(a)

(b)

σ_{12} (MPa)

-10 10 30 50 70 90 110 130 150 170 190
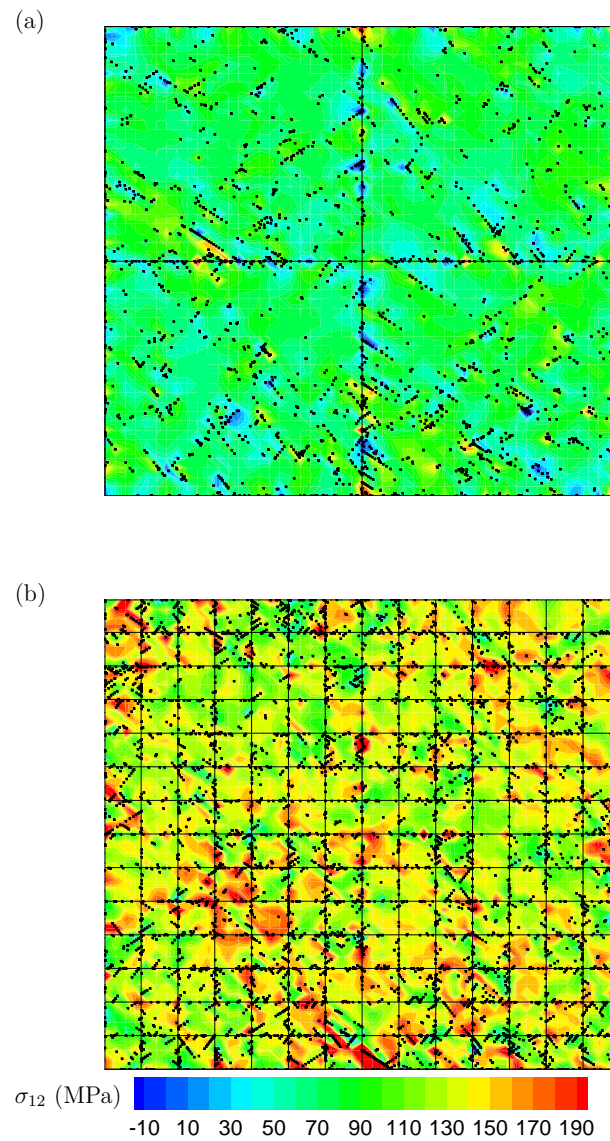
Fig. 64. Spatial distribution of dislocation structure superposed on internal stress (σ_{12}) distribution at 0.2% offset shear strain in the unit cell is shown for simulations with grain size of: (a) $d = 5.0$ μm; and (b) $d = 0.72$ μm.

at the central region of a grain and at the grain boundaries. The pile-ups at the central regions is due to dislocations blocked by point obstacles and dynamic obstacles. From the spatial distribution of dislocation structure in the unit cell with a grain size of $d = 0.72$ μm we observe that dislocation pile-ups are predominantly at the grain boundaries. Pile-ups within the central region of grains, as observed in the unit cell with grain size of $d = 5.0$ μm, was not observed. This observation reveals a transition from the material behavior dependency on dislocation-dislocation interactions to dislocation-grain boundary interactions. Also, we observe that the overall density of dislocations blocked at grain boundaries is more in the unit cell with grain size of $d = 0.72$ μm than in the unit cell with a grain size of $d = 5.0$ μm.

The spatial distribution of dislocation structure is correlated to the internal stress developed within the unit cell for simulations with two extreme grain sizes in Fig. 64. In both cases the two slip systems within the grains are symmetric with respect to the x_1-axis. Hence dislocation activity and consequently the stress distribution will be similar in both the slip systems. In both the unit cells high local stresses are observed near the location of dislocation pile-ups; be it within the central region of the grain or near the grain boundary. However, we notice that overall the stresses in the unit cell with grain size of $d = 0.72$ μm is higher than the stress in the unit cell with grain size of $d = 5.0$ μm. With decrease in grain size the area fraction of dislocations blocked at grain boundaries increases leading to large areas within the grains with high stresses.

Lefebvre et al. (2007) reported that in unit cells with grain size as large as $d = 2.0$ μm dislocation pile-ups dominate while at grain sizes around $d = 0.5$ μm the pile-ups are difficult to form but a significant density of dislocations nucleated from slip planes not favorably oriented for slip and blocked at grain boundaries dominate the deformation process. They found a linear dependence between dislocation density

and strain and that dislocation density decreases like the inverse of grain size. Based on the idea of storage rate of dislocations as suggested by Ashby (1970) they concluded that Hall-Petch relation is due to variation of dislocation storage rate when mean free path of dislocation is altered by grain boundaries. Balint et al. (2008) interpreted their results in terms of slip blocking/transmission. They observed that when the density of available sources are very small it is difficult to form continuous slip bands across adjacent grains. It is noted that the observation made by Lefebvre et al. (2007) and Balint et al. (2008) lead to build-up of GNDs at the grain boundaries. Ashby (1970) has shown that it is the build-up of GNDs at the grain boundaries which lead to the grain size dependence on flow stress observed in polycrystals.

Using the procedure outlined in Section. B contours of GND density for unit cells with different grain sizes can be determined. Fig. 65 shows the spatial distribution of GND density in unit cells with grain size of $d = 5.0$ μm and $d = 0.72$ μm at 0.2% offset shear strain. The spatial distribution of GND density is determined with a resolution size of 100×100 nm^2 (see Fig. 66 for GND contours shown at different resolution size). As noted earlier, the additional contribution to the GND density due to grain boundaries is not included in the plots, since lattice misorientations at grain boundaries are not explicitly represented. Nevertheless, one can qualitatively compare the fields due to deformation-induced GND density. It is observed that irrespective of the grain size the GND density is generally higher near the grain boundaries than at the central region of the grain. The pile-ups of dislocations and the dislocations blocked at the grain boundaries lead to a higher density of GNDs at the grain boundaries. Moreover, it is also observed that overall the GND density is higher in the unit cell with a grain size of $d = 0.72$ μm than in the unit cell with grain of size 5.0 μm. The corresponding GND maps at coarser resolution for the two unit cells are shown in Fig. 66.

(a)

(b)

$\rho_{\mathrm{GND}}\ (\mu\mathrm{m}^{-2})$

0   20   40   60   80   100 120
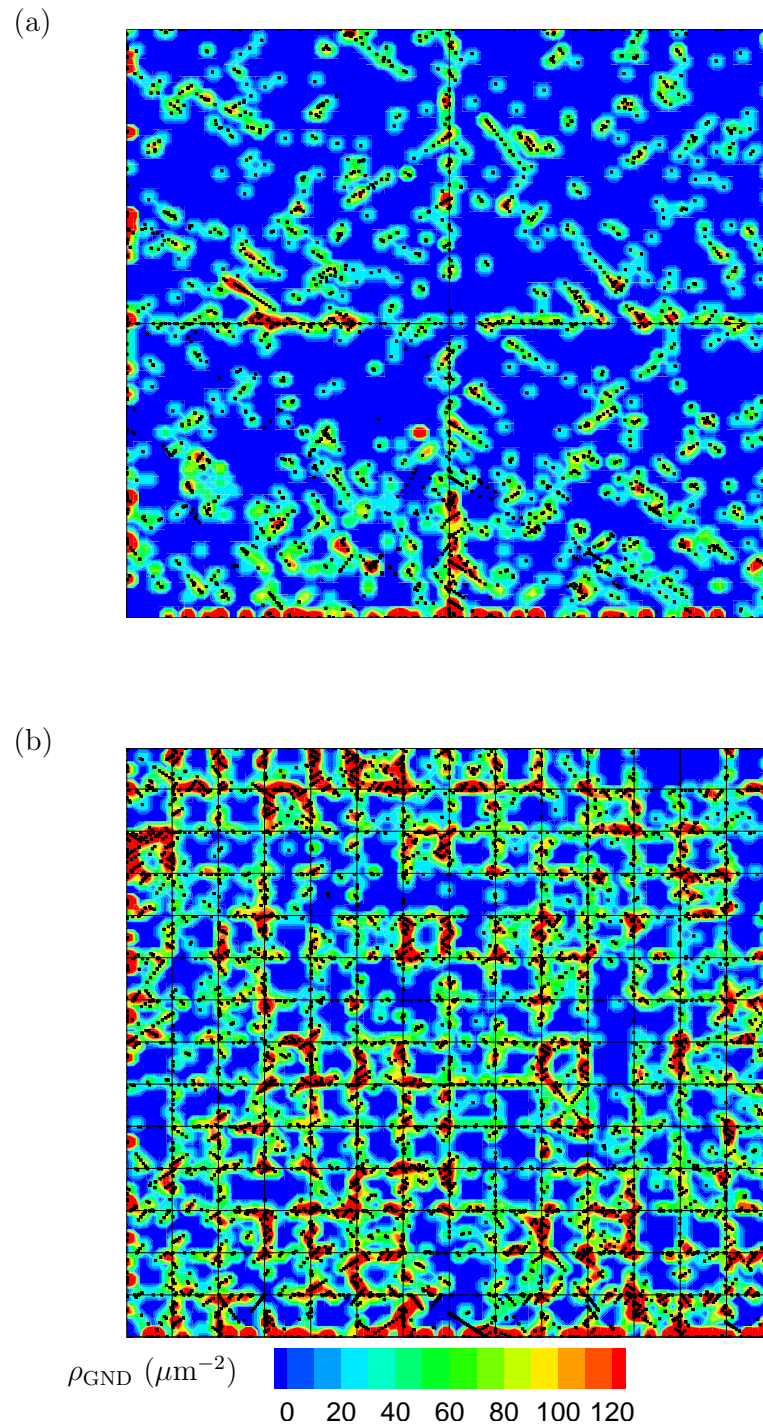
Fig. 65. Spatial distribution of dislocation structure superposed on GND density (ρ_{GND}) contours is shown at 0.2% offset shear strain in a unit cell with grain size of: (a) $d = 5.0\ \mu\mathrm{m}$; and (b) $d = 0.72\ \mu\mathrm{m}$. A resolution size of $100 \times 100\ \mathrm{nm}^2$ is used in the calculation of GND density.
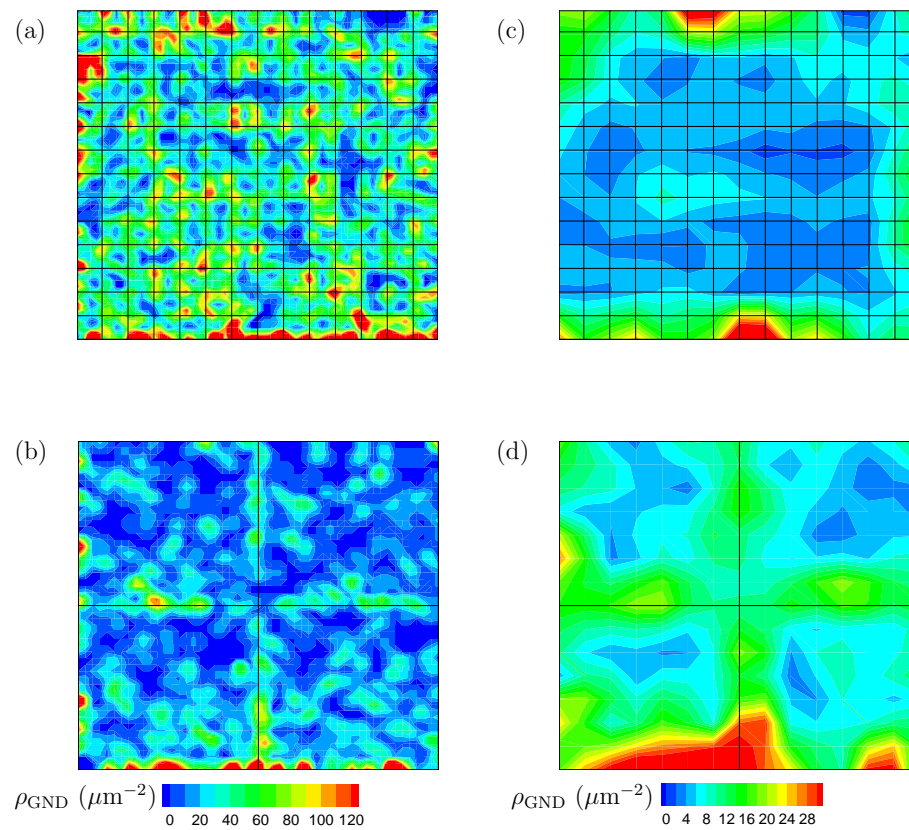
Fig. 66. Spatial distribution of GND density (ρ_{GND}) contours is shown at 0.2% offset shear strain in a unit cell with grain size of: (a) $d = 0.72$ μm and the resolution size used was 175×175 nm^2 ; (b) $d = 5.0$ μm and the resolution size used was 200×200 nm^2; (c) $d = 0.72$ μm and the resolution size used was 700×700 nm^2; and (d) $d = 5.0$ μm and the resolution size used was 715×715 nm^2.

E. Conclusions and outlook

This work set out to investigate the effect of grain size on ploycrystals using a 2D discrete dislocation dynamics (2D-DDD) framework. The 2D-DDD framework has been enriched by incorporating constitutive rules to account for, dislocation line tension, junction formation, junction stabilizing and nucleation of dislocations from stable junctions which act as anchoring points. Currently, the grain boundaries are considered to be impenetrable to dislocations, and GND densities due to lattice misorientations across the grain boundaries are not accounted for in the framework.

- For polycrystal unit cells with sufficiently large grain size ($d = 5.0$ μm) the simulations are able to capture hardening due to dislocation interaction with point and dynamic obstacles within the grain. There is a need to pursue such calculations to large strains in order to validate the predictions against experiments.

- An investigation of the grain size effect on yield strength revealed a Hall-Petch relation. This is a natural outcome from the simulations. Simulations showed that yield stress scales as $d^{-1/2}$ with the value of $k = 63.1$ MPa μm$^{1/2}$. This compares well with the experimental results on recrystallized aluminum.

- Analysis of dislocation structure revealed dislocation-dislocation interactions within the grains and dislocation-pileups at grain boundaries to be dominating deformation behavior in unit cells with large grain sizes. In smaller grain sizes dislocation-dislocation interactions within the grains are rare and deformation is characterized by dislocation pile-ups at the grain boundaries and dislocation blockage at grain boundaries. Down to the smallest grain size considered in this study, it is not expected that other mechanisms, such as grain boundary

sliding, are active.

- Simulations revealed the development of deformation-induced GND density in the vicinity of grain boundaries with their magnitude being higher in unit cells with smaller grain size than in larger grain size.

CHAPTER VII

CONCLUSIONS

A. Summary

The focus of the current work was to investigate the influence of structural and material length scales on the plastic behavior of materials. A continuum crystal plasticity model which can predict the material mechanical response and its underlying defect substructure is currently lacking. At length scales where one of the dimensions of the deformed body, its microstructural feature, or both, approach the size of the substructure size effects emerge. The study of material mechanical properties, in particular the flow strength and hardening behavior of materials, at reduced length scales is also motivated by: (a) a growing trend towards miniaturization in technology which demands understanding material mechanical properties for their design; (b) potential improvements in material mechanical properties which can be achieved by controlling different length scales to design efficient structural components; and (c) the capability of such an investigation to shed light on fine-scale physical phenomenon which affect the material macroscopic response. Towards this end, the following objectives were set for the study: (a) investigate scale and size effects due to dimensional constraints; (b) investigate size effects due to microstructural constraints; and (c) develop size dependent hardening model through coarse graining of dislocation dynamics. A summary of this research work is as follows:

- State of the art continuum models fall short in completely addressing the challenges involved in modeling and understanding the behavior of materials at reduced length scales. Atomistics and Molecular dynamics based simulations, though conceptually capable of meeting the challenges, become computationally

expensive and intensive. A promising alternative is to use discrete dislocation dynamics (DDD) framework. In this study, a 2D-DDD framework is used to address the objectives listed above.

- 2D-DDD is a mesoscale technique where plastic flow in the material is due to the nucleation, collective glide, and interactions of dislocations. Within this framework long-range interactions due to dislocations is naturally incorporated through elasticity. Key 3D dislocation short-range interactions are incorporated through constitutive rules within the framework. The short-range interactions include, junction formation, junction stabilization, and nucleation of dislocations from stable junctions which act as anchoring points. Using plane strain approximations, single crystals are modeled as planar crystals, and polycrystals as planar unit cells with square grains. This framework naturally accounts for the effect of structural and material length scale and the macroscopic response is an outcome of the simulations and not an input.

- Materials subjected to dimensional constraints were investigated by modeling micropillars as planar crystals subjected to nominally uniform compression. This study revealed strengthening upon scale reduction. A significant size effect was observed in both flow stress and strain hardening rate. This general observation was validated by undertaking a combined experimental and simulation study of size effects in Cu micropillars. Based on calibration process, attempt was made to represent the initial source and obstacle density and strength distribution in the simulations close to experimental samples. The simulations were able to capture the overall stress-strain response determined from experiments characterized by yield followed by steady hardening, which is size dependent. A good quantitative agreement was obtained on flowstress and strain hardening

rate predictions between simulations and experiments.

- In the simulations the observed size effect was rationalized to be due to the emergence of a non-vanishing density of geometrically necessary dislocations (GND), which emerges locally due to dislocation structure development and its interaction with the free surfaces. The GND density is dependent on the resolution of the analysis and vanishes at the scale of the sample, consistent with homogeneous state of macroscopic deformation in the simulations. The GND density emerges to accommodate local lattice rotations within the crystal. Electron back scatter diffraction studies on Cu micropillars revealed distributions of lattice misorientation within the crystals thus corroborating the simulation results.

- A review of literature on micropillars highlighted some differences in their observed mechanical behavior. All the studies reported strengthening upon reduction in sample size; however, there were differences in the reported flow stress scaling and strain hardening rates. 2D-DDD simulations performed at extreme values of initial dislocation source densities was able to capture the range of flow stress scaling exponents reported in the experiments. Further, this analysis revealed a transition from dislocation interaction controlled behavior to dislocation multiplication controlled behavior, when the initial dislocation source density was decreased. More precisely, a transition from forest hardening dominated behavior to exhaustion hardening dominated behavior was observed with reduction in initial dislocation source density. In forest hardening dominated regime, it is the evolving dislocation structure which leads to the observed size effect. On the other hand, in the exhaustion hardening dominated regime, source-truncation, source dynamics and rare events lead to the observed size

effects.

- A methodology based on the concept of Nye's tensor was developed to capture the spatial and temporal distribution of GND density in crystals during simulations. Subsequently, coarse graining of discrete dislocation dynamics technique was adopted to develop a phenomenological model to capture size effect on plastic flow stress and strain hardening. In this model, a complete description of plastic behavior is provided by giving two inherently different statements: a statement of evolution of structure accounting for athermal hardening, dynamic recovery and geometric storage; and, a kinetic statement specifying a hardening law in differential form. This model is limited to the case where the initial dislocation source density is high enough for forest hardening behavior to be dominant.

- Planar unit cells with square grains and subjected to doubly periodic pure shear conditions was considered to investigate the effect of microstructural constraints on material strength - yield stress and strain hardening. The grain size considered in the study falls within the range of microcrystalline to ultra-fine grained polycrystals. Within the framework, grain boundaries are considered to be impenetrable to dislocations. The simulations revealed that there is an increase in the yield stress and strain hardening rate with decrease in grain size. The scaling of the yield stress with grain size followed the Hall-Petch relation and is in good agreement with experimental data reported for recrystallized Al.

- Analysis of dislocation structure in unit cells with the largest and smallest grain sizes used in simulations revealed that transition of deformation process dominated by dislocation-dislocation interactions to dislocation-grain boundary interactions takes place by decreasing the grain size. The observed size effect

on yield and strain hardening is rationalized due to the presence of deformation induced GND density at the grain boundaries, with their overall magnitude increasing with decrease in unit cell grain size. The GND density emergence is due to dislocation pile-ups and dislocation blockage at the grain boundaries.

B. Recommendations for future work

The field of plasticity in bulk materials is mature; however, much work still needs to done before one can make a similar claim about materials with structural and material length scale restrictions. The ultimate goal would be to achieve this status with a seamless transfer of scientific knowledge from research stage to structural component design stage. The current research undertaking is only a small step towards this goal. Provided below is a list of recommendations for future work:

- In experiments, the base of the micropillars is attached to the bulk material from which it is fabricated or can be attached to a substrate of different material. Samples with size below 1.0 μm are mostly tapered and not perfect cylinders. These complexities are not incorporated in the current model. For a better agreement of results between simulations and experiments it is desirable to include these aspects in the model.

- Electron backscatter diffraction studies of micropillars fabricated using focus ion beam technique (FIB) have revealed the presence of defects which lead to internal lattice distortions leading to local gradients. However, none of the DDD simulations, both 3D-DDD as well as 2D-DDD in the current work, has considered this initial condition in the model. Almost all the simulations, 3D-DDD as well as 2D-DDD, start with an initial state with net Burger's vector zero. Modeling micropillars with an overall net Burger's vector due to local

gradients in the sample is within the scope of the 2D-DDD framework presented in the current work. Such a study can shed more light on the size affected strengthening in micropillars.

- The current investigation on the size effect due to microstructural constraints explored the range of grain sizes typical of microcrystalline (MC) and ultra-fine grained (UFG) materials. Most of the molecular dynamics simulations in the literature have explored the range of nanocrystalline (NC) materials with grain size of typically 10 nm or less. There is a range of grain size between 500 nm - 10nm which has not yet been carefully explored. This range of grain size is within the scope of analysis using the current 2D-DDD framework. However, such an analysis would require a detailed representation of grain boundaries. Experiments have shown evidence that in NC materials plastic deformation is grain boundary dominated with grain boundary sliding, nucleation of dislocations from grain boundary, and grain boundary absorption, being possible dominant mechanisms. More realistic grain morphologies also needs to be accounted for in the framework.

- Introducing nano-twins within grains has recently emerged as a potential technique to strengthen materials. These nano-twins act as barriers for free dislocation glide and hence act as a potential strengthener. A study of the effect of nano-twins on strengthening is possible using grain boundaries as impenetrable to dislocations in the 2D-DDD framework.

- The current work was focused on investigating the effect of structural and material length scales separately. A study on the coupling effect of these length scales on the plastic deformation was not within the scope of the objectives set. This coupling effect, however, becomes important to understand the mechanical

behavior of thin films with grain sizes between micron to nano range or thin films with nano-twins.

- Most of the work, including the current study, related to the investigation on the effect of reduced structural and material length scales on plastic deformation is applicable for materials at low homologous temperature. It is not understood how different length scales affect the high temperature behavior, like creep, in materials. To address this issue physical mechanisms like dislocation climb and vacancy diffusion must be included in the current 2D-DDD framework.

- Coupling of DDD with phase transformation to study mechanical behavior of technologically important multiphase carbon steels.

REFERENCES

Abu Al-Rub, R. K., Voyiadjis, G. Z., 2006. A physically based gradient plasticity theory. Int J Plasticity 22, 654–684.

Acharya, A., 2001. A model of crystal plasticity based on the theory of continuously distributed dislocations. J Mech Phys Solids 49, 761–784.

Acharya, A., 2004. Constitutive analysis of finite deformation field dislocation mechanics. J Mech Phys Solids 52, 301–316.

Acharya, A., Bassani, J. L., 2000. Lattice incompatibility and a gradient theory of crystal plasticity. J Mech Phys Solids 48, 1565–1595.

Acharya, A., Beaudoin, A. J., 2000. Grain-size effect in viscoplastic polycrystals at moderate strains. J Mech Phys Solids 48, 2213–2230.

Akarapu, S., Zbib, H. M., Bahr, D. F., 2010. Analysis of heterogeneous deformation and dislocation dynamics in single crystal micropillars under compression. Int J Plasticity 26, 239–257.

Amodeo, R. J., Ghoniem, N. M., 1990. Dislocation dynamics. I. A proposed methodology for deformation micromechanics. Phys Rev B41, 6958–6967.

Argon, A. S., 2008. Strengthening mechanisms in crystal plasticity. Oxford University Press, Oxford.

Argon, A. S., Brydges, W. T., 1968. Deformation of copper in easy glide. Phil Mag 18, 817–837.

Arsenlis, A., Parks, D., 1999. Crystallographic aspects of geometrically-necessary and statistically-stored dislocation density. Acta Mater 47, 1597–1611.

Arsenlis, A., Parks, D. M., Becker, R., Bulatov, V. V., 2004. On the evolution of crystallographic dislocation density in non-homogeneously deforming crystals. J Mech Phys Solids 52, 1213–1246.

Arzt, E., 1998. Size effects in materials due to microstructural and dimensional constraints: a comparative study. Acta Mater 46, 5611–5626.

Asaro, R. J., 1983. Crystal plasticity. J Appl Mech 50, 921–934.

Asaro, R. J., Rice, J. R., 1977. Strain localization in ductile single crystals. J Mech Phys Solids 25, 309–338.

Ashby, M. F., 1970. Deformation of plastically non-homogeneous materials. Phil Mag 21, 399–424.

Baek, S., Srinivasa, A. R., 2003. A variational procedure utilizing the assumption of maximum dissipation rate for gradient-dependent elastic-plastic materials. Int J Nonlin Mech 38, 659–662.

Balint, D. S., Deshpande, V. S., Needleman, A., Van der Giessen, E., 2005a. Discrete dislocation plasticity analysis of crack-tip fields in polycrystalline materials. Phil Mag 85, 3047–3071.

Balint, D. S., Deshpande, V. S., Needleman, A., Van der Giessen, E., 2005b. A discrete dislocation plasticity analysis of grain-size strengthening. Mater Sci Eng: A 400, 186–190.

Balint, D. S., Deshpande, V. S., Needleman, A., Van der Giesses, E., 2008. Discrete dislocation plasticity analysis of the grain size dependence of the flow strength of polycrystals. Int J Plasticity 24, 2149–2172.

Bassani, J. L., 2001. Incompatibility and a simple gradient theory of plasticity. J Mech Phys Solids 49, 1993–1996.

Bei, H., Shim, S., George, E. P., Miller, M. K., Herbert, E. G., Pharr, G. M., 2008a. Compressive strength of molybdneum alloy micro-pillars prepared using a new technique. Scr Mater 57, 397–400.

Bei, H., Shim, S., Pharr, G. M., 2008b. Effects of pre-strain of the compressive stress-strain response of Mo-alloy single-crystal micropillars. Acta Mater 56, 4762–4770.

Benzerga, A. A., 2008. An analysis of exhaustion hardening in micron-scale plasticity. Int J Plasticity 24, 1128–1157.

Benzerga, A. A., 2009. Micro-pillar plasticity: 2.5d mesoscopic simulations. J Mech Phys Solids 57, 1459–1469.

Benzerga, A. A., Bréchet, Y., Needleman, A., Van der Giessen, E., 2004. Incorporating three-dimensional mechanisms into two-dimensional dislocation dynamics. Modelling Simul Mater Sci Eng 12, 159–196.

Benzerga, A. A., Bréchet, Y., Needleman, A., Van der Giessen, E., 2005. The stored energy of cold work: Predictions from discrete dislocation plasticity. Acta Mater 53, 4765–4779.

Benzerga, A. A., Shaver, N. F., 2006. Scale dependence of mechanical properties of single crystals under uniform deformation. Scr Mater 54, 1937–1941.

Biner, S. B., Morris, J. R., 2002. A two-dimensinal discrete dislocation simulation of the effect of grain size on strengthening behavior. Modelling Simul Mater Sci Eng 10, 617–635.

Biner, S. B., Morris, J. R., 2003. The effects of grain size and dislocation source density on the strengthening behavior of polycrystals: A two-dimensional discrete dislocation simulation. Phil Mag 83, 31–34.

Brinckmann, S., Kim, J. Y., Greer, J. R., 2008. Fundamental differences in mechanical behavior between two types of crystals at the nanoscale. Phys Rev Lett 100, 155502.

Cao, A., Wei, Y., Mao, S. X., 2008. Alternating starvation of dislocatiosn during plastic yielding in metallic nanowires. Scr Mater 59, 219–222.

Cermelli, P., Gurtin, M. E., 2001. On the characterization of geometrically necessary dislocations in finite plasticity. J Mech Phys Solids 49, 1539–1568.

Chakravarthy, S. S., Curtin, W. A., 2010. Effect of source and obstacle strengths on yield stress: A discrete dislocation study. J Mech Phys Solids 58, 625–635.

Chokshi, A. H., Rosen, A., Karch, J., Gleiter, H., 1989. On the validity of the hall–petch relationship in nanocrystalline materials. Scripta Met. 23 (10), 1679–1683.

Cleveringa, H. H. M., Van der Giessen, E., Needleman, A., 1997. Comparison of discrete dislocation and continuum plasticity predictions for a composite material. Acta Mater 45 (8), 3163–3179.

Cleveringa, H. H. M., Van der Giessen, E., Needleman, A., 1999. A discrete dislocation analysis of bending. Int J Plasticity 15, 837–868.

Cleveringa, H. H. M., Van der Giessen, E., Needleman, A., 2000. A discrete dislocation analysis of mode I crack growth. J Mech Phys Solids 48, 1133–1157.

Dao, M., Lu, L., Asaro, R. J., De Hosson, J. T. M., Ma, E., 2007. Toward a quantitative understanding of mechanical behavior of nanocrystalline metals. Acta Mater 55, 4041–4065.

Dawson, P. R., 2000. Computational crystal plasticity. Int J Solids Structures 37, 115–130.

De Guzman, M. S., Neubauer, G., Flinn, P., Nix, W. D., 1993. The role of indentation depth on the measured hardness of materials. Mater Res Symp Proc 308, 613–618.

Deng, C., Sansoz, F., 2009a. Enabling ultrahigh plastic flow and work hardening in twinned gold nanowires. Nano Letters 9, 1517–1522.

Deng, C., Sansoz, F., 2009b. Size-dependent yield stress in twinned gold nanowires mediated by size-specific surface dislocation emission. Appl Phys Lett 95, 091914.

Desai, T. G., Millett, P., Wolf, D., 2008. Is diffusion creep the cause for the inverse hall-petch effect in nanocrystalline materials? Mater Sci Eng: A 493, 41–47.

Deshpande, V. S., Needleman, A., Van der Giessen, E., 2003. Finite strain discrete dislocation plasticity. J Mech Phys Solids 51, 2057–2083.

Deshpande, V. S., Needleman, A., Van der Giessen, E., 2005. Plasticity size effects in tension and compression of single crystals. J Mech Phys Solids 53, 2661–2691.

Diehl, J., 1956. Zugverformung von kupfer-einkristallen.1. Verfestigungskurven und oberflachenerscheinungen. Z. Metallkd 47, 331–343.

Dimiduk, D. M., Uchic, M. D., Parthasarathy, T. A., 2005. Size-affected single-slip behavior of pure nickel microcrystals. Acta Mater 53, 4065–4077.

Dimiduk, D. M., Woodward, C., LeSar, R., Uchic, M. D., 2006. Scale-free intermittent flow in crystal plasticity. Science 312, 1188–1190.

Ekinci, K. L., Roukes, M. L., 2005. Nanoelectromechanical systems. Rev Scientific Instruments 76, 061101–12.

El-Awady, J. A., Biner, S. B., Ghoniem, N. M., 2008. A self-consistent boundary element, parametric dislocation dynamics formulation of plastic flow in finite volumes. J Mech Phys Solids 56, 2019–2035.

El-Awady, J. A., Wen, M., Ghoniem, N. M., 2009. The role of the weakest-link mechanism in controlling the plasticity of micropillars. J Mech Phys Solids 57, 32–50.

Embury, J. D., 1971. Strengthening by dislocation substructures. Applied Sciences, Barking, UK.

Eshelby, J. D., Frank, F. C., Nabarro, F. R. N., 1951. The equillibrium of linear arrays of dislocations. Phil Mag 42, 351–364.

Espinosa, H. D., Panico, M., Berbenni, S., Schwarz, K. W., 2006. Discrete dislocation dynamics simulations to interpret plasticity size and surface effects in freestanding fcc thin films. Int J Plasticity 22, 2091–2117.

Estrin, Y., Mecking, H., 1984. A unified phenomenological description of work hardening and creep based on one-parameter models. Acta Metall 32, 57–70.

Evers, L. P., Parks, D. M., Brekelmans, W. A. M., Geers, M. G. D., 2002. Crystal plasticity model with enhanced hardening by geometrically necessary dislocation accumulation. J Mech Phys Solids 50, 2403–2424.

Ewing, J. A., Rosenhain, W., 1900. Experiments in micro-metallurgy: Effects of strain, preliminary notice. Proc Roy Soc London A 65, 85–90.

Fleck, N. A., Hutchinson, J. W., 2001. A reformulation of strain gradient plasticity. J Mech Phys Solids 49, 2245–2271.

Fleck, N. A., Muller, G. M., Ashby, M. F., Hutchinson, J. W., 1994. Strain gradient plasticity - Theory and experiment. Acta Metall Mater 42, 475–487.

Flinn, J. E., Field, D. P., Korth, G. E., Lillo, T. M., Macheret, J., 2001. The flow stress behavior of OFHC polycrystalline copper. Acta Mater 49, 2065–2074.

Forest, S., Sievert, R., 2003. Elastoviscoplastic constitutive frameworks for generalized continua. Acta Mech 160, 71–111.

Fourie, J. T., 1967. The plastic deformation of thin copper single crystals. Can J Phys 45, 777–786.

Fourie, J. T., 1968. The flow stress gradient between the surface and centre of deformed copper single crystals. Phil Mag 17, 735–756.

Frick, C. P., Clark, B. G., Orso, S., Schneider, A. S., Arzt, E., 2008. Size effect on strength and strain hardening of small-scale [111] nickel compression pillars. Mater Sci Eng: A 489, 319–329.

Gao, H., Huang, Y., Nix, W. D., Hutchinson, J. W., 1999. Mechanism-based strain gradient plasticity - i. theory. J Mech Phys Solids 47, 1239–1263.

Geers, M. G. D., Brekelmans, W. A. M., Janssen, P. J. M., 2006. Size effects in miniaturized polycrystalline fcc samples: Strengthening versus weakening. Int J Solids Structures 43, 7304–7321.

Gerberich, W. W., Jungk, J. M., Li, M., Volinsky, A. L., Hoehn, J. W., Yoder, K., 2003. Length scales for the fracture of nanostructures. Int J Frac 119, 387–405.

Gil Sevillano, J., 1993. Flow stress and work hardening. In: Cahn, R. W., Haasen, P., Kramer, E., Mughrabi, H. (Eds.), Materials science and technology. Vol. 6. VCH, Weinheim, pp. 19–88.

Gleiter, H., 1989. Nanocrystalline materials. Progr Mater Sci 33, 223–315.

Gracie, R., Ventura, G., Belytchko, T., 2007. A new fast finite element method for dislocation based on interior discontinuities. Int J Numer Meth Engng 69, 423–441.

Grayson, A. C. R., Shawgo, R. S., Johnson, A. M., Flynn, N. T., Li, M., Cima, M. J., Langer, R., 2004. A BioMEMS review: MEMS technology for physiologically integrated device. Proc IEEE 92, 6–21.

Greer, J. R., Nix, W. D., 2006. Nanoscale gold pillars strengthened through dislocation starvation. Phys Rev B 73, 245410.

Greer, J. R., Oliver, W. C., Nix, W. D., 2005. Size dependence of mechanical properties of gold at the micron scale in the absence of strain gradients. Acta Mater 53, 1821–1830.

Greer, J. R., Oliver, W. C., Nix, W. D., 2006. Size dependence of mechanical properties of gold at the micron scale in the absence of strain gradients. Acta Mater 54, 1705–1705, corrigendum.

Gruber, P. A., Bohm, J., Onuseit, F., Wanner, A., Spolenak, R., Arzt, E., 2008. Size effects on yield strength and strain hardening for ultra-thin Cu films with and without passivation: A study by synchrotron bulge test techniques. Acta Mater 56, 2318–2335.

Gurtin, M. E., 2002. A gradient theory of single-crystal viscoplasticity that accounts for the geometrically necessary dislocations. J Mech Phys Solids 50, 5–32.

Gurtin, M. E., 2006. The burgers vector and the flow of screw and edge dislocations in finite-deformation single-crystal plasticity. J Mech Phys Solids 54, 1882–1898.

Guruprasad, P. J., Benzerga, A. A., 2008a. A discrete dislocation analysis of the bauschinger effect in microcrystals. Acta Mater 56, 5477–5491.

Guruprasad, P. J., Benzerga, A. A., 2008b. Size effects under homogeneous deformation of single crystals: A discrete dislocation analysis. J Mech Phys Solids 56, 132–156.

Hall, E. O., 1951. The deformation and ageing of mild steel: III discussion of results. Proc Physical Society B64, 747–753.

Haouaoui, M., Karaman, I., Maier, H. J., 2006. Flow stress anisotropy and bauschinger effect in ultrafine grained copper. Acta Mater 54, 5477–5488.

Hill, R., 1966. Generalized constitutive relations for incremental deformation of metals crystals by multislip. J Mech Phys Solids 14, 95–102.

Hill, R., Rice, J. R., 1972. Constitutive analysis of elastic-plastic crystals at arbitrary strain. J Mech Phys Solids 23, 401–403.

Hirth, J. P., 1972. Influence of grain boundaries on mechanical properties. Met Trans A 3, 3047–3067.

Hirth, J. P., Lothe, J., 1968. Theory of Dislocations. McGraw-Hill, New York.

Hommel, M., Kraft, O., Arzt, E., 1999. A new method to study cyclic deformation of thin films in tension and compression. J Mater Res 14, 2373–2376.

Horstemeyer, M. F., Baskes, M. I., Plimpton, S. J., 2001. Length scale and time scale effects on the plastic flow of fcc metals. Acta Mater 49, 4363–4374.

Huang, H. B., Spaepen, F., 2000. Tensile testing of free-standing Cu, Ag and Al thin films and Ag/Cu multilayers. Acta Mater 48, 3261–3269.

Huang, X., Hansen, N., 2003. Flow stress and microstructures of fine grained copper. Mater Sci Eng: A 387, 186–190.

Hughes, D. A., Hansen, N., 1993. Microstructural evolution in nickel during rolling from intermediate to large strains. Met Trans A 24, 2021–2037.

Hull, A. W., 1919. The position of atoms in metals. Proc Am Inst Elec Eng 38, 1171–1192.

Kiener, D., Grosinger, W., Dehm, G., 2009a. On the importance of sample compliance in uniaxial microtesting. Scr Mater 60, 148–151.

Kiener, D., Grosinger, W., Dehm, G., Pippan, R., 2008a. A further step towards an understanding of size-dependent crystal plasticity: In situ tension experiments of miniaturized single-crystal copper samples. Acta Mater 56, 580–592.

Kiener, D., Motz, C., Dehm, G., 2008b. Dislocation-induced crystal rotations in micro-compressed single crystal copper columns. J Mater Sci 43, 2503–2506.

Kiener, D., Motz, C., Dehm, G., 2009b. Micro-compression testing: A critical discussion of experimental constraints. Mater Sci Eng: A 505, 79–87.

Kiener, D., Motz, C., Dehm, G., Pippan, R., 2009c. Overview on established and novel FIB based miniaturized mechanical testing using in-situ SEM. Int J Mater Res 100, 1074–1087.

Kiener, D., Motz, C., Schoberl, T., Jenko, M., Dehm, G., 2006. Determination of mechanical properties of copper at the micron scale. Adv Eng Mater 8, 1119–1125.

Kim, J., Jang, D., Greer, J. R., 2009. Insight into the deformation behavior of niobium single crystals under uniaxial compression and tension at the nanoscale. Scr Mater 61, 300–303.

Koch, C. C., 2003. Optimization of strength and ductility in nanocrystalline and ultrafine grained metals. Scr Mater 49, 657–662.

Kocks, U. F., Argon, A. S., Ashby, M. F., 1975. Thermodynamics and kinetics of slip. Progr Mater Sci 19, 1–289.

Kocks, U. F., Mecking, H., 2003. Physics and phenomenology of strain hardening: The FCC case. Progr Mater Sci 48, 171–273.

Kubin, L. P., Canova, G., 1992. The modeling of dislocation patterns. Scr Metall. 27, 957–962.

Kubin, L. P., Canova, G., Condat, M., Devincre, B., Pontikis, V., Bréchet, Y., 1992. Dislocation microstructures and plastic flow: a 3d simulation. Solid State Phenomena 23–24, 455–472.

Kuhlmann-Wilsdorf, D., 1999. The theory of dislocation-based crystal plasticity. Phil Mag 79, 955–1008.

Kumar, K. S., Van Swygenhoven, H., Suresh, S., 2003. Mechanical behavior of nanocrystalline metals and alloys. Acta Mater 51, 5743–5774.

Kumar, R., Nicola, L., Van der Giessen, E., 2009. Density of grain boundaries and plasticity size effects: A discrete dislocation dynamics study. Mater Sci Eng: A 527, 7–15.

Lefebvre, S., Devincre, B., Hoc, T., 2007. Yiled stress strengthening in ultrafine-grained metals: A two-dimensional simultion of dislocation dynamics. J Mech Phys Solids 55, 788–802.

Lemarchand, C., Devincre, B., Kubin, L. P., 2001. Homogenization method for a discrete-continuum simulation of dislocation dynamics. J Mech Phys Solids 49, 1969–1982.

Li, Z., Hou, C., Huang, M., Ouyang, C., 2009. Strengthening mechanism in micro-polycrystals with penetrable grain boundaries by discrete dislocation dynamics simulation and hall-petch effect. Comp Mater Sci 46, 1124–1134.

Maass, R., Van Petegem, S., Grolimund, D., H., V. S., Kiener, D., Dehm, G., 2008. Crystal rotation in Cu single crystal micropillars: In situ Laue and electron backscatter diffraction. Appl Phys Lett 92, 071905.

Maass, R., Van Petegem, S., Grolimund, D., Van Swygenhoven, H., Uchic, M. D., 2007. A strong micropillar containing a low angle grain boundary. Appl Phys Lett 91, 131909(1–3).

Maier, H. J., P., G., Gupta, N., Karaman, I., Haouaoui, M., 2006. Cyclic stress-strain response of ultrafine grained copper. Int J Fatigue 28, 243–250.

McDowell, D. L., 2008. Viscoplasticity of heterogeneous metallic materials. Mater Sci Eng:R 62, 67–123.

Mecking, H., Kocks, U. F., 1981. Kinetics of flow and strain-hardening. Acta Metall 29, 1865–1875.

Meyers, M. A., Mishra, A., Benson, D. J., 2006. Mechanical properties of nanocrystalline materials. Progr Mater Sci 51, 427–556.

Miller, R., Shilkrot, L. E., Curtin, W. A., 2004. A coupled atomistics and discrete dislocation plasticity simulation of nanoindentation into single crystal thin films. Acta Mater 52, 271–284.

Motz, C., Schoberi, T., Pippan, R., 2005. Mechanical properties of micro-sized copper bending beams machined by the focused ion beam technique. Acta Mater 53, 4269–4279.

Mughrabi, H., 1983. Dislocation wall and cell structures and long-range internal stresses in deformed metal crystals. Acta Metall 31, 1367–1379.

Nagdhi, P. M., 1990. A critical review of the state of finite plasticity. J Appl Math Phys 41, 316–394.

Ng, K. S., Ngan, A. H. W., 2008a. A monte carlo model for the intermittent plasticity of micro-pillars. Modelling Simul Mater Sci Eng 16, 055004.

Ng, K. S., Ngan, A. H. W., 2008b. Stochastic nature of plasticity of aluminum micro-pillars. Acta Mater 56, 1712–1720.

Nicola, L., Xiang, Y., Vlassak, J. J., Van der Giessen, E., Needleman, A., 2006. Plastic deformation of freestanding thin films: Experiments and modeling. J Mech Phys Solids 54, 2089–2110.

Nix, W. D., Gao, H., 1998. Indentation size effects in crystalline materials: A law for strain gradient plasticity. J Mech Phys Solids 46, 411–425.

Norfleet, D. M., Dimiduk, D. M., Polasik, S. J., Uchic, M. D., Mills, M. J., 2008. Dislocation structures and their relationship to strength in deformed nickel micro-crystals. Acta Mater 56, 2988–3001.

Nye, J. F., 1953. Some geometrical relations in dislocated crystals. Acta Metall 1, 153–162.

Ohno, N., Okumura, D., 2007. Higher-order stress and grain size effects due to self-energy of geometrically necessary dislocations. J Mech Phys Solids 55, 1879–1898.

Orowan, E., 1934. Zur kristallplastizitat. iii. uber den mechanismum des gleituorganges. Z Phys 89, 634–659.

Petch, N. J., 1953. The cleavage strength of polycrystals. J Iron and Steel Institution 174, 25–28.

Polanyi, V. M., 1922. Rontgenographische bestimmung von kristallanordnungen. Naturwissenschaften 10, 411–416.

Polanyi, V. M., 1934. Uber eine art gitterstorung, die einen kristall plastisch machen konnte. Z Phys 89, 660–664.

Prinz, F., Argon, A. S., 1980. Dislocation Cell Formation during Plastic Defomation of Copper Single Crystals. Phys. Status Solidi 57, 741–753.

Purswani, J. M., Spila, T., D, G., 2006. Growth of epitaxial Cu on Mg0(001) by magnetron sputter deposition. Thin Solid Films 515, 1166–1170.

Rao, S. I., Dimiduk, D. M., Parthasarathy, T. A., Uchic, M. D., Tang, M., Woodward, C., 2008. Athermal mechanisms of size-dependent crystal flow gleaned from three-dimensional discrete dislocation simulations. Acta Mater 56, 3245–3259.

Rao, S. I., Dimiduk, D. M., Tang, M., Parthasarathy, T. A., Uchic, M. D., Woodward, C., 2007. Estimating the strength of single-ended dislocation sources in micrometer-sized single crystals. Phil Mag 87, 4777–4794.

Roy, A., Acharya, A., 2006. Size effects and idealized dislocation microstructure at small scales: Predictions of a phenomenological model of mesoscopic field dislocation mechanics: Part ii. J Mech Phys Solids 54, 1711–1743.

Schmid, E., 1924. Bemerkungen über die plastiche deformation von kristallen. Z für physik 22, 328–333.

Senger, J., Weygand, D., Gumbsch, P., Kraft, O., 2008. Discrete dislocation simulations of the plasticity of micro-pillars under uniaxial compression. Scr Mater 58, 587–590.

Shan, Z. W., Mishra, R. K., Asif, S. A. S., Warren, O. L., Minor, A. M., 2008. Mechanical annealing and source-limited deformation in submicrometer-diameter ni crystals. Nat Mater 7, 115–119.

Sinclair, C. W., Saada, G., Embury, J. D., 2006. Role of internal stresses in co-deformed two-phase materials. Phil Mag 86, 4081–4098.

Spearing, S. M., 2000. Materials issues in microelectromechanical systems (MEMS). Acta Mater 48, 179–196.

Stölken, J. S., Evans, A. G., 1998. A microbend test method for measuring the plasticity length scale. Acta Mater 46, 5109–5115.

Suzuki, H., Ikeda, S., Takeuchi, S., 1956. Deformation of thin copper crystals. J Phys Soc Jpn 11, 382–393.

Swadener, J. G., George, E. P., Pharr, G. M., 2002. The correlation of the indentation size effect measured with indenters of various shapes. J Mech Phys Solids 50, 681–694.

Tang, H., Schwarz, K. W., Espinosa, H. D., 2007. Dislocation escape-related size effects in single-crystal micropillars under uniaxial compression. Acta Mater 55, 1607–1616.

Tang, H., Schwarz, K. W., Espinosa, H. D., 2008. Dislocation-source shutdown and the plastic behavior of single-crystal micropillars. Phys Rev Lett 100, 185503–4.

Taylor, G. I., 1934. The mechanism of plastic deformation of crystals. Proc Roy Soc London A 145, 362–387.

Taylor, G. I., 1938. Plastic strain in metals. J Inst Metals 62, 307–324.

Taylor, G. I., Elam, C. F., 1925. The plastic extension and fracture of aluminum crystals. Proc Roy Soc London A 108, 28–51.

Uchic, M. D., Dimiduk, D. M., Florando, J. N., Nix, W. D., 2004. Sample dimensions influence strength and crystal plasticity. Science 305, 986–989.

Uchic, M. D., Shade, P. A., Dimiduk, D. M., 2009. Plasticity of micrometer-scale single crystals in compression. Annu. Rev. Mater. Res 39, 361–386.

Van der Giessen, E., Needleman, A., 1995. Discrete dislocation plasticity: A simple planar model. Modelling Simul Mater Sci Eng 3, 689–735.

Van Swygenhoven, H., Spaczer, M. Caro, A., 1999. Microscopic description of plasticity in computer generated metallic nanophase samples: A comparison between cu and ni. Acta Mater 47, 3117–3126.

Verdier, M., Huang, H., Spaepen, F., Embury, J. D., Kung, H., 2006. Microstructure, indentation and work hardening of Cu/Ag multilayers. Phil. Mag. 86, 5009–5016.

Volkert, C. A., Lilleodden, E. T., 2006. Size effects in the deformation of sub-micron Au columns. Phil Mag 86, 5567–5579.

von Blanckenhagen, B., Gumbsch, P., Arzt, E., 2001. Dislocation sources in discrete dislocation simulations of thin-film plasticity and the hall-petch relation. Modelling Simul Mater Sci Eng 9, 157–169.

Weertman, J., 2002. Some unresolved issues concerning mechanical behavior of nanocrystalline metals. In: Ma, E and Atzmon, M and Koch, CC (Ed.), Metastable, mechanically alloyed and nanocrystalline materials. Vol. 386-3 of Mater Sci For. pp. 519–520.

Weygand, D., Poignant, M., Gumbsch, P., Kraft, O., 2008. Three-dimensional dislocation dynamics simulation of the influence of sample size on the stress-strain behavior of fcc single-crystalline pillars. Mater Sci Eng: A 483, 188–190.

Wolf, D., Yamakov, V., Phillpot, S. R., Mukherjee, A., Gleiter, H., 2005. Deformation of nanocrystalline materials by molecular-dynamics simulation:relationship to experiments. Acta Mater 53, 1–40.

Xiang, Y., Vlassak, J. J., 2006. Bauschinger and size effects in thin-film plasticity. Acta Mater 54, 5449–5460.

Yamakov, V., Wolf, D., Phillpot, S. R., Mukherjee, A. K., Gleiter, H., 2004. Deformation-mechanism map for nanocrystalline metals by molecular-dynamics simulation. Nat Mater 3, 43–47.

Zbib, H., Rhee, M., Hirth, J. P., 1998. On plastic deformation and the dynamics of 3D dislocations. Int. J. Mech. Sci. 40, 113–127.

Zhang, H., Schuster, B. E., Wie, Q., Ramesh, K. T., 2006. The design of accurate micro-compression experiments. Scr Mater 54, 181–186.

Zhang, X., Wang, H., Koch, C. C., 2004. Mechanical behavior of bulk ultrafine-grained and nanocrystalline zn. Rev Adv Mater Sci 6, 53–93.

Zhou, C., Biner, S. B., LeSar, R., 2010. Discrete dislocation dynamics simulations of plasticity at small scales. Acta Mater 58, 1565–1577.

APPENDIX A

SPATIAL DISTRIBUTION AND TEMPORAL EVOLUTION OF GND DENSITY

Using Eq. (2.18), maps of spatial distribution of GND density can be generated at desired resolution. Define a uniform and structured grid on body Ω; for example, the finite-element mesh used for computing the image fields is one such grid. The grid element size sets the resolution. The element-level values of GND density are then extrapolated to the nodes of the grid, which allows to generate contours of GND density. Because of the structured topology of the grid, we will exclusively use Eq. (2.18) in generating GND maps. GND density contours provide snapshots of the frozen dislocation structure.

Fig. 67 shows contours of ρ_{GND} in four specimens having different sizes, keeping the same resolution of $50 \times 50\text{nm}^2$. The nominal compressive strain $\varepsilon \equiv \varepsilon_{11}$, i.e., the imposed axial displacement per specimen length, is 0.06. Examples of dislocation structures are shown in Fig. 10 and are not superposed on the contours for clarity. Because of the double-slip configuration, dislocation intersections and subsequent reactions are more likely to occur in the central region of the specimens where stresses are also found to be higher. In sufficiently large specimens (Figs. 67a,b) the areas close to the two extreme slip plane intersections are preferred regions of high GND density. Out of these fan out narrow bands of relatively high GND density. In the continuum limit, these bands may be thought of as "weak shocks" in the sense that GND density jumps occur across them but displacements and stresses remain continuous.

With decreasing specimen size the dislocation structure no longer develops as it would had the free surfaces been farther apart from each other. This trend is clearly seen in Fig. 67 as one goes from the top specimen ($H = 12.8\mu\text{m}$ in (a)) to the
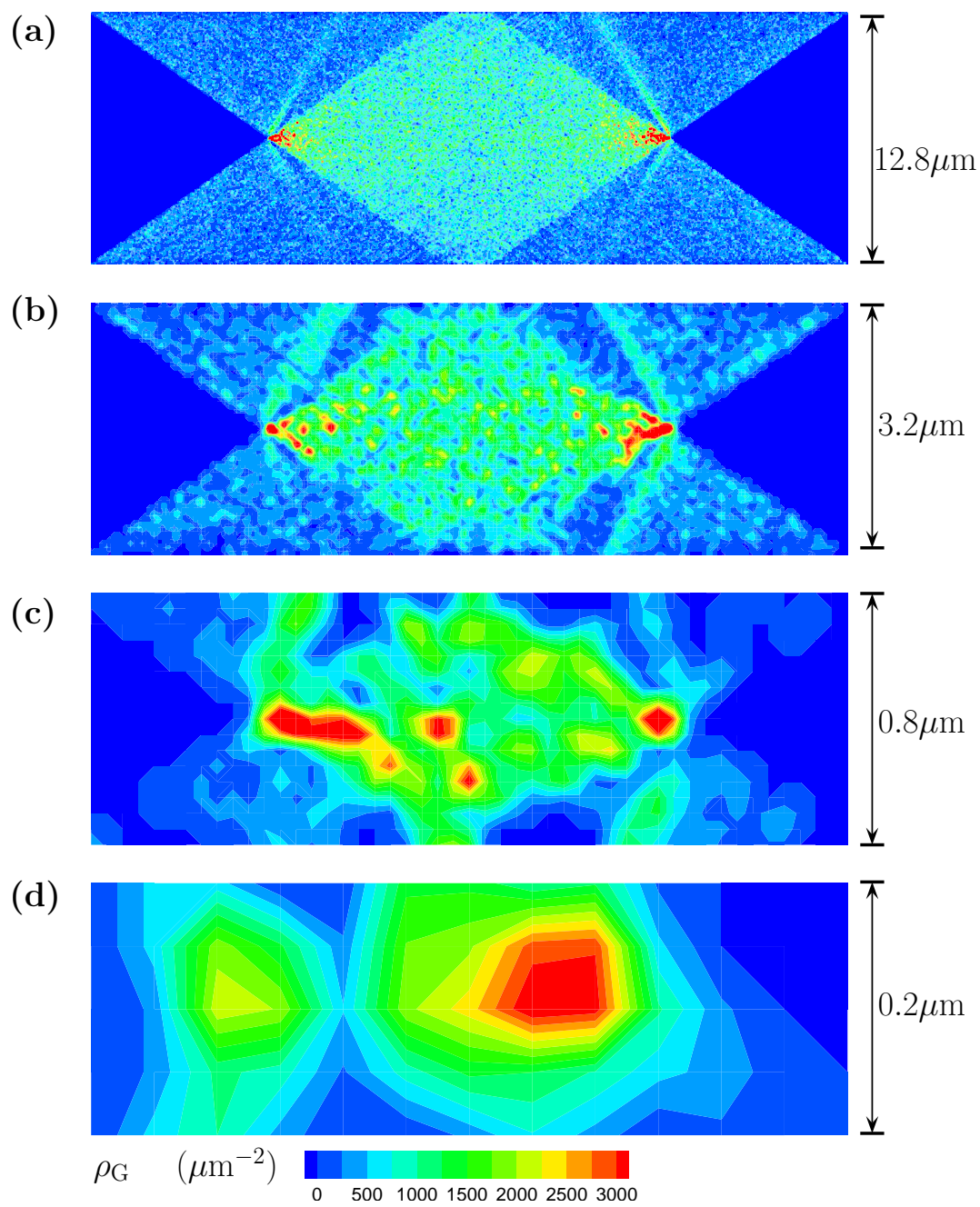
Fig. 67. Contours of GND density at $\varepsilon = 0.06$ in crystals of height (a) $H = 12.8$ μm; (b) $H = 3.2$ μm; (c) $H = 0.8$ μm; and (d) $H = 0.2$ μm.

bottom one ($H = 0.2\mu m$ in (d)). In particular, the peculiar spatial distribution of GND density shown in Figs. 67a,b completely disappears in Fig. 67d where the GND density maximum moves toward the center of the specimen.

The evolution of effective GND density, $\bar{\rho}_G$, as predicted from simulations is shown in Fig. 68. The effective GND density, $\bar{\rho}_G$, is computed from Eq. (2.19) using a resolution area of 50×600 nm^2 in all the simulations. It is emphasized here that the results are resolution-dependent but general trends remain the same. For a given resolution and topology, $\bar{\rho}_G$ is found to increase at a faster rate in smaller specimens as shown in Fig. 68. To highlight the scatter associated with very small samples simulation results from two realizations of the $H = 0.2$ μm specimen is shown. The value of the $\bar{\rho}_G$ is found to be as large as 40% of the total dislocation density in the $H = 0.2$ μm specimen while in the $H = 12.8$ μm specimen it is found to be 16%. This build-up of $\bar{\rho}_G$ takes place while there is essentially no net accumulation of GND density in the specimens.

From Fig. 68 we observe that the effective GND density increases with strain. However, their ratio, $\bar{\rho}_G/\rho$, remains nearly constant with strain as shown in Fig. 69. Overall a trend emerges where $\bar{\rho}_G/\rho$ increases with decrease in specimen size. Two different realizations are shown for the specimen with size $H = 0.2$ μm to highlight the scatter in very small samples.

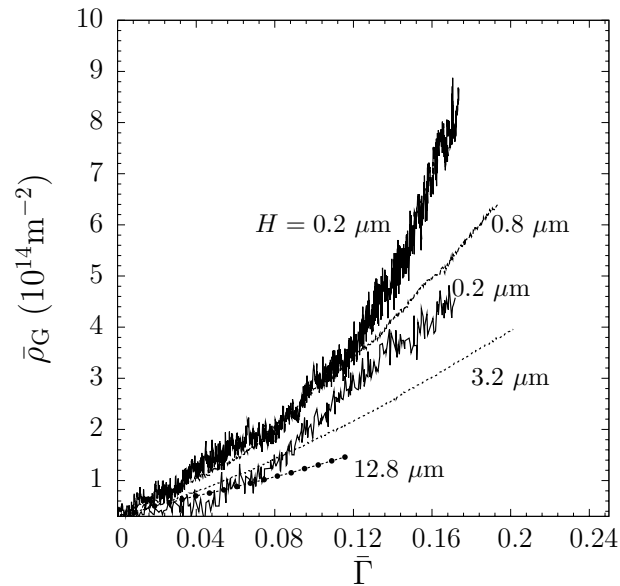Fig. 68. Evolution of the effective GND density, $\bar{\rho}_{\mathrm{G}}$, with cumulated slip, $\bar{\Gamma}$, for specimens with size $H = 0.2$ μm, 0.8 μm, 3.2 μm, and 12.8 μm. Cumulated slip: $\bar{\Gamma} = \left(\varepsilon - \sigma/\bar{E}\right)/f_s$; where, $\bar{E}$ is the plane strain elastic modulus.

Fig. 69. Evolution of the effective GND density, $\bar{\rho}_{\mathrm{G}}$, normalized by the total dislocation density, ρ, with cumulated slip, $\bar{\Gamma}$ for specimens with size $H = 0.2$ μm, 0.8 μm, 3.2 μm, and 12.8 μm. Cumulated slip: $\bar{\Gamma} = \left(\varepsilon - \sigma/\bar{E}\right)/f_s$; where, $\bar{E}$ is the plane strain elastic modulus.
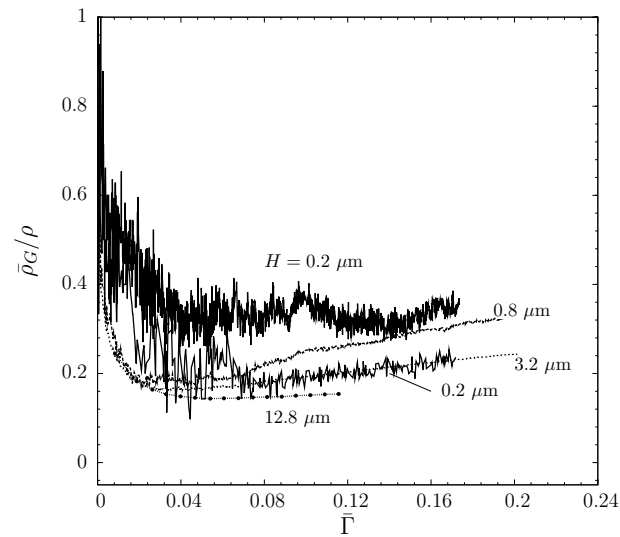
VITA

Guruprasad Padubidri Janardhanachar was born in the southern state of India, Karnataka. He obtained his Bachelor of Engineering degree in mechanical engineering from B. M. Sreenivasaiah College of Engineering, Bangalore, India. Subsequently, he did his Master of Science studies in aerospace engineering from the Indian Institute of Science, Bangalore, India. He arrived at College Station, Texas in the fall of 2005 to pursue doctoral degree in aerospace engineering at Texas A&M University and graduated with his Ph.D. in May 2010. During his stay in the graduate school, he has worked as a teaching assistant and as a research assistant in the Department of Aerospace Engineering. His primary research interest is in the broad area of computational materials science. Following his PhD, he will be working as a Post Doctorate at Centre des Matériaux, École des Mines de Paris, Paris, France. He may be contacted via email at: pjguru@gmail.com.

Mailing address:

Guruprasad, P. J.

Texas A&M University,

Department of Aerospace Engineering,

H. R. Bright Building, # 701, Ross Street - TAMU 3141,

College Station, TX 77843-3141

The typist for this thesis was Guruprasad Padubidri Janardhanachar.